Numerical Computation of Capillary Bridges between Directly Resolved Rough Interfaces

zur Erlangung des akademischen Grades DOKTORS DER INGENIEURWISSENSCHAFTEN (Dr.-Ing.) der Fakultät für Maschinenbau
der Universität Paderborn

genehmigte
DISSERTATION

von

Dr.-Ing. Melanie Gräßer

aus Wadern

Tag des Kolloquiums: 24. März 2023
Referent: Prof. Dr.-Ing. Hans-Joachim Schmid
Korreferent: Prof. Dr. Hans-Jürgen Butt

Acknowledgement

Ich bedanke mich bei meinem Doktorvater, Prof. Dr.-Ing. Hans-Joachim Schmid, für die Begleitung auf dem Weg der Promotion. Hajo, vielen Dank für die unzähligen konstruktiven Diskussionen und das stets kritische Hinterfragen der vielen Ansätze, die wir ausprobiert haben. Und vor allem vielen Dank dafür, dass du mir -gerade, wenn es mal nicht so gut lief- immer die Zuversicht gegeben hast, dass am Ende eine gute Arbeit entstehen wird. Ich habe sowohl fachlich als auch zwischenmenschlich sehr viel von dir lernen dürfen, vielen Dank dafür.
Ein besonderer Dank gilt Stefan Schmidt für die unglaublich spannende und konstruktive Zusammenarbeit. Stephan, vielen Dank für die unzähligen Diskussionen und gemeinsamen Arbeitsstunden, bis teilweise spät in die Nacht hinein. Ich danke dir außerdem für deine Geduld, mir die „echte“ Mathematik in einer für eine Ingenieurin verständlichen Sprache näher zu bringen. Ich habe sehr viel von dir lernen dürfen und die Zusammenarbeit mit dir wird meine Denkweise als Wissenschaftlerin immer prägen.
Neben der fachlichen Herausforderung hat das Verfassen dieser Arbeit für mich auch bedeutet, immer wieder mit Rückschlägen umzugehen. Ein großer Dank gilt hier Ulrike. Du hast mir immer ein offenes Ohr geschenkt, wenn ich es gebraucht habe und mich daran erinnert, dass ich einfach nur weiter gehen muss. Ganz besonders möchte ich mich auch bei Christina bedanken. Danke, dass du immer für mich da bist und mich fast ein halbes Jahr lang jeden Mittag angerufen hast, um dafür zu sorgen, dass ich eine halbe Stunde lang nicht auf meinen Bildschirm schaue. Du zeigst mir, dass Nähe und Entfernung keine Gegensätze sind und ich bin unglaublich dankbar, dass es dich in meinem Leben gibt. Außerdem möchte ich mich bei Akif bedanken, dafür, dass du mich aus meiner Wohnung raus geholt und zum Laufen animiert hast. Und vielen Dank, dass du dir dabei so interessiert meine ganzen Monologe über Dreiecke und deren Eigenschaften angehört hast. Ohne euch hätte ich den Stress und den Druck in der Endphase dieser Arbeit nicht bewältigt.
Abschließend möchte ich mich noch bei meiner Familie bedanken. Mama, Papa, Raphael und Timo, danke, dass ihr mich auf diesem Weg begleitet und mir immer wieder den Rücken gestärkt und frei gehalten habt. Ihr habt mir das Selbstvertrauen, die Zeit und die Ruhe gegeben, mich auf diese Arbeit zu konzentrieren. Ich habe euch lieb und freue mich, jetzt auch wieder mehr Zeit für euch zu haben.

Paderborn, 29. März 2023

Abstract

A novel method to compute capillary forces between directly resolved rough interfaces is presented. In particular, the free energy of the considered system is numerically minimized constrained to a predefined volume and given solid boundary. A good agreement between the novel algorithm and well known solutions for smooth interfaces is demonstrated. The investigation of rough interfaces requires a statistical approach since the integral root mean square roughness (RMS) exhibits an infinite number of realizations. It turns out that the accuracy of the mean capillary force is sufficiently good, whereas the statistical uncertainty of the standard deviation is dissatisfying. The application of the novel method to capillary bridges between a rough sphere and a smooth plate reveals complex and highly non-linear dependencies between the force distribution and the classical parameters, i.e., volume, gap distance and contact angle. In contrast, the relation between the standard deviation and the RMS is observed to be linear which is also pointed out for sphere-sphere systems, provided that one interface is smooth or both interfaces exhibit the same roughness. Finally, the results are discussed with respect to their application within a multi-scale DEM.

Zusammenfassung

Es wird eine neue Methode zur Berechnung von Kapillarkräften zwischen direkt aufgelösten rauen Oberflächen entwickelt. Hierfür wird die freie Energie des Systems unter den Nebenbedingungen eines konstanten Volumens und der vorgegebenen Festkörperoberflächen numerisch minimiert. Die grundsätzliche Eignung der Methode wird durch einen Vergleich mit Lösungen aus der Literatur gezeigt. Die Analyse von Kapillarbrücken zwischen rauen Oberflächen erfordert einen statistischen Ansatz, da die mittlere Rauheit durch eine unendliche Anzahl von Oberflächen realisiert werden kann. Es zeigt sich, dass der Mittelwert der Kapillarkraft mit guter Genauigkeit berechnet wird, wohingegen die statistische Unsicherheit der Standardabweichung nicht zufriedenstellend ist. Simulationen von Kapillarbrücken zwischen einer rauen Kugel und einer glatten Wand zeigen komplexe, nichtlineare Zusammenhänge zwischen der Kraftverteilung und den klassischen Parametern Volumen, Spaltabstand und Kontaktwinkel. Im Gegensatz dazu wird sowohl für das Kugel-Wand-System als auch für Kugel-Kugel-Systeme ein linearer Zusammenhang zwischen der Standardabweichung und der mittleren Rauheit beobachtet, sofern eine der beiden Oberflächen glatt ist oder beide die gleiche Rauheit aufweisen. Abschließend werden die Ergebnisse in Hinblick auf ihre Anwendbarkeit innerhalb einer mehrskaligen DEM bewertet.

List of previous publications

Related to this work

M. Gräßer, S. Schmidt, H.-J. Schmid. „Simulation of liquid Capillary Bridges between rough spheres“. In: *Journal of Colloid and Interface Science*
Submitted in January 2023

S. Schmidt, M. Gräßer, H.-J. Schmid. „Shape Newton Scheme for Deforming Shells with Application to Capillary Bridges“. In: *SIAM: Journal on Scientific Computing* 44.4 (2022)

Other publications

M. Gräßer, L. A. Bentrup, K. Temmen, H.-J. Schmid. „Entwicklung eines neuen Konzeptes zur Vermittlung von Lerntechniken und Selbstlernkompetenzen für Studierende des Maschinenbaus an der Universität Paderborn“. In: *Die Hochschullehre* Submitted (June, 2020), Waiting for final decision

M. Gräßer, A. Brümmer. „Influence of water and oil clearance flow on the operational behavior of screw expanders“. In: *Journal of process mechanical engineering* 231 (1) (2017)

M. Gräßer, A. Brümmer. „Influence of liquid in clearances on the operational behavior of twin screw expanders“. In: *9th International Conference on Compressors and their Systems, IOP Conf. Series: Materials Science and Engineering.* 90 012060 (2015)

M. Gräßer, A. Brümmer. „An analytic model of the incompressible one-phase clearance flow in liquid injected screw expanders“. In: *9th International Conference on Screw Machines 2014, VDI Bericht 2228* Pages 71-89 (2014)

Contents

Lists of symbols, operators, indices and abbreviations

Symbols

Symbol	Definition	SI Unit
A	area	m^2
$\mathcal{A}$	Hamaker constant	$kg{\cdot}m^2{\cdot}s^{-2}$
a	shortest distance between interfaces	m
a	acceleration	$m\ {\cdot}s^{-2}$
Bo	Bond number	-
C	continuous function	
Ca	Capillary number	-
CI_u	confidence interval of u	-
c	level-set	m
c_0, c_1, c_2	constants of a parabolic function	-
D	test statistic	-
E	total free energy	$kg{\cdot}m^2{\cdot}s^{-2}$
F_H	Helmholtz free energy	$kg{\cdot}m^2{\cdot}s^{-2}$
F	force	$kg{\cdot}m{\cdot}s^{-2}$
F_c	capillary force	$kg{\cdot}m{\cdot}s^{-2}$
F_i	interparticle force	$kg{\cdot}m{\cdot}s^{-2}$
F_p	pressure force	$kg{\cdot}m{\cdot}s^{-2}$
F_s	surface tension force	$kg{\cdot}m{\cdot}s^{-2}$
F_{vdw}	van der Waals force	$kg{\cdot}m{\cdot}s^{-2}$
f_1, f_2	fractional area	-
g	gravitational acceleration	$m{\cdot}s^{-2}$
H	mean curvature	m^{-1}
H_0	null hypothesis	-
h	height	m

I	moment of inertia	$\mathrm{kg{\cdot}m^2{\cdot}s^{-2}}$
K	Gauss curvature	$\mathrm{m^{-1}}$
k	iteration step	-
k	van der Waals coefficient	-
L	characteristic length	m
L	line	m
l	length	m
l_g	length in gravitational direction	m
m	mass	kg
n	number of samples	-
n	number of solid interfaces	-
n	amount of substance	-
n_t	number of mesh triangles	-
$\mathbf{n}$	unit normal vector	-
P	probability	%
p	pressure	$\mathrm{kg{\cdot}m^{-1}{\cdot}s^{-2}}$
p_i	inner pressure	$\mathrm{kg{\cdot}m^{-1}{\cdot}s^{-2}}$
p_o	outer pressure	$\mathrm{kg{\cdot}m^{-1}{\cdot}s^{-2}}$
p_v	vapor pressure	$\mathrm{kg{\cdot}m^{-1}{\cdot}s^{-2}}$
$\mathcal{R}$	universal gas constant	$\mathrm{kg{\cdot}m^2{\cdot}s^{-2}{\cdot}mol^{-1}{\cdot}K^{-1}}$
R	particle radius	m
R_f	roughness ratio	-
R_a	2D mean average height	m
R_q	2D root mean square roughness	m
$R_\mathrm{p}, R_\mathrm{v}, R_\mathrm{z}$	2D peak, valley and surface height	m
r	radius	m
r_d	droplet radius	m

r_H	mean radius of curvature	m
r_1, r_2	radii of principal curvature	m
S	entropy	$\mathrm{kg{\cdot}m^2{\cdot}s^{-2}\ K^{-1}}$
S_a	3D mean average height	m
S_q	3D root mean square roughness	m
$S_\mathrm{p}, S_\mathrm{v}$, S_z	3D peak, valley and surface height	m
S_dr	area fraction	-
s	sample standard deviation of $\tilde{F}_\mathrm{c}$	-
s_u	sample standard deviation of u	-
$\hat{s}$	relative sample standard deviation of $\tilde{F}_\mathrm{c}$	-
$\mathbf{s}$	position vector of vertex	m
T	temperature	K
t	time	s
U	electric potential	V
u	parameter	-
u	random parameter	-
V	volume	$\mathrm{m^3}$
V_0	target volume	$\mathrm{m^3}$
V_M	molar volume	$\mathrm{m^3{\cdot}mol^{-1}}$
v	arbitrary parameter	-
$\mathbf{V}$	vector field	-
$\mathbf{v}$	test function	-
W	work	$\mathrm{kg{\cdot}m^2{\cdot}s^{-2}}$
We	Weber number	-
x, y, z	cartesian coordinates	m
z, r, φ	cylindrical coordinates	m, m, rad
z	normally distributed random parameter	-

α	angle between Γ_{lg} and $\mathbf{F_c}$	rad
α	iteration step width	-
α	significance level	%
α	angular acceleration	rad $\cdot$s^{-2}
β	relative adhesion coefficient	-
Γ	interface shell	-
γ	incremental interface element	-
γ	confidence level	%
Δp	capillary pressure	kg$\cdot$m$^{-1}\cdot$s^{-2}
δ	Tolman length	m
ε	diffusion coefficient	-
θ	contact angle	rad
κ_1, κ_2	principal curvature	m^{-1}
λ	Lagrange multiplier	-
λ_{k}	Kelvin length	m
μ_{c}	chemical potential	kg$\cdot$m$^2\cdot$s^{-2}
μ_{u}	expected value of u	-
$\boldsymbol{\mu}$	co-normal unit vector	-
ξ	index of *python* function *random seed*	-
$\xi(\gamma)$	standard normal distributed value for γ	-
Π	calculation domain	-
π	mathematical constant Pi	-
ρ	density	kg$\cdot$m^{-3}
σ	surface tension	kg$\cdot$s^{-2}
σ_{u}	standard deviation of u	-
σ_0	surface tension at $T \to 0\,\mathrm{K}$	kg$\cdot$s^{-2}
σ_∞	surface tension for plain surfaces	kg$\cdot$s^{-2}

υ	sequence of random numbers	-
φ	relative humidity	-
φ	angle	rad
$\phi_{\max}$	charge density	$A{\cdot}s{\cdot}m^{-2}$
$\chi^2(\gamma)$	χ^2 distributed value of γ	-
ψ	filling angle	rad
Ω_{gp}	grand potential	$kg{\cdot}m^2{\cdot}s^{-2}$
Ω	body domain	
$\boldsymbol{\omega}$	displacement vector field	-

Operators and functions

Symbol	Definition
E^*	energy functional
d	total differential
$d[V]$	material derivative in the direction V
$F(u)$	function depending on function parameter u
$f(u)$	constraint depending on function parameter u
$f_{\mathrm{P}}(u)$	polynomial function of u
$h(x)$	spatial height function
Δ	difference
ϕ	level set function
Φ	CDF of the standard normal distribution
$\mathcal{L}$	Lagrange function
$\mathbb{R}$	set of real numbers
$\forall$	for all
$\in$	element of
∂	partial differential
∇	nabla operator
$\nabla_\Gamma \cdot$	tangential divergence
∞	infinity
$\subset$	subset
$\langle ., . \rangle$	canonical scalar product in $\mathbb{R}^3$
$:=$, $=:$	is defined as

Indices and accents

Index	Definition
a, b	homogeneous phases a and b
analytical	analytically computed value
a	asperity
C_6H_{12}	cyclohexane
CL	three-phase contact line
c	capillary
cb	Cassie Baxter [Cas44]
continuous	ideal values of a continuous geometry
crit	critical
discretized	numerical value of a discretized geometry
dörmann	Dörmann [Dör18]
ec	electric conductor
eff	effective
ei	electric isolator
emp	empirical
g	gas
H_2O	water
I	intersection
i	counter variable
j	counter variable
l	liquid
lg	liquid-gas
lv	liquid-vapor
m	number
ma	most accurate
max	maximum

n	number
new	new
old	old
orr	Orr et al. [Orr75]
r	rough
rel	relative
rm	remesh
sm	smooth
s	solid
se	selected
sg	solid-gas
sl	solid-liquid
t	target (pre-defined input value for optimization)
tan	tangential
theo	theorectial
this model	refers to values obtained by the presented model
u, v	lower and upper limit of a confidence interval
w	Wenzel [Wen36]
0	fixed reference value

$\tilde{}$	dimensionless form of parameter
$\bar{}$	mean value
$'$	first derivative with respect to space
$''$	second derivative with respect to space
$^+$	convex meniscus
$^-$	concave meniscus
$\mathbf{v}$	vector v indicated by bold symbol
$\hat{\mathbf{M}}$	matrix M indicated by bold symbol and circumflex accent

Abbreviations

Abbreviation	Definition
AFM	atomic force microscopy
cat	catenoid
CDF	cumulative distribution function
CFD	computational fluid dynamics
CFL	Courant–Friedrichs–Lewy number
CI	confidence interval
CMC	constant mean curvature
const.	constant
cs	converged simulations
cyl	cylinder
DEM	discrete element method
FECO	fringes of equal chromatic order
H_2O	water
nod	nodoid
ODE	ordinary differential equation
OTE	N-octadecyltrimethoxysilane
q-q-plot	quantile-quantile-plot
RMS	root mean square roughness
SFA	surface force apparatus
SiO_2	silicon dioxide
s.t.	subject to
sph	sphere
und	unduloid

Convention for the box plots

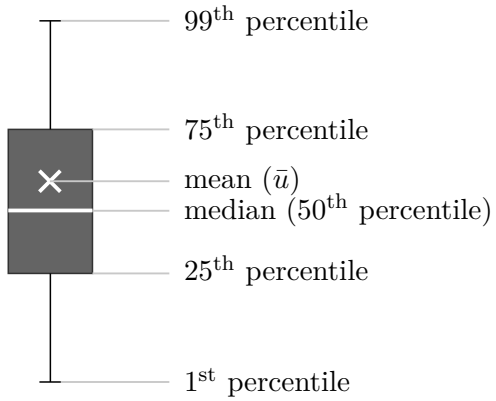

1. Introduction

Surface tension is a significant physical effect in nature, although it is frequently not consciously perceived. In fact, surface tension enables insects to walk on water and droplets to be ideally spherical under zero gravity. Moreover, the famous Lotus effect, i.e., the very low wetting of an interface, that is observed at the Nelumbo plant, is caused by surface tension. With respect to solid interfaces, the formation of a liquid meniscus, i.e., a capillary bridge, between these interfaces is observed, which causes an interaction force, i.e., the capillary force. In large systems usually forces such as gravity and inertia are dominant and the capillary forces are negligible. However, when downsizing a system, capillary forces as well as other interparticle forces become relevant for the characteristics of the system. A frequently considered example is the build of a sand castle: Dry sand simply tickles down and no sand castle can be build. In contrast, wet sand is malleable since the sand grains stick together, which is traced back to the occurrence of capillary forces between the grains.
Besides this ordinary and illustrative example, capillary forces are important in many industrial applications. The handling of wet powder and granular material is significantly determined by capillary forces. In particular, the appearance of capillary bridges reduces the flowability of bulk materials which can be either desired or undesired depending on the specific application [Grö03; Koh04; Lu07; Sch13; Sou06]. Furthermore, capillary bridges can be used for micro assembling. It is demonstrated, that the capillary force depends on the tilting angle of the tip, which, consequently, can be used to adjust the capillary force and to release and pick up very small objects [Cha07; Cha10]. Another interesting application is the development of capillary force actuators. Here, the contact angle is decreased by an electrical potential which leads to an increasing capillary force [Kno12]. By this technology, adhesive forces that are up to 100 times larger compared to conventional electrostatic actuators can be obtained [Kno12].
Due to this highly technical relevance, a detailed understanding and modeling of capillary forces is necessary. From experimental investigations it is concluded, that the menisci of the capillary bridges are very sensitive towards the geometry of the solid interface. In particular, roughness is assumed to significantly influence the

capillary forces. However, the complex governing equations have only been solved under strongly simplifying assumptions with respect to the particle geometry. In fact, most of the models consider an axisymmetric meniscus which implies a smooth solid interface. Theses simplified approaches are used to develop more complex models that involve roughness, for example by considering multiple menisci between several asperities. However, to the best of the authors knowledge, a method to compute menisci between directly resolved rough interfaces does not exist yet.
Thus, the main goal of this work is the development of a method that allows the simulation between arbitrarily shaped interfaces. In particular, the method should be capable of resolving high frequent rough solid interfaces. Therefore, the physical background of capillarity is described first (chapter 2). Subsequently, the state of the art and research of capillary bridges is presented (chapter 3). In particular, the existing simulation methods and rough force models are discussed. Based on this intensive review, the requirements of the novel method are specified more precisely (chapter 4). The capillary bridge model comprises the physical model as well as the mathematical formulation of the problem (chapter 5). Moreover, the complex numerical implementation is discussed, which is tailor-made for the capillary bridge problem. Since the developed method is completely novel, a intensive evaluation including a verification and an estimation of the numerical and statistical error is pointed out (chapter 6). Subsequently, capillary forces in rough sample systems, i.e., sphere-plate and sphere-sphere systems, are investigated and characteristic diagrams for the mean capillary force and the standard deviation are obtained (chapter 7). Finally, the existence, uniqueness and stability of the presented capillary bridges is discussed (chapter 8). Moreover, the results are particularly interesting with respect to an application in a discrete element method (DEM). Thus, the suitability for such a multi-scale approach is analyzed. Moreover, the hands-on experiences with the novel algorithm reveal optimization potential for the implemented algorithm which is described and should be considered for future work.

2. Physical background of capillarity

There is no uniform definition of capillarity in the literature. Traditionally, capillarity describes „the tendency of wetting liquids to be drawn into the confined space of a narrow tube or between at least two surfaces“ [van10]. A more general definition implies the existence of a meniscus, which is a curved liquid-gas interface [van10]. Similarly, Schubert [Sch82] states, that capillarity describes the surface tension dependent behavior of liquids and requires a phase interface. Moreover, capillarity is defined as „the study of the interfaces between two immiscible liquids, or between a liquid and air“ [Gen10]. In this work liquid capillary bridges between solid particles in a gaseous surrounding are analyzed, which is a capillary phenomenon according to all given definitions. Thus, in order to describe capillary bridges, the basic principle and fundamental equations of capillarity are outlined in this chapter.
First, the Gibbs interface model for plain and curved interfaces is presented. The concepts of surface tension and the contact angle are explained and the fundamental equations, i.e., the Young-Laplace equation, the Young-Equation and the Kelvin-Equation, are described including their limits. For the case of solid-gas-liquid systems the contact angle is defined at the three-phase contact line and the basic models for complex wetting on rough interfaces are introduced. Finally, the Kelvin equation, that describes systems in thermodynamic equilibrium, is covered.

2.1. Interfaces and surface tension

An interface is defined as the transition between different phases or immiscible liquids. The particular case of a liquid-vacuum-interface or a solid-vacuum-interface is called surface. However, since the vacuum is a theoretical concept, one may stick to the more practical definition of surfaces describing the interface between a liquid and its own vapor [Sch82].
Interfaces are not sharp transitions from one phase to another, but regions whose extent can only be determined by definition. Outside the transition region the phases are homogeneous while inside a heterogeneous mixture with undefined state variables exists. Thus, describing processes with different phases requires an interface model. The most relevant model is presented by Gibbs [Gib93]. The volume extension of

the transition region normal to the phase change is several orders smaller compared to the parallel extension. Therefore, the volume is frequently modeled by a sharp interface area. According to Gibbs' idea, the phases are assumed to be completely homogeneous with a jump at a dividing interface located within the transition region.

2.1.1. Plain interfaces

A stationary system of the homogeneous phases a and b that are separated by plain interfaces and consists of j components can be described by Gibbs' fundamental equation [Gib93]

$$\mathrm{d}F_\mathrm{H} = -S\mathrm{d}T + \sigma\mathrm{d}A - p\mathrm{d}V + \sum_{i=1}^{n} \mu_{\mathrm{c,i}}\mathrm{d}n_\mathrm{i}, \tag{2.1}$$

where F_H is the Helmholtz free energy, S the system entropy, T the absolute temperature, σ the surface tension, A the interface area, $\mu_{\mathrm{c,i}}$ the chemical potential of component i and n_i the amount of substance of component i. The Gibbs equation is universal whereas specific values of the parameters depend on the definition of the dividing interface area within the transition region. For isothermal processes eq. (2.1) reduces to

$$\mathrm{d}F_\mathrm{H} - \sum_{i=1}^{n} \mu_{\mathrm{c,i}}\mathrm{d}n_\mathrm{i} = \mathrm{d}\Omega_\mathrm{gp} = \sigma\mathrm{d}A - p\mathrm{d}V \tag{2.2}$$

with the grand potential Ω_gp. Note, that stationary interfaces are not static [Lan02]. There is always an exchange of molecules from one phase to the other. In the stationary equilibrium case, the number of evaporating molecules equals the number of condensing molecules.

The concept of surface tension is described for the first time in 1751 by Segner [Seg51] and is explained by considering a molecule at the inner part of the liquid. This molecule is attracted by cohesive forces of other molecules in any direction. However, a molecule directly on the interface is only attracted on its liquid side while on the vapor side the number of interaction partners is drastically reduced. Thus, interface molecules have a higher potential energy compared to inner molecules. The second law of thermodynamics states, that a closed system in equilibrium maximizes the entropy at constant inner energy which is equivalent to minimize its free energy for constant volume and temperature [Dem14]. According to this principle, the number of interface molecules is minimized as well which is equivalent to minimize the interface area. Increasing the interface area means transporting molecules from inside the

liquid to the interface which requires energy. The total amount of work ∂W needed is proportional to the increase of the interface area ∂A and the proportionality factor σ defined as

$$\sigma \coloneqq \left(\frac{\partial W}{\partial A}\right)_{\mathrm{T,V,n}} \tag{2.3}$$

is the surface tension with n being the number of molecules [Gen10]. Note, that this definition implies ∂W to be reversible and isothermal [Sch82].
For surfaces the influence of the vapor on surface tension σ_{lv} is insignificant if the vapor pressure is not too high. Analogously, at liquid-gas-interfaces that do not react physically or chemically and exhibit a gas pressure around 1 bar, the influence of the gas phase can be neglected [Sch82]. Thus, if not stated otherwise, in this work the surface tensions at the liquid-vapor σ_{lv} and the liquid-gas interface σ_{lg} always refer to the surface tension of the liquid σ_{l} neglecting the influence of vapor or gas:

$$\sigma_{\mathrm{lv}} = \sigma_{\mathrm{lg}} = \sigma_{\mathrm{l}} =: \sigma \tag{2.4}$$

The surface tension of liquids can be accurately determined by experimental methods which are described in detail by Rusanov and Prokhorov [Rus96]. Moreover, a review on measurement methods for fluid-fluid-interfaces is given by Drelich et al. [Dre02]. The surface tensions of different liquids at a temperature of 293 K are listed in table 2.1. Due to its hydrogen bonds, the surface tension of water is high compared to other liquids. As already mentioned above, the influence of vapor or gas pressure is negligible for moderate pressures [Sch82] and will therefor not be discussed in detail. In contrast, the influence of temperature might be significant.
The surface tension of pure fluids decreases with increasing temperature which is explained by Padday [Pad69]. Intermolecular forces are lower at high temperatures due to higher molecule distances. Thus, less energy is needed to transport molecules from the inner part of the fluid to the interface. The temperature dependency of the surface tension of water $\sigma_{\mathrm{H_2O}}$ is presented in figure 2.1 (a) at temperatures from $274 - 310$ K. The experimental values of the database REFPROP [Lem18] are measured along the

Table 2.1.: Surface tension of different liquids at 293 K [Lem18]

	water	ammonia	ethanol	methanol	R123
σ [mN·m^{-1}]	72.759	26.423	22.433	22.686	15.788

saturation curve. However, due to the negligible influence of the vapor and gas pressure, they are sufficiently accurate for any gas pressure below 10 bar. It is shown that the van der Waals approximation

$$\sigma(T) = \sigma_0 \left(1 - \frac{T}{T_{\text{crit}}}\right)^k \tag{2.5}$$

agrees well with the database values. The constants of eq. (2.5) must be determined experimentally for each liquid. A critical temperature $T_{\text{crit,H}_2\text{O}}$ of 647.10 K [Lem18] and $\sigma_{0,\text{H}_2\text{O}} = 117.9\,\text{mN}\cdot\text{m}^{-1}$ as well as $k_{\text{H}_2\text{O}} = 0.8$ [Sch82] are used for water.
Huge temperature gradients cause surface tension gradients that lead to convective flow. This so called Marangoni convection [Mar71] is especially relevant for melting and solidification processes, but will not be covered in here. Besides state variables, such as pressure and temperature, the geometry of the interface also influences the surface tension. Therefore, modeling of curved interfaces is discussed subsequently.

2.1.2. Curved interfaces

When analyzing curved interfaces two additional effects have to be considered. First, the pressure jumps across curved interfaces and is therefore different in each phase. The relation between the pressure difference and the curvature of the interface is described by the Young-Laplace equation which is deduced in section 2.2. Second, the interface area in curved regions changes with the radial position [Sch82]. In

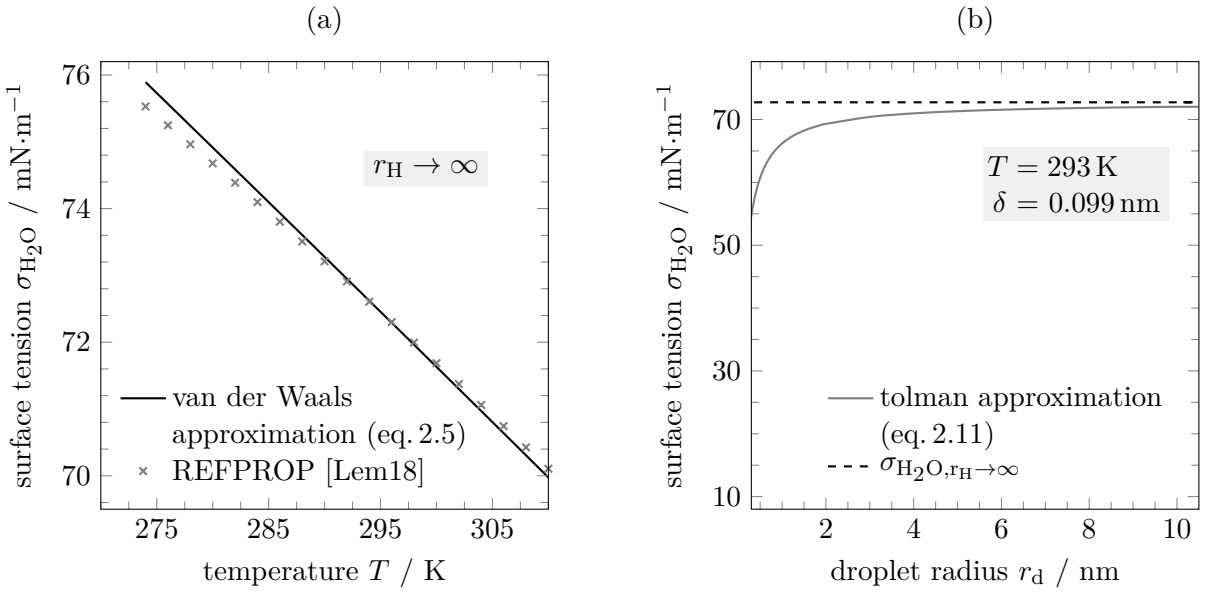

Figure 2.1.: Influence of temperature (a) and curvature (b) on the surface tension of water

contrast, at plain interfaces the size of the sharp interface area as introduced by Gibbs is independent of the location within the transition volume. This phenomenon becomes significant if the characteristic length scale of the system approaches the size of molecules. Considering these two effects, the grand potential for a curved interface with curvature radius r between two phases a and b is given by

$$\mathrm{d}\Omega_{\mathrm{gp}} = \sigma(r)\mathrm{d}A + \frac{\partial\sigma(r)}{\partial r}A\mathrm{d}r - p_{\mathrm{a}}\mathrm{d}V_{\mathrm{a}} - p_{\mathrm{b}}\mathrm{d}V_{\mathrm{b}}. \tag{2.6}$$

In order to specify curved interfaces properly, the mean curvature H and the Gauss curvature K are introduced. An arbitrarily curved interface is defined locally by the principal radii r_1 and r_2 and their corresponding curvatures

$$\kappa_1 \coloneqq \frac{1}{r_1} \quad \text{and} \quad \kappa_2 \coloneqq \frac{1}{r_2}. \tag{2.7}$$

The principal radii are determined at any point on the interface by identifying the interface normal at this point. Subsequently, a curve is constructed by intersecting the interface and an arbitrary plane containing the normal vector and the point. The first principal radius is defined by the circle of curvature of this curve at the considered point. The second radius is determined analogously by another section plane perpendicular to the first plane and also containing the normal vector and the point. The mean curvature is defined as the average of the principal curvatures

$$H \coloneqq \frac{1}{2}\left(\kappa_1 + \kappa_2\right) = \frac{1}{r_{\mathrm{H}}}. \tag{2.8}$$

According to a law of differential geometry, the mean curvature is independent of the orientation of r_1 and r_2 provided that the section planes are perpendicular [But10b]. Here, r_{H} is the mean radius of curvature that is defined by

$$\frac{1}{r_{\mathrm{H}}} \coloneqq \frac{1}{2}\left(\frac{1}{r_1} + \frac{1}{r_2}\right), \tag{2.9}$$

rather than by the arithmetic mean of the principal radii [Sch82]. In addition to the mean curvature, the Gauss curvature K is determined by the product of the principal curvatures

$$K \coloneqq \kappa_1\kappa_2. \tag{2.10}$$

For interfaces Γ that are described by a level-set function ϕ the mean curvature is given by

$$H = \frac{1}{2}\nabla_\Gamma \cdot \mathbf{n} = \frac{1}{2}\nabla_\Gamma \frac{\nabla_\Gamma \phi}{|\nabla_\Gamma \phi|}, \tag{2.11}$$

where $\mathbf{n}$ is the vector normal of the interface. The nabla operator ∇_Γ describes the divergence and gradient along the interface Γ rather than in any direction in space. The relation between the surface tension and the radius of curvature is described for spherical droplets by Tolman [Tol49a]

$$\sigma(r_\mathrm{H}) = \sigma_\infty \left(1 + \frac{2\delta}{r_\mathrm{H}}\right)^{-1}. \tag{2.12}$$

Here, σ_∞ is the surface tension for plain interfaces ($r_\mathrm{H} \to \infty$) and δ the Tolman length that describes the size dependent proportional contribution to the surface tension. An analogous expression to eq. (2.12) is derived for cylindrical menisci [Vog80]. According to Tolman [Tol49b], the Tolman length for water at 293 K is 0.099 nm. Using this value the curvature dependent surface tension of a water droplet is illustrated in figure 2.1 (b). Note, that for spherical droplets the droplet radius equals the radius of curvature ($r_\mathrm{d} = r_\mathrm{H}$). It is shown that the surface tension decreases with rising curvature. For $r_\mathrm{d} > 10\,\mathrm{nm}$ the influence of curvature is below 2 % and, therefore, might be neglected, which is consistent with Vogelsberger et al. [Vog80]. Schubert [Sch82] even gives a minimal value for using macroscopic surface tension of $r_\mathrm{d} > 3\,\mathrm{nm}$, which corresponds to a surface tension decrease of 6.19 % in figure 2.1 (b).
Still, an accurate determination of surface tension at high curvatures is a significant matter of research and inconsistent results are published [Blo10; Hor12]. On the one hand, quasithermodynamic [Hil52] and statistical approaches [Kir49] predict a positive Tolman length in good agreement with Tolman's classical work. On the other hand, numerical calculations lead to negative values and show a very small region of application of eq. (2.12) [Kog98; van09]. Using a higher-order approximation for the curvature dependent surface tension, Baidakov and Boltachev [Bai99] demonstrate a change of sign for the Tolman length. The surface tension of droplets exhibits a slight maximum of approximately +0.2 % at $r_\mathrm{d} = 10\,\mathrm{nm}$. With decreasing droplet radius a monotonously decreasing surface tension is observed. However, the maximum deviation to the plain surface tension σ_∞ is below 10 % implying a negligible effect of curvature. Using a Monte Carlo simulation Block et al. [Blo10] obtained a nearly linear correlation of Tolman length and droplet radius.

The different results clearly show that the curvature dependency of surface tension and the sign of the Tolman length are still disputed. The problem gets even more complex regarding capillary bridges, that usually have principal radii r_1 and r_2 with different signs. The influence of these complex curvatures has not been investigated. Although surface tension has not been fully explained yet, it is generally agreed that the Tolman length must be extremely small and depends on the droplet size and temperature [Fac14; Hor12; Mal12].

2.2. Young-Laplace equation

In this section, the Young-Laplace equation is introduced in order to calculate the pressure difference across curved interfaces, which is fundamental for analyzing capillary systems. At curved interfaces a pressure jump proportional to curvature is observed. This relation is captured by the Young-Laplace equation, which can be deduced by a balance of forces as it is described by Young [You05] and Laplace [Lap05]. In figure 2.2 the forces acting on an infinitesimal interface element $\mathrm{d}A$ without external fields are illustrated. The pressure difference Δp between the two sides of the interface leads to the pressure force $\Delta p\,\mathrm{d}A$ acting normal to the interface, while the other force component results from the surface tension and is calculated by $\sigma \mathrm{d}l_1$ and $\sigma \mathrm{d}l_2$, respectively. Thus, the balance of forces normal to the interface leads to

$$\Delta p\,\mathrm{d}A = \sigma \mathrm{d}l_1 + \sigma \mathrm{d}l_2. \tag{2.13}$$

Expressing $\mathrm{d}A$, $\mathrm{d}l_1$ and $\mathrm{d}l_2$ in terms of r_1, r_2, $\mathrm{d}\varphi_1$ and $\mathrm{d}\varphi_2$ gives

$$\Delta p\, r_1 \mathrm{d}\varphi_1\, r_2 \mathrm{d}\varphi_2 = \sigma \left(r_1 \mathrm{d}\varphi_1 \mathrm{d}\varphi_2 + r_2 \mathrm{d}\varphi_1 \mathrm{d}\varphi_2\right), \tag{2.14}$$

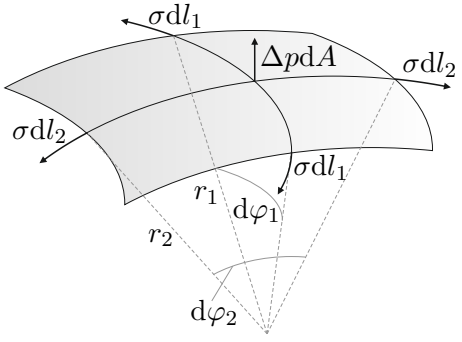

Figure 2.2.: Forces at an infinitesimal interface element

which is summarized as

$$\Delta p = \sigma \left(\frac{1}{r_1} + \frac{1}{r_2} \right) = 2\sigma H. \tag{2.15}$$

It is worth emphasizing that this equation is fundamental for understanding capillary phenomena. It states that the pressure jump and the mean curvature are proportional by the factor 2σ. Expressing the mean curvature H in terms of spatial coordinates, this relation can also be written as an ordinary differential equation. For the two-dimensional case of rotational symmetry around the x-axis

$$\Delta p = \sigma \left(\frac{y''}{(1+y'^2)^{\frac{3}{2}}} + \frac{y'}{y\,(1+y'^2)^{\frac{1}{2}}} \right) \tag{2.16}$$

is obtained. A detailed derivation of this equation as well as the general differential equations for three-dimensional coordinates is presented in [Lan02].
The Young-Laplace equation can equivalently be derived by an energy based approach [Gau30]. The total free energy of an interface is given by

$$E = \sigma A \tag{2.17}$$

assuming that potential and kinetic energy can be neglected. In order to minimize this equation for a predefined constant liquid volume the method of Lagrange multipliers is used. The idea of this method is illustrated in figure 2.3. In an unconstrained problem the minimum of $F(u)$ is located in the mid of the contour lines. Thus, the necessary optimality condition is given by $\nabla F(u) := 0$. However, when setting a constraint $f(u)$ any possible solution must be directly on the contour line of $f(u)$.

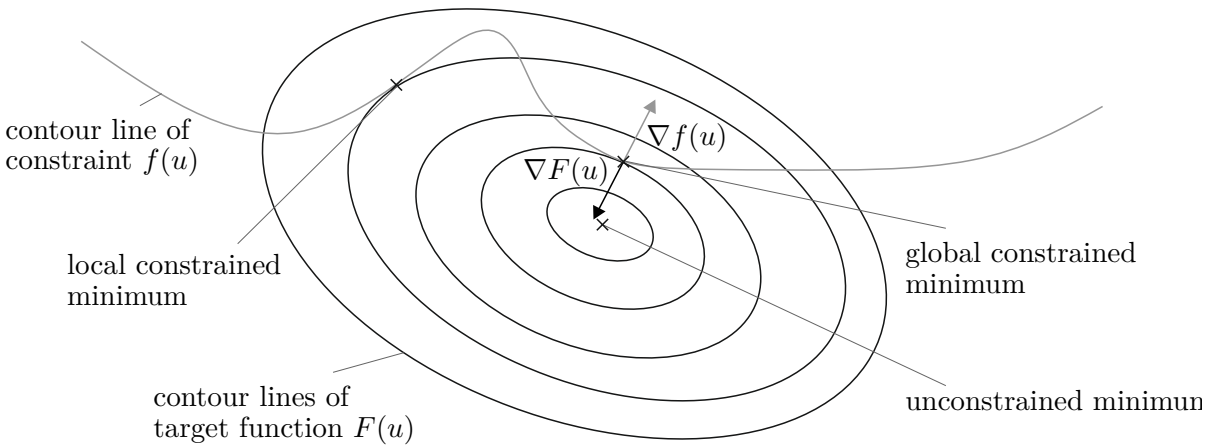

Figure 2.3.: Optimization problem with constraints

The constrained minimum is therefore given by the smallest value of $F(u)$ that is also part of $f(u)$. Thus, in the constrained minimum the contour lines tangentially touch each other which means that the gradients must be parallel. This condition is formulated as

$$\nabla F(u) \parallel \nabla f(u) \rightarrow \nabla F(u) = \lambda \nabla f(u) \Leftrightarrow \nabla F(u) - \lambda \nabla f(u) = 0 \tag{2.18}$$

where λ is a length adjustment factor between the vectors that is called Lagrange-Multiplier. This expression is the first derivative of the Lagrangian $\mathcal{L}$, i.e., $\nabla \mathcal{L} = 0$ is the necessary condition for the constrained minimum. From figure 2.3 it can already be seen that this condition applies for all local minima. Thus, from a physical perspective it cannot be concluded that the solution is physically stable.
The Lagrange method is formulated more generally for n constraints, i.e., the problem is to find local maxima or minima of a function $F(u_1, ..., u_\mathrm{m})$ subject to the constraints $f_\mathrm{n}(u_1, ..., u_\mathrm{m}) = 0$. In this general case the Lagrangian is given by

$$\mathcal{L}(u_1, ..., u_\mathrm{m}, \lambda_1, ..., \lambda_\mathrm{n}) = F(u_1, ..., u_\mathrm{m}) - \sum_{i=1}^{n} \lambda_\mathrm{i} f_\mathrm{i}(u_1, ..., u_\mathrm{m}) \tag{2.19}$$

with n Lagrange-Multipliers λ_1, ...,λ_n. Applying this method to the minimization of the free energy subject to a fixed volume and using the capillary pressure Δp as Lagrange-Multiplier the Lagrange-Equation

$$\mathcal{L} = \sigma A - \Delta p (V - V_0) \tag{2.20}$$

is derived, where V_0 is the the target volume of the capillary bridge. Note, that minimizing eq. (2.20) is equivalent to minimizing the grand potential Ω_gp (eq. (2.6)) for a curvature independent surface tension. Expressing A and V in terms of coordinates and minimizing $\mathcal{L}$ leads to eq. (2.16) for the two-dimensional case as shown by Langbein [Lan02]. Minimization of energy and balance of force approaches are equivalent for reversible systems. Hence, the considered forces must be conservative and no irreversible energy changes may occur [Lan02] which also corresponds to the isothermal implication of the grand potential. Note that eq. (2.15) is a constraint for the mechanical equilibrium and valid even if the physical-chemical equilibrium is not yet achieved [Sch82].
The Young-Laplace equation has an important implication. Neglecting gravity, the pressure inside a static liquid must be constant because otherwise a flow field from high to low pressure would result. Following eq. (2.15), a constant pressure implies a

constant mean curvature (CMC). In 1841, Delaunay [Del41] described CMC interfaces of revolution from a mathematical perspective. His results are assigned to axisymmetric capillary bridges by Plateau [Pla64] whose work is also known as Plateaus sequence of capillary shapes. A detailed description of CMC interfaces and their application to axisymmetric capillary bridges is given in section 3.2.

2.3. Contact angle and wetting

In a system of three immiscible components with at least two fluids, three interfaces exist which meet in an intersection region. On a molecular level, the situation is very complex and not yet described properly [Lin15; Sch82; van10]. From a macroscopic perspective, the dividing interfaces can be extrapolated to meet in an intersection line [Buf57]. In this work, specifically static solid-gas-liquid systems are covered, since this special case corresponds to the capillary bridges.

2.3.1. Young equation

Three fluid phases are illustrated in figure 2.4 with the three-phase contact line being perpendicular to the plain of projection and indicated by the gray dot. The solid is assumed to be rigid and ideally smooth. In a static equilibrium, the forces at the contact line must balance each other. The shear stress normal to the solid interface is counterbalanced by the rigid solid [Lan02]. The tangential balance of forces leads to

$$\cos(\theta) = \frac{\sigma_{\mathrm{sg}} - \sigma_{\mathrm{sl}}}{\sigma}, \tag{2.21}$$

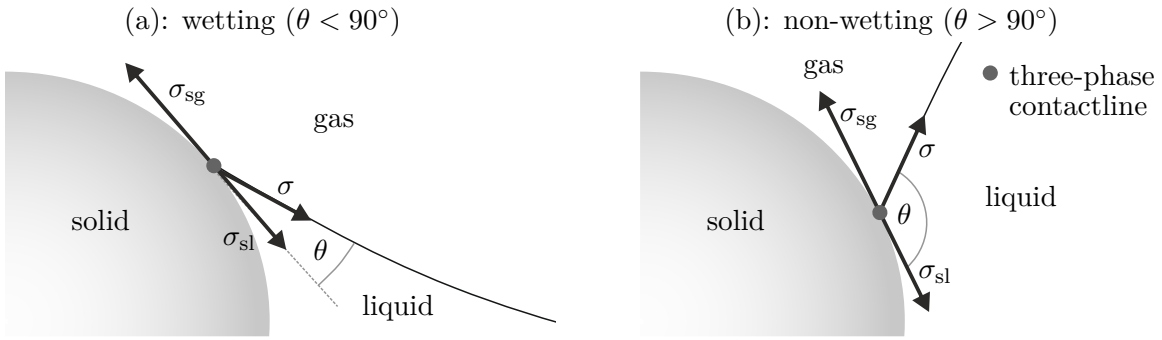

Figure 2.4.: Surface tension at the three-phase contact line for wetting and non-wetting according to the classical definition

provided σ_{sg} and σ_{sl} are homogeneous and isotropic. Eq. (2.21) is known as Young equation [You05], which can also be derived by minimizing the free energy of the system [Neu74]. A satisfying experimental determination of the solid surface tensions σ_{sg} and σ_{sl} is not possible, yet [Sch82]. An overview to directly measure the contact angle θ is given in [Yua13] and the three most common approaches, namely the sessile drop, the Wilhelmy balance and the Washburn capillary rise, are discussed in [Bru18]. Combining these experimental methods with eq. (2.21) the difference of the solid surface tensions $(\sigma_{sg} - \sigma_{sl})$ can be determined indirectly [Lan02; van10].
As presented in figure 2.4, liquids are usually distinguished by means of the contact angle between wetting ($\theta < 90°$) and non-wetting ($\theta > 90°$) types [Sch82]. Regarding water hydrophilic and hydrophobic materials are defined analogously. Nevertheless, other definitions are found in the literature [Sam11]. Law [Law14] argues that no interface property changes at $\theta = 90°$. However, in this work the classical definition of hydrophilic and hydrophobic is used.
This theory of contact angles only applies for a static contact line and ideally smooth solid surfaces. A moving contact line leads to dynamic effects, such as contact angle hysteresis. Focusing on static capillary bridges, dynamic contact angles are not discussed in here, however, further information is given in [Ada97; Isr11; Lin15]. Considering real surfaces involving roughness also leads to a much more complex situation that is described subsequently.

2.3.2. Wetting of rough interfaces

Today, complex wetting phenomena are not yet completely understood. Real surfaces are usually neither chemically nor physically homogeneous and even simple and periodic patterns lead to complex and varied effects on the wetting behavior [Isr11]. Thus, the microscopic contact might be different from the macroscopic contact angle that is measured. Bhushan and Jung [Bhu11] point out four mechanisms for the difference between the apparent (macro) and real (micro) contact angle: (1) Due to long distance van der Waals forces and the resulting disjointing pressure stable thin films of water might occur. These thin films lead to a transformation from a spherical shape into a precursor layer near the three-phase contact line. (2) Real interfaces always exhibit roughness and chemical heterogeneity that influence the apparent contact angel. (3) Dynamic effects cannot be eliminated completely and therefore the static contact angle is not well defined. (4) Contact line tension might have to be considered for very small droplets and triple lines with high curvature.

In order to consider roughness effects for the estimation of the apparent contact angle several models are proposed. One of the first models for wetting on rough interfaces is presented by Wenzel [Wen36]. As shown in the illustration in figure 2.5 (a) the liquid is assumed to completely fill the depressions created by roughness. The Wenzel contact angle of the rough interface θ_{w} is given by

$$\cos\theta_{\mathrm{w}} = R_{\mathrm{f}} \cos\theta, \tag{2.22}$$

using the roughness ratio R_{f}, that is defined by the ratio of the real interface area to the projected smooth interface area. The area factor S_{dr} relates the additional area resulting from roughness to the projected smooth area an can therefore be used to calculate the roughness ratio:

$$R_{\mathrm{f}} = S_{\mathrm{dr}} + 1. \tag{2.23}$$

The mathematical definition and discussion of the area factor S_{dr} is given in section 3.7.1 in the context of parameters describing rough topology. In figure 2.5 (a) the relation between the smooth contact angle θ and the Wenzel contact angle θ_{w} is illustrated for different roughness ratios where $R_{\mathrm{f}} = 1$ corresponds to the smooth interface. According to this model, for $\theta < 90°$ the Wenzel contact angle is lower compared to the smooth contact angle whereas a higher Wenzel contact angle is observed for $\theta > 90°$. Thus, the physical behavior of the interface, i.e., hydrophilic or hydrophobic, is enhanced by roughness. For $\theta = 90°$the effect of roughness vanishes which is physically not correct [Isr11].
Another model suggested by Cassie and Baxter [Cas44] is originally developed to calculate the effective apparent contact angle θ_{eff} for chemically heterogeneous, smooth interfaces. It is given by

$$\cos\theta_{\mathrm{eff}} = f_1 \cos\theta_1 + f_2 \cos\theta_2 \tag{2.24}$$

where f_1 and f_2 are the fractional areas of each material and $f_1 + f_2 = 1$. This heterogeneous model is transferred to homogeneous rough interfaces by taking the gas as the second component. As illustrated in figure 2.5 (b) the rough depressions are assumed not to be filled with liquid. Inserting the solid as component 1 with

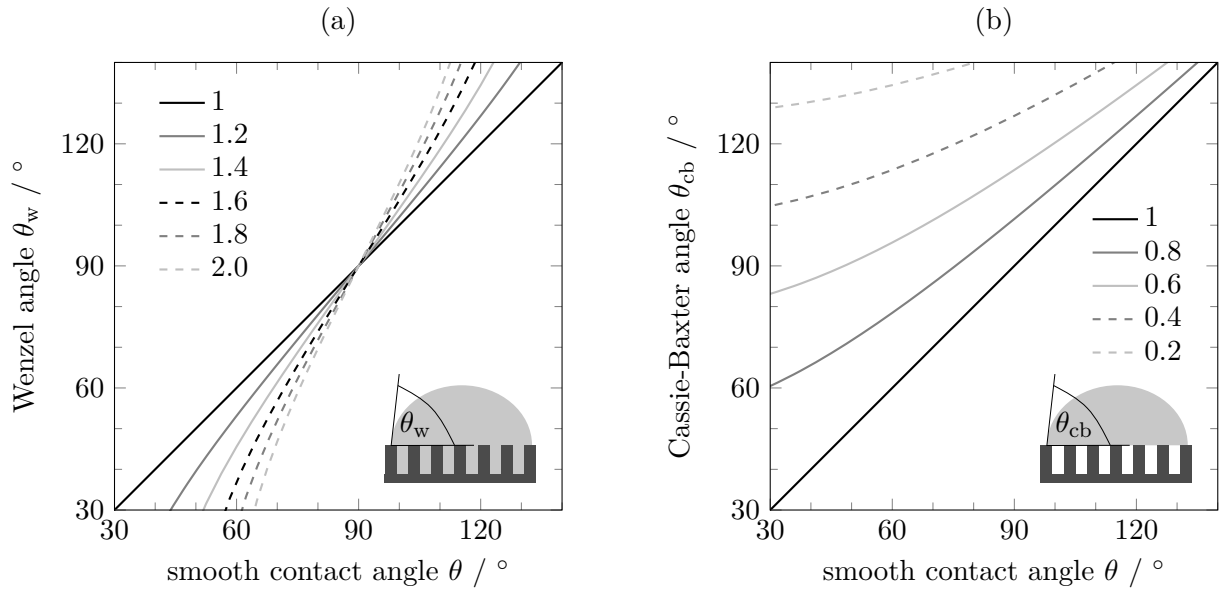

Figure 2.5.: Rough apparent contact angle according to the Wenzel model [Wen36] for different roughness ratios R_f (a) and according to the Cassie and Baxter model [Cas44] for different solid fractional areas f_s (b)
(Roughness increases with increasing R_f or decreasing f_s.)

the smooth contact angle θ and the contact angle of liquid and gas $\theta_2 = 180°$ into eq. (2.24) leads to

$$\cos\theta_{cb} = f_s \cos\theta - 1 + f_s \tag{2.25}$$

which is usually known as the Cassi-Baxter equation. The resulting Cassie-Baxter contact angles θ_{cb} are shown in figure 2.5 (b). In contrast to the Wenzel model, roughness leads to a more hydrophobic behavior for all contact angles. This is traced back to the assumption of non-wetted rough depressions. Note, that it is also possible to apply eq. (2.24) for liquid filled depressions by inserting $\theta_2 = 0°$. In this case, more hydrophilic contact angle results are predicted for rough interfaces.
The applicability of the Wenzel and Cassie-Baxter models are discussed intensively in the literature [Bar07; Bhu11]. An analysis by Marmur [Mar06] showed, that Wenzel's model is valid for drops that are two to three orders of magnitude larger than the roughness scale. Moreover, both models are good approximations of the most stable contact angle [Mar09]. However, experimental investigations of Gao and McCarthy [Gao07] reveal that roughness under the bulk of the droplet does not influence the apparent contact angel and therefore fractional area approaches are physically not correct. Thus, in order to account for non-uniform roughness, using three-dimensional roughness factors ($R_f(x, y)$ and $f_s(x, y)$ respectively) is by Nosonovsky [Nos07].

2.4. Kelvin equation

The Kelvin equation relates the mean radius of curvature r_H to the fraction of the vapor pressure at plain interfaces p_v^∞ and at curved interfaces p_v:

$$\frac{r_\mathrm{H}}{2} = \frac{\sigma V_\mathrm{M}}{\mathcal{R}T}\left(\ln\frac{p_\mathrm{v}^\infty}{p_\mathrm{v}}\right)^{-1} = \lambda_\mathrm{k}\left(\ln\frac{p_\mathrm{v}^\infty}{p_\mathrm{v}}\right)^{-1}, \tag{2.26}$$

where V_M is the molar Volume, T the temperature and $\mathcal{R}$ the universal gas constant. This equation supposes an ideal gaseous behavior of the vapor and an incompressible liquid [Sch82].

Applying eq. (2.26) to water and humid air, the pressure ratio equals the relative humidity φ [Sch82]. Even if the moisture content is below saturation, condensation of water may occur, however, exhibiting negative Kelvin radius and negative curvature. Condensation at $\varphi < 1$ is usually refereed to as capillary condensation with the characteristic length scale given by the Kelvin length λ_k [But08]. With rising humidity from zero to one, the absolute values of the mean radius of curvature increases or in other words the absolute value of mean curvature and capillary pressure decrease. At the saturation point ($\varphi = 1$) curvature and the capillary pressure equal zero. This is well defined for catenoidal capillary bridges with $r_1 = -r_2$. For humidity above saturation, convex geometries, that could be either capillary bridges or droplets, may arise from condensation. However, for convex geometries the thermodynamic equilibrium is unstable as explained subsequently.

If the mean radius of curvature r_H is assumed to be larger than the equilibrium radius according to the Kelvin equation this leads to additional condensation of water. Thus, a droplet or a convex capillary bridge grows due to condensation since both positively defined radii r_1 and r_2 increase, which consequently leads to an ever larger mean radius of curvature. In the other case, i.e., the mean radius of curvature is assumed to be smaller than the equilibrium radius, the liquid completely evaporates since both radii decrease. Thus, in either case, a slight perturbation of the equilibrium state leads to a move away from this state and, hence, the thermodynamic equilibrium is unstable for convex interfaces, i.e., $\varphi > 1$. In contrast, for the concave geometries r_1 and r_2 have reversed signs. If now liquid condenses since r_H larger than the equilibrium radius, the two radii r_1 and r_2 approach each other and, consequently, the mean radius of curvature r_H decreases. Thus, a perpetuated system moves back in the direction of the thermodynamic equilibrium. The same consideration is can be made for a smaller r_H and the evaporation of liquid. Overall, a thermodynamic equilibrium

can be obtained for any humidity, however, for $\varphi < 1$ this is stable and for $\varphi > 1$ unstable.

It shoulde be noted, that capillary bridges only emerge directly from a capillary condensation, if the adsorption layers on the solid interface touch each other which implies a relatively small gap distance. However, if the interfaces of such a bridge are very slow separated, i.e., there is always enough time for the liquid to condense or evaporate in order to keep thermodynamic equilibrium, also thermodynamically stable bridges between larger gap distances can occur.

Finally, the Kelvin equation uses macroscopic parameters to describe capillary condensation. Thus, the applicability with respect to the system size has to be considered. For water a minimal mean radius of curvature of $r_\mathrm{H} = 3.0\,\mathrm{nm}$ is given by Schubert [Sch82] and the applicability of the Kelvin equation down to $r_\mathrm{H} = 10\,\mathrm{nm}$ is demonstrated [Koh00]. However, as it is previously shown for the surface tension concept (section 2.1.2), condensation at the nano level and below is still an extensive field of research that cannot be presented in detail at this point. The reader should rather be aware of the applicability limits when considering systems at the nano scale and below.

3. State of the art and research of capillary bridges

Capillary bridges are an important field of research as the appearance of a liquid meniscus between two or more particles leads to an attractive or even repulsive force between the solids that is called capillary force. Capillary forces significantly influence interparticle behavior on the micro- and nano-scale. In this chapter an overview of the capillary bridge problem and the current state of the art is given. First, a brief introduction of interparticle forces and their characteristics is given in order to point out the fundamental relevance of capillary forces compared to other interparticle force types. Subsequently, system parameters and coordinate systems are defined and the general equations for determining the dimensionless capillary force and the capillary torque are deduced by the balance of forces. Thus, it becomes clear that capillary bridge problems are more complicated than it might seem first, since many physical aspects have to be considered. Theoretical analysis is, however, determined by the modeling possibilities and therefore an overview of the simulation approaches is given. The theoretical discussion is complemented by a brief description of the commonly used experimental methods. Especially at the nano scale measuring interparticle forces is not straight forward. Based on the theoretical and experimental investigation methods, the main issues of static capillary bridges are introduced. Finally, with respect to the topic of this work, the influence of roughness is comprehensively discussed.

3.1. Interparticle forces

The characteristics of powder and granular materials strongly depend on the ratio between interparticle forces F_i and weight mg, which drastically changes with the system size. Valsamis et al. [Val13] distinguish between micro- and macro-engineering as illustrated in figure 3.1 (a). Capillary force, which is a dominant part of interparticle forces, and weight are plotted over the characteristic length L of an arbitrary system. The more the geometry is scaled down the more capillary force dominates weight. Thus, in micro-engineering capillary force exceeds weight which is approximately at characteristic length scales below $10^{-3}\,\mathrm{m}$. Schubert [Sch82] points out a reasonable neglect of gravitation already at $R < 10^{-3}\,\mathrm{m}$ for particle interactions, whereas Lambert

and Delchambre [Lam05] state a characteristic lenght of $L = 2.7 \cdot 10^{-3}\,\mathrm{m}$ at which the surface tension and gravitational force are of the same order of magnitude. These values demonstrated, that the transition region from micro- to macro-engineering is not sharply defined, however, it is consistend to be around a characteristic lenght of $10^{-3}\,\mathrm{m}$. Thus, a comprehensive understanding of powders and other applications involving small particles requires a reliable determination of capillary forces.
Generally, the interparticle force is the net force acting on two or more particles. In many applications the adhesive regime of the interparticle force is studied and, therefore, it is also often referred to as adhesive force. However, in this work, the more general term of interparticle force is used. It consists of several force types arising from different physical phenomena. Van der Waals force, capillary force and electrostatic forces are the most relevant ones and are briefly discussed here, however, solid bridges and positive connections might also exist. Depending on the system parameters such as size, humidity and particle roughness the magnitude and the relative contribution of each force changes fundamentally. In figure 3.1 (b) different interparticle force types are shown for a sphere located in front of a plate with a distance of $a = 4 \cdot 10^{-10}\,\mathrm{m}$ [Rum74]. Note, that this distance is interpreted as direct particle contact. The surfaces of the sphere and the plate are assumed to be ideally flat. The capillary force is approximately three to five times larger than the van der Waals

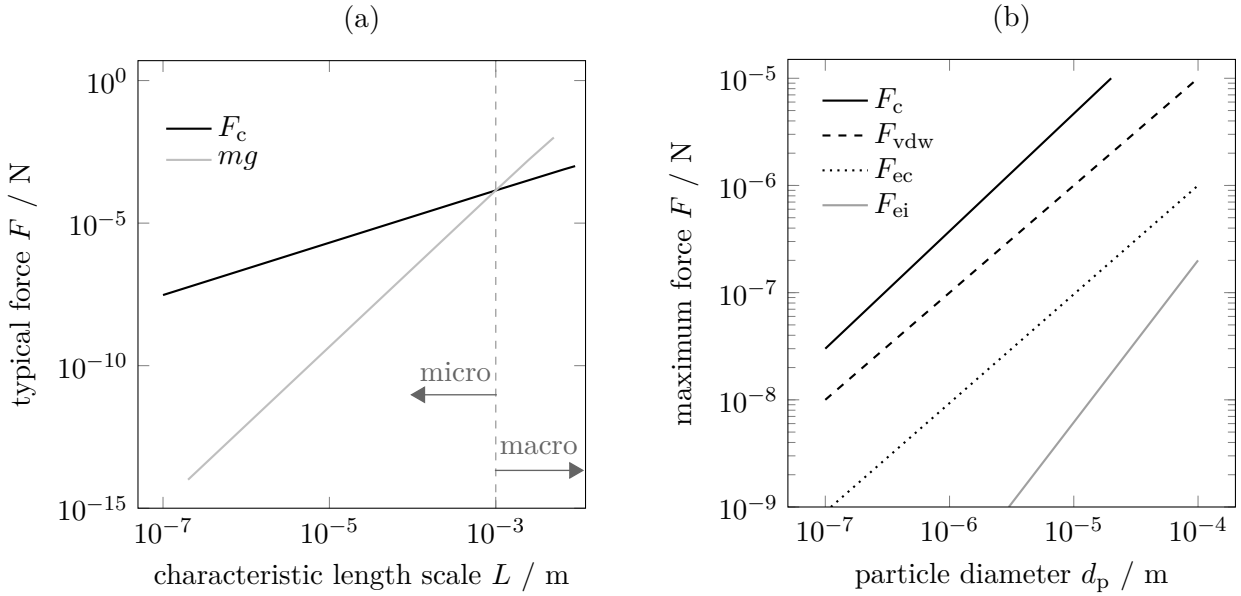

Figure 3.1.: (a) Weight mg and capillary forces F_c calculated according to the scaling law [Val13] (b) Capillary F_c (H_2O; $\theta = 20°$), van der Waals F_{vdw} ($\mathcal{A} = 8 \cdot 10^{-19}\,\mathrm{J}$), electric conductor F_{ec} ($U = 0.5\,\mathrm{V}$) and electric isolator F_{ei} ($\phi_{max} = 1.602^{-5}\,\mathrm{As \cdot m^{-2}}$) forces for a sphere-plate system with $a = 4 \cdot 10^{-10}\,\mathrm{m}$ (contact distance) [Rum74]

force. This observation is independent of the particle diameter. Moreover, electrostatic forces are very small compared to both, capillary and van der Waals forces, and may be neglected. However, under specific circumstances such as large particle distances, their influence is significant and dominates the other forces. By analyzing the effects of roughness and the sphere-plate distance four general tendencies are formulated [Rum74]:

1. In the case of adhesion capillary forces exceed other interparticle forces and due to condensation they also exist in dry systems.

2. Van der Waals forces are extremely sensitive to roughness which is confirmed by Rabinovich et al. [Rab00a; Rab00b], however, for adhering particles they exceed electrostatic forces almost always.

3. Electrostatic forces may be dominant for dry systems with very large particles.

4. For $a > 10^{-6}\,\mathrm{m}$ or $a \cdot R^{-1} > 0.1$ neither capillary nor van der Waals forces exist. Thus electrostatic forces are dominant and influence agglomeration processes before adherence.

The influence of humidity on the interparticle force is remarkable. With increasing humidity, a jump in the interparticle force is observed. The value of the critical humidity varies from around 20 % [Sed00], below 20 % [Thu93; Xu98] and $30 - 60\,\%$ [Rab02], however, the effect is consistently traced back to the existence of a liquid meniscus. Moreover, the electrostatic potential decreases under humid conditions, leading to even lower electrostatic forces [Bun07]. The Hamaker constant $\mathcal{A}$, that is proportional to the van der Waals force, is also significantly reduced by water as transfer medium [But10b]. For example, the calculated Hamaker constant for silicon dioxide particles surrounded by vacuum is $68 \pm 3 \cdot 10^{-21}\,\mathrm{J}$ and reduces to $4.6 \pm 1.6 \cdot 10^{-21}\,\mathrm{J}$ if water occurs between the particles [Ack96; Ber97]. Both effects lead to a decreasing van der Waals force implying an increasing impact of the capillary force. Experimental investigations at different ambient conditions, i.e., in air and fully immersed in water, allow conclusions about the composition of the interparticle force. Ouyang et al. [Ouy01] demonstrate for a humidity of 50 %, that both, van der Waals and capillary forces, are relevant, however, their proportion strongly varies with the materials. Thus, under ambient conditions good models for both, capillary and van der Waals forces, are required in order to evaluate the flow characteristics of small particles [You13]. This work focuses exclusively on capillary forces being dominant

for many applications in mico-engineering. Therefore, the physical background of capillarity and the calculation of capillary forces are described next.

3.2. Definitions

Depending on the type of capillary bridge problem, the parameters of interest are the capillary force F_c, the liquid Volume V and the pressure difference at the interface Δp which is also known as the capillary pressure

$$\Delta p \coloneqq p_i - p_o. \tag{3.1}$$

Note, that this definition is not consistent in the literature and reversed signs are also used. In many cases it is reasonable to describe the capillary bridge in a dimensionless form which is subsequently indicated by the tilde symbol. Using a characteristic length L and the surface tension σ, the dimensionless physical variables are defined as

$$\tilde{F} \coloneqq \frac{F}{\sigma L}, \quad \tilde{V} \coloneqq \frac{V}{L^3}, \quad \tilde{A} \coloneqq \frac{A}{L^2}, \quad \tilde{l} \coloneqq \frac{l}{L}, \quad \tilde{H} \coloneqq HL, \quad \text{and} \quad \tilde{p} \coloneqq \frac{pL}{\sigma}. \tag{3.2}$$

In this work, the particle radius R is used as the characteristic length if not mentioned otherwise.

Figure 3.2 shows the defined coordinate system for a two-dimensional sample system of a capillary bridge between spherical particles. The coordinate system originates in the center of mass of the first solid body, that could be an arbitrarily formed particle while the second body could be either a particle or a plate. The x- and y-axis are illustrated in figure 3.2, while the z-axis is perpendicular to the figure plane. The

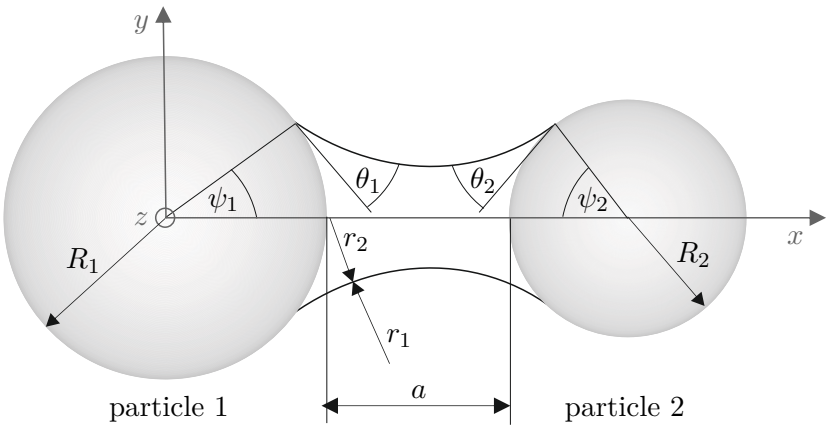

Figure 3.2.: Coordinate system and definitions for a sample system between spherical particles

parameter a corresponds to the shortest distance between the solid bodies and can analogously be expressed in the dimensionless form $\tilde{a}$. Contact angles θ_1 and θ_2 as well as filling angles ψ_1 and ψ_2 are defined for both solid bodies. However, usually only one of the filling angles is predefined and the other one is calculated by the geometrical constraints.
The curvature is described by the principal radii of curvature r_1 and r_2, which are in the literature often referred to as the meridional meniscus r ($=r_1$) and the azimutal radius l ($=r_2$). In this work, the sign convention is positive for radii inside the meniscus and negative for radii outside the meniscus, respectively. Thus, for a meniscus transition from concave to convex, r_1 changes its sign from negative to positive, whereas r_2 is always positively defined.
Assuming the absence of external fields and a constant wetting, the capillary bridge forming between two bodies of revolution is axisymmetric [Sch82] and exhibits a constant mean curvature which directly results from the Young-Laplace equation. In 1841 Delaunay [Del41] already studied interfaces of revolution with constant mean curvature (CMC) and classified them into nodoid (nod), catenoid (cat), unduloid (und), cylinder (cyl) and sphere (sph). In 1864 these geometries are applied to the capillary bridge problem by Plateau in 1864 [Pla64]. He found the constant sequence of CMC interfaces with rising volume:

$$\text{nod}^- \rightarrow \quad \text{cat} \quad \rightarrow \quad \text{und}_0^- \quad \rightarrow \quad \text{und}_1^- \quad \rightarrow \quad \text{und}_0^+ \quad \rightarrow \quad \text{sph} \quad \rightarrow \quad \text{nod}^+$$

Here, $^-$ indicate concave and $^+$ convex menisci and the index (0 or 1) gives the number of unduloid inflection points. This sequence has been studied intensively. It is validated by an elliptic integral approach for $\tilde{a} = 0$ and $\theta_1 + \theta_2 \leq 180°$ [Orr75].
The nod$^- \rightarrow$ bridges are characterized by a negative curvature. These bridges emerge from condensation below saturation. A minimal interface area is not equivalent to a mathematically defined minimal interface that exhibits zero mean curvature $H = 0$. The only minimal interface of the Plateau sequence is the special case of a catenoid that occures at the saturation point. Moreover, a vanishing capillary force is observed for spherical bridges. Assuming $\tilde{a} \neq 0$ the sequence of Plateau significantly changes [Rub14]. With rising particle distance unduloids appear even for very small filling angles and the pressure changes sign more than once. Additionally, multiple solutions of the Young-Laplace equation are demonstrated, which results in the open question of stability.

3.3. Capillary forces and capillary torque

The capillary force can be determined using two different physical principles which are equivalent [Lam08]. The first option is calculating the energy change during an infinitesimal reversible change of the equilibrium configuration [Her19]. The force is then given by the derivative of the total free energy with respect to the particle distance a

$$F_\mathrm{c} = \frac{\partial E}{\partial a}. \tag{3.3}$$

The second option is based on the integration of local forces according to the free-body principle of mechanics. The capillary force generally consists of the two components, i.e., the capillary pressure force F_p, resulting from the pressure difference Δp, and the surface tension force F_s, that arises from the surface tension σ [Fis26]. In figure 3.3 (a) a free-body diagram of a meniscus is shown. First, the inner pressure p_i acts at the intersection area Γ_I, whereas the outer pressure p_o acts on the solid-gas interface Γ_sg and the liquid-gas interface Γ_lg, respectively. Second, the surface tension acts along the intersection line L_I that encloses the intersection area Γ_I. The direction of the resulting force component is tangential to the liquid-gas interface and normal to the intersection plane which is mathematically defined as the co-normal given by the co-normal unit vector $\boldsymbol{\mu}$. Integration along the intersection line leads to the net force

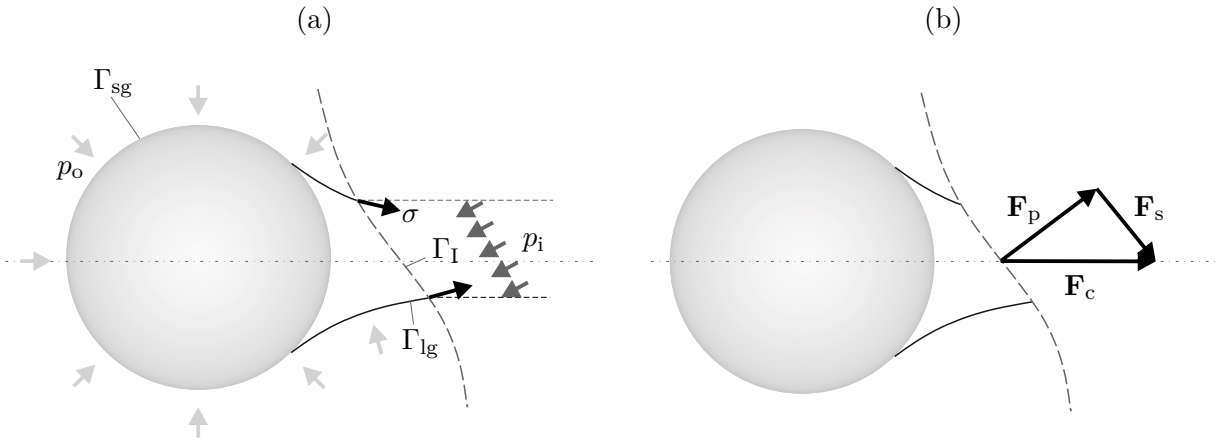

Figure 3.3.: Surface tension and pressure in a free body diagram (a) and the resulting components of the capillary force (b)

vector $\mathbf{F_s}$. Thus, in the general case of an arbitrary intersection plane the capillary force is given by

$$F_\mathrm{c} = |\mathbf{F}_\mathrm{c}| = |\mathbf{F_p} + \mathbf{F_s}| = \left| -p_\mathrm{o} \left(\iint_{\Gamma_\mathrm{sg}} \mathbf{n} \mathrm{d}\gamma + \iint_{\Gamma_\mathrm{lg}} \mathbf{n} \mathrm{d}\gamma \right) - p_\mathrm{i} \iint_{\Gamma_\mathrm{I}} \mathbf{n} \mathrm{d}\gamma + \sigma \oint_{\mathrm{L_I}} \boldsymbol{\mu} \mathrm{d}l \right| \quad (3.4)$$

where $\mathrm{d}\gamma$ and $\mathrm{d}l$ are incremental interface and intersection line elements, respectively. Since the overall interfaces are closed, the effective area of the outside pressure can be written as

$$\iint_{\Gamma_\mathrm{sg}} \mathbf{n} \mathrm{d}\gamma + \iint_{\Gamma_\mathrm{lg}} \mathbf{n} \mathrm{d}\gamma = - \iint_{\Gamma_\mathrm{I}} \mathbf{n} \mathrm{d}\gamma. \quad (3.5)$$

Therefore, eq. (3.4) reduces to

$$F_\mathrm{c} = \left| -\Delta p \iint_{\Gamma_\mathrm{I}} \mathbf{n} \mathrm{d}\gamma + \sigma \oint_{\mathrm{L_I}} \boldsymbol{\mu} \mathrm{d}l \right| \quad (3.6)$$

which can also be expressed in the dimensionless form

$$\tilde{F}_\mathrm{c} = \left| -\Delta \tilde{p} \iint_{\tilde{\Gamma}_\mathrm{I}} \mathbf{n} \mathrm{d}\tilde{\gamma} + \oint_{\tilde{\mathrm{L}}_\mathrm{I}} \boldsymbol{\mu} \mathrm{d}\tilde{l} \right| \quad (3.7)$$

by using the definitions given in eq. (3.2). Note, that the capillary force is independent of the chosen intersection plane. As illustrated in figure 3.3 (b), for an inclined intersection both, the pressure and the surface tension force, have a non-axial component which directly cancel out leading to the axial direction of the overall capillary force. However, a pure axial force exists only for symmetric bridges, whereas the force direction of non-symmetric bridges is unknown and must be taken from the force vector $\mathbf{F_c}$. As already indicated by figure 3.3 (b) in this work an attractive capillary force is defined positive whereas the repulsive case is indicated by negative sign. Commonly, the capillary force is calculated at the three phase interface or at the minimal meniscus diameter. In the case of axisymmetric bridges Γ_I is circular and eq. (3.6) reduces to

$$F_\mathrm{c} = -\Delta p \pi r_\mathrm{I}^2 + \sigma 2\pi r_\mathrm{I} \cos\alpha \quad (3.8)$$

where r_I is the radius of Γ_I and α the angle between the meniscus interface Γ_lg and the direction of the capillary force.

The surface tension force is always attractive, whereas the capillary pressure force can be either attractive or repulsive. Capillary bridges emerging from condensation

always exhibit an attractive capillary pressure force which directly results from combining the Kelvin equation (eq. (2.26)) and the Young-Laplace equation (eq. (2.15)). The relevance of each force component has been investigated for many configurations. However, it is essential to note, that any relation between the two force components is only valid for one specific intersection plane of a capillary bridge system. In figure 3.4 (a) the dimensionless meniscus shape of a capillary bridge between two equally sized spheres with different contact angles is shown. An analysis of the capillary force components along this meniscus reveals the influence of the chosen intersection area. On the left particle the ratio $\tilde{F}_\mathrm{s}/\tilde{F}_\mathrm{c}$ is 0.46 whereas on the right particle the ratio is 0.18. For a conservative estimation of the force component impact, the minimal intersection area should be evaluated in case of the surface tension force and the maximum intersection area in case of the capillary pressure force, respectively. At these intersection areas the respective force component reaches its maximum which allows conclusions about simplified force models neglecting this particular component.
In some force models the surface tension force is neglected because it is assumed to be insignificant compared to the capillary pressure force [Isr11; Mar93]. Especially for a vanishing gap between a sphere and a plane, the surface tension component can be one order of magnitude smaller than the pressure force [Lam05]. However, this relation completely switches with a rising gap. Additionally, for small particles with high curvature and states close to saturation, the surface tension force dominates the

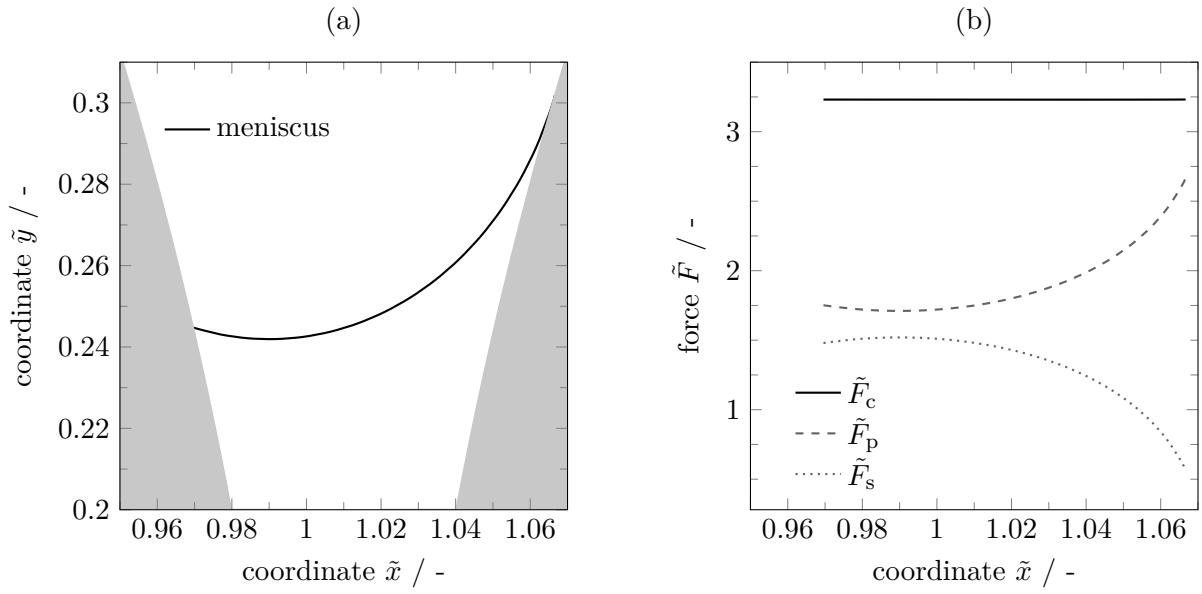

Figure 3.4.: Meniscus shape between two equally sized spheres with different wetting angles $\theta_1 = 60°$(a) and $\theta_2 = 0°$and the resulting pressure force $\tilde{F}_\mathrm{p}$ and surface tension force $\tilde{F}_\mathrm{s}$ along the meniscus (b)

capillary pressure force and must be taken into account [Laz99]. This is supported by Dörmann [Dör18], who showed for equally sized spheres that the capillary pressure force dominates if $R > 1\,\mu$m. This is explained by the fact that the pressure force scales quadratically with the meniscus radius, whereas the surface tension force scales linear. Thus, with rising particle and meniscus size the surface tension force might be neglected. However, it is also demonstrated that the ratio of the pressure force decreases with rising relative humidity because of the decreasing capillary pressure [Dör18]. From the different investigations reported in the literature it is deduced, that neglecting a particular force component is only acceptable for highly specific system configurations. Therefore, a general force model should include both, the capillary pressure force and the surface tension force.

The influence of different parameters on the overall capillary force is studied intensively. However, general conclusions are almost impossible due to high interdependencies of the system parameters. For example, assuming a simple sphere-plane configuration in contact, the capillary force is almost independent of the liquid volume and humidity, respectively, if the particles are relatively large [Isr11]. Pakarinen et al. [Pak05] use a numerical scheme to calculate the exact meniscus geometry and demonstrate a humidity independent capillary force for $R > 1\,\mu$m as well as a strong humidity dependence for $R < 1\,\mu$m. From everyday life experiences, for example sand castles, an increasing cohesion of granular and powder materials with increasing humidity is known [But05]. For conical particles a significantly increasing capillary force with rising liquid volume is demonstrated theoretically and experimentally [Lam05]. However, numerical analysis by Lian and Seville [Lia16] reveals, a decreasing capillary force with increasing humidity between equally and unequally sized spheres at zero distance which is confirmed by the theoretical investigations of Mehrotra and Sastray [Meh80], who demonstrate the decreasing capillary force with respect to increasing liquid volume. In figure 3.5 the dimensionless capillary force is shown depending on the relative humidity (a) and the meniscus volume (b) for a sphere-plane and sphere-cone geometry. The curves are obtained by the toroidal approach [Tse03] that is described in section 3.4.1. For zero distance, the capillary force of the sphere-plane configuration decreases, whereas a maximum is observed at a dimensionless distance of 0.01. This is traced back to two opposing effects [Dör18]: On the one hand, the capillary force increases with humidity due to an increasing meniscus diameter. On the other hand, according to eq. (2.26), the capillary pressure decreases leading to a lower force. However, for the cone-plane geometry the capillary force significantly increases at high humidity. Thus, in order to analyze the

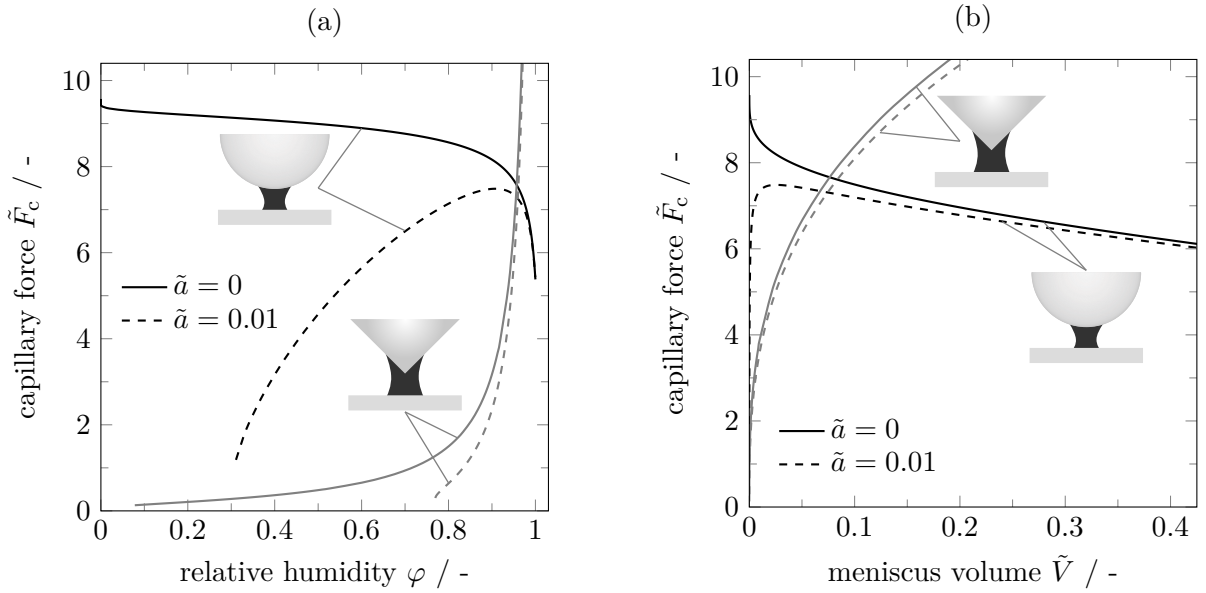

Figure 3.5.: Capillary force depending on relative humidity (a) and meniscus volume (b) for sphere-plane (black) and cone-plane (gray) geometries at different distances $\tilde{a}$. Calculations are performed using toroidal equations (see appendix A) for $\theta = 40°$ and a cone opening angle of 70°

effect of humidity, both, the particle geometry and the separation distance must be considered.

As stated above, the humidity dependence is strongly correlated with other parameters. The high sensitivity of the force-humidity and force-volume curve, respectively, already indicates a significant influence of roughness that corresponds to small geometry variations. The detailed effects of roughness are discussed in section 3.7. The remarkable interdependence of the parameters as well as the high geometry sensitivity make general correlations hard to predict. However, some important tendencies are summarized as follows:

- On hydrophilic interfaces the capillary force is affected by humidity, while an independence is observed for hydrophobic interfaces [Far06; Xia00].
- The capillary force decreases with increasing contact angel due to an inferior wetting of the solid particles [Che11; Fuj99; Lam05; Qia17].
- Rising particle distance leads to a decreasing capillary force [Ard14; Che11; Lam05; Lia16; Mar93; Rab05; Wil00] even when taking gravity into account [Ada02]. This decrease is nearly linear for a sphere-plane geometry employing a constant humidity boundary condition, whereas a non-linear decrease is observed using a constant liquid volume constraint [But09].

- The capillary force increases with increasing particle size [Dör15]. According to scaling laws, this relation is proportional for microscopic particles [Sch82]. At the nano-scaled level a non-linear relation with a stronger increase of the capillary force is found [Che08; Dör15].
- The capillary force is proportional to the surface tension if the non-linear influence on the contact angles is neglected. For example, a high surface tension causes a high contact angle that again leads to a lower capillary force [Lam05].
- The surface tension force F_s scales linear with the particle size whereas the pressure force F_p scales quadratically. Thus, with decreasing particle size the surface tension becomes dominant.

For non-symmetric capillary bridges a capillary torque occurs that is given by

$$\tau = -\sigma \frac{\partial A}{\partial \phi}. \tag{3.9}$$

By a balance of momentum the expression

$$\tilde{\tau} = \left| -\Delta\tilde{p} \iint_{\tilde{\Gamma}_\mathrm{I}} (\mathbf{r} \times \mathbf{n}) \, \mathrm{d}\tilde{\gamma} + \oint_{\tilde{\mathrm{L}}_\mathrm{I}} (\mathbf{r} \times \boldsymbol{\mu}) \, \mathrm{d}\tilde{l} \right| \tag{3.10}$$

is deduced analogously to eq. (3.7) for the dimensionless capillary force $\tilde{F}_\mathrm{c}$. The additional parameter $\mathbf{r}$ is the rotation axis for the momentum.
Capillary torque is investigated only by a few studies. Virozub et al. [Vir09] and Bedakar and Wu [Bed09] independently analyze capillary bridges between the shell surfaces of two non-parallel cylinders. With either increasing distance or contact angle a decreasing torque is observed. These tendencies have also been determined for the capillary force. For contact angles above 70° the torque is negligible small. A vanishing torque is calculated for parallel cylinders and interestingly also for the perpendicular configuration. However, it is shown that only in the first case a stable equilibrium exists. In this case small perturbations lead to a torque that forces the cylinders back to parallelism. Additionally, the torque increases with the liquid volume. The inverse relation is, however, determined by Takei et al. [Tak10]. They investigated capillary torque between non-circular plates theoretically and experimentally using a magnetic field technique. In accordance with Virozub et al. [Vir09] and Bedakar and Wu [Bed09] they found an increasing torque with an increasing distortion angle of the plates.

3.4. Simulation methods

Theoretical methods for evaluating capillary bridges can be classified based on different categorization parameters such as simplification, methodology or even application. An overview of the different methods is presented in figure 3.6. On the highest level there is a division into two groups: axisymmetric and non-symmetric problems. This categorization is chosen, since assuming a two-dimensional system significantly reduces the problem, which allows simplified calculations. Using assumptions beyond symmetry, such as an approximated meniscus shape, relatively simple closed-form equations for the capillary force are obtained. However, using only the symmetry assumption, the two-dimensional Young-Laplace equation must be solved numerically, which is done by an elliptic integral approach or a shooting method. A general three-dimensional formulation of the capillary bridge problem is much more complex and requires sophisticated non-symmetric methods. Energy minimization methods (section 3.4.2), computational fluid dynamics (CFD) [Dar10; Sun16; Was17] and in particular Lattice Boltzmann methods [Shi07; Wik12] and molecular dynamics [Gio16; Lau17; Tan18; Zha17] are described in the literature.
All of these methods are classified into pressure and volume methods. The pressure methods start from either a predefined capillary pressure, humidity or mean curvature. In thermodynamic equilibrium, these three parameters are directly linked by the Kelvin equation (eq. (2.26)) and the Young-Laplace equation (eq. (2.15)). The pressure methods are usually favorable for practical purposes and experimental investigations of volatile liquids, e.g. water and humid air, since the capillary force is constrained by humidity and particle geometry. In contrast, the volume methods start from a predefined constant volume and the capillary pressure must be obtained

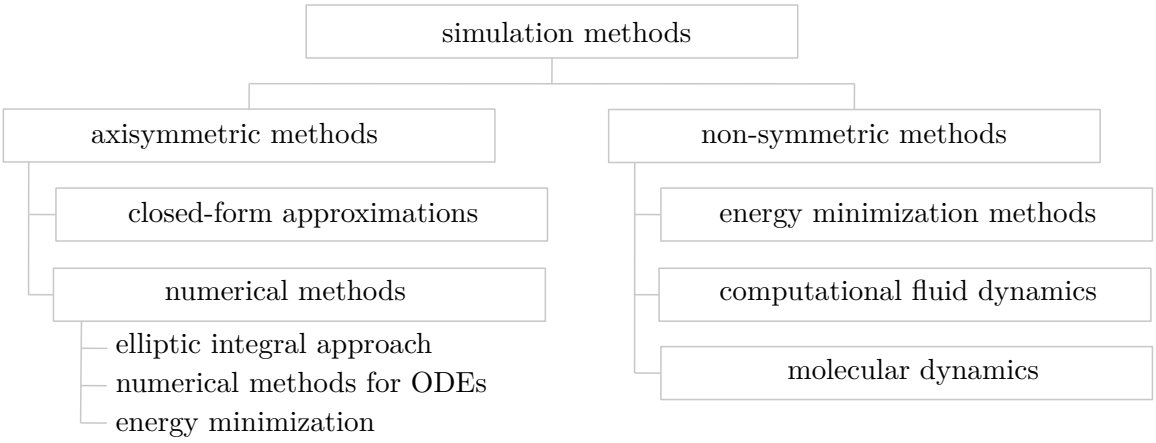

Figure 3.6.: Simulations methods for investigating capillary bridges

during calculation. All energy minimization methods are of this type because they minimize the interface energy subject to a given volume. If thermodynamic equilibrium is assumed, an iteration method must be used to find the volume corresponding to a given humidity. With respect to particle separation, the two methods are associated with the limiting cases of an infinitely slow (constant pressure) or fast (constant volume) particle movement (section 3.6).
Axisymmetric methods, energy minimization and CFD approaches implicitly assume the meniscus to be treated as continuum. Depending on the system size, this might be a strong assumption which is already indicated by the limits of the surface tension concept (section 2.1.2) and the Kelvin equation (section 2.4). Besides these limitations also adsorption layers [Asa10], line tension [Ami04; Mar09] and disjoint pressure might have to be considered in very small systems. However, in this work the continuum theory is applied and therefore intermolecular effects are neglected.

3.4.1. Axisymmetric methods

The different calculation methods for axisymmetric systems, as illustrated in figure 3.6, are discussed. First, closed-form equations, i.e., toroidal and parabolic approximations, are presented. Subsequently, numerical methods for solving eq. (2.16) in terms of elliptic integrals or using numerical methods for ordinary differential equation (ODE) are described. A chronological overview of the theoretical models developed until 1980 is given by Mehrotra and Sastry [Meh80].

Closed-form approximations for axisymmetric liquid bridges

The development of closed-form approximations requires an a priori chosen meniscus shape. The idea of approximating the meniscus by a circular arc is already introduced by Haines [Hai25] and Fischer [Fis26] early in the twentieth century. Note, that many different capillary force models are based on a toroidal meniscus, rather than “the“ unique toroidal approximation. Generally, a toroidal shape is applied with acceptable deviations if $|r_1| < |r_2|$. The toroidal meniscus profile is given by [Pep00]

$$y(x) = r_2 \pm r_1 \mp \sqrt{r_1^2 - x^2}, \tag{3.11}$$

where the origin of the coordinate system is at the narrowest meniscus point. The upper arithmetic operators refer to concave menisci and the lower ones to convex menisci, respectively. According to the assumption of a toroidal meniscus shape, the radius of curvature r_1 is constant. Since r_2 varies along the meniscus, the mean

curvature is not rigorously constant. This implies a spatial dependency of the capillary force. Evaluation at the three-phase contact line overestimates the capillary force and therefore, it is usually determined at the minimal meniscus diameter. This method is referred to as "gorge method" [Hot74; Lia93]. However, also averaging methods for r_2 are presented in order to approximate the capillary force [Meh80].
An explicit toroidal approximation for the capillary force between a sphere and a plane is given by Israelachvili [Isr11]

$$F_\mathrm{c} = 4\pi R\sigma \left(\cos\theta - \frac{a}{r_1}\right), \tag{3.12}$$

which reduces to

$$F_\mathrm{c} = 4\pi R\sigma \cos\theta \tag{3.13}$$

for zero distance. This model is widely applied in the analysis of capillary forces [Boc98; But09; Isr11; Lia16] and can be used if $R \gg r_2 \gg r_1, a$ and $\theta_1 \gg 0°$ and $\psi \approx 60°$ [But09]. The last two assumptions ensure a minor influence of the surface tension force which is neglected in this particular toroidal approximation. Eq. (3.12) estimates the capillary force depending on the curvature. A constrained volume formulation [Isr11]

$$F_\mathrm{c} = \frac{4\pi R\sigma \cos\theta}{1 + ad^{-1}} \tag{3.14}$$

is derived equivalently, with

$$d \coloneqq -a + \sqrt{a^2 + \frac{V}{\pi R}} \tag{3.15}$$

for a sphere-plane configuration [Rab05]. Eq. (3.12) and eq. (3.14) are transferred to a sphere-sphere system by using the Derjaguin approximation [Der34]. Following Derjaguin, the interparticle force between two spheres is estimated by the interaction energy between two planes. Therefore, an effective radius

$$R_\mathrm{eff} \coloneqq \frac{R_1 R_2}{R_1 + R_2}. \tag{3.16}$$

is introduced and replaces R. Moreover, an effective contact angle

$$\cos\theta_{\text{eff}} \coloneqq \frac{\cos\theta_1 + \cos\theta_2}{2} \tag{3.17}$$

is used to apply different wetting properties of the solids [But09]. A comparison of eq. (3.12) and a numerical method is performed for a sphere-plane geometry with perfectly wetted surfaces [Wil00]. The deviation is below 10 % for small distances and increases with the gap distance up to 20 %. Interestingly, for a large liquid volume the error decreases with increasing gap distance from $\approx 25\,\%$ to a minimum of $\approx 7\,\%$ at a medium distance. Moreover, Lambert et al. [Lam08] show very good agreement between eq. (3.12) and experimentally obtained capillary forces, that are measured for a low liquid volume between millimeter scaled unequal spheres. However, for large liquid volumes unacceptable deviations occur that clearly show the limits of the proposed model. Since the surface tension force is neglected in eq. (3.12), the model cannot be applied to large gap distances and thermodynamic states close to saturation (section 3.3). Rabinovic et al. [Rab05] demonstrate good agreement with experimental values by adding an extra surface tension term to eq. (3.14). In contrast, the analysis of Lambert et al. [Lam08] shows, that for large liquid volumes adding a surface tension term does not lead to acceptable deviations between theoretical and experimental values and might therefore be unnecessary.

For zero gap distance (eq. (3.13)), the estimated capillary force is independent of humidity and volume, respectively, which is explained by two opposing effects [But09]: With increasing humidity r_2 increases, leading to a larger cross section of the meniscus. However, since r_1 also increases, the capillary pressure decreases. These two effects directly cancel out and thus, the capillary force remains constant. This is confirmed by experimental investigations between cylindrical mica surface and using cyclohexane ($\sigma_{C_6H_{12}} = 26.6\,\text{mN}\cdot\text{m}^{-1}$) as liquid, whereas the investigations with water show a rising capillary force with humidity [Fis81]. This humidity independence is, however, inconsistent with many other theoretical and experimental investigations and can only be applied for relatively large particles. For example, Pakarinen et al. [Pak05] demonstrate a reasonable application of the model for $R > 1\,\mu\text{m}$).

A more complex toroidal force model estimates the capillary force of a sphere-plane system by [Tse03]

$$F_{\text{c}} = \pi\sigma R \sin\psi\,[2\sin(\psi + \theta_1) - R2H\sin\psi] \tag{3.18}$$

with the radii of curvature

$$r_1 = -\frac{R(1-\cos\psi)+a}{\cos(\psi+\theta_1)+\cos\theta_2} \quad \text{and} \quad r_2 = R\sin\psi + r_1\left[1-\sin(\psi+\theta_1)\right]. \tag{3.19}$$

Moreover, equations for all possible combinations of different spheres, cones and planes are derived by various authors. An overview of these equations is given by Tselishchev and Val'tsifer [Tse03] and pointed out in appendix A. A drawback of these equations is, that they can only be formulated as a constant volume method. Thus, they must be solved iteratively with respect to humidity, i.e., the wetting angle ψ must be varied in order to find the solution for a constrained humidity [But10b]. Moreover, many variations and enhanced toroidal models are reported in the literature, for example [Ard14; Che11; Har15; Pay11; Sun18b]. Acceptable deviations between a toroidal force model and numerical solutions are shown by Lian et al. [Lia93] ($< 10\,\%$) and de Lazzer et al. [Laz99] ($< 5\,\%$) for a wide range of parameters. Also Orr et al. [Orr75] investigate a sphere-plane system with zero distance and demonstrate deviations of toroidal and numerical mean curvatures below $6.5\,\%$ if $\theta_1 \leq 60°$ and $\psi \leq 10°$. These conditions imply a small bridge volume and humidity, respectively. Farshchi-Tabrizi et al. [Far06] model AFM tips by superposing two spheres with different radii into each other leading to a good qualitative agreement with experimental investigations. However, especially in the context of AFM measurements, the toroidal approximation might not be sufficient enough to estimate forces in very small systems. This is also pointed out by Dörmann and Schmid [Dör14] who demonstrate a good agreement between the toroidal approximation and numerical solutions for micrometer scaled particles, however, unacceptable large deviations a the nano scale. This is due to the fact that the assumption $|r_1| < |r_2|$ is not fulfilled for very small menisci.

One problem associated with the toroidal approximation is the changing sign of r_1 if the meniscus develops from concave to convex. In the concave situation as shown in figure 3.2, r_1 is outside the meniscus and according to the convention negatively defined. However, in convex situations r_1 is inside the meniscus and thus, exhibits a positive sign. This jumpy change of sign causes numerical difficulties in the transition region [Pep00]. However, in many applications the humidity is varied from $0 < \varphi < 1$, leading to only concave menisci and avoiding the problem of sign change. In order to estimate the error induced by the toroidal approximation of concave and convex menisci, Megias-Alguacil and Gauckler [Meg11] introduce the toroidal profile functional (eq. (3.11)) between equally sized spheres into the two-dimensional

Young-Laplace equation (eq. (2.16)) and calculate the resulting root mean squared error along the profile. These errors turn out to be below 10 % for concave menisci and around 30 % for convex menisci. Generally, an increasing error with increasing contact angle and decreasing gap distance is observed.
Analogous to the toridal approximation the meniscus can assumed to be parabolic with the profile [Pep00]

$$y(x) = c_0 x^2 + c_1 x + c_2. \tag{3.20}$$

The coefficients c_0, c_1 and c_2 are to be determined, whereas the toroidal profile is determined by r_1, r_2 and a. One advantage of the parabolic approximation is the smoothly changing sign of r_1 that avoids numerical problem when menisci change from concave to convex. Moreover, Pepin et al. [Pep00] show that the parabolic approximation is slightly more accurate compared to the toroidal approximation in estimating rupture distance and contact angles.
However, in both, the toroidal and parabolic approximation, the choice of an a priori chosen geometry of the meniscus is based on an apparent shape rather than a physical law. Thus, deviations in the capillary force might result. Lambert and Delchambre [Lam05] investigate systems with a characteristic length of 1 mm and show a confidence interval of 5 % when comparing the approximated capillary force to numerical solutions. Especially for very small gaps, the toroidal and parabolic approximation are not consistent while they converge to each other with increasing gap distance.
These approximation methods are very powerful as they provide closed-form equations for the capillary force that are easy to use. Thus, they can serve as a basis when considering more complicated effects such as roughness or dynamics. Moreover, they can be implemented directly in discrete element simulations (DEM) in order to study the behavior of granular material. Nevertheless, the limits of application must always be considered. Thus, if systems are analyzed that do not fulfill the assumptions or if more accurate solutions are needed, the two-dimensional Young-Laplace equation is solved by numerical methods in order to obtain the exact meniscus geometry.

Numerical solutions of the two-dimensional Young-Laplace equation

The two-dimensional Young-Laplace equation (eq. (2.16)) is an ODE of second order that cannot be solved analytically. The numerical methods are based on three different principles: First, a solution in terms of constant mean curvature (CMC) interfaces

are obtained. These interface types are expressed by elliptic integrals which are numerically evaluated. The second option is discretizing the meniscus geometry and incrementally evaluating the shape in order to fit the boundary conditions. Third, an equation for the free energy is derived that is minimized under the constraint of a constant volume for an axisymmetric system.
Based on the classical work of Delaunay [Del41] and Plateau [Pla64], the problem of axisymmetric capillary bridges has been formulated as a CMC problem in different ways [Ben14; Ken80]. From a mathematical perspective it is possible to describe CMC interfaces as solution to an isoperimetric problem of variational calculus, where a fixed volume is enclosed by a minimal interface area [Eel87]. This formulation is used in energy minimization methods that are discussed in their general formulation in section 3.4.2. Transforming eq. (2.16) to the dimensionless form and applying suitable substitutions, lead to an ODE of first order, that can be solved in terms of elliptic integrals. Evaluating these integral types requires their transformation to the first and second kind of Legendre's canonical form of elliptic integrals. The transformation equations must be defined separately for each type of CMC interface leading to an extensive set of equations [Sch82]. The solution for concave nodoids is evaluated precisely by Melrose [Mel66] to analyze menisci arsing from capillary condensation. Orr et al. [Orr75] derive approximately 60 equations for the different CMC interface types. Their investigations are limited to zero gap distance and are, therefore, extended by Rubinstein and Fel [Rub14] who demonstrate, that multiple solutions might occur which results in the open question of local stability (section 3.4.3). The elliptic integral equations are expressed in terms of the filling angle ψ and therefore, the pressure and the volume must be obtained during calculation.
Besides solving the Young-Laplace equation in terms of elliptic integrals, numerical procedures for the solution of ODEs can be used. Using theses approaches, the meniscus geometry is described by a finite number of line elements or points. Lian et al. [Lia93] describe the solution of the Young-Laplace equation by a truncated Taylor series and used the modified Euler method to obtain the solution of the ODE. They investigate capillary bridges between equally sized spheres and apply the symmetry about the y-axis to derive suitable boundary conditions.
Another numerical approach is using a shooting method which converts a boundary value problem to an initial value problem. First, a meniscus trajectory is developed from a given starting point and according to the predefined mean curvature. This initial value problem is solved by a Runge-Kutta-Method. In particular, explicit Euler methods are usually applied. In order to fit a certain boundary condition, e.g.

a contact angle at the second particle, the starting point is varied until the condition is fulfilled with a certain accuracy. The variation of the starting point is usually done by a bisection or Newton scheme. Thus, the overall problem is to find a solution to the initial value problem (i.e., the meniscus trajectory for a given filling angle and mean curvature) that also solves the boundary value problem (i.e., contact angle at the second particle). This method is described early by Hotta et al. [Hot74] and often applied with slight differences [Dör18; Lam05; Pak05; Qia17; Sáe90].
Shooting methods are constant pressure methods and an additional outer iteration has to be applied if the volume should be predefined. A shooting method with such a doubled iteration scheme for the liquid volume is presented by Lambert and Delchambre [Lam05]. Their model is validated by the analytic case of a catenoid between two parallel planes showing a relative error of approximately 1.5 %. Moreover, theoretical and experimental capillary forces of a sphere plane system show good agreements with the developed model. Another version of a shooting method is prescribing the capillary pressure as it is presented by Dörmann [Dör18] to analyze capillary bridges in thermodynamic equilibrium. Starting from humidity, the capillary pressure is given by the Kelvin equation (eq. (2.26)) and the mean curvature is subsequently determined by the Young-Laplace equation (eq. (2.15)). The filling angle is iteratively varied untill the meniscus fits the contact angle condition at the second particle. Thus, using this method the liquid volume results from the prescribed humidity.
The third principle, i.e., the energy minimization principle, is used by De Bisschop and Rigole [Bis82] who derived a second order differential equation for the meniscus geometry by minimizing the system's total free energy constrained to fixed volume. The capillary pressure and the meniscus profile are obtained by numerical integration. The calculated values show good agreements with experimental results and also comparison to numerical solutions of *Surface Evolver* match [Kus10]. Another energy minimization method is proposed by Sun and Sakai [Sun18b] who formulate the energy functional in terms of a discretized meniscus. For the optimization procedure three constraints are applied: (1) constant volume, (2) meniscus endpoints must be placed on the solid interfaces and (3) the meniscus nods are positioned equidistantly, which is not necessary, however, it improves convergence. Thus, the meniscus profile is developed from an initial guess which is chosen to be a straight cylinder. The results agree very well with experimental data obtained by Rabinovich et al. [Rab05] and Lambert et al. [Lam08].
Generally, the numerical solutions of the Young-Laplace equation are more accurate compared to the closed-form equations, since they calculate the exact meniscus ge-

ometry. However, their computational effort is a lot higher and must be taken into account. Nevertheless, they require axisymmetry and therefore, more general energy minimization methods are described subsequently.

3.4.2. Energy minimization

The problem of capillary bridges can also be formulated via variational calculus which is minimizing the energy constrained to a fixed volume and geometric boundaries. This can mathematically be written as [Hor90]

$$E^* = min\{E : \Omega \subset \Pi, V = V_0\} \qquad \text{with} \qquad V = \int_\Omega \mathrm{d}\Omega \tag{3.21}$$

where E is the energy functional that is to be minimized for the prescribed volume V_0. Ω is the domain that is filled with liquid and must be within the solid boundary domain Π in space $\mathbb{R}^3$. Here, energy minimization methods that are based on a Finite Element Method are considered. Using these methods, the geometry of the capillary bridge is derived by an optimization procedure.
The most commonly used software tool is *Surface Evolver* that is developed by Brakke [Bra92b]. The algorithm is designed to minimize interface energy taking surface tension, gravity or other energy forms into account. The general idea behind *Surface Evolver* is to represent an interface by the sum of finite triangles. The optimization is subsequently done on the vertex level where the interface is developed by the conjugate gradient method. This method is classified as discretized-optimized procedure and, therefore, requires an approximation for the curvature of the interface, since on a triangular mesh the curvature would actually be zero on each triangle and infinity on all edges. *Surface Evolver* allows to specify either geometrical constraints on vertex positions or integral constraints. For the capillary bridge problem the integral liquid volume is usually predefined. To ensure fast convergence and to analyze eigenvalues, the Hessian is implemented [Bra97]. The major advantage of *Surface Evolver* is its general implementation that enables its application to various problems. One of the first applications of *Surface Evolver* is presented by Mittelman [Mit93] who calculated symmetric capillary interfaces in a cube. With respect to capillary bridges, non-symmetric systems [Cha07; Vir09; Bed09; Bro13], stability [Far15; Ata17], the influence of gravity [Sun18a], lateral capillary forces [Mas10], the stability of liquid bridges between three spherical particle [Sem16; Wan17] and the liquid redistribution in consequence of rupture [Wu19] are investigated using *Surface Evolver*.

Similar discretized optimized-methods for the optimization with constraints on a vertex level are presented in the literature [Che08; Dzi06; Pol02]. A significant drawback of these methods is their requirement for high mesh quality during all iterations. This includes a regular distribution of vertices as well as properly shaped triangles. One option to overcome this issue is minimizing a least square energy functional instead of the commonly used interface area functional [Pan12]. This method allows to optimize the interface area and the mesh quality at the same time by using an extended centroidal Voronoi tessellation. The idea is modified by Renka [Ren15] who implements a different energy functional. He derives a non-linear least square system by using the prescribed volume constraint as shape control parameter and by adding a density function to the squared area functional presented earlier in [Ren95; Ren14]. The optimization is done via a trust region method. A major advantage of this method is that neither a reasonable initial guess, nor a high quality start mesh are mandatory.
A Newton-like energy minimization approach is developed by Iliev [Ili95] who solved the variational problem of eq. (3.21) by an iterative algorithm based on a direct evaluation of virtual displacements. Although generally possible, the algorithm has not yet been applied to the capillary bridge problem. Instead, the method is extended [Ili06] for studying contact angle hysteresis on periodically shaped interfaces [Ili16; Ili18].
Another method is presented by Ardito et al [Ard14]. The calculation of an ideal stiff thin membrane is classically known as mechanical problem. Starting from the formulation of the total potential energy the problem is formulated analogous to the classical principle of virtual power. This implies a weak constrained formulation for the constant mean curvature and the contact angle. For axisymmetric configurations the results match with the CMC interface theory according to Kenmotsu [Ken80]. However, comparisons with molecular dynamic simulations by Ko et al. [Ko10] show significant deviations of the calculated capillary force and the predicted maximum separation distance. Moreover, it is stressed that the method is capable of analyzing capillary bridges between arbitrarily shaped particles, however, this is not demonstrated.
A general problem of the described methods is the possible existence of multiple solutions which must be evaluated with regard to their physical correctness. Thus, the stability of the obtained solutions is briefly discussed in the next section.

3.4.3. Stability of the solution of the Young-Laplace equation

In the context of capillary bridges, different types of stability are considered. On the one hand, there are physical stability problems. For example, finding the maximum distance for which a static meniscus exists is often described as stability problem, i.e., the mechanical stability. Moreover, in dynamic systems oscillation and dynamic forces lead to dynamic stability issues. On the other hand, for a given system configuration multiple solutions to the Young-Laplace equation might exist, where only one is assumed to be physically correct and stable. Thus, mathematically correct solutions must be analyzed with respect to their physical correctness. This type of stability is briefly discussed here, whereas the static rupture distance is covered in section 3.6. Dynamic stability issues are not considered in this work.

The existence of multiple solutions of the Young-Laplace equation between parallel plates is discussed by Fortes [For82]. He evaluated the Helmholtz energy to identify stable solutions. Lian et al. [Lia93] plot several parameters over the separation distance under the constraint of a constant volume. As an example, the filling angle is shown in figure 3.7 (a). For each distance, two corresponding solutions are obtained that converge to one solution with rising distance. This behavior is qualitatively confirmed by other investigations [Erl71; Wan16; Wil00]. The convergence point is often assumed to be the physical rupture distance as discussed in section 3.6. A formulation of the Gibbs free energy leads to an explicit criterion for stable and unstable solutions as shown in figure 3.7 (b). The different energy levels of two corresponding solutions are demonstrated and thus, the solution with the lower free surface energy is the physically stable solution.

Moreover, the stability of different CMC interfaces is investigated. Fel and Rubinstein [Fel15] develop a non-spectral stability approach for isoperimetric problems involving two-dimensional functionals that are minimized. Thus, application to capillary bridges enables the identification of stable existence regions for catenoid and cylindrical menisci between differently shaped particles. Moreover, stability of the other CMC surface types is investigated between two planes. Another stability analysis is presented by Vogel [Vog06], who investigated liquid bridges between two spheres and a relatively large liquid volume. He demonstrates that convex unduloid menisci correspond to stable local energy minima, whereas convex nodoid menisci are unstable. This is supported by theoretical and experimental force stability analysis of Niven [Niv06], who showed, that menisci exerting a repulsive capillary force on the particles are mechanically unstable. Hence, convex nodoids are unstable and the maximum liquid volume to from a stable capillary bridge is defined by a spherical

meniscus exhibiting zero capillary force (section 3.2). The occurring instability at large liquid volumes is also investigated taking gravity into account [Sáe90]. By a perturbation analysis the maximum volume of stable liquid menisci is investigated depending on the Bond number and the contact angles. A comprehensive overview of static and dynamic stability analysis of capillary interfaces is given by Bostwick and Steen [Bos15].

3.5. Experimental methods

Experimental methods for the analysis of capillary bridges are divided into two groups: visualization of the meniscus shape and direct measurement of the capillary forces. Visualization approaches are rather simple as the meniscus is directly imaged. Farmer and Bird [Far15] analyze menisci between glass beds ($R = 2\,\mathrm{mm}$) attached to needles that are brought into contact. The water volume is positioned on the bed rather than emerging from condensation. Thus, instabilities at large liquid volumes, i.e., convex menisci, are observed. Similarly, Gagneux et al. [Gag16] ($R = 8\,\mathrm{mm}$) and Nguyen et al. [Ngu19] ($R = 7\,\mathrm{mm}$) image the meniscus between two beds and a bed and a plane, respectively. Their meniscus shapes agree well with theoretical values derived by the CMC surface theory, which is then used to calculate the unknown capillary pressure. Further visualizations of the meniscus are reported [Ata17; Bro12; Sun18a]. A significant drawback of visualization methods is their restriction to relatively large

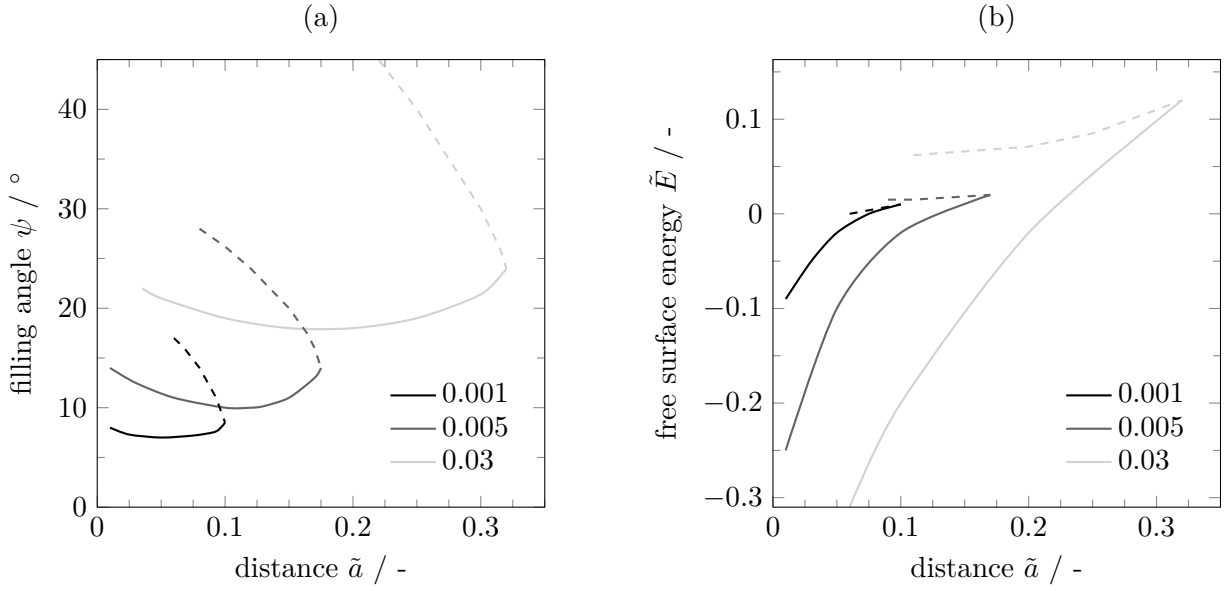

Figure 3.7.: Stable (——) and unstable (- - - -) solutions of the Young-Laplace equation for different dimensionless liquid volumes $\tilde{V}$ taken from Lian et al. [Lia93]

geometries as indicated by the given bed radii. An application at the micro scale and below is not possible. Moreover, the capillary force is not directly measured and must be calculated from the apparent geometry. However, the direct measurement of capillary forces is not straightforward. One issue is, that only the overall adhesive force can be measured rather than the single capillary force. Thus, at least van der Waals forces and probably electrostatic forces are included in the measured values. Since interparticle forces are short ranged, both, a very sensitive force detection system and a precise distance control are required. Moreover, roughness and contamination of the solid interface significantly influence the measurements [But10b]. A comprehensive overview of experimental methods for intermolecular, interparticle and surface forces is given by Israelachvili [Isr11] and additionally a historical perspective on surface force measurement methods is pointed out by Craig [Cra97]. The most commonly used methods, i.e., the surface force apparatus (SFA) and the atomic force microscope (AFM), are subsequently described.

The SFA is developed by Tabor and Winterton [Tab69] and Israelachvili and Tabor [Isr72]. It is originally designed to measure van der Waals forces between crossed cylindrical mica interfaces ($R \approx 1\,\mathrm{cm}$). The idea of choosing crossed cylindrical geometries is introduced by Tomlinson [Tom28], since it avoids orientation issues that might occur when using plane interfaces. Locally, the cylindrical configuration corresponds to a sphere-plane system. Using an SFA, the force is directly obtained by measurement springs with a sensitivity of $\approx 10^{-8}\,\mathrm{N}$ [Isr11]. Thus, reliable measurements depend on the precise information about the spring constant [But10b]. The distance control is realized by a three stage system that consists of screws and springs on the larger scales and a piezoactuator with a precision of $\approx 1\,\mathrm{nm}$ on the finest stage. During measurements, the distance is precisely detected by multi beam interferometry [Tol48] that uses „fringes of equal chromatic order“ (FECO) [Isr11]. Even the absolute zero distance, i.e., molecular contact of the interfaces, can be determined [But10b]. Besides separation distance, also the thickness of adsorption layers and thermal drift of the interfaces are tracked. In fact, the direct visual monitoring is a great advantage of the SFA, since damages are directly observed [Isr11]. The resolutions in the normal ($\approx 0.1\,\mathrm{nm}$) and lateral ($\approx 1\,\mu\mathrm{m}$) direction vary significantly. The low lateral resolution is a significant disadvantage of the SFA. Moreover, due to the large scale of the cylinders, a relative large area has to be kept free from contamination which is a serious issue. Another disadvantage is, that the interface structure can only by determined indirectly by the FECO fringes. Thus, the SFA is often combined with another direct surface morphology measuring method, e.g. microscopy

and spectroscopy analysis [Isr11]. The solid interfaces usually consist of silica cylinders which are covered with thin sheets of mica, since mica exhibits a molecularly smooth interface. Moreover, it is flexible, chemically stable, inert with respect to most liquids and exhibits a high shear stress and tensile strength [But10b]. Using other materials is generally possible, however, they have to be transparent in order to use the multi beam interferometry [Isr11]. The SFA is used intensively to study capillarity and capillary forces [Fis81; Koh00; Mae06; Res02].
The other option to measure capillary forces is the AFM that is developed by Binnig et al. [Bin86]. It is used either to obtain forces between a tip and a sample at a certain point or to image interface topology by interpreting spatial variations of force-distance curves. A very comprehensive overview of AFM measurements, including a detailed description of the method and a discussion of various surfaces forces, is given by Butt et al. [But05]. In an AFM a sharp tip is attached to the end of a micro-structured cantilever. Note, that in the special case of attaching a particle to the end of the cantilever, the method is reffered to as colloidal probe technique. When the tip is brought into contact with the sample the cantilever deflects due to the surface forces. The backside of the cantilever reflects a laser beam, which is captured by a split photodiode. Thus, the measured deflection-position curve must be transformed into a force-distance curve [But10b]. The sensitivity of an AFM is about $10^{-12} - 10^{-11}$ N and determined by the spring stiffness and accuracy of the displacement measuring [Isr11]. Thus, the spring constant should always be calibrated in order to be as accurate as possible [But10b].
As already mentioned, a general issue of measuring capillary forces is the existence of other interparticle forces that cannot be removed. At the same time, the existence of a liquid meniscus might interfere with other experimental investigations, e.g. imaging interface topology, since under ambient conditions menisci might undesirably emerge from condensation. An option to gain more insight into the contribution of each force is changing the ambient conditions, which is possible with an AFM. For example, capillary forces are avoided by performing measurements fully immersed in water [Ouy01; Wei89]. This investigation of pure van der Waals forces allows conclusions about the ratio of van der Waals and capillary forces in air conditions. Another option to reduce capillary forces is the use of hydrophobic interfaces, since the force decreases significantly with increasing contact angle and menisci cannot emerge from condensation on strongly hydrophobic interfaces (section 3.3).
A great advantage of the AFM technique is that contamination is a minor issue, since the investigated areas are very small. Additionally, no limitations with respect to the

materials exist. An important drawback is, however, the determination of the zero distance which cannot be done by an independent methods such as the FECO fringes in the SFA [But10b]. Moreover, the data interpretation is complex, e.g. heterogeneity on a smooth interface and roughness on a homogeneous interface might provide very similar data [Isr11]. Another, critical issue is the high sensitivity of the method which leads to large fluctuations of the results and a considerable influence of tip wear. Chung et al. [Chu05] demonstrate considerable structural changes of the AFM tip, even under extremely low normal load. This is supported by Farshichi-Tabrizi et al. [Far06], who used the AFM to analyze capillary forces. Their results exhibit two kinds of fluctuations: a random noise and a larger time scale variation. The random noise cannot be traced back to a statistical process of the system, however, its magnitude corresponds well with the theoretically estimated overall measurement error. The large time scale fluctuations are explained by the structural changes of the AFM tip resulting from high stresses during the measurement. Thus, due to the continuously changing tip geometry the results are not satisfactorily reproducible. Besides these measurements, many others investigations of capillary forces with AFM are reported [Ata02; Cha10; Jon02; Sed00; Sir06; van08; Xia00; Xu98].

3.6. Overview of static capillary bridge issues

The general system of a capillary bridge is described in detail in the previous sections. However, usually simplified systems are analyzed in order to reduce the complexity. For static capillary bridges different issues, that can be taken into account, are identified:

- influence of external fields
  - gravity[1]
  - electrostatic fields[2] [Kli04; Pel01]
- rupture distance[1]
- solid interface constraints
  - particle shape[1]
  - roughness (section 3.7)
  - multi particle systems[2] [Lie17; Ryn03; Sem16; Urs99; Wan17]

[1]General issue, briefly discussed in this section
[2]Specific issue, not discussed in this work. For more information see references.

The influence of roughness is discussed comprehensively in section 3.7, since it is extended by the theory of topological rough interface. All issues are considered for static or quasi-static problems and there are strong interdependencies between them. For example, the rupture distance might be significantly influenced by a gravitational field. When taking dynamics into account, further stability issues such as oscillation might occur and dynamic forces have to be considered. Thus, a significant influence of dynamics on all of the listed issues exists. As an example, Mazzone et al. [Maz87] showed that the static maximum separation distance is much lower than the dynamic one which is explained by the fact that viscous forces rather than surface forces dominate the dynamic behavior. Nevertheless, this work focuses on static capillary bridges and therefore, dynamic effects are not taken into account.

Influence of gravity in static capillary bridge systems

For most capillary applications neglect of gravity is reasonable. Assuming a gravitational acceleration g that acts in the direction z, the Young-Laplace equation (eq. (2.15)) is extended to

$$\Delta p_0 + g(z - z_0)\,(\rho_\mathrm{l} - \rho_\mathrm{g}) = \sigma 2H \tag{3.22}$$

with the liquid and gas density ρ_l and ρ_g. This formulation implies the definition of a reference point z_0 directly on the interface where the pressure difference is Δp_0, however, this is usually not mentioned explicitly in the literature. Instead, the origin of the coordinate system is set at $z_0 = 0$. Thus, a short derivation including a more general formulation with a gravitational vector $\mathbf{g}$ is given in appendix B. Eq. (3.22) states that the mean curvature H linearly changes in the direction of gravitation with the slope $g\Delta\rho/(2\sigma)$. This equation can be obtained by either adding gravitational force to eq. (2.13) or by adding a potential energy term to eq. (2.17). For the estimation of the gravitational effect the Bond number

$$Bo := \frac{L^2 \Delta\rho g}{\sigma} \tag{3.23}$$

is usually considered. Again, the particle radius R is used as characteristic length L. The Bond number relates volume forces i.e., gravitation to the surface tension force

and should be $\ll 1$ for neglecting gravity. A more conservative criterion taking the mean curvature into account is developed by Orr et al. [Orr75]

$$\frac{Bo}{|HR|} < 0.01. \tag{3.24}$$

They demonstrated for axisymmetric capillary bridges between a sphere and a plane deviations in the solutions of calculations neglecting gravity and taking gravity into account below 0.4 % if eq. 3.24 is satisfied. Using the definition of the Bond number and the Young-Laplace equation, eq. 3.24 is formulated as

$$\frac{\Delta\rho g l_{\mathrm{g}}}{|\Delta p|} < 0.01. \tag{3.25}$$

where the particle radius R is replaced by the maximum length of the capillary bridge in the direction of the gravitational field l_{g}. This equation reveals, that the pressure difference induced by gravity must be less than 1 % of the capillary pressure [Sch82]. It also becomes clear that even for small capillary bridges gravity might be significant if the capillary pressure tends to zero i.e., close to saturation. An enhanced classification of gravitational regimes from gravity free to complete draining is presented by Adams et al. [Ada02] for perfectly wetting spheres and shown in table 3.1. Following these investigations, the dimensionless parameter $\tilde{V}Bo$ is used to estimate the influence of gravity rather than the pure Bond number. Further investigations considering gravity theoretically [Bou82; Sáe90; Sun18a] and experimentally [Bay87] are presented in the literature.

Table 3.1.: Gravitational regimes of capillary bridges according to Adams et al. [Ada02]

$\tilde{V}Bo$	regime	description
< 0.01	gravity free	insignificant effect of gravity
$0.01 - 0.15$	transitional	significant decrease in rupture distance and change in the force by half the bridge weight
$0.15 - 2.0$	gravity controlled	bridge rupture by draining mechanism
$2.0 <$	complete draining	stable bridges do not exist

Quasi-static rupture distance of capillary bridges

Rupture distance is defined as the maximum separation distance at which a stable meniscus can form. Thus, it can also be interpreted as existence problem of a capillary bridge or as a criterion for condensation. Especially in the context of DEM simulations, the maximum separation distance is of great interest, as it directly gives the maximum interacting radius of the capillary force. The term "rupture" is commonly used in the literature although it associates dynamically separating particles. However, the problem is usually considered in a static way, i.e., the static capillary bridge is calculated for different separation distances. In this context, two limiting cases are considered: On the one hand, calculations under the constraint of a constant humidity are interpreted as an infinitely slow separation of the particles so that thermodynamic equilibrium is reached for each state. Thus, liquid is condensing to or evaporating from the meniscus and the mean curvature is kept constant. However, the kinetics of condensation, as for example described by Kohonen et al.[Koh99], are completely neglected. On the other hand, an infinitely fast separation leads to a constant liquid volume and the mean curvature is changing during this process. In this case, dynamic effects of stretching or compressing the meniscus, such as oscillation, are neglected [Dar10; Mol93; Zha96].
A relatively simple approach for the maximum separation distance is derived in the framework of the toroidal model [But08]

$$\tilde{a}_{\max} < \tilde{r}_1(\cos\theta_1 + \cos\theta_2), \tag{3.26}$$

since the right side of this equation is the maximum distance an arc can span. Thus, only for smaller gap distances a meniscus can form. This rather simple condition is very useful for modeling capillary bridges between rough interfaces, since the areas in which liquid condenses are easily identified. Another criterion is proposed by de Bisschop and Rigole [Bis82]. Analogous to the results illustrated in figure 3.7 (a), they observe a minimum of the filling angle ψ with respect to the distance. This minimum is assumed to be the maximum distance. However, experimental investigations predict larger distances [Mas65]. Thus, the distance at which the numerically obtained two solutions converge to a single solution is proposed as rupture distance [Erl71; Lia93]. Using this criterion,

$$\tilde{a}_{\max} = (1 + 0.5\theta)\sqrt[3]{\tilde{V}}. \tag{3.27}$$

is derived by a fitting to quasi-static numerical results [Lia93]. This equation is valid for contact angles below 40°. However, for a sphere and a plane, eq. (3.27) overestimates the rupture distance as shown by measurements of Willett et al. [Wil00]. Using a curve fit for their experimental data

$$\tilde{a}_{\max} = \left(1 + \frac{\theta}{4}\left(\frac{R_1}{R_2} + 1\right)\right)\left(\sqrt[3]{\tilde{V}} + \left(\frac{R_2}{2R_1} - \frac{2}{5}\right)\sqrt[3]{\tilde{V}}^2\right) \tag{3.28}$$

is proposed as a more accurate prediction of the maximum separations distance.
Moreover, the maximum separation distance of capillary bridges is influenced by gravitation. Adams [Ada02] proposes a modification of eq. 3.27

$$\tilde{a}_{\max} \approx (1 - 0.48\tilde{V}Bo)\sqrt[3]{\tilde{V}} \tag{3.29}$$

to estimate the separation distance in a gravitational field for $\theta = 0°$. Obviously, the maximum distance $\tilde{a}_{\max}$ decreases with increasing influence of gravity and for very large Bond numbers stable menisci might not exist even if the particles are in contact. For $0.15 < \tilde{V}Bo < 2$ rupture is completely controlled by draining mechanisms and for $\tilde{V}Bo > 2$ a stable bridge does not exist (table 3.1). Mazzone et al. [Maz86] also demonstrate a decreasing rupture distance with increasing Bond number, however, this gravity influence is related to the liquid volume and may be neglected at low volumes.
Moreover, approaches based on other physical considerations are described in the literature. Pepin et al. [Pep00] predict rupture at the distance where the liquid-gas interface of the meniscus equals the liquid-gas interface of the remaining droplets on the particles in a volume conservative system. Comparison of the estimated rupture distance with experimental results shows an error below 4 %. The interface criterion is later applied by Darabi et al. [Dar10] to calculate capillary bridge evolution and rupture by a numerical CFD study. They confirm a reasonable application of the quasi-static Pepin approach for $Ca < 10^{-3}$, $We < 10^{-2}$, $Bo < 1$ and equal contact angles. Dai an Lu [Dai98] apply the theory of the stability of a liquid cylinder immersed in a immiscible liquid, that is originally proposed by Walstra [Wal83], to the capillary bridge problem. Thus, the Young-Laplace equation does not need to be solved. Their model underestimates the maximum separation distance and is therefore extended by a correction factor obtained from a fitting with experimental results. Although the physical criterion is very different, the results agree well with eq. (3.27). Another approach is presented by Yang et al. [Yan10]. They use a toroidal approximation for the meniscus and estimate the rupture distance based on the Griffith energy

balance criterion which states very general that at the mechanical stability limit the overall change of the interfacial energy of the capillary bridge equals the change in the surface energy of the two remaining droplets [Boe07]. Applying this model to a sphere plane system, an increasing maximum separation distance with increasing contact angle, particle radius and humidity, respectively, is demonstrated. Moreover, for $R > 600\,\text{nm}$ agreement with the models of Lian et al. [Lia93] and Willett et al. [Wil00] is shown.

Non-symmetric particle shapes

The prevailing majority of capillary bridge investigations is focused on symmetric bridges between spheres, cones and planes. However, due to the development of more general simulation methods, analyzing arbitrary particle geometries becomes possible. The investigations of Virozub et al. [Vir09] and Bedakar et al. [Bed09] for capillary bridges between the shell surface of non-parallel cylinders are already summarized in section 3.3 in the context of capillary torque.
Chau et al. present a theoretical [Cha07] and experimental [Cha10] study of capillary forces between a plane and a cone of pyramid corresponding to an AFM tip. The simulations are carried out using *Surface Evolver* and match well with the experimental results. An important observation is that the capillary force significantly depends on the tilt of the AFM tip, which is used to control the capillary force in micro assembling applications.
Moreover, non-symmetric bridges in a slit pore geometry are presented [Bro12]. Two hydrophobic plane interfaces are patterned with a hydrophilic stripe and the three-dimensional capillary bridge is simulated using *Surface Evolver*. With increasing separation distance and a constant volume approach the aspect ratio, i.e., length per width, decreases. However, the pinning angle increases and thus, the menisci develop from concave to convex. The calculated overall capillary force is found to be always attractive although the pressure component is repulsive for convex menisci.
A very interesting investigation is presented by Farmer and Bird [Far15]. Although they consider spherical symmetric particle shapes, they experimentally observe non-symmetric menisci. In accordance with the presented theory, images of borosilicate glass beds ($a = 2\,\text{mm}$) show axisymmetric bridges for relatively low liquid volumes. However, as the liquid volume increases up to convex menisci the capillary bridge spontaneously shifts out of the symmetry axis. This phenomenon is simulated by inducing an asymmetric perturbation to a previously calculated symmetric capillary bridge. The system will either evolve back to axisymmetry in case this configura-

tion is a stable equilibrium or a new asymmetric steady state is calculated. These asymmetric steady states exist for bridge volumes that are above the volume of the spherical bridge exhibiting the same contact angles. Moreover, theoretical considerations illustrate, that for a given constant volume and contact angel the interface energy of the asymmetric state is lower compared to the symmetric state.

3.7. Capillary bridges between rough solids

Manufacturing ideally smooth and homogeneous solid interfaces on a molecular level is impossible. Approximately smooth interfaces exhibit roughness at the nanometer scale and above. The characteristic length scale of the capillary force is given by the Kelvin length which is for water under ambient conditions about 0.537 nm. Relating the Kelvin length to roughness scales, a significant influence on the capillary force is already indicated [But08]. Moreover, several experimental results cannot be explained by a smooth theory. In fact, different and inconsistent results for the humidity dependency are reported in the literature that are often traced back to roughness. However, when modeling capillary bridges on rough interfaces, a theoretical description of such a topology is required first.

3.7.1. Theory of topological rough interfaces

Interface topology is studied intensively in order to find interdependencies between the topology and physical characteristics of various systems. Therefore, parameters describing several aspects of roughness are introduced and subsequently the most common topology models are discussed.

Parameters to describe rough topology

Describing rough interfaces is complicated and cannot be done by a single parameter. Various parameters for three-dimensional interfaces are defined in [ISO12]. The three-dimensional quantities are indicated by S, whereas the corresponding two-dimensional quantities are indicated by R. Height parameters such as the maximum peak S_p, valley S_v and surface height S_z are defined in [ISO12] and their two-dimensional versions R_p, R_v and R_z are illustrated in figure 3.8 (a) for a given interface length l. In this schematic diagram the x-axis corresponds to the centerline of the interface,

i.e., the integral deviations from this line are zero. Roughness is often characterized by the mean averaged height

$$R_\mathrm{a} \coloneqq \frac{1}{l}\int_\mathrm{l} |z(x)|\mathrm{d}x \qquad \text{and} \qquad S_\mathrm{a} \coloneqq \frac{1}{A}\iint_\mathrm{A} |z(x,y)|\mathrm{d}x\,\mathrm{d}y \tag{3.30}$$

or by the root mean square roughness (RMS)

$$R_\mathrm{q} \coloneqq \sqrt{\frac{1}{l}\int_\mathrm{l} z^2(x)\mathrm{d}x} \qquad \text{and} \qquad S_\mathrm{q} \coloneqq \sqrt{\frac{1}{A}\iint_\mathrm{A} z^2(x,y)\mathrm{d}x\,\mathrm{d}y} \tag{3.31}$$

that describes the standard deviation from the mean line in a Cartesian coordinate system. l and A are the length and area of the investigated two and three-dimensional interface. Height parameters reduce the complex rough interface structure to single quantities making conclusions about the profile impossible. Thus, also spatial parameters are defined that use auto correlation functions to analyze preferred directions. Height and spatial parameters are combined to obtain hybrid quantities, e.g. the area fraction S_dr. The additional area resulting from roughness is related to the projected smooth area A and the area fraction is given by

$$S_\mathrm{dr} \coloneqq \frac{A_\mathrm{r} - A}{A} = \frac{1}{A}\iint_\mathrm{A} \sqrt{1 + \left(\frac{\partial z(x,y)}{\partial x}\right)^2 + \left(\frac{\partial z(x,y)}{\partial y}\right)^2}\,\mathrm{d}x\,\mathrm{d}y - 1 \tag{3.32}$$

where A_r is the rough interface area. Thus, this quantity is interpreted as magnitude of roughness and is zero for ideal smooth interfaces. However, for practical purposes it is not straightforward to determine the area fraction [Sto00], but it is very useful when

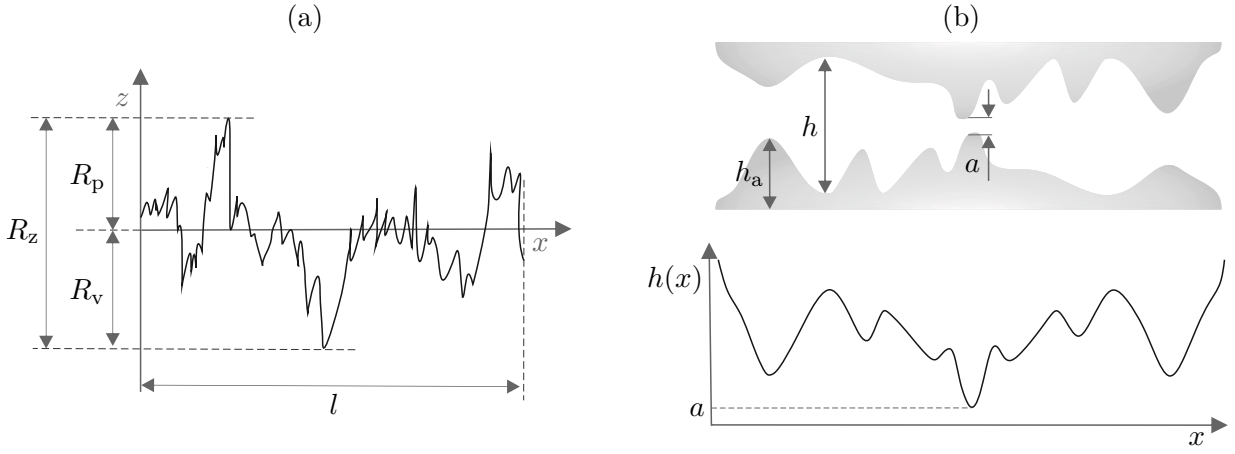

Figure 3.8.: Two dimensional roughness parameters (a) and height distribution function of a rough gap (b)

considering roughness in wetting models such as the Wenzel model (section 2.3.2). In addition to the above described parameters, also parameters of defined functions and mixed parameters to describe texture directions are defined in [ISO12].
When describing gaps between rough interfaces, a gap height distribution function $h(x)$ is defined as illustrated in figure 3.8 (b). This function can also be obtained for smooth geometries, however, is predominantly used in the context of roughness. As described subsequently, many topology models use a probability distribution for the asperity heights h_a to model roughness which is often referred to as height distribution function. The difference between the gap height distribution $h(x)$ and the asperity height distribution should be noted carefully.

Mathematical models for rough topology

Most research of rough surface topology is found in the context of contact mechanics in order to evaluate solid contact forces. The results for modeling rough interface topology are qualitatively presented in this section, however, details of the mathematical equations as well as contact models are not considered in here. For the characterization of randomly rough interfaces statistical, fractal and hierarchical approaches exist [Bhu13].
Statistical models describe the dimensions of asperities, i.e., height h_a and radius, by a probability density function. It is usually assumed to approximate the shape of a single asperity by a hemisphere [Gre66; Maj90; Nay71; Rob01], however, other models such as conical shapes [His75] are also proposed. A normal distribution of asperity radii is presented by Nayak [Nay71]. However, the benefit of a size distribution is questioned [Gre01] and most statistical models focus on the asperity height distribution assuming a constant asperity size. The most applied height distribution is the normal distribution but also non-normal approaches exist [Luo13; Man10]. Greenwood and Williamson [Gre66] proposed one of the first models of a normal height distribution in order to calculate the real area of contact of two solids. An important advantage of the Gaussian roughness is that the density function is mathematically relatively easy and efficient to handle. Many technical surfaces are described accurately enough by this model.
A major drawback of statistical models is that they cannot explain the scan length dependency of measured rough parameters [Big12; Bor05]. Thus, they are not suitable for the development of general models [Rob01; Wan20]. Although, the statistical approaches and especially the Gaussian distribution are widely applied, other studies suggest a fractal character of roughness that is accordant with the scan length

dependency. An extraordinary apology is published by Greenwood and Wu [Gre01]. Reviewing the classical theory of Greenwood and Williamson [Gre66], they still agree with the assumptions that the height distribution of asperities is approximately Gaussian for a certain range and that the geometry of an asperity may be represented by a constant hemisphere. However, the 3-point peak theory is doubted. According to this theory a peak is defined by a sample point higher than its immediate neighbor and these peaks correspond to the asperities of the interface. Instead, modeling roughness by a multi scale model as it is already proposed by Archard [Arc57] in 1957 is suggested. Remarkably, Archard described fractal interfaces about 20 years before the term *fractal* has been formed by Mandelbrot [Man77]. A fractal structure exhibits a fractal dimension and is characterized by self-similarity (figure 3.9 (a)) and scale invariance so that neither dilatation nor contraction change the object's shape [Dim11]. There are different ways to define the fractal dimension mathematically that depend on the fractal object itself. A special characteristic of the fractal dimension in contrast to the usual understanding of a dimension is, that it must not necessarily be integer. A famous example of a fractal object is the Koch curve [Koc04] that has a fractal dimension of ≈ 1.26. Starting from a straight line at stage (0) the first three steps of constructing the fractal curve are presented in figure 3.9 (b).
The fractal concept describes interfaces as superimposition of roughness of different length scales [Avo08]. Some of the first fractal approaches for surface topology are proposed by Majumdar and Bhushan [Maj90] and Yan and Komvopoulos [Yan98] and an overview of the advancements in contact mechanics is given by Wang et al. [Wan20]. An interesting fractal approach for interfaces is presented by Robbe-Valloire [Rob01]. He distinguishes two levels of topology, i.e., roughness and waviness, where a wave element consist of several rough elements. A Gaussian distribution for the asperity height is applied on the waviness level, whereas the Gaussian distribution of the radii

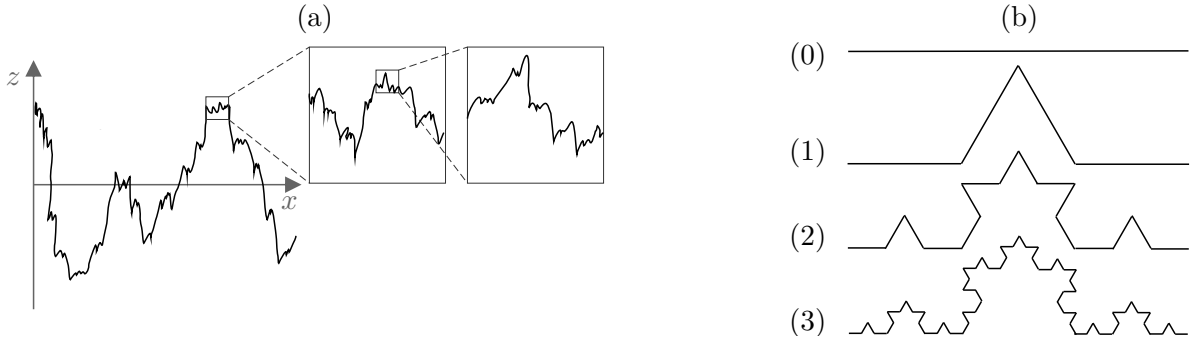

Figure 3.9.: Self affinity of rough interfaces [Bhu13] (a) and Koch curve [Koc04] (b)

is applied on the roughness level. An important advantage of this model is that post-processing is not required to obtain an interface profile.
The variety of models and approaches to describe rough interfaces demonstrates the challenges of topological problems. Moreover, as already mentioned in the description of the AFM (section 3.5), measuring roughness at the nano scale is not straightforward. These issues already indicate the complexity of modelling capillary bridges between rough solids is.

3.7.2. Modeling capillary forces between rough interfaces

As mentioned previously, experimental investigations of interparticle forces lead to inconsistent results that cannot be explained by a smooth capillary bridge theory. In figure 3.10 the force humidity curves obtained by AFM measurements of Xiao and Qian [Xia00] (a) and Rabinovic et al. [Rab02] (b) are exemplary shown to demonstrate the different curves, however, many more results are reported, e.g. [Del07; Jon02; Far06; Fis81; Sed00]. The interparticle force of OTE/SiO_2 is independent from humidity, which is traced back to the hydrophobic behavior of the material. Thus, no liquid menisci arise from condensation and the measured force is traced back to van der Waals forces. The interparticle force of the hydrophilic SiO_2 increases for $\varphi > 0.3$ with a maximum around 0.7. With further increasing humidity the interparticle force decreases. In contrast, the force humidity curves presented in figure 3.10 (b) do not

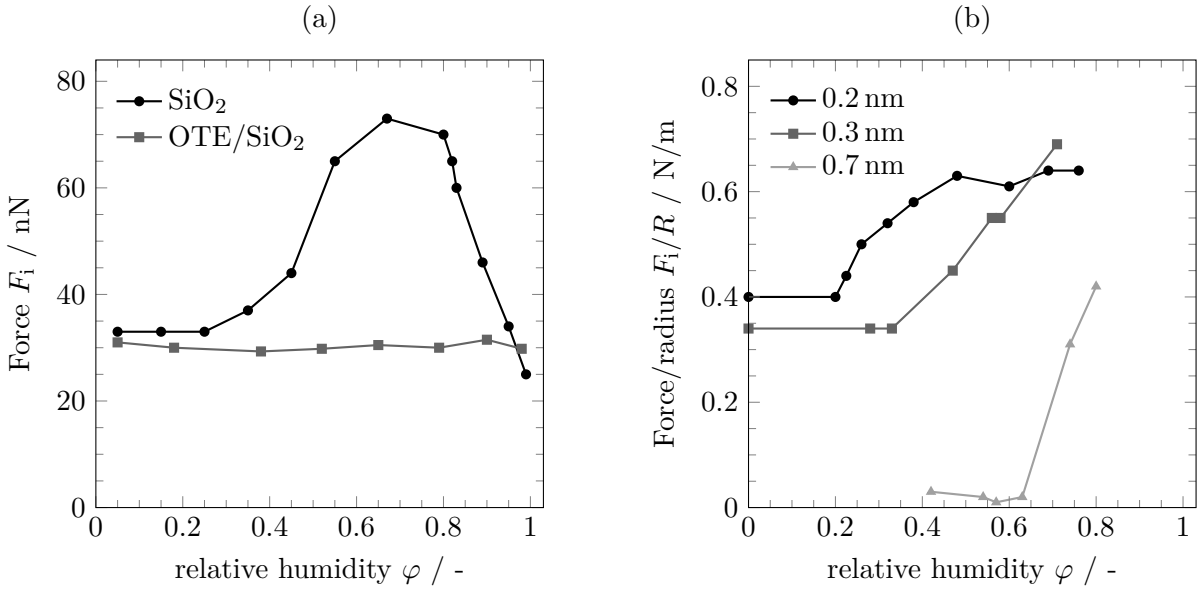

Figure 3.10.: Interparticle forces obtained from AFM measurements for SiO_2 and OTE/SiO_2 by Xiao and Qian [Xia00] (a) and for different RMS S_q by Rabinovic et al. [Rab02] (b) (materials: oxidized silicon $S_q = 0.2\,nm$ and PE-CVD substrate $S_q = 0.3$ and $0.7\,nm$)

show a maximum. All curves are constant until a certain humidity is reached. This jump is already described in section 3.1 and usually explained by the appearance of the condensed water menisci. In figure 3.10 (b) the critical humidity is lower the smoother the surface is. Moreover, it is shown that the interparticle force decreases with increasing roughness. While the $S_q = 0.3$ and 0.7 nm curves show a continuous increase after reaching the critical humidity, the $S_q = 0.2$ nm curve increases up to a maximum value and remains nearly constant afterwards. Farshchi-Tabrizi et al. [Far06] classified three different force humidity curves: (1) low maximum, (2) high maximum and (3) continuous increase without maximum. This classification should be extended by a constant force regime below a critical humidity as exemplary shown in figure 3.10 (b). It is generally assumed, that the qualitative differences between the curves are caused by interface roughness, which, therefore, must be considered in adequate models that explain the experimental results and predict interparticle forces with satisfying accuracy. Several models for calculating capillary adhesion between rough solid interfaces have been proposed. Some of them include capillary and van der Waals forces and most neglect the other force types. Since this work focuses on capillary forces, the van der Waals models are not described in detail, however, these forces are included in all experimental data inherently and thus are considered in several theoretical approaches.

Three different liquid volume regimes are defined by Halsey and Levine [Hal98] and illustrated in figure 3.11. The asperity regime is characterized by low liquid volume and humidity, respectively, and the capillary force arises from very few or even a single meniscus at the closest contact points. Thus, this region is around the critical humidity, where the capillary forces arise, however, they are very small. With rising volume, menisci emerge over a statistically rough region and the interparticle force increases linearly with the liquid volume. This model is supported by the

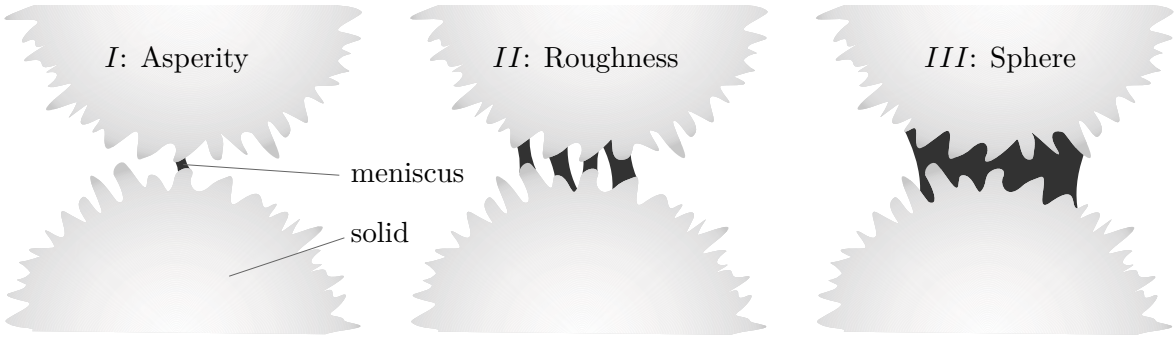

Figure 3.11.: Volume dependent wetting regimes of rough interfaces according to Halsey and Levine [Hal98]

AFM measurements of Ando [And00]. He investigated the adhesion force between a flat, squared AFM tip and a multiple asperity array as well as between the tip an a single asperity. An increasing adhesion force with humidity is measured for the array, whereas a constant force is observed at the single asperity. Moreover, a force histogram shows an increasing number of peaks that have constant maximum. Thus, it is concluded that the force on a single asperity is constant with respect to humidity, however, the number of contributing asperities increases on an asperity array. In the second regime the macroscopic shape of the solid does not yet influence the capillary bridge. This is the case in the third regime, i.e., the spherical region, where roughness can be neglected and the liquid bridge formation is dominated by the particle shape. This can be interpreted as a capillary force on a large single asperity and, thus, the interparticle force is assumed to be independent of humidity.
In order to consider roughness in the calculation of the capillary force, an extension to the toroidal model of two identical smooth spheres according to eq. (3.13) is suggested by Bocquet et al. [Boc98]. Their observation, that the interparticle force of granular beds increases drastically over time with the increasing humidity, is not consistent with the used toroidal force equation. The increase is traced back to the fact, that roughness significantly reduces the wetted area compared to smooth interfaces. Thus, an effective area is introduced to the model. This area is calculated by a factor that takes the typical width of the roughness distribution into account. Moreover, a time factor is proposed to include the time dependency of condensation in the model.
A very simple rough capillary force model is the calculation of an effective particle distance as proposed by Pietsch [Pie68]. It is assumed, that instead of direct contact a gap arises due to the asperities. This idea is applied to unequal sized spheres using a toroidal meniscus approximation [Naz12] and also to a smooth plane and an AFM tip geometry [Far06]. Another approach is calculating interparticle forces by

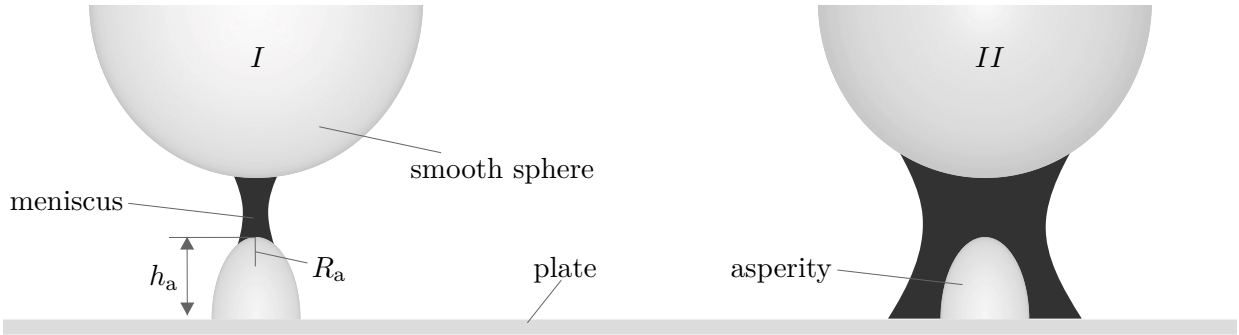

Figure 3.12.: Different cases for liquid menisci at a single asperity according the roughness model of Ata et al. [Ata02]

taking the asperity radius R_a into account [Rum74]. Using this model a significant roughness effect on the van der Waals forces is demonstrated, which is later confirmed by a more sophisticated van der Waals force approach [Rab00a; Rab00b]. It is demonstrated, that capillary forces are less sensitive towards roughness and exceed van der Waals forces in both, smooth and rough, models. A combination of these two approaches is proposed by Ata [Ata02]. His AFM measurements show that the experimentally obtained capillary force significantly exceeds the theoretical value predicted by eq. (3.13). Thus, roughness is considered in the calculations by distinguishing the two different cases presented in figure 3.12. In the first case, the meniscus diameter is below the asperity radius and thus, eq. (3.13) can be applied using the asperity radius R_a instead of the particle radius. In the second case, where the meniscus completely covers the asperity, a correction factor based on the effective area of the condensed vapor phase is introduced to eq. (3.13), that can also be interpreted as an effective distance. Thus, a better agreement between the theoretical and experimental values is achieved. This approach is also used by Rabinovic et al. [Rab02] who considered the jump in the interparticle force at the critical humidity. Below this critical humidity a dry adhesion force model taking roughness into account is applied, whereas above the second case illustrated in figure 3.12 is used. A Similar two case model of low and high humidity on a single asperity is proposed by Li et al. [Li20].
A hierarchical roughness model of two superposed sinus waves is suggested by Wang et al. [Wan09]. Again, different wetting regimes depending on the relative humidity are defined. For the roughness controlled regime it is shown, that the meniscus smoothly increases with humidity if a one-level roughness, i.e., a smooth sinus wave, is considered. However, by superposing a second sinus wave with a much smaller wavelength the meniscus increase gets discrete with large jumps. The jumps are explained by a pinning effect of the meniscus at the sub roughness. Therefore, an energy barrier has to be overcome by the rising meniscus to jump to the next bigger sub asperity. The pinning effect is assumed to be negligible in the high humidity regime.
Instead of describing roughness by a single asperity, a patterned interface composed of multiple asperities is developed to model roughness. Especially in the second regime either a multi asperity approach or an asperity distribution must be considered [But09]. Farshchi-Tabrizi et al. [Far06] proposed a smooth sphere in contact with a plane that is covered by hexagonally arranged conical or hemispherical asperities. Thus, wetting regimes similarly to figure 3.11 are described: At very low humidity, a meniscus arises only between the central asperity and the sphere. With rising hu-

midity, the asperities of one ring after another will form menisci which corresponds to the second regime. Finally, in the third regime, after reaching a critical humidity, a single meniscus covers all asperities and the influence of roughness is minor.
In order to calculate the tangential stiction force, Li and Talke [Li92] also considered the appearance of liquid menisci. The capillary force is given by the sum of hemispherical asperities for which the two cases of contact and non-contact are distinguished. Following the Greenwood and Williamson model, a Gaussian distribution of asperity height is implemented. Another model involving an arbitrary asperity height distribution is proposed by Butt [But08]. Assuming $r_1 \ll r_2$ the surface tension force is neglected and a toroidal approximation is applied. Moreover, thermodynamic equilibrium is assumed. The condensation criterion (eq. (3.26)) is combined with the gap height distribution (figure 3.8) of the rough interfaces in order to calculate the force of the existing menisci. This overall gap height distribution is superposed by two parts, i.e., the gap height function of the smooth geometry that describes the apparent interface and the distribution arising from the asperities. Convolution and integration lead to the integrated gap height distribution function that is used to calculate the capillary force. This method could also be used to handle heterogeneous interfaces. Similarly, Ardito et al. [Ard13] applied a Gaussian asperity height distribution to the condensation criterion for plane interfaces and combined their capillary force model with an also Gaussian distributed van der Waals force model. The approach presented by Butt [But08] is extended by You and Wan [You13; You14] by introducing a fractal roughness model of Gaussian asperity height distributions at different scales. Their interparticle force model also considers the van der Waals force and elastic deformation of the solid interface.
It is generally agreed, that the capillary force decreases with increasing roughness. Moreover, a complicated and not yet completely understood influence of roughness on the humidity dependency of the interparticle force is noticed. The theoretical approaches usually distinguish different humidity regimes and model the capillary force either on a single asperity or take a height distribution into account. The major problem is that even nanometer scaled roughness significantly influences capillary forces, However, measuring interface topology at this scale is impossible [But09].

4. Outline of thesis

Capillary bridges significantly influence the behavior of wet granular materials. Although the Young-Laplace equation has been researched for more than a century, a general solution for complex interfaces is not yet obtained. In fact, one of the most common assumptions for the computation of capillary forces is a smooth and axisymmetric solid interface. However, a significant influence of the particle geometry on the capillary force is demonstrated in the literature (section 3.3) and, consequently, it is very reasonable to conclude, that the assumption of a smooth interface is severe. This is supported by experimental investigations that indicate, that even slight wear of the AFM tip strongly influences the capillary force (section 3.5). Moreover, measured relations between the relative humidity and the interparticle force reveal an important impact of roughness (figure 3.10) which should consequently be considered in appropriate models. Nevertheless, the existing roughness capillary force models require substantial simplifications with respect to the solid geometry (section 3.7) rather than directly resolve the rough interface.

The main goal of this work is to develop and evaluate a method for the simulation of capillary bridges between arbitrary interfaces, i.e., no a priori assumptions with respect to the interfaces are made. The mathematical formulation of the problem is very general, providing a good basis for future research of capillary bridges. Although no simplifications with respect to the geometry are made, it is already clear that limits are determined by the numerical resolution and stability. To the best of the authors knowledge, such a method does not exist at present.

The model and the novel method are presented in chapter 5. The model is based on an energy minimization approach and the governing equations are formulated as a constrained optimization problem, i.e., minimizing the total free energy subject to a volume and a contact constraint. In contrast to previous energy minimization formulations (eq. 2.19 and eq. 3.21) the formulation presented in this work explicitly requires contact between the liquid and the solid. Moreover, in previous approaches the approximation of the curvature usually causes large numerical instabilities and inaccuracies when resolving a high frequent rough solid interface. Thus, in our novel method the approximation of the curvature is avoided. Moreover, the numerical

implementation is designed specifically for the capillary bridge problem. In contrast, the main advantage of the frequently used open source tool *Surface Evolver* is its applicability to various problems, which, however, limits its performance for a specific application. Hence, in this work, the classical optimization schemes are complemented by specific algorithms which, for example, ensure a stable development of the three-phase contact line.

Since the presented method is completely novel, an intensive evaluation of the applicability and the accuracy is presented in chapter 6. First, the method is verified by a comparison with previous approaches from the literature. In order to ensure accurate results, mesh convergence is discussed and the magnitude of numerical error is estimated. Moreover, the direct resolution of a rough interface requires a statistical approach for the analysis of the capillary force, since the root mean square roughness (RMS) can be realized by an infinite number of interfaces. Hence, the capillary force is obtained by computing the forces between a huge number of samples that have the same RMS but a different realization on an interface level. Consequently, statistical uncertainties of the mean capillary force as well as the standard deviation are estimated.

Based on this comprehensive evaluation, the capability of the novel method is demonstrated by applying it to rough sphere-plate and sphere-sphere systems. The corresponding results are presented in chapter 7. In particular, the distribution of the capillary force is investigated by considering the mean capillary force and the standard deviation. First, the dependencies between the distribution and the classical parameters, i.e., contact angle, volume, gap distance are revealed and, second, also the impact of a varying roughness is pointed out.

Conclusively, in chapter 8, the applicability of the presented results for future work is discussed. In particular, the existence, uniqueness and stability are critically questioned. Moreover, a possible future application within a discrete element method is considered. Finally, the hands-on experiences with the algorithm and the intensive evaluation of the data reveal comprehensive optimization potentials for the numerical implementation of the method. These potentials are described and their impact on the numerical performance is demonstrated.

5. Model and methods

Simulating capillary bridges between rough interfaces is challenging, since a general three-dimensional method is required. According to figure 3.6, energy minimization methods, computational fluid dynamics (CFD) or molecular dynamics (MD) can be considered. MD methods simulate the interaction of the molecules and are therefore restricted to very small systems that are not considered in here. CFD approaches are generally optimized for flow simulations rather than finding a static steady state like the capillary bridge. Moreover, the two most common multi-phase approaches, i.e., volume-of-fluid [Hir81; Ubb97] and level-set [Osh88; Sus94], represent interfaces implicitly. Thus, additional models such as the continuum surface force model [Bra92a] are required to include the surface tension force into the conservation equations. Due to numerical inaccuracies this introduces artificial velocities (parasitic currents) to the system [Har06]. Hence, the implicit multi-phase approaches work well, if these artificial velocities are minor compared to the physical flow velocity of the system. However, the flow velocity of the capillary bridge problem is zero and consequently, parasitic currents are a crucial issue. Besides the described implicit multi-phase approaches also explicit interface representation methods such as the moving-mesh-method [Tuk12] or a front-tracking algorithm [Unv92] exist. The main drawback of explicit methods is, that they cannot handle large deformations at the interface. Thus, they do not seem to be suitable to compute a capillary bridge between complex rough interfaces. Nevertheless, capillary bridges have been simulated using CFD [Dar10; Sun16; Was17]. However, these approaches only consider relatively simple smooth particles rather than complex arbitrary geometries. Since numerically stable computations on a CFD mesh that resolves small roughness asperities is not straight forward, this approach is not considered in here.

Finally, an energy minimization method seems to be most suitable for the three dimensional capillary bridge problem. As described in section 3.4.2, several approaches are already presented, in particular, the open source available tool *Surface Evolver* [Bra92b]. Although it is stated that arbitrarily geometries can be simulated, no publications with geometries as complex as a rough interface are found in the literature.

Especially the approximation of the curvature in this discretized-optimized method leads to numerical issues with non-smooth geometries.
Thus, a novel optimized-discretized energy minimization approach is developed, that does not require an explicit approximation of the curvature. Moreover, the developed algorithm is optimized for the capillary bridge problem and contains specialized stabilization methods such as a triangle correction at the three-phase contact line. The model is described first in this chapter (section 5.1) and includes the physical assumptions and the mathematical formulation of the problem. The physical assumptions (section 5.1.1) determine the applicability of the model on the one hand and, however, the limitations on the other hand. Based on the physical model, the mathematical formulation of the energy minimizing optimization problem and the governing equations are derived (section 5.1.2). Subsequently, the methods to solve the optimization equations are described (section 5.2). The Finite Element Method based algorithm for the solution of partial differential equations is implemented in *python* using the open source computing platform *FEniCS* [Log12]. The discrete rough interface representation of the solids (section 5.2.1) and the optimization schemes (section 5.2.2) are discussed in detail. Moreover, mesh quality is significant in order to achieve convergence and, thus, methods to ensure a sufficiently high mesh quality during computation are implemented (section 5.2.3).

5.1. Model

Applying an energy minimization approach to analyze capillary bridges between rough interfaces requires several physical assumption. These simplifications of the real system are required to obtain mathematical equations that are numerically solved.

5.1.1. Physical assumptions of the capillary bridge model

The objective of the simulation is to find a static steady state of the capillary bridge constrained to the liquid volume and the solid geometry (volume method, section 3.4). Thermodynamic equilibrium is not explicitly postulated. Instead, the equilibrium humidity can be calculated according to the Kelvin equation (eq. (2.26)) after the simulation. The system is considered to be static and, hence, dynamic forces and specific dynamic effects such as oscillation are excluded. The fluids are assumed to be continua and molecular effects are not explicitly resolved in the model. As already described in section 3.4 this excludes effects such as adsorption layers, line tension and disjoint pressure. Moreover, the surface tension is considered to be constant and

the curvature dependency, that is only relevant for very high curvatures arising in very small systems (section 2.1.2), is neglected.
The solids are chemically homogeneous and perfectly clean. A constant contact angle boundary condition for each solid is implemented. Note, that molecular and dynamic mechanisms, that cause the difference between the micro and macro contact angle (section 2.3.2), are explicitly excluded from the model. The existing rough wetting models of Wenzel and Cassie-Baxter calculate an integral macro contact angle for the rough solid (section 2.3.2). However, in the presented model the contact angle boundary condition is met at any point of the rough interface. Thus, this contact angle is interpreted as the micro contact angle.
A normal asperity height distribution is applied to describe roughness. Thus, a statistical model is used rather than a fractal model although it is generally agreed that roughness exhibits a fractal character (section 3.7.1). However, a fractal model requires a very high mesh resolution that implies huge computational resources and most probably even a parallelized algorithm that is not implemented straightforward. Thus, only the first fractal dimension of roughness is considered which might be extended in the future. The numerical representation of the rough interfaces is described in detail in section 5.2.1. Moreover, only capillary bridges with a relatively large volume compared to the dimension of the asperities are considered, which corresponds to the sphere regime in figure 3.11. In the asperity and roughness regime a complex analysis of the geometry is required in order to identify the areas at which capillary bridges exist. Additionally, if thermodynamic equilibrium is assumed, the multiple bridges in the roughness regime have the same capillary pressure rather than the same volume. Thus, the whole problem as well as the boundary conditions need to be formulated differently in these regimes.
External force fields, e.g. gravitation, are neglected in this investigation although they can easily be included in the model [Sch22]. However, in order to reduce parameters and to analyze the influence of roughness independent from possible other effects, external forces are neglected. In particular, neglecting gravity is reasonable for sufficiently small Bond numbers (section 3.6).
This work focuses on classical capillary bridges between two solids, i.e., two particles or a particle an a plate, with at least one of them being rough. However, the problem formulation is very general and provides an application to multiple solid interfaces as well. Thus, analyzing multi-particle systems is principally possible with the proposed model.

The solids are fixed in space and absorb the capillary forces. Moreover, the solids are assumed to be perfectly rigid. As shown in [But10a; You13], elastic particle deformation due to the van der Waals and capillary forces might be a considerable effect, since these forces are highly geometry dependent.
Generally, the model is set up in a dimensionless form using the parameters defined in eq. (3.2). Note, that all geometrical parameters such as coordinates, lengths or areas are related to a particle radius R that is choosen as characteristic length of the system. Thus, the results of the developed algorithm are independent of the system size and the surface tension. Assuming a constant surface tension the shape of the capillary bridge is independent of the liquid characteristics. The major advantage of the dimensionless form is its applicability to many system configurations. For example, the temperature dependency of the surface tension (section 2.1.1) can be easily considered by computing the dimensional capillary force at different surface tensions based on the same non-dimensional capillary force. However, all assumptions with respect to the system size, e.g. a curvature independent surface tension, neglect of molecular effects and gravitational free regimes, have to be checked, when transferring the non-dimensional results to specific dimensional applications. The main physical assumptions are summarized as follows:

- volume approach without postulation of thermodynamic equilibrium
- static system implying neglect of all dynamic effects
- neglect of all molecular effects (continuum approach)
- constant surface tension
- constant (micro) contact angle
- statistical (normal) asperity height model for rough solid interfaces
- neglect of external force fields (e.g. gravity)
- perfectly rigid solids that are fixed in space

5.1.2. Mathematical formulation of the optimization problem

Subsequently, the physical model has to be formulated by a mathematical formalism that is transferred into a computational algorithm. The problem is formulated in general for $i = 1...n$ solid interfaces and the definitions are illustrated in figure 5.1 for a two sphere system ($n = 2$). The liquid body domain $\Omega \subset \mathbb{R}^3$, i.e., the capillary

bridge, has a capillary interface $\Gamma_c = \partial\Omega$ that is composed by the liquid-gas interface Γ_{lg} and n solid-liquid interfaces $\Gamma_{sl,i}$, i.e.,

$$\Gamma_c = \Gamma_{lg} \cup \bigcup_{i=1}^{n} \Gamma_{sl,i}. \tag{5.1}$$

The outer normal of Γ_c is denoted by $\mathbf{n}$ and the three-phase contact lines are given by $\partial\Gamma_{sl,i}$ for all solids i. The co-normal $\boldsymbol{\mu}_i$ is defined perpendicular to the three-phase contact line $\partial\Gamma_{sl,i}$ and tangent to the liquid-gas interface $\Gamma_{lg,i}$. The dimensionless interface area $\tilde{A}$ and the dimensionless volume $\tilde{V}$ of the capillary bridge are given by

$$\tilde{A}(\Gamma_c) := \int_{\Gamma_c} 1 \mathrm{d}\tilde{\mathbf{s}} \quad \text{and} \quad \tilde{V}(\Gamma) := \int_{\Gamma_c} \frac{1}{3} \langle \tilde{\mathbf{s}}, \mathbf{n}(\tilde{\mathbf{s}}) \rangle \mathrm{d}\tilde{\mathbf{s}} \tag{5.2}$$

where $\tilde{\mathbf{s}}$ is the dimensionless position vector of a vertex and $\langle ., . \rangle$ the canonical scalar product in $\mathbb{R}^3$.
Using these definitions, the capillary bridge problem is formulated as a constrained optimization problem by

$$\begin{aligned} \min_{\Gamma_c} \quad & \tilde{A}(\Gamma_{lg}) - \left(\sum_{i=1}^{n} \beta_i \tilde{A}(\Gamma_{sl,i}) \right) \\ \text{s.t.} \quad & \\ & \tilde{V}(\Gamma_c) = \tilde{V}_0 \\ & \Gamma_{sl,i} \subset \Gamma_{s,i} \quad \forall i = 1, ..., n. \end{aligned} \tag{5.3}$$

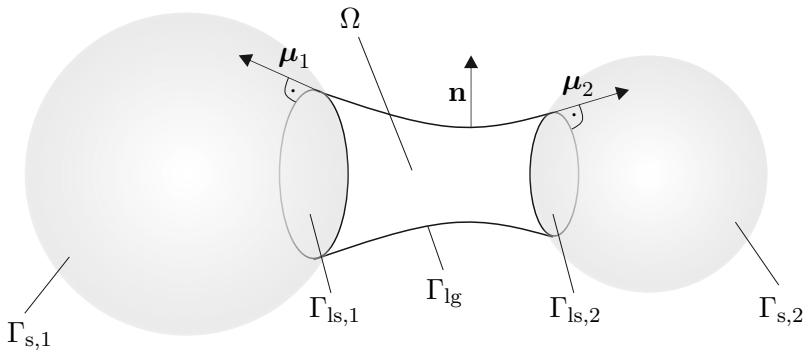

Figure 5.1.: Definitions for the mathematical formulation of the capillary bridge problem in a two particle system ($i = 1, 2$)

The non-dimensional relative adhesion coefficient β_i describes the relation of the liquid-gas and liquid-solid interface i. This is interpreted as contact angle boundary condition and $\beta_\mathrm{i} = \cos(\theta_\mathrm{i}) > 0$ results from Young's equation (eq. (2.21)). The optimization objective of eq. (5.3) is to minimize the energy of the overall interface Γ_c subject to a dimensionless volume $\tilde{V}_0$ and the geometrical boundaries of the i solids $\Gamma_{\mathrm{s,i}}$. The second constraint is formulated as a contact condition, i.e., the liquid solid interface of the capillary bridge $\Gamma_{\mathrm{sl,i}}$ matches with the solid interface $\Gamma_{\mathrm{s,i}}$. In contrast to a former formulation of the energy minimization problem (eq. (3.21)), this new formulation explicitly requires contact between the liquid and the solid, whereas one possible solution of eq. (3.21) would be an ideal droplet free in space. Note, that a gravitational term could easily be added to the problem formulation, however, in this work gravitation is neglected in general. A complete derivation including this extra term is demonstrated in [Sch22].
For solving a constrained optimization problem the method of Lagrange multipliers is used (section 2.2) and, hence, the Lagrangian according to eq. (2.19) needs to be set up. Therefore, the contact condition between the solid-liquid interface $\Gamma_{\mathrm{sl,i}}$ and the corresponding solid interface $\Gamma_{\mathrm{s,i}}$ is formulated on a discretized mesh by

$$\tilde{c}(\tilde{\mathbf{s}}_{\mathrm{i,j}}, \Gamma_{\mathrm{s,i}}) = 0, \quad \forall \text{ verticies } \tilde{\mathbf{s}}_{\mathrm{i,j}} \text{ of } \Gamma_{\mathrm{sl,i}} \tag{5.4}$$

where $\tilde{c}$ is a dimensionless level-set, i.e., the distance between the vertex $\tilde{\mathbf{s}}_{\mathrm{i,j}}$ and the solid interface $\Gamma_{\mathrm{s,i}}$. Using eq. (5.4), the Lagrangian

$$\begin{aligned} \mathcal{L}(\Gamma_\mathrm{c}, \lambda_\mathrm{V}, \lambda_{\mathrm{i,j}}) :=& \tilde{A}(\Gamma_\mathrm{lg}) - \left(\sum_{i=1}^{n} \beta_i \tilde{A}(\Gamma_{\mathrm{sl,i}}) \right) \\ & - \lambda_\mathrm{V}(\tilde{V}(\Gamma_\mathrm{c}) - \tilde{V}_0) + \sum_{i=1}^{n} \sum_{j=1}^{m} \lambda_{\mathrm{i,j}} \tilde{c}(\tilde{\mathbf{s}}_{\mathrm{i,j}}, \Gamma_{\mathrm{s,i}}) \end{aligned} \tag{5.5}$$

is derived, where λ_V and $\lambda_{\mathrm{i,j}}$ are the Lagrange multipliers. The upper terms are the objective function and the lower terms are the two zero formulated constraints. This Lagrangian formulation corresponds to eq. (2.20) including the additional constraint of contact between the liquid and the solid. In order to minimize eq. (5.5)

$$d\mathcal{L}(\Gamma_\mathrm{c}, \lambda_\mathrm{V}, \lambda_{\mathrm{i,j}})[\mathbf{V}] \stackrel{!}{=} 0 \quad \forall\, \mathbf{V} \in C^1(\mathbb{R}^3, \mathbb{R}^3) \tag{5.6}$$

has to be solved, where $\mathbf{V}$ is a vector field that assigns a displacement vector to each vertex. The major issue in formulating eq. (5.6) is, that the terms of eq. (5.5) have to

be derived with respect to the integrands. This leads to two possible formulations of the derivatives $d\tilde{A}(\Gamma)[\mathbf{V}]$ and $d\tilde{V}(\Gamma)[\mathbf{V}]$, i.e.,

$$d\tilde{A}(\Gamma)[\mathbf{V}] = \int_{\Gamma} \nabla_{\Gamma} \cdot \mathbf{V} \mathrm{d}\tilde{\mathbf{s}} = \int_{\Gamma} \langle \mathbf{V}, \mathbf{n} \rangle 2\tilde{H} \mathrm{d}\tilde{\mathbf{s}} + \int_{\partial\Gamma} \langle \mathbf{V}, \mathbf{n} \rangle \mathrm{d}\tilde{\mathbf{l}} \tag{5.7}$$

and

$$d\tilde{V}(\Gamma)[\mathbf{V}] = \int_{\Omega} \nabla \ \cdot \mathbf{V} \mathrm{d}\tilde{\mathbf{s}} = \int_{\Gamma} \langle \mathbf{V}, \mathbf{n} \rangle \mathrm{d}\tilde{\mathbf{s}}, \tag{5.8}$$

where $\tilde{H}$ is the curvature defined in eq. (2.11) and $\mathrm{d}\tilde{\mathbf{l}}$ an incremental three-phase contact line element. It is important to note, that only the second formulation of $d\tilde{A}(\Gamma)[\mathbf{V}]$ contains the mean curvature $\tilde{H}$. Thus, a complex and inaccurate approximation of the curvature is avoided by applying the first formulation of eq. (5.7) to eq. (5.6). The derivative of the level-set function $\tilde{c}(\tilde{\mathbf{s}}_{\mathrm{i,j}}, \Gamma_{\mathrm{s,i}})$ is given by

$$d\tilde{c}(\tilde{\mathbf{s}}, \Gamma_{\mathrm{sl,i}})[\mathbf{V}] = \langle \nabla \tilde{c}(\tilde{\mathbf{s}}, \Gamma_{\mathrm{sl,i}}), \mathbf{V}(\tilde{\mathbf{s}}) \rangle. \tag{5.9}$$

Introducing all three derivatives (eq. (5.7), eq. (5.8) and eq. (5.9)) into eq. (5.6) finally leads to

$$\begin{aligned} d\mathcal{L}(\Gamma_{\mathrm{c}}, \lambda_{\mathrm{V}}, \lambda_{\mathrm{i,j}})[\mathbf{V}] = & \int_{\Gamma_{\mathrm{lg}}} \nabla_{\Gamma} \cdot \mathbf{V} \mathrm{d}\tilde{\mathbf{s}} - \left(\sum_{i=1}^{n} \int_{\Gamma_{\mathrm{ls,i}}} \beta_i \nabla_{\Gamma} \cdot \mathbf{V} \mathrm{d}\tilde{\mathbf{s}} \right) \\ & - \lambda_{\mathrm{V}} \int_{\Omega} \nabla \cdot \mathbf{V} \mathrm{d}\tilde{\mathbf{s}} + \sum_{i=1}^{n} \sum_{j=1}^{m} \lambda_{\mathrm{i,j}} \langle \nabla \tilde{c}(\tilde{\mathbf{s}}_{\mathbf{i,j}}, \Gamma_{\mathrm{sl,i}}), \mathbf{V}(\tilde{\mathbf{s}}) \rangle \\ \stackrel{!}{=} & \ 0 \quad \forall \ \mathbf{V} \in C^1(\mathbb{R}^3, \mathbb{R}^3) \end{aligned} \tag{5.10}$$

which is the necessary optimality condition.
However, the relation between eq. (5.10) and the classical Young-Laplace equation is not directly clear. Thus, as a theoretical consideration and in order to obtain a more physically interpretable equation, the second formulations of the derivatives $d\tilde{A}(\Gamma)[\mathbf{V}]$ and $d\tilde{V}(\Gamma)[\mathbf{V}]$ are inserted into eq. (5.5). Moreover, the explicit claim of contact ($\Gamma_{\mathrm{sl,i}} \subset \Gamma_{\mathrm{s,i}}$) is neglected for this consideration, since the Young-Laplace equation is

valid for any curved free interface regardless of whether there is solid contact or not. By applying these considerations

$$\begin{aligned} d\mathcal{L}(\Gamma_\mathrm{c},\lambda_\mathrm{V})[\mathbf{V}] = &\int_{\Gamma_\mathrm{lg}} \langle \mathbf{V},\mathbf{n}\rangle 2\tilde{H}\mathrm{d}\tilde{\mathbf{s}} - \sum_{i=1}^{n}\int_{\Gamma_\mathrm{sl,i}} \langle \mathbf{V},\mathbf{n}\rangle \beta_\mathrm{i} 2\tilde{H}\mathrm{d}\tilde{\mathbf{s}} \\ &+ \sum_{i=1}^{n}\int_{\partial\Gamma_\mathrm{sl,i}} \langle \mathbf{V}, \boldsymbol{\mu}_\mathrm{lg} - \beta_\mathrm{i}\boldsymbol{\mu}_\mathrm{sl,i}\rangle \mathrm{d}\tilde{\mathbf{l}} - \lambda_\mathrm{V}\int_{\Gamma_\mathrm{c}} \langle \mathbf{V},\mathbf{n}\rangle \mathrm{d}\tilde{\mathbf{s}} \\ &\stackrel{!}{=} 0 \quad \forall\ \mathbf{V}\in C^1(\mathbb{R}^3,\mathbb{R}^3) \end{aligned} \tag{5.11}$$

is derived. Since there is no explicit claim of contact, this equation describes both cases, i.e., a three phase contact problem (capillary bridge) with the contact angle boundary condition $\beta_\mathrm{i} = \cos(\theta_\mathrm{i})$ or a two phase non-contact problem (a bubble or a droplet free in space). In the non-contact case the second and third summand on the right side vanish since there is no liquid-solid interface Γ_sl and consequently no three-phase contact line $\partial\Gamma_\mathrm{sl}$. In the contact case, the second summand forces a displacement of the liquid-solid interface vertices that is normal to their interface. However, after contact between the liquid-solid interface $\Gamma_\mathrm{sl,i}$ and the solid interface Γ_s is reached, a displacement normal to these interfaces would directly violate the touch constraint. Thus, in order to find an equilibrium that complies with the touch constraint, all vertices $\tilde{s}_\mathrm{i,j}$ of the solid-liquid interface can only be displaced tangentially to $\Gamma_\mathrm{sl,i}$. Thus, by deleting the normal displacement of $\Gamma_\mathrm{sl,i}$ (second addend) one finally obtains

$$\begin{aligned} d\mathcal{L}(\Gamma_\mathrm{c},\lambda_\mathrm{V})[\mathbf{V}] = &\int_{\Gamma_\mathrm{lg}} \langle \mathbf{V},\mathbf{n}\rangle 2\tilde{H}\mathrm{d}\tilde{\mathbf{s}} \\ &+ \sum_{i=1}^{n}\int_{\partial\Gamma_\mathrm{sl,i}} \langle \mathbf{V}, \boldsymbol{\mu}_\mathrm{lg} - \beta_\mathrm{i}\boldsymbol{\mu}_\mathrm{sl,i}\rangle \mathrm{d}\tilde{\mathbf{l}} - \lambda_\mathrm{V}\int_{\Gamma_\mathrm{lg}} \langle \mathbf{V},\mathbf{n}\rangle \mathrm{d}\tilde{\mathbf{s}} \\ &\stackrel{!}{=} 0 \quad \forall\ \mathbf{V}\in C_{\Gamma_\mathrm{sl}} \end{aligned} \tag{5.12}$$

which is transformed to

$$\begin{aligned} d\mathcal{L}(\Gamma_\mathrm{c},\lambda_\mathrm{V})[\mathbf{V}] = &\int_{\Gamma_\mathrm{lg}} (2\tilde{H} - \lambda_\mathrm{V}) \langle \mathbf{V},\mathbf{n}\rangle \mathrm{d}\tilde{\mathbf{s}} \\ &+ \sum_{i=1}^{n}\int_{\partial\Gamma_\mathrm{sl,i}} \langle \mathbf{V}, \boldsymbol{\mu}_\mathrm{lg} - \beta_\mathrm{i}\boldsymbol{\mu}_\mathrm{sl,i}\rangle \mathrm{d}\tilde{\mathbf{l}} \\ &\stackrel{!}{=} 0 \quad \forall\ \mathbf{V}\in C_{\Gamma_\mathrm{sl}}. \end{aligned} \tag{5.13}$$

Since this expression must vanish for all possible $\mathbf{V} \in C_{\Gamma_{\mathrm{sl}}}$, the two integrals cannot cancel each other out and must both vanish independently of each other. Thus, the conditions

$$2\tilde{H} - \lambda_{\mathrm{V}} \equiv 0 \quad \wedge \quad \langle \mathbf{V}, \boldsymbol{\mu}_{\mathrm{lg}} - \beta_{\mathrm{i}} \boldsymbol{\mu}_{\mathrm{sl,i}} \rangle \equiv 0 \quad \forall\, \mathbf{V} \in C_{\Gamma_{\mathrm{sl}}} \tag{5.14}$$

are derived. The first condition states that the mean curvature $\tilde{H}$ must be spatially constant, since $\lambda_{\mathrm{V}} \in \mathbb{R}$ is constant. In particular, it follows that $\lambda_{\mathrm{V}} = \Delta\tilde{p}$ leading to $2\tilde{H} = \Delta\tilde{p}$ which is the dimensionless form of the Young-Laplace equation as formulated in eq. (2.15). Moreover, $\langle \mathbf{V}, \boldsymbol{\mu}_{\mathrm{lg}} - \beta_{\mathrm{i}} \boldsymbol{\mu}_{\mathrm{sl,i}} \rangle$ must vanish on the three-phase contact line i, which is only possible for tangential displacement of the vertices. Thus, the vector field $\mathbf{V}$ must be restricted by

$$\mathbf{V} = \alpha(\tilde{\mathbf{s}}) \tilde{\boldsymbol{\mu}}_{\mathrm{ls,i}}(\tilde{\mathbf{s}}) \text{ on } \partial\Gamma_{\mathrm{sl,i}} \tag{5.15}$$

on the three-phase contact line. The two conditions of the theoretical analysis, i.e., $\lambda_{\mathrm{V}} = \Delta\tilde{p}$ and the restricted displacement on the three-phase contact line, must also hold for eq. (5.10), since the different formulations of the derivatives are equal (eq. (5.8) and 5.7) and 5.11 is less constrained. The restricted displacement condition gives the displacement of the three-phase contact line vertices in the direction of optimality, i.e., to reach the energy minimum, and is used later for the Newton scheme (section 5.2.2). By applying the pressure condition to eq. (5.10),

$$\begin{aligned} d\mathcal{L}(\Gamma_{\mathrm{c}}, \Delta\tilde{p}, \lambda_{\mathrm{i,j}})[\mathbf{V}] = & \int_{\Gamma_{\mathrm{lg}}} \nabla_\Gamma \cdot \mathbf{V} \mathrm{d}\tilde{\mathbf{s}} - \left(\sum_{i=1}^{n} \int_{\Gamma_{\mathrm{ls,i}}} \beta_i \nabla_\Gamma \cdot \mathbf{V} \mathrm{d}\tilde{\mathbf{s}} \right) \\ & - \Delta\tilde{p} \int_\Omega \nabla \cdot \mathbf{V} \mathrm{d}\tilde{\mathbf{s}} + \sum_{i=1}^{n} \sum_{j=1}^{m} \lambda_{\mathrm{i,j}} \langle \nabla \tilde{c}(\tilde{\mathbf{s}}_{\mathbf{i,j}}, \Gamma_{\mathrm{sl,i}}), \mathbf{V}(\tilde{\mathbf{s}}) \rangle \\ \stackrel{!}{=} & \; 0 \quad \forall\, \mathbf{V} \in C^1(\mathbb{R}^3, \mathbb{R}^3) \end{aligned} \tag{5.16}$$

is derived. This final formulation of the necessary minimum condition is solved using a Finite Element Method that is implemented within the *FEniCS* framework. In particular, the capillary bridge problem is solved by finding an interface Γ_{c} so that eq. (5.16) becomes zero.

5.2. Methods

The optimization problem (eq. (5.3)) is solved by finding the zero of the Lagrangian derivative (eq. (5.16)) with a Finite Element Method. The required triangulated

meshes are generated by the finite element mesh generator *gmsh* [Geu09] and the partial differential equations are solved by applying functions from the open source computing platform *FEniCS* [Log12]. The flow chart of the computation algorithm is illustrated in figure 5.2. The input parameters are classified into physical and numerical parameters. The physical parameters are the target volume of the capillary bridge V_0 as well as the contact angles θ_i and roughness parameters ($\tilde{S}_\mathrm{q,i}$, $\varepsilon_\mathrm{t,i}$, ξ_i (section 5.2.1)) for each solid boundary i. The numerical parameters (table 6.1), such as the level-set order, the iteration step size and the remesh intervals, control the computation as well as the accuracy of the solution.

For the computation of the level-set fields a background mesh for the whole computational domain is required. The background mesh is composed by sub-meshes for each solid i and a sub-mesh for the gaseous phase between the solids. According to figure 5.2, a tetrahedron mesh of the solid smooth geometry is computed first by *gmsh* and subsequently roughness is added to this mesh. A smooth and a rough mesh of a sphere-plate sample case are illustrated in figure 5.3. Note, that the gaseous phase mesh also consist of tetrahedrons that are not illustrated in figure 5.3. The particles are generally represented as hemispheres in order to reduce computational effort. The algorithm of the *rough interface computation*, i.e., how the roughness is added, is described in detail in section 5.2.1. Note, that this step is generally optional since the capillary bridge can also be obtained for a smooth interface.

The discrete level-set fields $\phi_\mathrm{i}(\tilde{\mathbf{s}}) = \tilde{c}$ are calculated on the background mesh for each solid interface i. The level-set field assigns the dimensionless distance $\tilde{c}$ from the interface i to the position vector $\tilde{\mathbf{s}}$. Thus, these fields are zero directly on the solid interface and non-zero anywhere else. The discrete level-set field is represented by a three-dimensional polynomial per tetrahedron. The order of the polynomial is called the level-set order and must be at least two, since the second order derivative of the level-set field is required later for the Newton scheme. Generally, a relatively smooth level-set field is advantageous for numerical stability and can be obtained either by increasing the number of tetrahedrons or by increasing the level-set order. In case of analytically defined particle shapes, such as a smooth sphere or a plane, analytical level-set functions $\phi_\mathrm{i}(\tilde{\mathbf{s}})$ are used rather than discretized numerical fields. This is very accurate and enables efficient calculations. The applicability of level-set functions is demonstrated in [Sch22]. However, it is restricted to analytically defined smooth interfaces.

After computing the level-set fields, an initial mesh for the capillary bridge interface Γ_c is required which is also generated using *gmsh*. However, in contrast to the background

mesh (tetrahedron volume mesh) the capillary bridge is represented by a closed shell mesh that consists of finite two-dimensional elements. Here, triangles are used, since their great advantage is that they are always planar. A cylindrical initial mesh and the final mesh are illustrated in figure 5.4. Following eq. (5.1) the overall capillary bridge mesh (Γ_c) consists of $n+1$ interfaces, i.e., the liquid-gas interface Γ_{lg} and n solid-liquid interfaces $\Gamma_{sl,i}$. It is important to note, that a particular triangle is assigned to one interface for the whole computation and cannot switch from one interface to another. Thus, the three-phase contact line is a priori known, since it is always

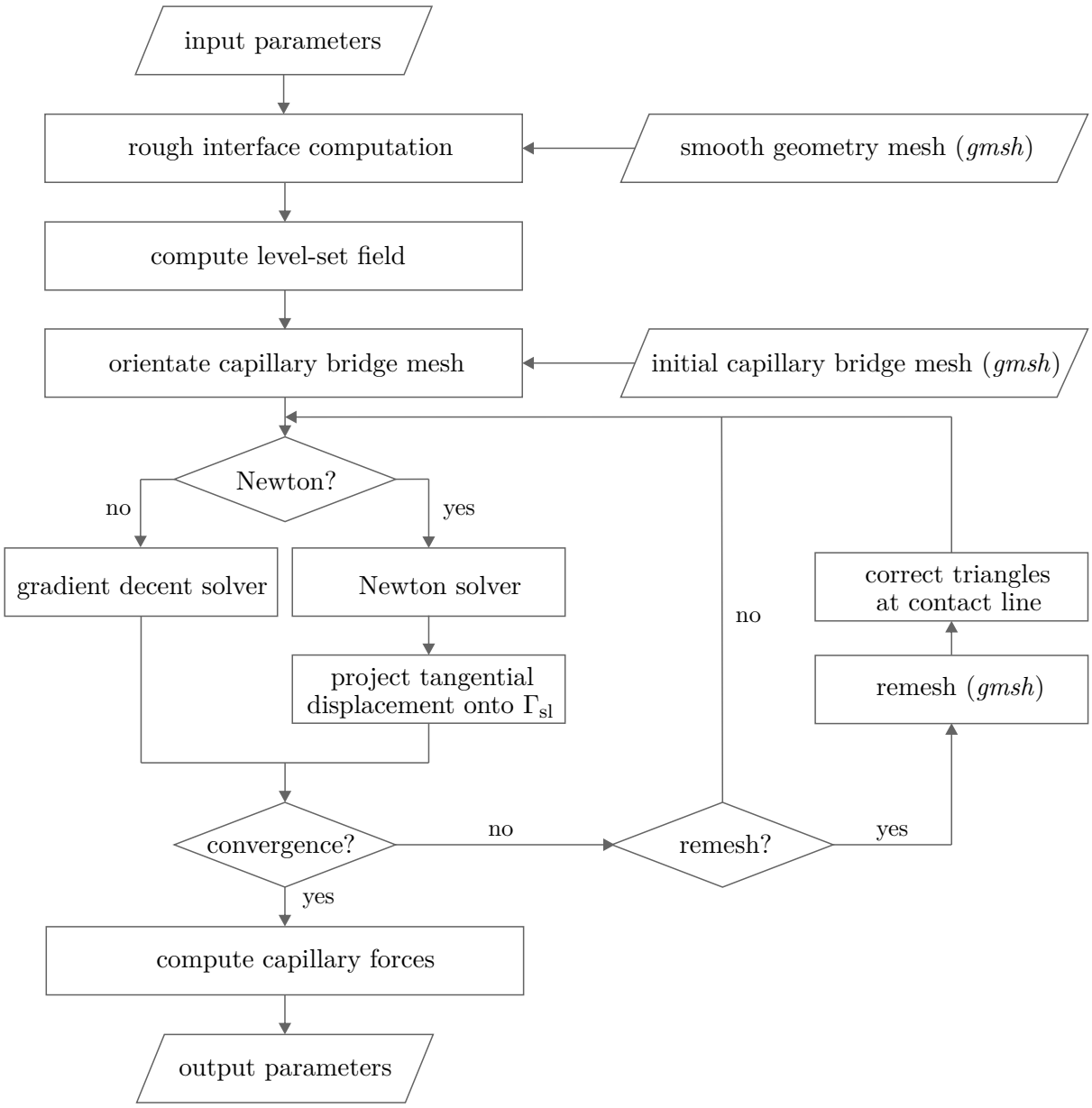

Figure 5.2.: Flow chart of the computation of the capillary bridge between rough interfaces

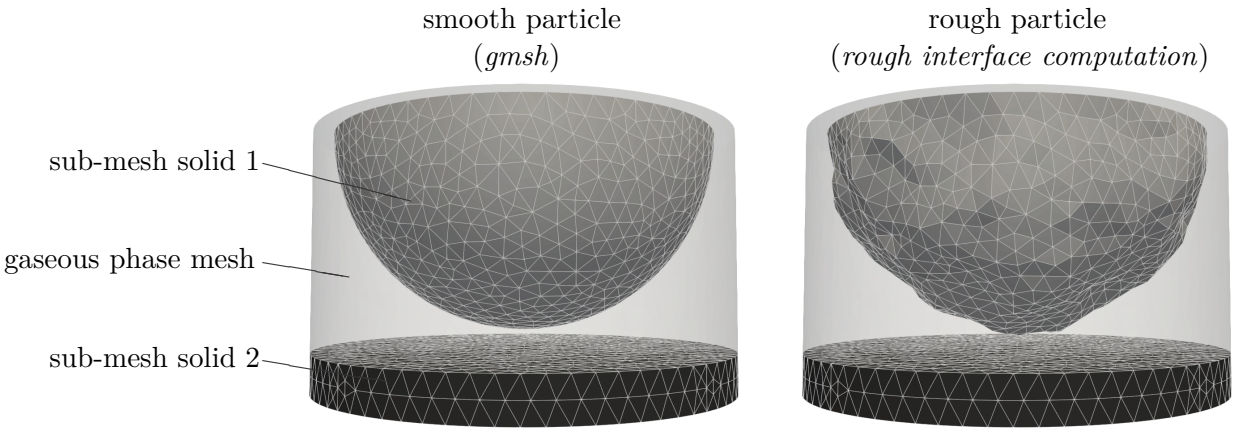

Figure 5.3.: Background mesh (tetrahedron volume mesh) of the solid geometry and the gaseous phase before and after adding roughness to the particle

located between the same triangles. Also the remeshing is performed seperately for each interface.

In figure 5.4 it is shown, that the initial guess and the final mesh do neither have the same volume nor the same number of triangles. During the computation the volume is adapted to fulfill the constraint V_0, however, since the algorithm is not volume conservative the initial volume can be arbitrary. Moreover, the number of mesh triangles is controlled by the remesh (figure 5.2) which ensures a sufficiently high mesh quality. The mesh quality control is described in more detail in section 5.2.3. Generally, the algorithm does not require a high quality initial guess and thus, all computations start from the same cylindrical shape. Before the optimization loop starts, all triangle normals are oriented to point outside the capillary bridge (figure 5.2).

For the optimization two different solvers are implemented. First, a slow but robust first order gradient decent solver is used to get close to the final solution. Generally, it is also possible to compute an accurate solution with this solver, however, this is very slow and consequently expensive with respect to the computational time. Thus,

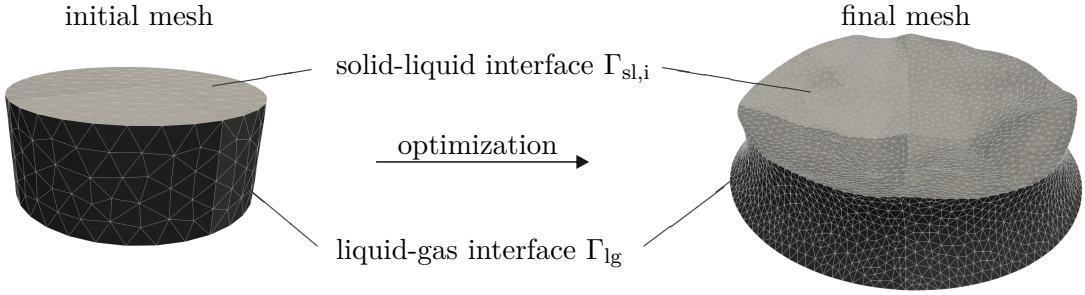

Figure 5.4.: Capillary bridge mesh (triangular shell mesh)

after reaching a relatively good solution, the second order Newton solver is used to efficiently converge the simulations. The control of the gradient decent and Newton solver is simply done by switching at a fixed iteration number.
One problem of the optimization is, that the solution is invariant with respect to a vertex displacement that is tangential to the interface. Thus, the first derivative becomes zero in the tangential direction, i.e., $\nabla\mathcal{L}(\Gamma_\mathrm{c}, \Delta\tilde{p}, \lambda_\mathrm{i,j})[\mathbf{V}_\mathrm{tan}] = 0$. This is no issue for the gradient decent solver, since it is of first order. However, the second order derivatives, that are required in the Newton scheme, cannot be obtained. Therefore, the displacement of the vertices must be restricted in the Newton scheme which, however, causes an insufficient mesh quality at the three-phase contact line. This problem is solved by projecting the tangential displacement of the three-phase contact line onto Γ_sl. This procedure as well as the two optimization schemes and the convergence criterion are discussed more detailed in section 5.2.2.
After the optimization has finished, the capillary forces $\tilde{F}_\mathrm{c,i}$ are computed (eq. (3.7)) at the three-phase contact line of each solid i. Theoretically, theses forces must be equal. However, due to numerical inaccuracies they are not exactly equal. The deviations are mesh dependent and thus, they are discussed in more detail in the mesh study in section 6.2. Since there is no reasonable argument for evaluating the capillary force at only a certain particle, the finale force is computed by the mean of $\tilde{F}_\mathrm{c,i}$, i.e.,

$$\tilde{F}_\mathrm{c} = \frac{1}{n}\sum_{i=1}^{n} \tilde{F}_\mathrm{c,i}. \tag{5.17}$$

Subsequent to this general overview the major steps of the algorithm are described in more detail. In particular, the rough interface algorithm, the optimization schemes and the mesh quality are discussed.

5.2.1. Rough interface algorithm

In order to compute a normally distributed rough interface, the triangulated smooth base geometry is modified (figure 5.3). In particular, the edge points of each triangle, i.e., the vertices with the position vector $\tilde{\mathbf{s}}_\mathrm{sm}$, are displaced normal to the interface. Generally, it is also possible to displace the points in an arbitrary direction, however, from a mathematical point of view, only the normal displacement components lead to a statistically different interface shape, since the tangential components cancel each other statistically out. Moreover, a combined normal and tangential displacement might lead to undesirably large distortions which significantly reduces the mesh qual-

ity. Thus, in this work the normal displacement option is implemented. The position vector of each vertex j of the rough interface $\tilde{\mathbf{s}}_{\mathrm{r,j}}$ is computed by

$$\tilde{\mathbf{s}}_{\mathrm{r,j}} = \tilde{\mathbf{s}}_{\mathrm{sm,j}} + \frac{\tilde{S}_{\mathrm{q}}}{\tilde{S}_{\mathrm{q,0}}} \boldsymbol{\omega}(\tilde{\mathbf{s}}_{\mathrm{sm,j}}) \tag{5.18}$$

where $\boldsymbol{\omega}$ is a vector field for the displacements. It consists of three polynomials $f_{\mathrm{P},1}(s_{\mathrm{sm,x}})$, $f_{\mathrm{P},2}(s_{\mathrm{sm,y}})$ and $f_{\mathrm{P},3}(s_{\mathrm{sm,z}})$ and assigns a displacement vector to each vertex $\tilde{\mathbf{s}}_{\mathrm{sm,j}}$. The factor $\tilde{S}_{\mathrm{q}}/\tilde{S}_{\mathrm{q,0}}$ is required to adjust the root mean square roughness (RMS) of the interface. The computation of the single components of eq. (5.18) is explained subsequently.

First, a sequence $\boldsymbol{\upsilon}$ of standard normal distributed random numbers is generated and one number is assigned to each vertex. Therefore, the pre-defined *python* function *random seed*$(\xi) = \boldsymbol{\upsilon} \in \mathbb{R}^{\mathbb{N}}$ is used, where ξ is an integer specifying the sequence. Thus, by varying ξ different interface shapes with the same integral roughness parameters are generated. Note, that the sequences are the same on each computer which makes the calculations perfectly reproducible for a given ξ.

Since there are no dependencies between the numbers of the random sequence $\boldsymbol{\upsilon}$, the resulting displacements might lead to large gradients between neighboring points on the interface. Thus, before displacing the points, the sequence is smoothed by using the Laplace equation

$$\int_{\Gamma_{\mathrm{s}}} \left[\varepsilon \langle \nabla_{\Gamma_{\mathrm{s}}} \boldsymbol{\omega}(\tilde{\mathbf{s}}), \nabla_{\Gamma_{\mathrm{s}}} \mathbf{v} \rangle + \langle \mathbf{v}, \boldsymbol{\omega}(\tilde{\mathbf{s}}) \rangle\right] d\tilde{\mathbf{s}} = \int_{\Gamma_{\mathrm{s}}} \langle \boldsymbol{\upsilon}\mathbf{n}, \mathbf{v} \rangle d\tilde{\mathbf{s}} \quad \forall \mathbf{v} \in CG_1. \tag{5.19}$$

Here, $\mathbf{v}$ is the test function that must be an element of CG_1. This means, that $\mathbf{v}$ is a two-dimensional function that is represented by discrete values at vertices and a linear interpolation between these vertices. The smoothing corresponds to a physical diffusion process. The diffusion coefficient ε characterizes the magnitude of the smoothing and for $\varepsilon \to \infty$ it follows that $\boldsymbol{\omega}(\tilde{\mathbf{s}}) \to 0$. Thus, for an infinite diffusion the displacement vector field approaches zero, i.e., the rough sphere approaches the smooth sphere. The solution of eq. (5.19) is the displacement vector field $\boldsymbol{\omega}(\tilde{\mathbf{s}})$ that can now be applied to eq. (5.18).

However, if the vertices are displaced according to $\boldsymbol{\omega}(\tilde{\mathbf{s}})$ the resulting rough interface exhibits a random RMS $\tilde{S}_{\mathrm{q,0}}$. In order to create defined and comparable interfaces the RMS should be adjustable. Hence, the RMS $\tilde{S}_{\mathrm{q,0}}$, that would result from displacing the vertices by $\boldsymbol{\omega}(\tilde{\mathbf{s}})$, is computed and the displacements are scaled by the factor $\tilde{S}_{\mathrm{q}}/\tilde{S}_{\mathrm{q,0}}$, where $\tilde{S}_{\mathrm{q}}$ is the desired RMS.

Note, that the shortest distance between the solid interfaces $\tilde{a}$ can only specified for the smooth geometry. After the roughness is added the shortest distance is changed as indicated in figure 5.3. Since it is complex and computationally expensive to adjust the shortest distance between two arbitrarily shaped interfaces, the parameter $\tilde{a}$ generally refers to the smooth base geometry.
Examples of rough particles are presented in figure 5.5 for different relative RMS $\tilde{S}_\mathrm{q}$ and diffusion coefficients ε. Note, that the created particles are not fully mesh independent. In previous works the number of vertices is used to adjust the frequency of the asperities [Dör18]. However, the Laplace smoothing (eq. (5.19)) leads to a partial decoupling of the number of mesh points and the frequency of asperities. This effect is pointed out in figure 5.5 where all particles have the same number of tetrahedrons, however, the particles become smoother with increasing ε. Nevertheless, the maximum frequency of asperities that can be represented is restricted by the number of vertices. Moreover, on a finer mesh a larger diffusion coefficient ε is required to achieve the same smoothing compared to a coarser mesh. Consequently, both, the number of vertices and the diffusion coefficient are required in order to completely specify the interface topology. Nevertheless, *gmsh* does not provide a function to set

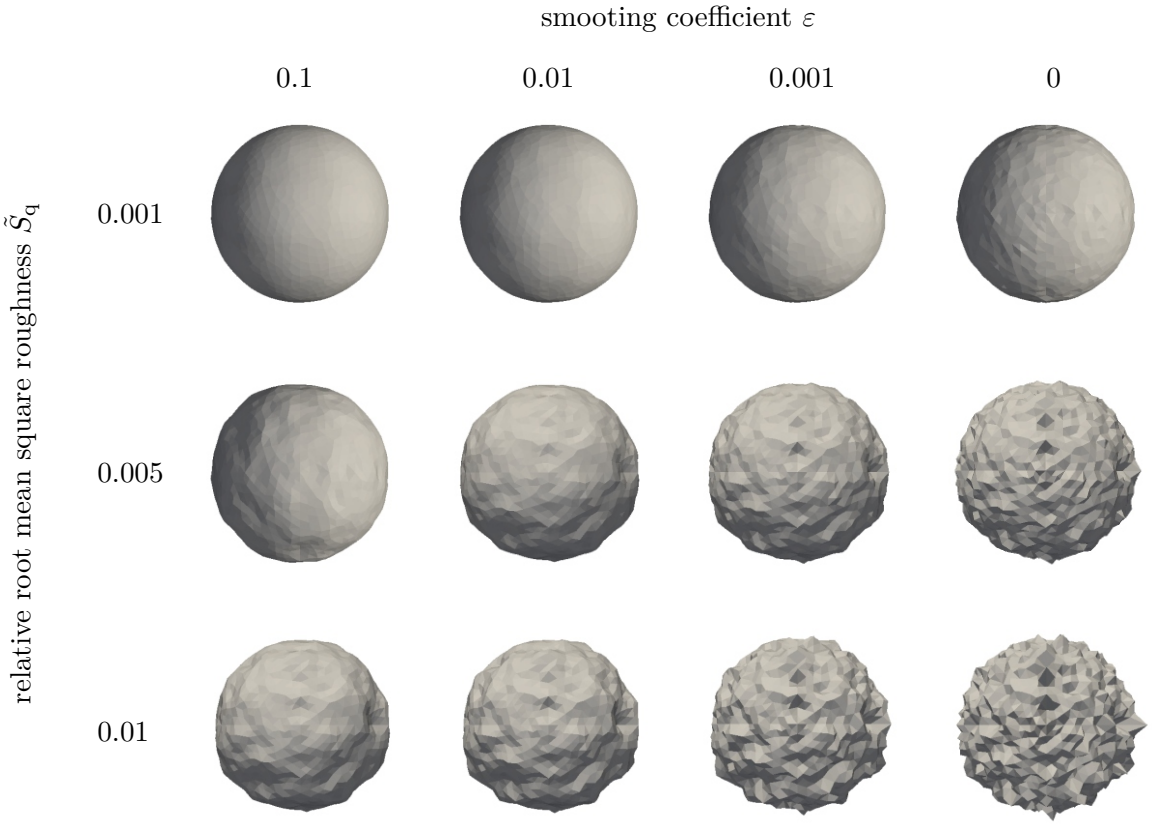

Figure 5.5.: Images of rough particles with the random seed number $\xi = 0$

the number of tetrahedrons. Instead, the mesh element size at each mesh point is specified. In this work, the mesh element size parameter is set to 1 for all mesh points. This ensures a uniform mesh resolution for the whole computational space. Thus, only the diffusion coefficient ε and the relative RMS $\tilde{S}_\mathrm{q}$ are used to adjust the roughness, whereas the mesh resolution, i.e., the size of the mesh elements, is kept constant. Note, that this implies a different number of elements for different geometries, whereas the element size is kept constant. In particular, computations for sphere-plate or sphere-sphere systems or even for different gap distances are performend on meshes with a varying number of background mesh cells but a constant mesh resolution.
It is stated previously, that for $\varepsilon \to \infty$ the particles approach the smooth sphere. Already for $\varepsilon = 0.1$ a relatively smooth interface is expected, however, combined with $\tilde{S}_\mathrm{q} = 0.01$ a relatively rough particle is illustrated in figure 5.5 (left column, lowest row). This is traced back to the fact that the relative RMS value is adjusted after the Laplace smoothing. From $\boldsymbol{\omega}(\tilde{\mathbf{s}}) \to 0$ it follows that $\tilde{S}_{\mathrm{q},0} \to 0$ and consequently $\tilde{S}_\mathrm{q}/\tilde{S}_{\mathrm{q},0} \to \infty$. Thus, even for very large diffusion coefficients ε the interfaces do not approach the smooth sphere, since they are forced to have the RMS $\tilde{S}_\mathrm{q}$. However, for $\tilde{S}_\mathrm{q} = 0$ the rough interface corresponds to the smooth interface independently of ε, which directly follows from eq. (5.18).
For $\varepsilon > 0.1$ the differences between the interfaces at a constant RMS are marginal, since $\boldsymbol{\omega}(\tilde{\mathbf{s}})$ already approaches zero. Therefore, the maximum diffusion coefficient considered in this work is $\varepsilon = 0.1$. Generally, a high diffusion coefficient is advantageous for numerical stability of the computation and allows simulations with a higher RMS. As an example, for $\varepsilon = 0$ (right column in figure 5.5) the simulations are only stable for $\tilde{S}_\mathrm{q} = 0.001$ whereas for $\varepsilon = 0.1$ (left column in figure 5.5) all three particle can be simulated. If low diffusion coefficients should be combined with a high RMS, the resolution of the capillary bridge mesh must be increased significantly compared to the meshes that are used in this work. Nevertheless, this is generally possible with enough computational resources.

5.2.2. Optimization schemes

The optimization consists of two different solvers, i.e., a first order gradient decent and a second order Newton solver. In figure 5.6 (a) the schemes are illustrated for an unconstrained optimization. The gradient decent scheme uses information from the first order derivative to converge towards the minimum, i.e., the solution is optimized

in some direction of a descending gradient. The value of the parameter u, that is described by the function $F(u)$, in the iteration step $k+1$ is calculated by

$$u_{\mathrm{k+1}} = u_{\mathrm{k}} - \alpha \hat{\mathbf{I}} \nabla F(u_{\mathrm{k}}) \tag{5.20}$$

where $\hat{\mathbf{I}}$ is the identity and α the step width. One option to reduce the number of iterations is using the direction of the steepest decent. This corresponds to a right angle between the contour lines of $F(u_{\mathrm{k}})$ and the gradient $\nabla F(u_{\mathrm{k}})$. From figure 5.6 (a) it can already be seen that the steepest gradient decent scheme converges faster compared to an arbitrary gradient decent scheme. However, both schemes are relatively slow, since they both converge on a zigzag path. In contrast, the Newton scheme finds a faster path to the minimum by considering the second derivative, i.e.,

$$u_{\mathrm{k+1}} = u_{\mathrm{k}} - \hat{\mathbf{H}}(x_{\mathrm{k}})^{-1} \nabla F(u_{\mathrm{k}}) \tag{5.21}$$

where $\hat{\mathbf{H}}$ is the Hessian that is defined by

$$\hat{\mathbf{H}}(u) \coloneqq \left(\frac{\partial^2 F}{\partial u_{\mathrm{i}} \partial u_{\mathrm{j}}}(u) \right)_{\mathrm{i,j=1,\dots,m}} = \begin{pmatrix} \frac{\partial^2 F}{\partial u_1 \partial u_1}(u) & \cdots & \frac{\partial^2 F}{\partial u_1 \partial u_{\mathrm{m}}}(u) \\ \vdots & \ddots & \vdots \\ \frac{\partial^2 F}{\partial u_{\mathrm{m}} \partial u_1}(u) & \cdots & \frac{\partial^2 F}{\partial u_{\mathrm{m}} \partial u_{\mathrm{m}}}(u) \end{pmatrix}. \tag{5.22}$$

In figure 5.6 (a) the general idea of the different schemes is illustrated for an unconstrained optimization. However, the capillary bridge problem is to minimize the total free energy subject to a volume V_0 and the geometry Γ_{s}. Thus, $F(u_{\mathrm{k}})$

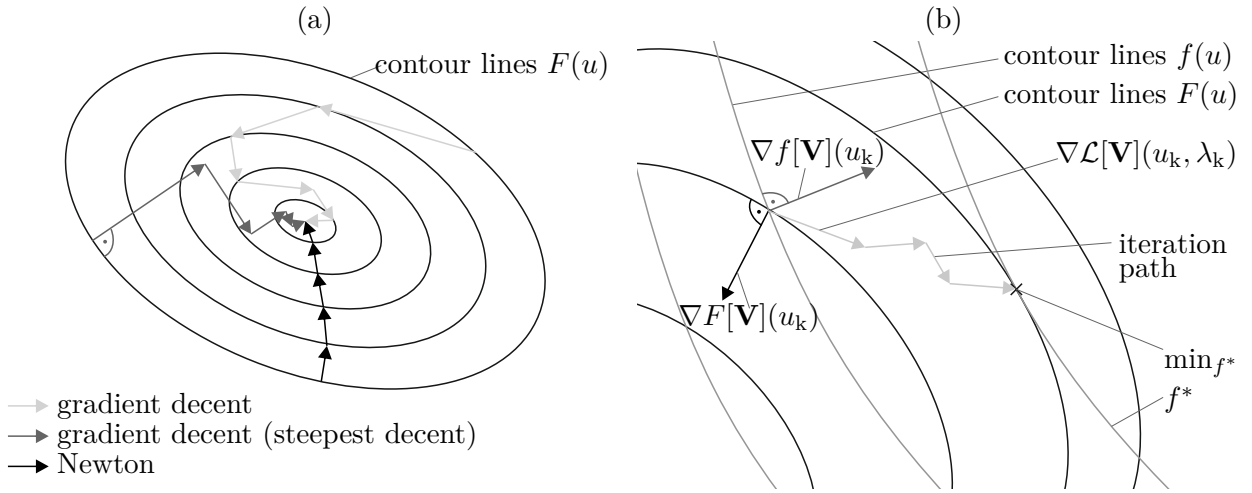

Figure 5.6.: Illustration of unconstrained (a) and constrained (b) optimization schemes

in eq. (5.20) and eq. (5.21) corresponds to the Langrangian (eq. (5.5)) $\mathcal{L}(u_\mathrm{k})[\mathbf{V}]$ where $u_\mathrm{k} = \Gamma_{\mathrm{c,k}}, \Delta\tilde{p}_\mathrm{k}, \lambda_{\mathrm{i,j,k}}$. The constrained optimization is illustrated in figure 5.6 (b). The direction of the optimization, i.e., $\nabla\mathcal{L}(u_\mathrm{k})$ is composed by the the gradient of the target function $\nabla F(u_\mathrm{k})$ and the gradient of the constraint $\nabla f(u_\mathrm{k})$. However, both, the direction and the magnitude of $\nabla\mathcal{L}(u_\mathrm{k})$ strongly depend on the Lagrange-Multipliers $\Delta\tilde{p}$ and $\lambda_{\mathrm{i,j,k}}$.

Generally, the gradient decent scheme is robust with respect to numerical stability but due to its slow convergence it is computationally expensive. The drawback of the faster Newton scheme is, however, that it requires a relatively good initial guess for numerical stability. In order to develop a robust but also relatively fast algorithm, the two schemes are combined, i.e., the gradient decent scheme is used to compute a good starting point for the Newton scheme.

As previously mentioned, the solution of the optimization problem is invariant with respect to an inner vertex ($\tilde{\mathbf{s}} \notin \partial\Gamma_{\mathrm{sl,i}}$) displacement that is tangential to the interface. From a physical perspective this means, that a tangential displacement of an inner vertex does not influence the energy of the capillary bridge resulting in $\nabla\mathcal{L}(u_\mathrm{k})[\mathbf{V}_\mathrm{tan}] = 0$ for $\tilde{\mathbf{s}} \notin \partial\Gamma_{\mathrm{sl,i}}$. Eq. (5.20) shows that this simply leads to $u_{\mathrm{k+1,tan}} = u_{\mathrm{k,tan}}$, i.e., no tangential displacement occurs in the gradient decent scheme. However, in the Newton scheme this leads to undesired zero entries in the Hessian, since the second derivative of zero is still zero. As a consequence, the Hessian is not invertible which causes a very fast destruction of the mesh. Therefore, in the Newton scheme the displacement of the vertices is restricted to the normal direction $\mathbf{n}$ of the interface as illustrated in figure 5.7. However, this causes a problem for all vertices of the three-phase contact line $\tilde{\mathbf{s}} \in \Gamma_\mathrm{lg} \cap \Gamma_\mathrm{sl}$, since they have two normal directions. Note, that in section 5.2 it is stated, that the normal displacement of the three-phase contact line vertices is restricted, once contact is reached. This is not explicitly necessary for a discretized problem formulation since contact is never exactly reached, i.e., there is always a slight difference between Γ_sl and Γ_s (figure 5.7).

On option to overcome displacement issue at the three-phase contact line is to fix these vertices $\tilde{\mathbf{s}} \in \Gamma_\mathrm{lg} \cap \Gamma_\mathrm{sl}$. However, this requires the solution of the gradient solver to already be very good, since the three-phase contact line would remain constant in the Newton scheme. Practically, this means a relatively slow convergence resulting in long simulation times. Moreover, if the solution of the gradient solver is not good enough, i.e., the three-phase contact line needs to be adapted, the Newton solver might not converge. In fact, this option has been tested and the convergence is slow and also quite unstable if the Newton solver is activated too early.

Another option is, to restrict the displacement of the three-phase contact line vertices in a certain direction. In particular, eq. (5.15) states, that on $\partial\Gamma_{\mathrm{sl,i}}$ a displacement in the direction of $\tilde{\boldsymbol{\mu}}_{\mathrm{sl}}$ leads towards optimality, which, however, invalidates the touch constraint. In fact, eq. (5.15) is derived without the explicit claim of contact. Thus, in addition to the displacement towards optimality, a displacement to account for the touch constraint is required. Here, the second co-normal $\tilde{\boldsymbol{\mu}}_{\mathrm{lg}}$ is used and, consequently, a displacement within a corridor spanned by $\tilde{\boldsymbol{\mu}}_{\mathrm{lg}}$ and $\tilde{\boldsymbol{\mu}}_{\mathrm{sl}}$ is implemented (figure 5.7). Thus,

$$\mathbf{V}(\tilde{\mathbf{s}}_{\mathrm{j}}) = \begin{cases} \alpha_1(\tilde{\mathbf{s}}_{\mathrm{j}})\tilde{\boldsymbol{\mu}}_{\mathrm{lg}}(\tilde{\mathbf{s}}_{\mathrm{j}}) + \alpha_2(\tilde{\mathbf{s}}_{\mathrm{j}})\tilde{\boldsymbol{\mu}}_{\mathrm{sl,i}}(\tilde{\mathbf{s}}_{\mathrm{j}}), & \tilde{\mathbf{s}}_{\mathrm{j}} \in \Gamma_{\mathrm{lg}} \cap \Gamma_{\mathrm{sl}} \\ \alpha_1(\tilde{\mathbf{s}}_{\mathrm{j}})\tilde{\mathbf{n}}(\tilde{\mathbf{s}}_{\mathrm{j}}), & \text{otherwise} \end{cases} \tag{5.23}$$

is obtained for the vertex displacement in the Newton scheme, where α_1 and α_2 are $CG_1(\Gamma_{\mathrm{c}})$ functions. Note, that instead of the second co-normal $\tilde{\boldsymbol{\mu}}_{\mathrm{lg}}$, also any other vector, that is linear independent of $\tilde{\boldsymbol{\mu}}_{\mathrm{sl}}$ and perpendicular to the three-phase contact line, could have been used to ensure the touch constraint. A different choice is discussed in detail in section 8.3.2.

Eq. (5.23) implies, that the triangles of Γ_{sl} cannot move after the contact constraint with Γ_{s} is met (eq. (5.4)), i.e., all inner vertices of Γ_{sl} are fixed. As already mentioned, there is of course a negligible numerical displacement since the contact condition cannot be exactly fulfilled in a discretized problem. Nevertheless, the three-phase contact line vertices might still be displaced with a considerably larger order of magnitude. Thus, the outer triangles of Γ_{sl} can be significantly distorted, since they are composed by fixed and moving vertices. In fact, the algorithm has been tested using this method and a low mesh quality at the three-phase contact line turned out to be the main reason for numerical instability and crashed simulations.

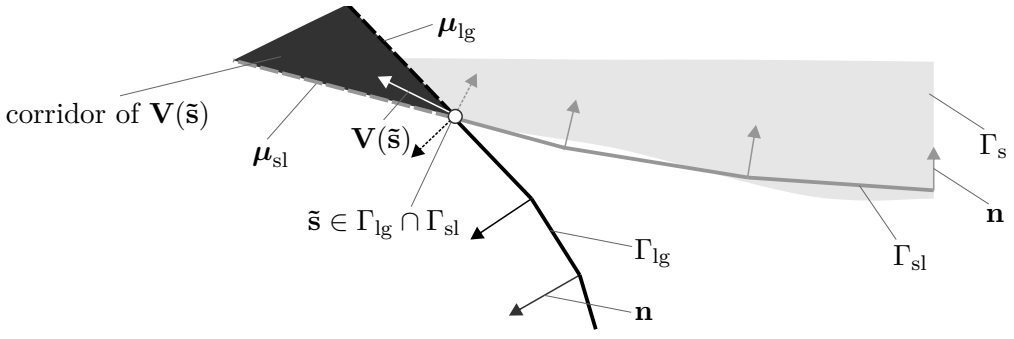

Figure 5.7.: Projection of the tangential displacement $\Delta u_{\mathrm{lg,tan}}$ of Γ_{lg} on Γ_{sl} for two different vertices

A solution to this problem is projecting the tangential displacement of the three-phase contact line vertices ($\tilde{\mathbf{s}}_{\mathrm{CL}} \in \Gamma_{\mathrm{lg}} \cap \Gamma_{\mathrm{sl}}$) onto Γ_{sl} after each Newton step. In particular, the tangential component $\mathbf{V}_{\tan}(\tilde{\mathbf{s}}_{\mathrm{CL}})$ is projected onto $\tilde{\mathbf{s}}_{\mathrm{j}} \in \Gamma_{\mathrm{sl}}$ with a linear gradient from the three-phase contact line to the center. Note, that the set up of the mesh in quarters (figure 5.4) ensures a well defined center point. The displacement projection corresponds to a stretching of the triangles if the three-phase contact line increases and a compressing in the decreasing case. Thus, the displacement of the inner vertices of Γ_{sl} is composed of the normal component $\alpha_1(\tilde{\mathbf{s}}_{\mathrm{j}})\tilde{\mathbf{n}}(\tilde{\mathbf{s}}_{\mathrm{j}})$ resulting from the Newton iteration and the tangential component that is calculated from the projection of $\mathbf{V}_{\tan}(\tilde{\mathbf{s}}_{\mathrm{CL}})$. Finally, the vertex displacement in the Newton algorithm is given by

$$\mathbf{V}(\tilde{\mathbf{s}}_{\mathrm{j}}) = \begin{cases} \alpha_1(\tilde{\mathbf{s}}_{\mathrm{j}})\tilde{\boldsymbol{\mu}}_{\mathrm{lg}}(\tilde{\mathbf{s}}_{\mathrm{j}}) + \alpha_2(\tilde{\mathbf{s}}_{\mathrm{j}})\tilde{\boldsymbol{\mu}}_{\mathrm{sl,i}}(\tilde{\mathbf{s}}_{\mathrm{j}}), & \tilde{\mathbf{s}}_{\mathrm{j}} \in \Gamma_{\mathrm{lg}} \cap \Gamma_{\mathrm{sl}} \\ \alpha_1(\tilde{\mathbf{s}}_{\mathrm{j}})\tilde{\mathbf{n}}_{\mathrm{lg}}(\tilde{\mathbf{s}}_{\mathrm{j}}), & \tilde{\mathbf{s}}_{\mathrm{j}} \in \Gamma_{\mathrm{lg}} \wedge \tilde{\mathbf{s}}_{\mathrm{j}} \notin \Gamma_{\mathrm{ls}} \\ \alpha_1(\tilde{\mathbf{s}}_{\mathrm{j}})\tilde{\mathbf{n}}_{\mathrm{ls}}(\tilde{\mathbf{s}}_{\mathrm{j}}) + \zeta(\tilde{\mathbf{s}}_{\mathrm{j}})\mathbf{V}_{\tan}(\tilde{\mathbf{s}}_{\mathrm{CL}}), & \tilde{\mathbf{s}}_{\mathrm{j}} \in \Gamma_{\mathrm{ls}} \wedge \tilde{\mathbf{s}}_{\mathrm{j}} \notin \Gamma_{\mathrm{lg}}, \end{cases} \tag{5.24}$$

where $\zeta(\tilde{\mathbf{s}}_{\mathrm{j}}) \in \mathbb{R}$ accounts for the linear decrease from the three-phase contact line to the center. Note, that a projection of the tangential displacement at three-phase contact line could also be implemented for the vertices of the liquid-gas interface Γ_{lg}. Nevertheless, the test simulations showed that this is not necessary for numerical stability. This is traced back to the fact that theses vertices are free to move in the normal direction during the whole iteration whereas the vertices of the solid-liquid interface Γ_{sl} are rapidly fixed by the contact condition.

Using this procedure a stable Newton scheme is implemented. However, the additional displacement of the inner vertices of $\Gamma_{\mathrm{sl,i}}$ after the classical iteration affects the optimization behavior. As shown in eq. (5.21) Newton schemes do usually not have a step width or in other words, the Newton step width is implicitly set to 1. The first test simulations showed oscillating solutions that did not converge. These oscillations vanish with a reduced Newton step. Although a Newton step below 1 is very untypical it works well for the presented method.

Moreover, the convergence criterion is influenced by the manual projection of the tangential displacement. Ideally, the displacement projection is only used to ensure well defined triangles on Γ_{sl}, however, there is of course a slight change of the overall interface. This influences the the right hand side of the optimization equation (eq. (5.6)) which is classically used as residuum. It turned out that usually values between $10^{-2} - 10^{-3}$ are obtained although the capillary interface and the capillary

force do not change with further iteration steps. Thus, the actual displacement of the Newton iteration Δu_k is chosen as convergence criterion which is formulated as

$$\int_{\Gamma_\mathrm{c}} \parallel \Delta u_\mathrm{k} \parallel ds = \parallel \hat{\mathbf{H}}^{-1} \nabla \mathcal{L}(\Gamma_{\mathrm{c,k}}, \Delta\tilde{p}_\mathrm{k}, \lambda_{\mathrm{i,j,k}})[\mathbf{V}] \parallel \overset{!}{<} 10^{-5}. \tag{5.25}$$

This criterion states that the optimization is considered to be converged if the sum of all displacements of the capillary interface Γ_c is below 10^{-5}. Note, that this criterion uses an integral value and therefore 10^{-5} is a very small residuum.
Finally, it should be noted that a convergence criterion only describes how good the solution in terms of the chosen number of triangles is. However, it cannot be concluded how accurate the solution is with respect to the smooth physical model. For example, on a very coarse mesh the optimization might reach a very high level of convergence, whereas the capillary forces are not accurate due to the bad resolution of the geometry. Therefore, the accuracy of the solution must also be evaluated with respect to the mesh resolution as discussed in section 6.2.

5.2.3. Mesh quality

A high mesh quality is mandatory for a robust numerical calculation. During the optimization procedure the nodes are displaced which might lead to poorly shaped triangles. In figure 5.4 it is already illustrated, that displacements from the initial mesh to the final mesh might be relatively large. Thus, a remesh is used to ensure properly shaped triangles. Here, the remesh function of *gmsh* is used and embedded to the calculation algorithm via an interface [Mar11; Rem10]. In this procedure the mesh is triangulated completely new on the interface of the current iteration and the resolution of the new mesh is easily controlled by a resolution parameter (table 6.1, remesh resolution factor). Thus, the resolution of the initial mesh is not very important, since a finer mesh is obtained by the remesh. Since the Newton scheme is very sensitive with respect to the triangle shapes, a remesh immediately before the Newton solver is activated turned out to be advantageous. Nevertheless, the recalculation of the mesh leads to a slightly different capillary interface which implies an increase of the residuum. Thus, the remesh slows down convergence and cannot be used too often.
Although the remesh is needed for a sufficiently high mesh quality, it causes interpolation problems at the three-phase contact line. In figure 5.8 a capillary bridge mesh is shown before and after the remesh as well as several iterations later. Before the remesh a relatively sharp edge is obtained at the three-phase contact line (1). Subse-

quently, this edge is smoothed by the interpolation algorithm of the remesh (2a). The triangles seem to be properly shaped, however, a view from a different angle shows a tilted triangle (2b) which is colored in white. After several iterations this triangle leads to a destroyed mesh (3).

The mechanism is explained by the two-dimensional schematic illustration of the three-phase contact line in figure 5.9. The interfaces of the capillary bridge, Γ_{lg} and Γ_{sl}, are represented by finite triangles. On the left and right side of figure 5.9 two possible positions for a three-phase contact line triangle of Γ_{sl} are illustrated (1). Here, θ_{rm} is the contact angle directly after the remesh. Due the contact condition between Γ_{sl} and Γ_s (eq. (5.4)) all triangles of Γ_{sl} converge as fast as possible in the direction of the solid interface Γ_s. Thus, the triangle illustrated on the left side turns right and after several iterations it reaches the second position (2). However, on the right side the triangle directly after remesh (1) is tilted more to the left side. In this case, the shortest way to the solid interface is to turn left (2). Consequently, the

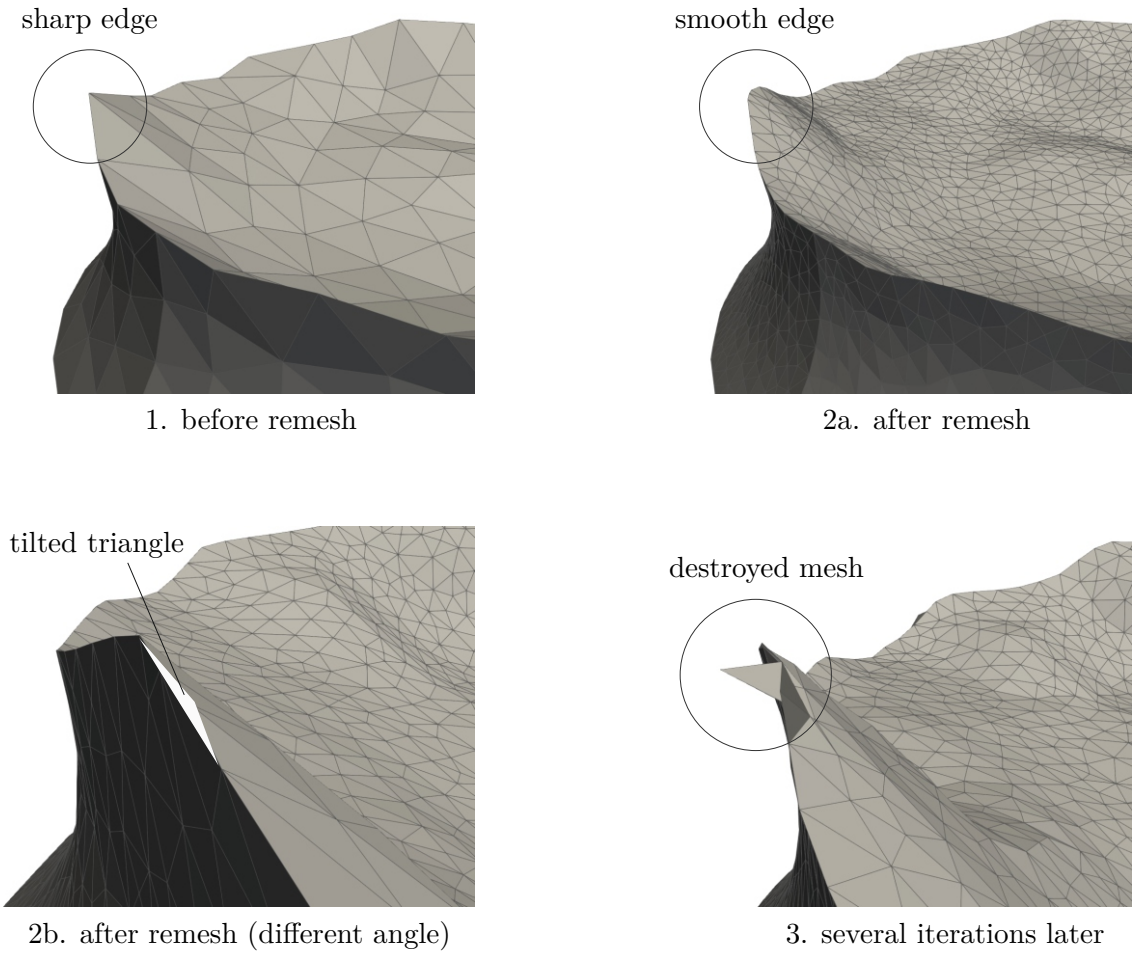

Figure 5.8.: Tilted triangles at the three-phase contact line resulting from the remesh

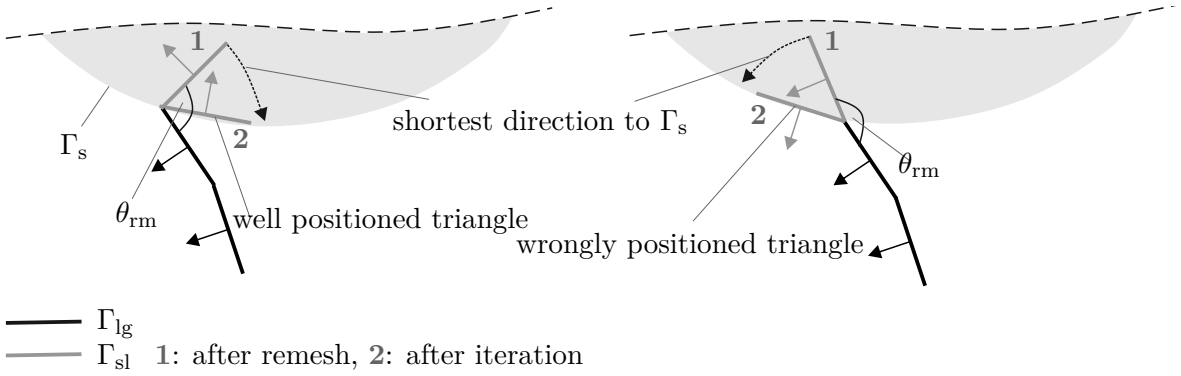

Figure 5.9.: Two-dimensional schematic illustration of the three-phase contact line triangles after the remesh

triangle is positioned on the wrong side of Γ_{lg} and the normal points in the wrong direction. Finally, this leads to a self-intersected destroyed mesh as illustrated in figure 5.8 (3).

In order to avoid this mesh instability at the three-phase contact line a correction step is implemented directly after the remesh (figure 5.2, *correct triangles at contact line*). However, since the moving direction of the triangles complexly depends on their position and the local topology of Γ_s, it is impossible to exactly predict which triangles will converge in an undesired direction. Thus, as a relatively rough criterion, the triangle is corrected in the wetting case ($\theta < 90°$) if $\theta_{rm} > 90°$ and vise versa in the non-wetting case. Using this conservative criterion, critical triangles along the three-phase contact line are identified. Subsequently they are tilted in the direction of the solid interface so that $\theta_{rm} = \theta$. Hence, the contact angle boundary condition between the liquid-gas and solid-liquid interface triangles is met and wrongly oriented normals during the following iterations are avoided. Note, that the surrounding triangles are slightly distorted by this correction. However, the error introduced by deforming the mesh is insignificant for the final solution, since it is corrected by the subsequent iteration steps.

In conclusion, a complex method to solve the constrained minimizing problem of eq. (5.3) is developed and presented in this chapter. This continuum approach simulates a static capillary bridge for a given volume and an arbitrary particle geometry. In this work, rough interfaces are considered which are derived by adding a normally distributed roughness to a smooth base geometry. The mathematical formulation of the constrained optimization problem leads to the Lagrangian equation that is solved by a combined gradient decent and Newton scheme with additional features that are tailor made for the capillary bridge problem. The numerical stability is improved by the remesh that increases the mesh quality. Since this method is new and has not

been applied yet, a verification against well known methods from the literature as well as a detailed discussion of its accuracy is presented subsequently.

6. Evaluation of the simulation method

The general applicability of the presented method is verified by comparison with results from the literature (section 6.1). This can, however, only be done for smooth particle geometries, since a model that directly resolves a rough solid interface does, to the best of the authors knowledge, not yet exist. In order to evaluate the accuracy of the presented method, the numerical error is estimated by an extensive mesh analysis (section 6.2). Moreover, simulating capillary bridges between rough interfaces involves a random sequence of normally distributed numbers to create different interfaces with the same integral roughness. In order to analyze the roughness dependent distribution of the capillary force the number of simulation samples must be large enough to provide results within a certain confidence interval (section 6.3). However, both, a fine mesh resolution and a large sample number, are computationally expensive and, therefore, a compromise between accuracy and simulation time needs to be found. Moreover, the two error types, i.e., the numerical and statistical error, should have a comparable order of magnitude to obtain a small overall error. For example, simulating only a few capillary bridges at a very high mesh resolution leads to a negligible numerical error on the one hand, and a huge statistical uncertainty on the other hand. Thus, a balance of both error types must be found (section 6.4).
The simulations are performed on the high performance cluster OCuLUS of the Paderborn Center for Parallel Computing (PC^2). Thus, all n simulations of a sample can be simulated in parallel. The numerical settings are presented in table 6.1. Only the remesh resolution factor must be analyzed with respect to the numerical error, since it determines the resolution of the capillary mesh (section 6.2). The other parame-

Table 6.1.: Numerical parameters for the simulation of capillary bridges

iteration settings		remesh settings			
level-set order	3	remesh intervals	20	50	200
linear step width	0.25	remesh frequency	5	10	50
Newton step width	0.1	remesh resolution factor	0.02 for $\tilde{V} < 0.2$ and		
start Newton iteration	51		0.03 for $\tilde{V} \geq 0.2$		

ters do not influence the numerical accuracy, however, they determine the numerical stability. The level-set order is set to 3, i.e., the level-set field is represented by a polynomial of third order which is smooth enough for the simulations presented in this work. The iteration steps of the linear scheme and the Newton scheme are 0.25 and 0.1, respectively. As explained in section 5.2.2, a Newton step below 1 is very unusual. However, convergence turned out to be much better using a smaller Newton step which is traced back to the fact, that the Newton scheme consists of two parts: the classical iteration and the manual projection of the tangential displacement at Γ_{sl}. The Newton scheme is activated after 51 iterations which is directly after a remesh. Generally, the remesh is performed in three intervals where a frequency and a resolution must be specified for each interval. Thus, according to table 6.1, the remesh completely stops after 200 iterations. The frequency of the remesh decreases with increasing convergence, since large distortions of the capillary bridge mesh mainly occur at the initial steps. As already described in section 5.2.3, the residual increases after each remesh, which slows down convergence. Moreover, the remesh itself requires a significant simulation time. Thus, the remesh should be performed just often enough to ensure a sufficient mesh quality for numerical stability. Note, that the numerical parameters are chosen according to hands-on experiences with the novel method, except for the remesh resolution factor.

The resolution factor determines the size of the mesh triangles, where a lower factor corresponds to smaller triangles, i.e., a higher mesh resolution, and vise versa. The volume dependent values of 0.02 and 0.03 result from the mesh study (section 6.2). It should be mentioned, that it is generally possible to use different mesh resolutions in each remesh interval. For example, the remesh in the first and second interval could be relatively coarse, since it is only required to ensure a high mesh quality rather than an accurate result. Only in the third interval a very high resolution could be used. However, a higher numerical stability is obtained for most simulations if the remesh resolution factor is the same for all three intervals. The step size and the mesh resolution are related, i.e., a finer mesh resolution requires a smaller step for numerical stability. This effect is also known from other numerical simulations such as computational fluid dynamics (CFD) where it is usually expressed by the so called CFL condition [Hir07; LeV02]. Generally, it is possible to simulate a coarse mesh using a fine step which is, however, not reasonable since, it is computationally expensive without gaining more accuracy. Nevertheless, in this work the iteration steps are kept constant. Thus, step optimization is not part of this work and provides a good option for reducing the simulation time in the future.

When simulating a whole sample of n capillary bridges, a result can often not be obtained for all simulations. There are very different reasons for terminated computations such as a broken triangle, an unfavorable relation of the mesh and step size or even an exceed of the requested simulation time. However, if too many simulations do not converge, a systematic cause cannot be excluded. In this case, the distribution of the capillary force might be distorted by a systematic error, since, for example, simulations with particularly high or low capillary forces do not converge. The analysis of unconverged simulations is very elaborate because the origin of a broken mesh must be analyzed manually for each single simulation. Thus, as a practical approach, a tolerance interval of 2 % unconverged simulations is defined. If at least 98 % of the simulations converge, the influence of a possible systematic error is ensured to be minor.

6.1. Verification

The main motivation to develop a new energy based method for the simulation of capillary force is its application to rough particles. However, to the best of the authors knowledge, the existing rough models require relatively large simplifications with respect to the geometry (section 3.7). Therefore, they are not suitable for a comparison with this method. The presented model is formulated for an arbitrary geometry and thus, it must also be able to adequately simulate capillary bridges between smooth particles. Thus, the results are compared to the elliptic integral approach of Orr et al. [Orr75] and the shooting method presented by Dörmann [Dör18]. According to figure 3.6, both methods are restricted to axisymmetric capillary bridges.
In table 6.2 a comparison of the dimensionless capillary force and the pressure between elliptic integral approach ($\tilde{F}_{\mathrm{c,orr}}$, $\Delta\tilde{p}_{\mathrm{orr}}$) and this model ($\tilde{F}_{\mathrm{c}}$, $\Delta\tilde{p}$) is presented. The setup is a smooth sphere-plate system with zero distance ($\tilde{a} = 0$) and contact angles of $\theta_1 = \theta_2 = 40°$. The values of ψ, $\tilde{V}$, $\tilde{F}_{\mathrm{c,orr}}$ and $\Delta\tilde{p}_{\mathrm{orr}}$ are explicitly tabulated in [Orr75]. However, the capillary force $\tilde{F}_{\mathrm{c,orr}}$ must be multiplied by π in order to agree with the definition of the dimensionless force in this work (eq. (3.2)). Moreover, instead of the dimensionless pressure the values of $2HR = 2\tilde{H}$ are given in [Orr75] which are, however, equal to $\Delta\tilde{p}_{\mathrm{orr}}$ according to the dimensionless Young-Laplace equation.
Table 6.2 shows, that the relative deviation between the capillary forces is always below 1 %. Moreover, the deviation between the pressure differences and the mean curvature, respectively, is maximally around 1 % for $\tilde{V} = 0.0107$ and below 0.2 % for all other points. This is remarkable, since the approximation of the curvature is usually a challenging issue on discretized interfaces. Thus, although the curvature of

the capillary interface is not required during the computation, the algorithm predicts the final mean curvature with a very good accuracy.
Since the two methods are fundamentally different, a deviation of less then 1 % in the capillary force and less than 1.1 % in the capillary pressure and the curvature, respectively, is an excellent result. Orr et al. [Orr75] also provide values for $\theta_1 = \theta_2 = 0°$. However, a contact angle of exactly zero cannot be handled by the presented method. In order to verify the model for a broader range of parameters a comparison with the Dörmann [Dör18] model is discussed subsequently.
The shooting method of Dörmann [Dör18] is fundamentally different from both, the Orr et al. [Orr75] model and the model of this work, since it presumes thermodynamic equilibrium between the liquid and the gas phase. At the beginning of the computation the humidity φ is predefined (pressure method, section 3.4) rather than the volume or the wetting angle (volume method, section 3.4). Thus, a direct comparison of the same capillary volumes requires an iteration of the humidity. In order to avoid this procedure the results of both models are plotted in a $\tilde{V}$-$\tilde{F}_\mathrm{c}$-diagram instead of directly comparing all single points. Thus, the exact deviations at a certain point are unknown, however, the agreement of the general tendencies is pointed out. Note, that the values of the Dörmann model are computed by the author of this work using the original algorithm implemented by Dörmann.
In figure 6.1 the comparison of the two models is shown for a sphere-plate system. In the left diagram the contact angles are $\theta_1 = \theta_2 = 10°$ and in the right diagram $\theta_1 = \theta_2 = 40°$. Moreover, the gap distances $\tilde{a}$ are 0.004, 0.05, 0.1 and 0.2. These distances are chosen, since they are used later in this work to analyze rough sphere-plate systems. The black lines are the values of the Dörmann [Dör18] algorithm and the gray areas mark an interval of +2 % of these values. Thus, the magnitude of the difference between the two models can be better estimated.

Table 6.2.: Comparison of the elliptic integral approach presented by Orr et al. [Orr75] and the method developed in this work (sphere-plate, $\tilde{a} = 0$, $\theta_1 = \theta_2 = 40°$)

ψ	$\tilde{V}$	$\tilde{F}_{\mathrm{c,orr}}$	$\tilde{F}_\mathrm{c}$	deviation / %	$\Delta\tilde{p}_\mathrm{orr}$	$\Delta\tilde{p}$	deviation /%
20°	0.0107	8.5841	8.5835	0.01	-18.2938	-18.1115	1.01
30°	0.0527	8.0139	8.0766	0.78	-6.4447	-6.4397	0.08
40°	0.1650	7.4088	7.4727	0.44	-2.6435	-2.6391	0.17
50°	0.4063	6.7654	6.8027	0.55	-1.0589	-1.0595	0.05
60°	0.8668	6.0799	6.0272	0.27	-0.3061	-0.3054	0.23

The general tendency of both models agrees very well for all simulated values. Even the slight maximum at $\tilde{a} = 0.004$ and very low volumes is reproduced by this method. For contact angles of $\theta_1 = \theta_2 = 10°$ most of the values are approximately 2 % larger compared to the Dörmann [Dör18] model. At the largest gap distance of $\tilde{a} = 0.2$ the deviations are even above this 2 % interval. For $\theta_1 = \theta_2 = 40°$ the deviations between the models are significantly smaller. In fact, all values are within the 2 % interval and most of the deviations are even below 1 %.
Interestingly, all values calculated by this method are larger compared to the Dörmann model [Dör18]. In order to get a deeper understanding of the correlations, a direct comparison of four capillary bridges is presented in table 6.3. Therefore, the Dörmann algorithm is iterated to obtain the desired volume $\tilde{V} = 0.1$. Since this iteration is performed manually, a relative deviation of 0.05 % between $\tilde{V}_{\text{Dörmann}}$ and 0.1 is accepted. The values given in table 6.3 are all calculated by

$$v = \frac{v_{\text{this model}} - v_{\text{Dörmann}}}{v_{\text{this model}}} \cdot 100\%. \tag{6.1}$$

Only the relative ratio of $F^*_{\text{s,rel}}$ refers to this model and does not represent a deviation to the Dörmann model. In particular, $F^*_{\text{s,rel}}$ gives the ratio of the surface tension force to the capillary force.
The results presented in table 6.3 agree well with figure 6.1. The deviations of the capillary force F_{c} are around 2 % for $\theta_1 = \theta_2 = 10°$ and below 1 % for $\theta_1 = \theta_2 = 40°$,

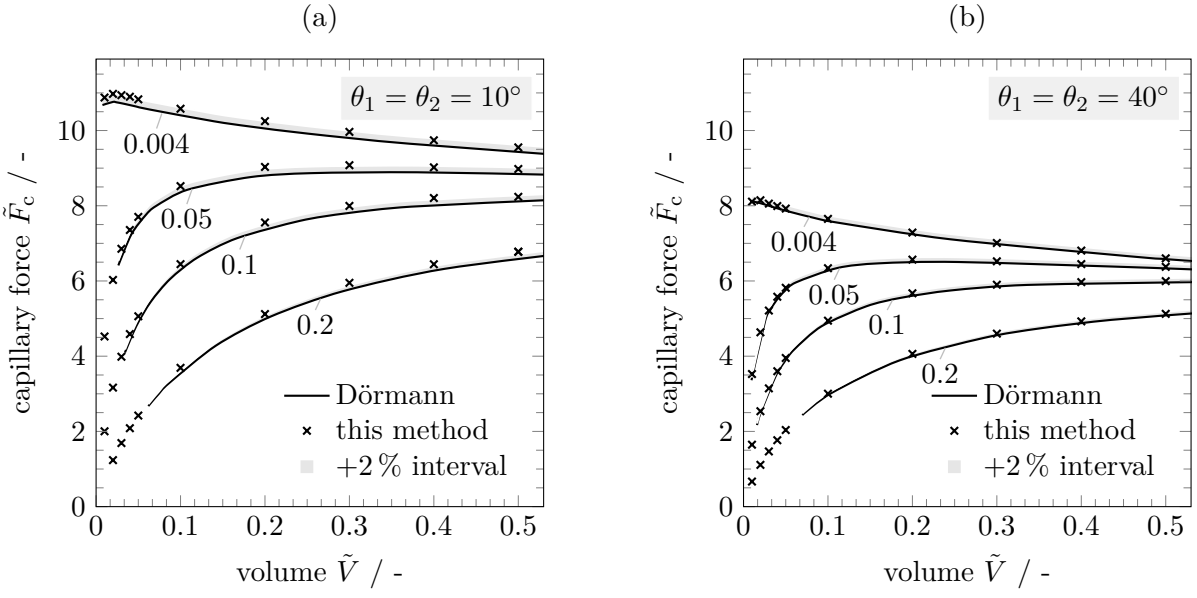

Figure 6.1.: Comparison between the shooting method of Dörmann [Dör18] and this model for a sphere-plate system with different gap distances $\tilde{a} = 0.004, 0.05, 0.1$ and 0.2

respectively, and they slightly increase with an increasing gap distance $\tilde{a}$. Thus, the iteration error, i.e., a maximum relative deviation of 0.05 % of the volumes, is assumed to be minor compared to the deviations that result from the methods. Also for the capillary pressure a good accordance between the two models is observed, since the deviations are below 1 % for all contact angles.

An evaluation of the capillary force $F_{\mathrm{c,i}}$ at the sphere ($i = 1$) and plate ($i = 2$), respectively, shows that the deviations of the capillary forces are larger at the plate. Note, that the capillary force must analytically be the same at any point of the capillary bridge ($F_{\mathrm{c,i}} = \text{const.}$), however, due to numerical inaccuracies there are differences. For a more detailed analysis the capillary force is split into the capillary pressure force $F_{\mathrm{p,i}}$ and the surface tension force $F_{\mathrm{s,i}}$.

The capillary pressure force $F_{\mathrm{p,i}}$ is estimated with nearly the same accuracy at the sphere and at the plate. With an increasing contact angle the deviation of $F_{\mathrm{p,i}}$ slightly reduces by an order of magnitude of 0.5 %. Overall, the capillary pressure forces of this model and the Dörmann model [Dör18] differ below 2 % which is very good. In contrast, the surface tension forces show substantial deviations between the models. These deviations are significantly larger at the plate and increase with a decreasing contact angle. In particular, this causes deviations around 2 % in the best case ($\theta_1 = \theta_2 = 40°$ at the sphere) and around 37 % in the worse case ($\theta_1 = \theta_2 = 10°$ at the plate).

One reason for these large deviations might be the numerical representation of the three-phase contact line. In this model the three-phase contact line is a completely discretized three-dimensional polygonal curve, whereas it is a perfectly two-dimensional circle in the Dörmann model. Thus, the length of the three-phase contact line $l_{\mathrm{CL,i}}$ is evaluated for both models and the deviations are given in table 6.3. The negative

Table 6.3.: Deviation in % between this method and the Dörmann method [Dör18] for $\tilde{V} = 0.1$ and
1: $\theta_1 = \theta_2 = 10°$; 2: $\theta_1 = \theta_2 = 40°$;
a: $\tilde{a} = 0.004$; b: $\tilde{a} = 0.1$;
*: ratio in % of $\tilde{F}_{\mathrm{s}}/\tilde{F}_{\mathrm{c}}$ computed with this model

	total		sphere (i=1)					plate (i=2)				
	F_{c}	Δp	$F_{\mathrm{c,1}}$	$F_{\mathrm{p,1}}$	$F_{\mathrm{s,1}}$	$l_{\mathrm{CL,1}}$	$F^{*}_{\mathrm{s,rel,1}}$	$F_{\mathrm{c,2}}$	$F_{\mathrm{p,2}}$	$F_{\mathrm{s,2}}$	$l_{\mathrm{CL,2}}$	$F^{*}_{\mathrm{s,rel,2}}$
1a	1.74	-0.50	1.13	-1.67	8.29	-0.42	28.09	2.34	-1.83	36.68	-0.60	10.75
1b	2.31	-0.64	1.72	-1.82	9.10	-0.39	32.41	2.89	-1.86	32.76	-0.55	13.57
2a	0.64	-0.42	-0.06	-1.12	1.16	-0.31	46.17	1.34	-1.09	5.84	-0.33	35.14
2b	0.96	-0.86	0.42	-1.49	2.01	-0.28	54.35	1.49	-1.41	5.30	-0.26	43.41

sign of all values of $l_{\mathrm{CL,i}}$ indicates that the three-phase contact line is usually estimated smaller by this model. Consequently, a smaller surface tension force would be expected which is clearly not the case. Moreover, the maximum absolute deviation of the three-phase contact lines is 0.60 % which cannot cause a deviation of nearly 37 % in the surface tension force, since their relation is linear. Thus, according to eq. (3.7), a relatively inaccurate calculation of the co-normal vector $\tilde{\boldsymbol{\mu}}_{\mathrm{lg}}$ seems to be responsible for the large deviations. In fact, the deviation between the models can be reduced by using a significantly higher mesh resolution. Since this is a convergence issue, it is explained more detailed in section 6.2.
Overall, the different accuracies of $\theta_1 = \theta_2 = 10°$ (figure 6.1 (a)) and $\theta_1 = \theta_2 = 40°$ (figure 6.1 (b)) are mainly caused by the surface tension force. However, although the surface tension force is computed with poor precision at the low contact angles, the influence on the capillary force is minor which is traced back to a dominant capillary pressure force. In particular, the largest deviations of the surface tension force (36.68 % and 32.76 %) come along with a minor proportion on the capillary force (10.75 % and 13.57 %). Nevertheless, this finding must be considered when simulating capillary bridges with low contact angles or a dominant surface tension force.
Note, that for this particular case of a smooth sphere and plate it might be reasonable to evaluate the capillary force at the sphere rather than averaging over all i interfaces (eq. (5.17)). However, when considering arbitrary shapes and even rough particles it cannot be predicted at which solid-liquid interface the most accurate capillary force is obtained. Only in case of different contact angles an evaluation at the interface with the largest contact angle might be considered. However, in this work the contact angles are kept equal and thus, averaging over all interfaces is used further on.
In figure 6.1 it is also illustrated that for the large gap distance and the small volumes no capillary bridges are obtained with the Dörmann model [Dör18]. One reason could be, that no thermodynamic equilibrium exists which is presumed by Dörmann and, however, not considered in this model. Nevertheless, the results obtained by this model show a well defined concave capillary bridge with a negative capillary pressure. Thus, there is no reason to assume that these bridges could not potentially exits in a thermodynamic equilibrium. A combination of the Kelvin equation (2.26) and the Young-Laplace equation (eq. (2.15)) leads to

$$\varphi = \exp\left(\frac{\Delta p \lambda_{\mathrm{k}}}{\sigma}\right) = \exp\left(\frac{\Delta \tilde{p} \lambda_{\mathrm{k}}}{R}\right). \tag{6.2}$$

This equation relates the relative humidity φ to the corresponding capillary pressure in a thermodynamic equilibrium. By considering the dimensionless capillary pressure $\Delta\tilde{p}$ it is obvious that the existence of the thermodynamic equilibrium is size dependent, since eq. (6.2) contains the characteristic length scale, i.e., the particle radius R. For the very small bridges the capillary pressure rapidly decreases. From limit value considerations it follows, that $\Delta p \to -\infty$ leads to $\varphi \to 0$. Of course, Δp cannot become infinite low, since at some point the liquid volume is too small to fill the gap. However, for the small bridges presented in figure 6.1 the capillary pressure rapidly decreases with slight changes of the humidity φ. In fact, the values of Dörmann are derived by adjusting the humidity at the 10^{th} decimal for $\tilde{V} < 0.5$. A finer adjustment is not possible with the current implementation of the algorithm. Thus, it is assumed that the values for very small volumes cannot be obtained by the Dörmann model due to the limited accuracy of the humidity.
In addition to the described sphere-plate system, a sphere-sphere system with equally sized spheres ($R_1 = R_2 = R$) is investigated. The results for the different contact angles $\theta_1 = \theta_2 = 10°$ and $\theta_1 = \theta_2 = 40°$ are presented in figure 6.2. Again, a very good agreement between the two models is observed. The tendencies are the same as described for the sphere-plate system. In particular, this model always overestimates the capillary force compared to the Dörmann [Dör18] model which is again traced back to the overestimation of the surface tension force. This inaccuracy also leads to

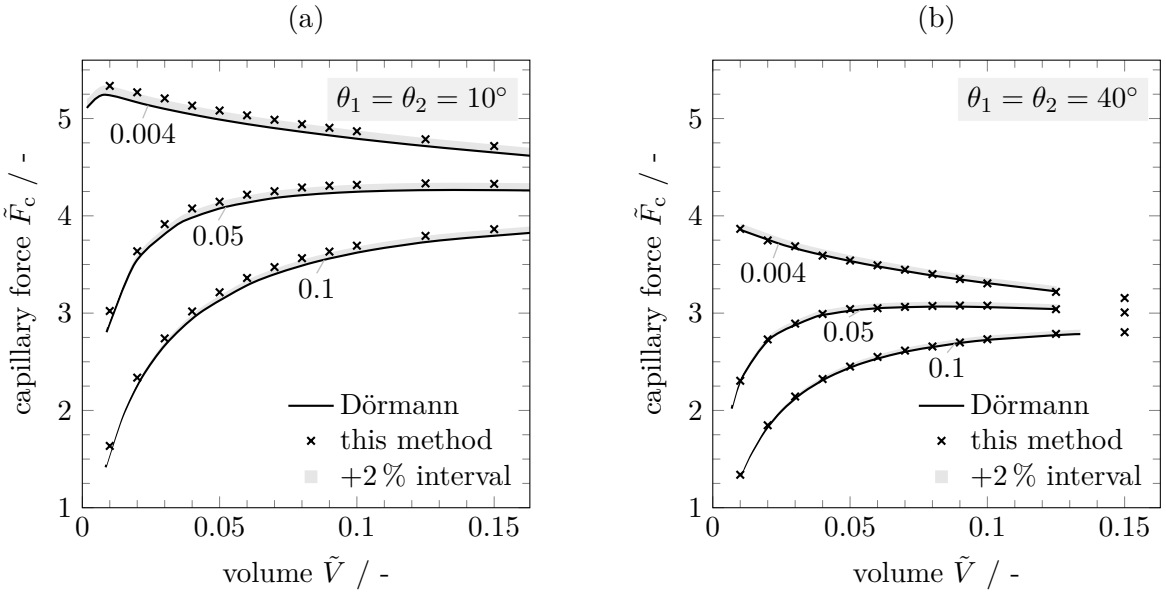

Figure 6.2.: Comparison between the shooting method of Dörmann [Dör18] and this model for a sphere-sphere system with different gap distances $\tilde{a} = 0.004, 0.05$ and 0.1

the higher deviations for the smaller contact angles ($\theta_1 = \theta_2 = 10°$) whereas for the large contact angles ($\theta_1 = \theta_2 = 40°$) an almost exact agreement is observed.
Again, some values cannot be obtained using the Dörmann [Dör18] model. However, for the sphere-sphere system this occurs for large volumes rather than the small volumes in the sphere-plate system. In fact, the capillary bridges that are calculated with this model at at $\tilde{V} = 0.15$ and $\theta_1 = \theta_2 = 40°$ are convex and exhibit a positive capillary pressure $\Delta\tilde{p} > 0$. Thus, an unstable thermodynamic equilibrium exists above saturation ($\varphi > 1$), which is not implemented in the Dörmann model.
In conclusion, the high agreement of the methods is a good indication that the presented method works well and is suitable for theoretical investigations of capillary bridges. The deviations between the elliptic integral method of Orr et al. [Orr75] is around 1 % whereas a comparison to the shooting method of Dörmann [Dör18] reveals a deviation below 2 % for most points. Generally, the agreement is relatively good for small contact angles and excellent for larger contact angles. However, the computation of the surface tension force is not satisfactory and will be analyzed more in detail by the subsequent mesh study.

6.2. Numerical error

The objective of the mesh analysis is to find a remesh resolution factor that ensures sufficiently accurate results at an acceptable simulation time. Thus, the magnitude of the numerical error must be estimated. However, the remesh resolution factor does not provide direct information about the mesh resolution and therefore, it is not reasonable to use it for the discussion. Instead, the number of mesh triangles n_t is used.
The objective parameters of the simulations are the expected value of the capillary force $\mu_{\tilde{\mathrm{F}}_\mathrm{c}}$ and the corresponding standard deviation $\sigma_{\tilde{\mathrm{F}}_\mathrm{c}}$. However, due to an infinite number of rough particles, both values cannot be obtained exactly. Thus, the mean capillary force $\bar{\tilde{F}}_\mathrm{c}$ and the standard deviation of the sample $s_{\mathrm{F}_\mathrm{c}} = s$ are used as an estimation for $\mu_{\tilde{\mathrm{F}}_\mathrm{c}}$ and $\sigma_{\tilde{\mathrm{F}}_\mathrm{c}}$, respectively. Consequently, these two parameters are chosen for the mesh analysis and later also for the statistical analysis (section 6.3).
The mean of n values of the parameter u is denoted by $\bar{u}$ and given by

$$\bar{u} = \frac{1}{n} \sum_{i=1}^{n} u_\mathrm{i}. \tag{6.3}$$

Since all parameters presented in the following chapters are dimensionless, the convention $\bar{\tilde{u}} = \bar{u}$ is used for a better legibility, i.e., $\bar{\tilde{F}}_\mathrm{c} = \bar{F}_\mathrm{c}$. Moreover, the empirical standard deviation of the sample of u is given by

$$s_\mathrm{u} = \sqrt{\frac{1}{n-1}\sum_{i=1}^{n}\left(u_\mathrm{i} - \bar{u}\right)^2}. \tag{6.4}$$

For the numerical investigations it is useful to show the results in terms of the most accurate solutions. Thus,

$$\Delta v = \frac{v - v_\mathrm{rv}}{v_\mathrm{rv}} \cdot 100\% \tag{6.5}$$

is defined, where v could be any parameter of interest such as the mean capillary force $\bar{F}_\mathrm{c}$ or the standard deviation of the capillary force s. Thus, Δv directly expresses the relative percentage deviation from the reference values v_rv. For the mesh analysis v_rv is given by the solution of the finest mesh and for the statistical analysis it is defined by the simulation with the largest sample size.

The mesh study is performed for the sphere-plate and the sphere-sphere system. Since it is very expensive with respect to the computational resources, not all parameter combinations can be investigated. In particular, the influence of the gap distance $\tilde{a}$ on the accuracy is assumed to be minor compared to the influence of the volume $\tilde{V}$, contact angle θ and the root mean square roughness (RMS) $\tilde{S}_\mathrm{q}$. This seems to be reasonable according to figure 6.1 and 6.2 as well as table 6.3. Thus, the gap distance is kept constant for the mesh study at $\tilde{a} = 0.1$ (sphere-plate) and $\tilde{a} = 0.05$ (sphere-sphere), respectively. For the sphere-plate system the influence of volume and the contact angle is analyzed and the RMS is fixed at $\tilde{S}_\mathrm{q} = 0.005$. The influence of roughness is investigated for the sphere-sphere system at the constant volume of $\tilde{V} = 0.05$. Since this work focuses on the evaluation of the new method and the simulation of rough interfaces, the contact angles at the solids are kept equal, i.e., $\theta = \theta_1 = \theta_2$.

Finally, it is important to note that convergence of the mean capillary force $\bar{F}_\mathrm{c}$ and the empirical standard deviation $s_{\text{›}}$ does not necessarily imply convergence of all other parameters. In particular, the convergence of the surface tension force at low contact angles needs to be analyzed in detail as indicated by the comparison with the Dörmann model.

The sphere-plate system consists of a smooth plate ($\tilde{S}_\mathrm{q} = 0$) and a rough sphere ($\tilde{S}_\mathrm{q} = 0.005$ and $\varepsilon = 0.1$). The volume is varied by $\tilde{V} = 0.01$, 0.1, 0.2 and 0.5. A

visualization of the mesh resolution is given in figure 6.3 for three different meshes of the capillary bridge with $\tilde{V} = 0.1$. In figure 6.4 the mesh study is shown for a single capillary bridge where the random seed number is $\xi = 100$. The relative deviation of the capillary force $\Delta\tilde{F}_\mathrm{c}$ is plotted as a function of the number of triangles n_t (figure 6.4 (a)). Note, that all curves end at a zero deviation, which is consistent with the definition of the relative deviation (eq. (6.5)). The numerical error leads to a clear overestimation of the capillary force. For all four volumes the deviation asymptotically decreases with an increasing mesh resolution, i.e., an increasing number of triangles. Thus, the meshes generally show a good convergence behavior. At very low resolutions the capillary force might slightly increase, however, these meshes are so coarse that the liquid-gas interface might be represented by only three to four triangles along the axis (figure 6.3, left capillary bridge). Thus, the non-monotone behavior at very low mesh resolutions is traced back to an insufficient resolution of the liquid-gas interface.

The differences between $\tilde{V} = 0.1$, 0.2 and 0.5 are minor. Only for $\tilde{V} = 0.01$ the maximum number of triangles is relatively low and the mesh is not fully converged. Capillary bridges with $\tilde{V} = 0.01$ are, however, 10 to 50 times smaller compared to the other volumes. In figure 7.2 images of capillary bridges for different volumes are illustrated and it becomes clear, that using the same number of mesh triangles means a very high triangle density and very small triangles for the small bridges. In fact, the most accurate solution of $\tilde{V} = 0.01$ ($n_\mathrm{t} = 6330$) exhibits a higher triangle density than all other most accurate solutions although their number of triangles is at least six times higher. The main problem in simulating $\tilde{V} = 0.01$ with more triangles is the very small triangle size. With the selected step sizes it is not possible to simulate these small triangles, since the vertex displacement per step exceeds the triangles size. Reducing the step size would be one option to overcome this issue, however, this rapidly increases the simulation time and has not been done in this work. Instead, a higher numerical error at the small volume is accepted as it is explained subsequently. The finest mesh, i.e., the last point of each curve, represents the most accurate numerical solution rather than the exact solution. Thus, the numerical error is larger than indicated in figure 6.4 (a). For example, if the maximum number of triangles n_t would be 10^4, the zero level of $\tilde{V} = 0.1$ and 0.2 would be approximately 1% higher or, in other words, the curves would shift down by 1%. Consequently, the numerical error would seem to be a lot smaller. In order to avoid this problem it must be ensured, that the most accurate simulation is very close to the exact solution, i.e., the remaining numerical error of the most accurate solution is negligible. This could be

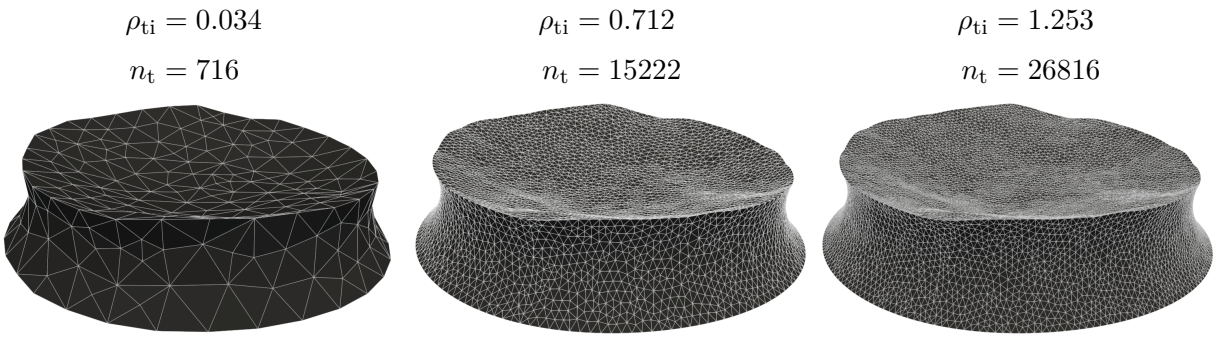

Figure 6.3.: Capillary bridges between a rough sphere and a smooth plate with different mesh resolutions ($\tilde{V} = 0.1$, $\theta = 40°$, $\tilde{a} = 0.1$, $\tilde{S}_{\mathrm{q}} = 0.005$, $\varepsilon = 0.1$ and $\xi = 100$)

demonstrated by simulations with even finer meshes. Unfortunately this is not possible, since more than $4 \cdot 10^4$ triangles cause memory problems on the computational nods.

Another option of estimating the quality of the most accurate solution is considering the gradient of the deviation $\Delta\tilde{F}_{\mathrm{c}}$ as illustrated in figure 6.4 (b). The gradients are all negative, since the numerical capillary force overestimates the most accurate solution. Note, that the large and sometimes positive gradients at the very low mesh resolution are not plotted, since they are of minor interest and would require a very different scaling of the y-axis. For the three large volumes the gradients approache zero with increasing triangle density. Thus, a further increase of the number of triangles does

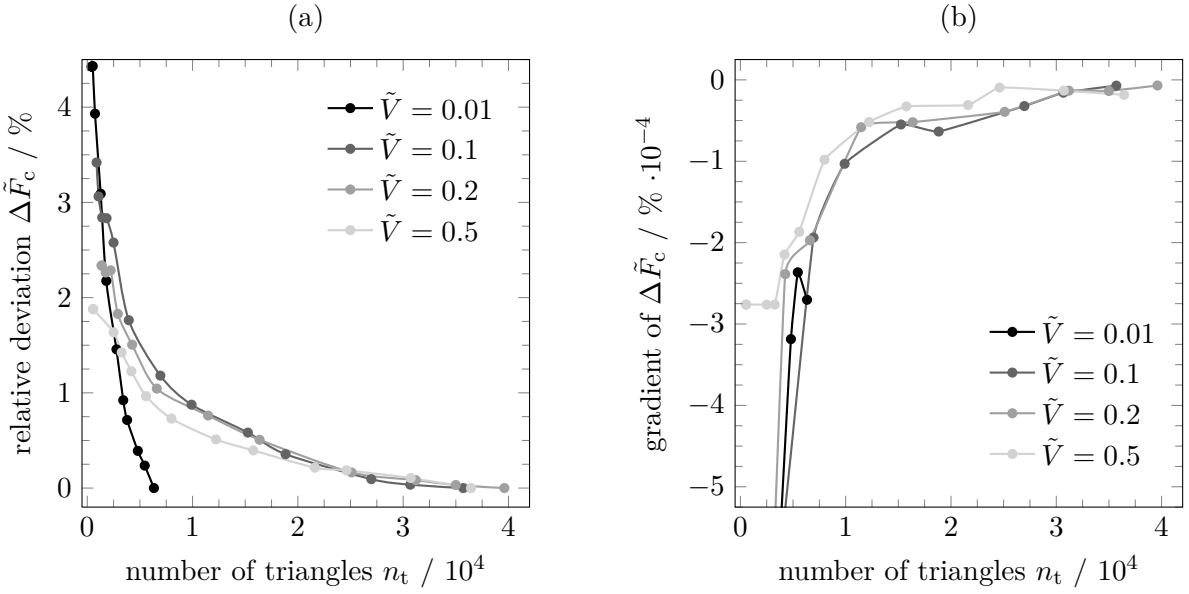

Figure 6.4.: Relative deviation of the capillary force (a) and the corresponding gradient for different mesh resolutions of a single capillary bridge ($\xi = 100$) between a rough sphere and a smooth plate with $\tilde{S}_{\mathrm{q}} = 0.005$, $\varepsilon = 0.1$, $\theta = 40°$ and $\tilde{a} = 0.1$

most probably not lead to significant changes of the capillary force. The absolute value of the gradient between the most accurate solution and the next coarser mesh is below 0.2 % per 10^4 triangles for all three volumes. This means, that increasing the number of triangles by $3 \cdot 10^4$, which is nearly a doubling of the triangle number, leads to a deviation in the capillary force of less than 0.6 % for $\tilde{V} = 0.1$, 0.2 and 0.5. However, this is a very conservative estimation, since the gradient itself is not constant and approximates zero as shown in figure 6.3 (b). Finally, the numerical error of a particular mesh is estimated by the sum of the relative deviation of the mesh $\Delta\tilde{F}_\mathrm{c}(n_\mathrm{t})$ and 0.6 %.

However, for $\tilde{V} = 0.01$ the difference between the most accurate solution and the exact solution cannot be estimated by 0.6 %. Since the relative deviation of $\tilde{V} = 0.01$ shows a continuous decrease that is very similar to the larger volumes, it seems to be reasonable to assume an analogous convergence. In particular, this is done by shifting the $\tilde{V} = 0.01$ curve by approximately +1 %. Consequently, the numerical error for $\tilde{V} = 0.01$ is predicted by the relative deviation $\Delta\tilde{F}_\mathrm{c}(n_\mathrm{t})$ plus 1.6 %.

Besides the capillary force of a particular capillary bridge it is also important to analyze the convergence of the distribution of capillary forces for n samples. The sample size is set to $n = 1000$. In figure 6.5 (a) the deviation of the mean capillary force $\Delta\bar{F}_\mathrm{c}$ is plotted as a function of the mean number of triangles $\bar{n}_\mathrm{t}$. The mean capillary force of the highest mesh resolution $\bar{F}_\mathrm{c,ma}$ is used as most accurate solution in eq. (6.5). The

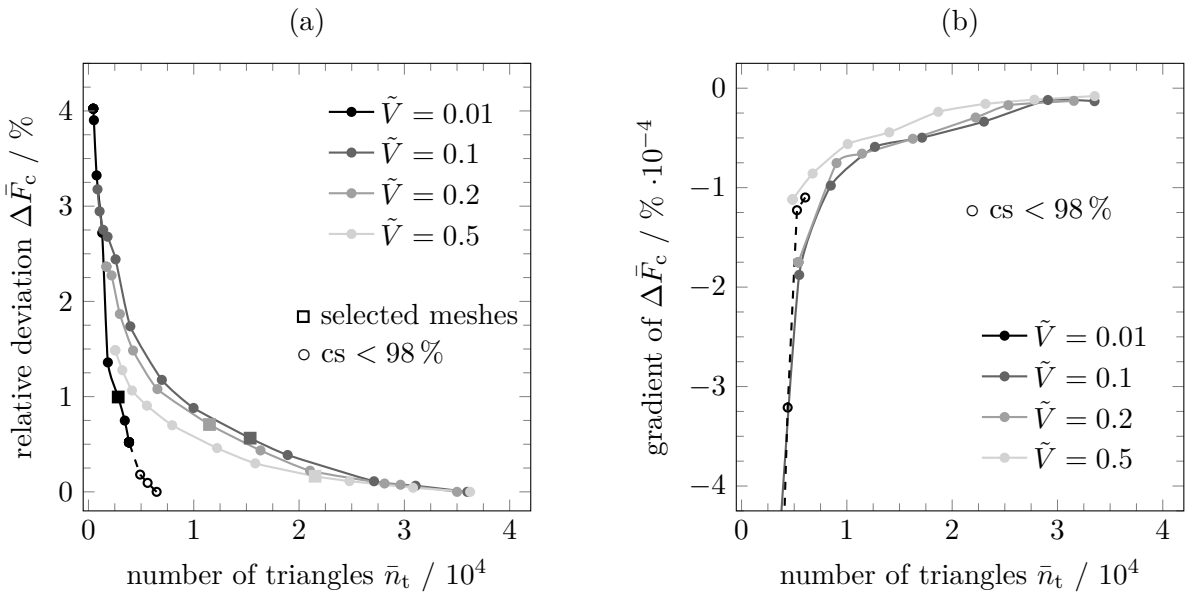

Figure 6.5.: Relative deviation of the mean capillary force (a) and the corresponding gradient (b) for different mesh resolutions of the distribution ($n = 1000$) of a capillary bridge between a rough sphere and a smooth plate with $\tilde{S}_\mathrm{q} = 0.005$, $\varepsilon = 0.1$, $\theta = 40°$ and $\tilde{a} = 0.1$

deviation of the mean capillary force $\Delta\bar{F}_\mathrm{c}$ asymptotically decreases with an increasing number of triangles $\bar{n}_\mathrm{t}$. The convergence of the whole distribution is very similar to the results of a single capillary force (figure 6.4). Again, more than approximately $0.8 \cdot 10^4$ triangles cannot be applied to the small volume of $\tilde{V} = 0.01$. For the three highest resolutions of $\tilde{V} = 0.01$ the distribution is not completely converged. This means, that less than 98 % of the simulations converged. Nevertheless, the results are presented, since convergence is achieved for 96 % which is still relatively high.
The numerical error is estimated analogously to the numerical error of a single capillary bridge. Thus, the gradients of the relative deviation $\Delta\bar{F}_\mathrm{c}$ are considered to evaluate the quality of the most accurate solution. For the large volumes, i.e., $\tilde{V} = 0.1$, 0.2 and 0.5, the absolute values of the gradients are between 0.08 % and 0.14 % per 10^4 triangles. Thus, a rather conservative estimation leads to an additional deviation for $3 \cdot 10^4$ more triangles of 0.6 %. Again, it is assumed that this error is approximately 1 % higher for $\tilde{V} = 0.01$.
In figure 6.5 (a) the finally selected meshes are indicated by a square. This means, that the results presented in chapter 7 are obtained using these particular meshes. They correspond to remesh resolution factors of 0.02 for $\tilde{V} = 0.01$ and 0.1 as well as 0.03 for $\tilde{V} = 0.2$ and 0.5. The meshes are selected with respect to a manageable computational time. Note, that each simulation point includes 1000 simulations. Thus, an increased simulation time of several hours for a single capillary bridge is very significant for the total simulation time. The average simulation time $\bar{t}$ and the maximum simulation time $t_\mathrm{i,max}$ of the selected meshes are given in table 6.4. The average simulation times are relatively low. However, the requested time must be above the maximum simulation time for all $n = 1000$ samples, since it is not a priori known how long the computation of a certain capillary bridge takes. Moreover, the maximum time is not known and, therefore, the requested time must be estimated conservatively. Unfortunately, the allocation time, i.e., the waiting time until the simulation is assigned to a certain computational nod, significantly increases with the requested time. Thus, 1000 simulations with $\tilde{V} = 0.5$ usually take a real simulation

Table 6.4.: Average and maximum pure simulation time for a single simulation of the selected meshes in hh:mm

	$\tilde{V} = 0.01$	$\tilde{V} = 0.1$	$\tilde{V} = 0.2$	$\tilde{V} = 0.5$
average simulation time $\bar{t}$	00:07	01:07	00:43	01:24
maximum simulation time $t_\mathrm{i,max}$	00:19	03:16	04:36	10:30

time of one to two days although the average time per simulation is only approximately 01 : 24 hours. The real time significantly depends on the work load of the cluster. Finally, it also has to be considered, that the simulation time increases with a decreasing contact angle and gap distance and with an increasing roughness. Taking all these factors into account, the selected meshes are considered to be a good compromise between the real simulation time and numerical accuracy.

In conclusion, the total numerical error of the mean capillary force is evaluated by the sum of $\Delta\bar{F}_\mathrm{c}(\bar{n}_\mathrm{t,se})$ of the selected meshs and the estimated deviation between the most accurate solution and the exact solution, i.e., 0.6 % for $\tilde{V} = 0.1$, 0.2 and 0.5 and 1.6 % for $\tilde{V} = 0.01$. This leads to a numerical error of 2.6 % for $\tilde{V} = 0.01$. With an increasing volume this error is reduced and approximated by 1.2 % for $\tilde{V} = 0.1$. For $\tilde{V} = 0.2$ the accuracy of the mesh slightly increases because of the higher remesh factor. Thus, the numerical error is 1.3 % for $\tilde{V} = 0.2$ and decreases down to 0.8 % for $\tilde{V} = 0.5$.

Another important parameter to characterize a distribution is the standard deviation of the capillary force s. Thus, the mesh convergence is also analyzed with respect to the standard deviation of the capillary force $s_{\mathrm{F_c}} = s$. The relative deviation Δs between the standard deviation s and the most accurate standard deviation is presented in figure 6.6 (a). Since the values represent the same simulations as shown in figure 6.5, the unconverged values of $\tilde{V} = 0.01$ occur at the same number of triangles.

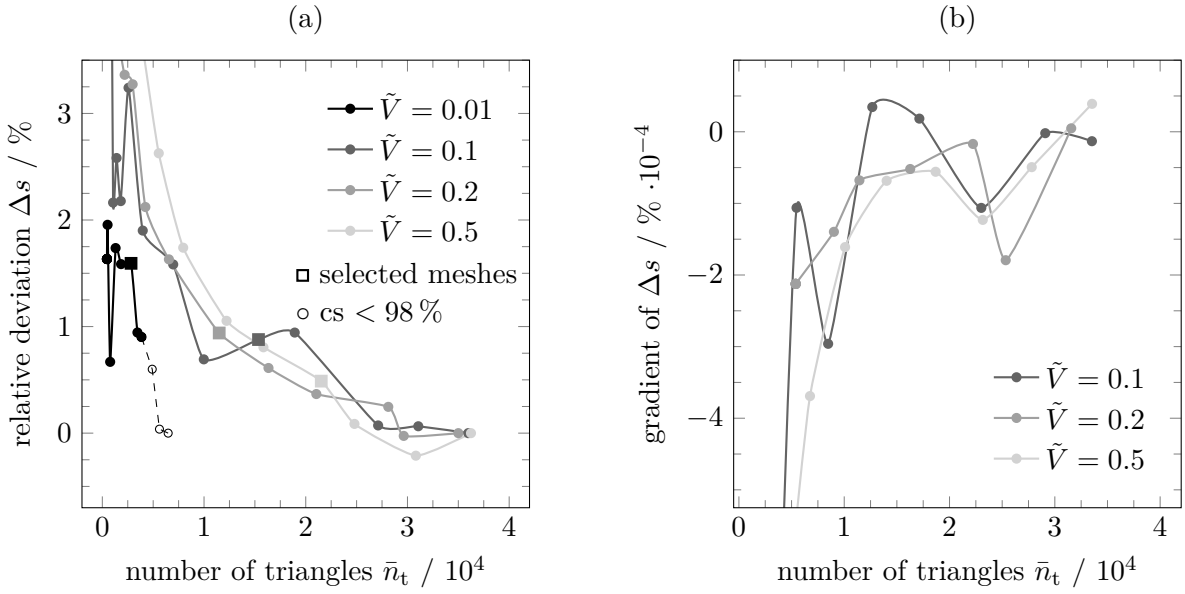

Figure 6.6.: Relative deviation of the standard deviation (a) and the corresponding gradient (b) for different mesh resolutions of the distribution ($n = 1000$) of a capillary bridge between a rough sphere and a smooth plate with $\tilde{S}_\mathrm{q} = 0.005$, $\varepsilon = 0.1$, $\theta = 40°$ and $\tilde{a} = 0.1$

Overall, a decreasing relative deviation Δs with an increasing number of triangles $\bar{n}_\mathrm{t}$ is observed. However, in contrast to the relative deviation of the capillary force (figure 6.5) this decrease is neither monotone nor asymptotic.
The standard deviation is generally more sensible then a mean value. In particular, the influence of one value on the mean value is always n^{-1}, whereas the standard deviation can significantly be changed by only a few values. From the previous results it is reasonable to assume, that the capillary force always decreases with increasing mesh resolution. This corresponds to a left shift of the distribution in a frequency distribution plot. Since the absolute gradient of the decreasing capillary force is not exactly equal for all n samples, the distribution is also deformed. A decreasing standard deviation corresponds to a compressing of the distribution and an increasing standard deviation to a stretching. Finally, with an increasing mesh resolution and a convergence of all n capillary forces, both, the shifting of the distribution (mean value $\bar{F}_\mathrm{c}$) and the distortion (s) decline and the results become mesh independent.
Although the relative deviation Δs deceases with an increasing mesh resolution, convergence is only observed for $\tilde{V} = 0.1$. Generally, a further convergence of Δs is expected, since the deviations of the capillary forces converge. Again, the gradients of Δs are considered in order to estimate the numerical error. In figure 6.6 (b) the gradients of the three large volumes are presented. Note, that the gradients of $\tilde{V} = 0.01$ are not illustrated, since they are too large for the scaling of the y-axis. The gradients of the other three volumes generally approach zero. However, in contrast to the gradients of $\Delta\bar{F}_\mathrm{c}$ (figure 6.5 (b)), there are still considerable fluctuations. Thus, by evaluating only the last gradient the estimation might not be conservative enough, since a slight increase of the gradient at a higher mesh resolution is still possible. It seems to be more reasonable to use the average of the absolute values of the last three gradients. This leads to 0.40 % per 10^4 triangles for $\tilde{V} = 0.1$, 0.67 % per 10^4 triangles for $\tilde{V} = 0.2$ and 0.70 % per 10^4 triangles for $\tilde{V} = 0.5$. In order to conservatively estimate the deviation between the most accurate solution and the exact solution, a nearly doubled mesh resolution, i.e., an increase of $3 \cdot 10^4$ triangles, is considered. Again, for $\tilde{V} = 0.01$ this deviation is assumed to be 1 % higher than the values obtained for $\tilde{V} = 0.1$, i.e., 2.2 %.
Finally, the total numerical error of the standard deviation is obtained analogously to the numerical error of the mean capillary force. By considering the values of the selected meshes in figure 6.6 (a), i.e., $\Delta s(\bar{n}_{\mathrm{t,se}})$, a numerical error of 3.8 % is estimated for $\tilde{V} = 0.01$. Since this is a relatively large error, it is worth mentioning that it must be interpreted as an upper limit for the smallest volume considered in this work.

With increasing volume this error significantly decreases down to 2.1 % for $\tilde{V} = 0.01$, 3.0 % for $\tilde{V} = 0.2$ and 2.6 % for $\tilde{V} = 0.5$.
Generally, the influence of the volume is minor, provided that the capillary bridges are represented by the same number of triangles. This, however, requires a volume dependent remesh resolution factor. Thus, the slightly different numerical errors between the volumes result from practical approach of only distinguishing two different remesh resolution factors.
The comparison with the Dörmann model already reveals an influence of the contact angle on the accuracy of the presented method (section 6.1). In particular, it is demonstrated that the computation of the surface tension force is not very exact. Thus, a mesh analysis at two different contact angles is performed in order get a deeper understanding of the presented method.
In figure 6.7 the relative deviation of the mean capillary force $\Delta\tilde{F}_\mathrm{c}$ (a) and the relative deviation of the standard deviation s (b) are presented for two different contact angles. The curves of $\theta = 40°$ correspond to the curves of $\tilde{V} = 0.1$ in figure 6.5 (a) and 6.6 (a). Note, that a mesh study for an even smaller contact angle ($\theta = 10°$) is not possible, since for more than $2 \cdot 10^4$ triangles not enough simulations converge. Nevertheless, all tendencies are demonstrated for $\theta = 20°$ and it is assumed, that they are stronger for smaller contact angles.
In figure 6.7 (a) it is shown, that the capillary force converges slower for the smaller contact angle ($\theta = 20°$). However, for $\bar{n}_\mathrm{t} > 1.5 \cdot 10^4$ the accuracy is nearly equal and, hence, for the selected meshes the numerical error has the same order of magnitude. The convergence of the standard deviation of the sample s (figure 6.7 (b)) is similar for both contact angles. Although there are still significant fluctuations, that are already explained for the different volumes (figure 6.6 (a)), the relative deviation Δs is around 1 % for the selected meshes and clearly below 1 % for higher mesh resolutions.
For a deeper analysis of the differences between the contact angles, the convergence of the capillary pressure force and the surface tension force are presented in figure 6.8. Since these force components are different at the sphere and the plate, they are evaluated at both solids. In figure 6.8 (a) it is shown, that the capillary pressure force is estimated too small compared to the most accurate solution. In fact, this is unexpected because the overall capillary force is overestimated for all previously shown simulations. Nevertheless, the convergence of the different contact angles is similar although the smaller contact angle converges slightly slower. It is important to note, that for both contact angles the differences between the accuracy at the sphere and the plate are negligible for $\bar{n}_\mathrm{t} > 1 \cdot 10^4$. Thus, the accuracy is not influenced by

the roughness of an interface. Overall, the convergence of the capillary pressure force is excellent and even better than the convergence of the overall capillary force.
The convergence of the surface tension force is illustrated in figure 6.8 (b) and shows a very different behavior. First, the large scaling of the y-axis should be noted which clearly demonstrates the slow convergence. Moreover, the surface tension force deviates significantly upwards from the most accurate solution. This effect superimposes the underestimation of the capillary pressure force and causes the overestimation of the overall capillary force. Again, the smaller contact angle converges slower, however, the differences between the contact angles are significantly larger compared to the capillary pressure force. In fact, the deviations between the contact angles are only negligible for $\bar{n}_\mathrm{t} > 3 \cdot 10^4$.
The probably most important aspect of figure 6.8 (b) is, however, the difference between the sphere and the plate. Although this difference is larger for $\theta = 20°$, it is also significant for $\theta = 40°$. Note, that the convergence is better at the rough sphere rather than on the smooth plate and, consequently, the inaccuracies cannot be caused by roughness. The surface tension force is calculated according to eq. (3.7). Thus, an inaccurate result might be traced back to either the three-phase contact line or the co-normal $\tilde{\boldsymbol{\mu}}_\mathrm{lg}$. However, the very good convergence of the capillary pressure force as well as the better convergence of the rough interface (sphere), imply a good estimation of the capillary bridge geometry. Moreover, the results presented in table 6.3

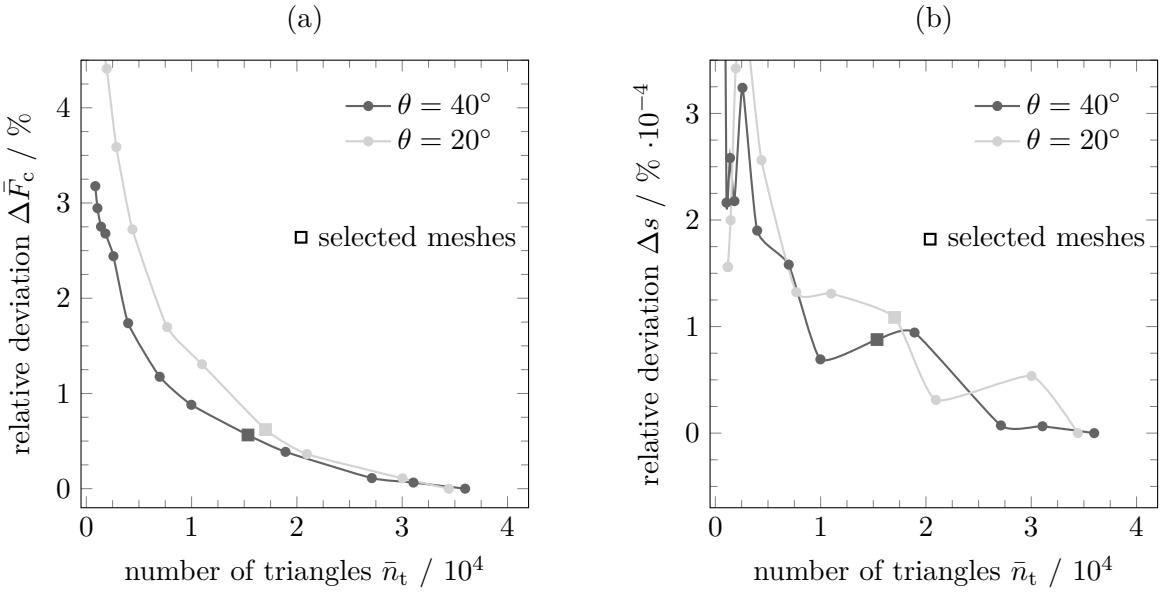

Figure 6.7.: Relative deviation of the mean capillary force (a) and the standard deviation (b) for different mesh resolutions of the distribution ($n = 1000$) of a capillary bridge between a rough sphere and a smooth plate with $\tilde{S}_\mathrm{q} = 0.005$, $\varepsilon = 0.1$, $\tilde{V} = 0.1$ and $\tilde{a} = 0.1$

show a good accordance of the three-phase contact line. Thus, it is reasonable to analyze the computation of the co-normal more in detail.

In figure 6.9 the situation at the three-phase contact line of a sphere and a plate is schematically illustrated for small and large contact angles θ. The overall geometry of the capillary force and in particular the liquid-gas interface is approximated well ($\Gamma_{\mathrm{lg,continuous}} \approx \Gamma_{\mathrm{lg,discretized}}$). This is consistent with the good convergence of all pressure related parameters. However, there is a significant deviation between the co-normal of the continuous and the discretized geometry. On the discretized level the co-normal is computed first order which means, that only the triangle directly at the three-phase contact line is considered. However, a small contact angle implies a strong bending of the capillary bridge at the contact line. Thus, the mesh resolution must be very high in order to capture this geometry. Otherwise, a deviation between the co-normals $\tilde{\boldsymbol{\mu}}_{\mathrm{lg,continuous}}$ and $\tilde{\boldsymbol{\mu}}_{\mathrm{lg,discretized}}$ results as illustrated in figure 6.9. Moreover, it is shown, that the bending is generally higher at the plate compared to the sphere. Thus, for both, the small and the large contact angle, the convergence is slower at the plate (figure 6.8 (b)).

The deviation of the continuous and the first order discretized co-normal can also be interpreted as an overestimation of the effective contact angle $\theta_{\mathrm{discretized}}$. In fact, the contact angle is not explicitly claimed as a boundary condition by the algorithm. Instead, the dimensionless adhesion coefficient β (eq. (5.3)) is implemented which is,

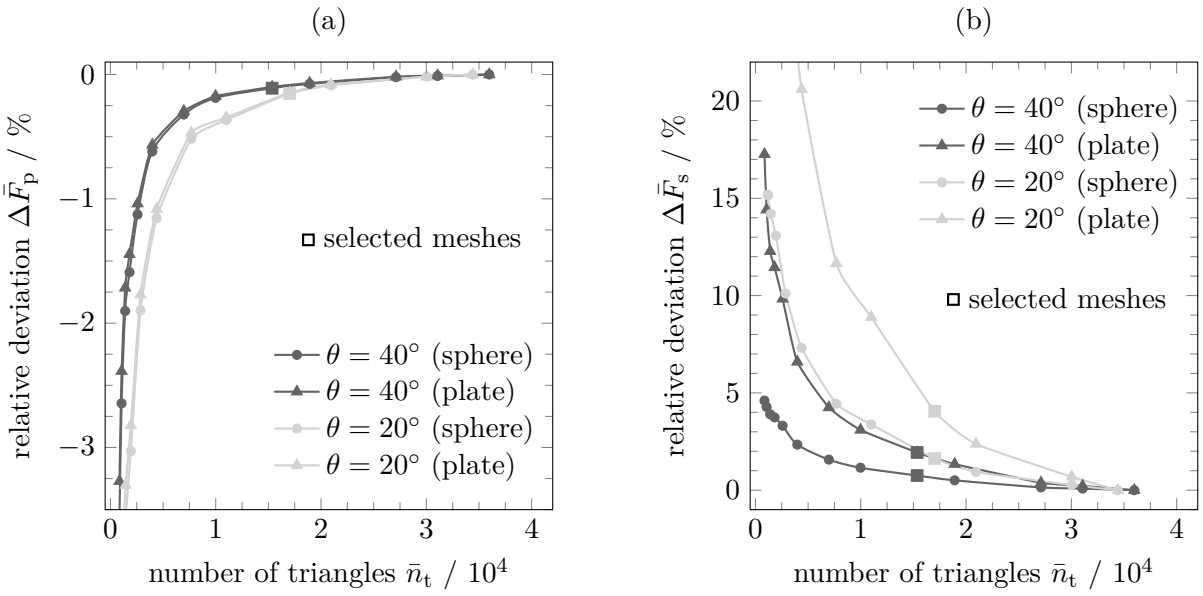

Figure 6.8.: Relative deviation of the capillary pressure force (a) and the surface tension force (b) for different mesh resolutions of the distribution ($n = 1000$) of a capillary bridge between a rough sphere and a smooth plate with $\tilde{S}_{\mathrm{q}} = 0.005$, $\varepsilon = 0.1$, $\tilde{V} = 0.1$ and $\tilde{a} = 0.1$

strictly speaking, a relation between the liquid-gas and the liquid solid interface, i.e., Γ_{lg} is rated as one and $\Gamma_{\mathrm{ls,i}}$ is rated as $-\beta_{\mathrm{i}}$. In a continuous setting this relation can be interpreted as a contact angle. Consequently, $\beta_{\mathrm{i}} = \cos(\theta_{\mathrm{i}})$ is only valid for $n_{\mathrm{t}} \to \infty$. From a physical perspective an increasing contact angle is usually associated with a decreasing capillary force. This is, however, a comparison of two completely different capillary bridges, i.e., the whole bridge geometry changes. Here, it is only an overestimation of the contact angle while keeping all other parameters, such as the contact line or the capillary pressure, constant. In an axisymmetric case the surface tension force is given by the second addend of eq. (3.8) with $\cos(\alpha) = \sin(\psi + \theta)$ and $\cos(\alpha) = \sin(\theta)$ directly on the three-phase contact line of a sphere and plate, respectively. Thus, it becomes clear, that in the wetting case a larger contact angle leads to an overestimation of the surface tension force if all other parameters are constant. Overall, there is a relatively good convergence of the capillary bridge geometry during the iteration, whereas an accurate first order evaluation of the co-normal μ requires a much higher convergence. This problem significantly increases with a decreasing contact angle. However, from figure 6.7 it follows, that for $\theta = 20°$ the numerical error is only slightly increase. Nevertheless, from the comparison with the Dörmann model (section 6.1) it is concluded that the numerical error significantly increases for $\theta < 20°$. Thus, the very few simulations that are performed with $\theta = 10°$ have to be considered with a 2 % higher numerical error of the capillary force. In section 8.3.1 possible solutions for a more accurate calculation of the co-normal are discussed.

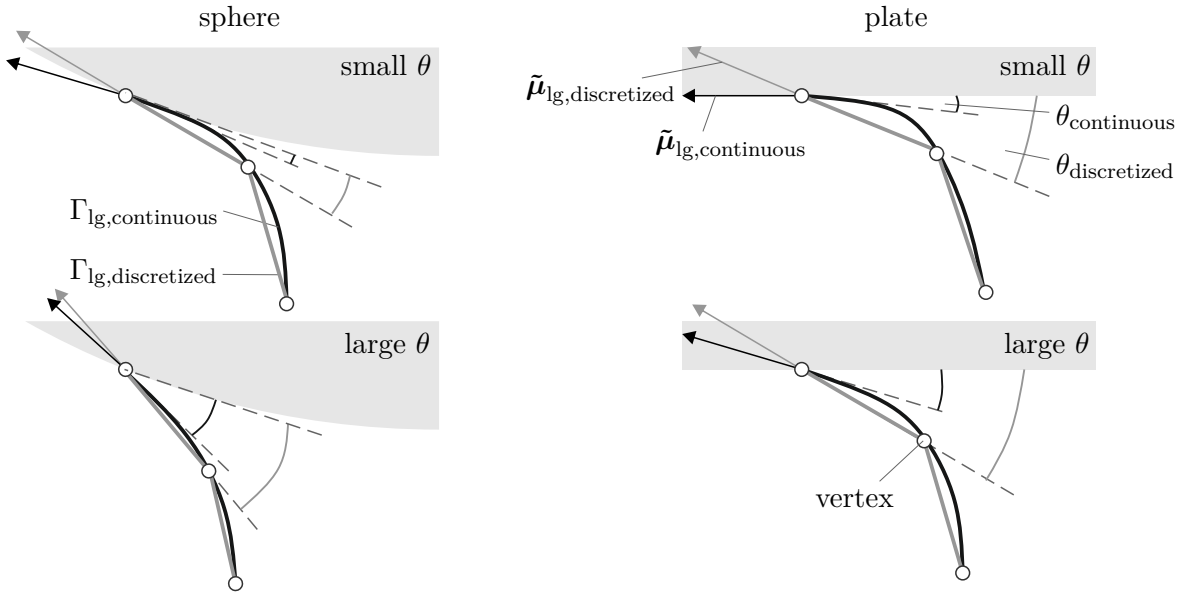

Figure 6.9.: Deviation between the continuous co-normal $\tilde{\boldsymbol{\mu}}_{\mathrm{lg,continuous}}$ and the first order discretized co-normal $\tilde{\boldsymbol{\mu}}_{\mathrm{lg,discretized}}$

In addition to the sphere-plate system the mesh convergence is analyzed for a sphere-sphere system. For this investigation the volume is kept constant at $\tilde{V} = 0.05$ and the roughness of the solid interfaces is varied. In particular, the RMS values are chosen to be $\tilde{S}_{1\backslash 2} = 0\backslash 0$, $\tilde{S}_{1\backslash 2} = 0.002\backslash 0$, $\tilde{S}_{1\backslash 2} = 0.007\backslash 0$ and $\tilde{S}_{1\backslash 2} = 0.005\backslash 0.005$. Thus, the first system is the completely smooth system, i.e., a single capillary bridge. The second and third systems are composed by a smooth and a rough sphere and the fourth system consists of two equally rough spheres. The sample size of all rough systems is again $n = 1000$. In order to avoid any kind of symmetry the random seed number ξ is always different on the two rough spheres. The diffusion coefficient is $\varepsilon = 0.1$ for all rough spheres and the contact angles and gap distances are $\theta = 40°$ and $\tilde{a} = 0.05$, respectively.

In figure 6.10 (a) the relative deviation of the mean capillary force $\bar{F}_\mathrm{c}$ and the most accurate solution $\bar{F}_\mathrm{c,ma}$ is presented. All three curves show a monotone and asymptotic decrease with an increasing number of triangles $\bar{n}_\mathrm{t}$. Note, that again not all simulations converged with a rate of 98 %. In particular, the highest mesh resolutions of $\tilde{S}_{1\backslash 2} = 0.007\backslash 0$ has a convergence rate of 97 % and for $\tilde{S}_{1\backslash 2} = 0.005\backslash 0.005$ the two highest mesh resolutions have convergence rates of 97 % and 96 %, respectively. The increasing number of unconverged simulation with an increased mesh resolution is traced back to the required positive definition of the Hessian (eq. (5.22)). With both, an increasing number of triangles and an increasing number of mesh cells, the

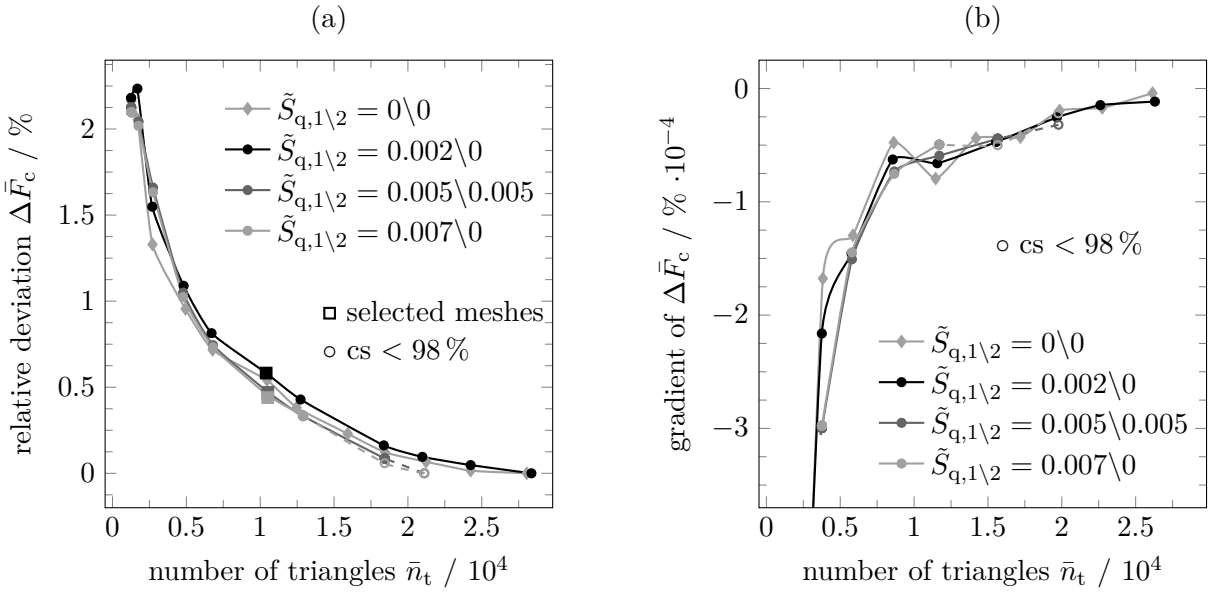

Figure 6.10.: Relative deviation of the mean capillary force (a) and the corresponding gradient (b) for different mesh resolutions of the distribution (1000 samples) of a capillary bridge between two equally sized spheres with $\tilde{V}_\mathrm{q} = 0.05$, $\varepsilon = 0.1$, $\theta = 40°$ and $\tilde{a} = 0.05$

positive definition slowly deteriorates which might finally lead to an abortion of the simulation.

The differences between the curves illustrated in figure 6.10 (a) are minor which means, that the RMS $\tilde{S}_\mathrm{q}$ does not have a significant influence on the mesh convergence of the mean capillary force. In fact, even the completely smooth system convergences analogous to all three rough systems. The two curves with the higher roughness, i.e, $\tilde{S}_{1\backslash 2} = 0.005\backslash 0.005$ and $\tilde{S}_{1\backslash 2} = 0.007\backslash 0$, are slightly below the low roughness curve ($\tilde{S}_{1\backslash 2} = 0\backslash 0$ and $\tilde{S}_{1\backslash 2} = 0.002\backslash 0$). This is traced back to the lower mesh resolution of the most accurate solution which leads to a downshifting of the curves. It is very reasonable to assume, that the high roughness curves are shifted up and agree with the low roughness curves if values for higher resolved meshes are added. This is supported by the high agreement of the gradients of $\Delta\bar{F}_\mathrm{c}$ (figure 6.10 (b)), that are independent of the most accurate solution. Thus, the numerical error of the mean capillary force is independent of roughness and evaluated for an arbitrary configuration in figure 6.10. Thus, the best converged simulations, that are $\tilde{S}_{1\backslash 2} = 0\backslash 0$ and $\tilde{S}_{1\backslash 2} = 0.002\backslash 0$, are used. In particular, the absolute values of the gradient between the two highest mesh resolutions are 0.04 % and 0.12 % per 10^4 triangles. For a conservative estimation the higher gradient is used to evaluate the deviation between the most accurate and the exact solution. Moreover, a doubled mesh resolution, i.e., roughly $3 \cdot 10^4$ triangles, are considered. The relative deviation of the mean capillary force $\Delta\bar{F}_\mathrm{c}(\bar{n}_\mathrm{t,se})$ is taken

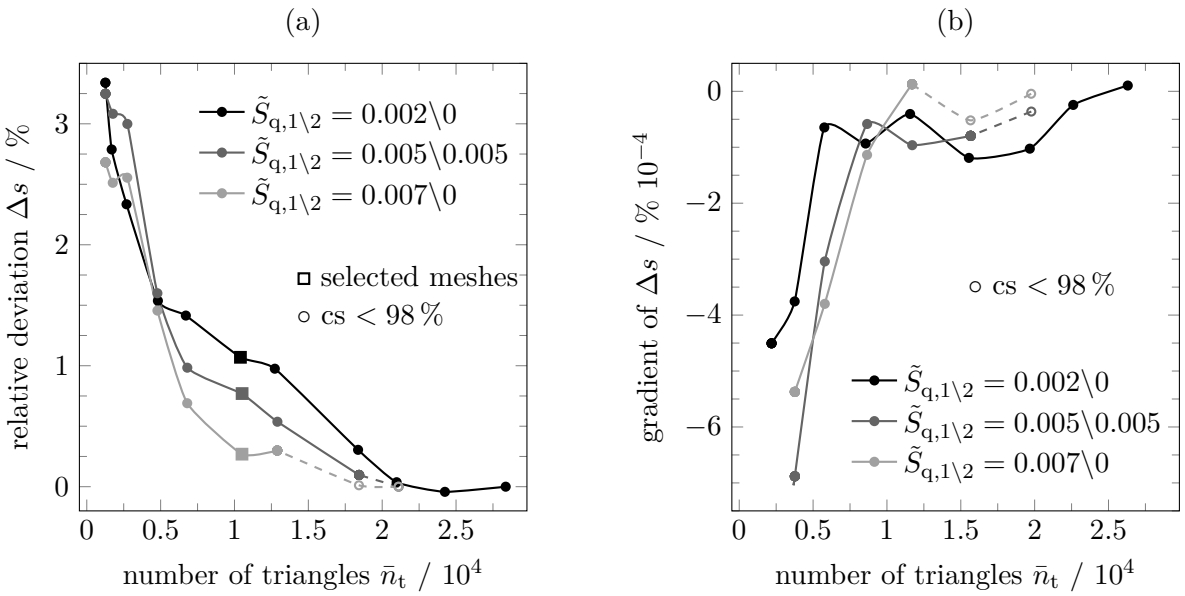

Figure 6.11.: Relative deviation of the standard deviation (a) and the corresponding gradient (b) for different mesh resolutions of the distribution (1000 samples) of a capillary bridge between two equally sized spheres with $\tilde{V} = 0.05$, $\varepsilon = 0.1$, $\theta = 40°$ and $\tilde{a} = 0.05$

from figure 6.10 (a), i.e., 0.6 %. Finally, this leads to a total numerical error of 0.96 % for $\tilde{S}_{1\backslash 2} = 0.002\backslash 0$. In order to ensure a conservative limit for all three curves, the numerical error of the mean capillary force is roughly estimated to be below 1 %. The selected meshes correspond to a remesh resolution factor of 0.02 for all rough simulations.

The relative deviation of the standard deviation Δs is plotted in figure 6.11 (a). Note, that only rough systems are considered, since there is no distribution of the capillary force in a smooth system. All curves decrease with an increasing mesh resolution. The results indicate a faster convergence of $\tilde{S}_{1\backslash 2} = 0.005\backslash 0.005$ and $\tilde{S}_{1\backslash 2} = 0.007\backslash 0$ compared to $\tilde{S}_{1\backslash 2} = 0.002\backslash 0$. However, this is again traced back to the lower resolution of the most accurate solution that leads to a downshifting of the curves. Although the curves are not as similar as the curves of the relative deviation $\Delta \bar{F}_\mathrm{c}$ (figure 6.10 (a)), it is reasonable to assume that the convergence curves of Δs are closer to each other if a more accurate solution could be obtained for $\tilde{S}_{1\backslash 2} = 0.005\backslash 0.005$ and $\tilde{S}_{1\backslash 2} = 0.007\backslash 0$. Therefore the numerical error is again estimated conservatively for $\tilde{S}_{1\backslash 2} = 0.002\backslash 0$ and it is assumed that the order of magnitude is also valid for the higher roughness, i.e., the influence of roughness on the numerical accuracy of the standard deviation s is assumed to be minor.

The gradients of Δs are illustrated in figure 6.11 (b). All gradients approach zero with an increased number of triangles. Nevertheless, the curves do not monotonically increase and, therefore, analogously to the sphere-plate system, the last three gradients are considered for the estimation of the exact solution. For $\tilde{S}_{1\backslash 2} = 0.002\backslash 0$ and average of 0.46 % per $\cdot 10^4$ triangles is obtained. The threefold of this value is again added to the relative deviation $\Delta s(\bar{n}_\mathrm{t})$ of the selected mesh, i.e., 1.1 %. Finally, a total estimated numerical error of 2.48 % or roughly 2.5 %, is obtained. In this section, a sample size of $n = 1000$ is a priori set. Subsequently, this sample number is discussed with respect to the statistical error.

6.3. Statistical error

The simulation of capillary forces between rough interfaces requires a statistical analysis, since the same roughness can be realized by an infinite number of interfaces. Thus, the result of a rough simulation is a distribution of the capillary force that is described by parameters such as the mean capillary force $\bar{F}_\mathrm{c}$ and the standard deviation s of the sample. However, these values depend on the specific sample and differ from the expected value $\mu_{\bar{\mathrm{F}}_\mathrm{c}}$ and the standard deviation $\sigma_{\bar{\mathrm{F}}_\mathrm{c}}$ of the whole population. The deviation is strongly influenced by the number of simulations n, i.e., for $n \to \infty$

it follows that $\bar{F}_c \to \mu_{\bar{F}_c}$ and $s \to \sigma_{\bar{F}_c}$. Therefore, a statistical analysis is performed in order to define the size of a sample, i.e., the number of simulations n, that is sufficiently large to obtain a small statistical error.
Again, the analysis is performed for both, a sphere-plate and a sphere-sphere system. However, a detailed statistical investigation requires a huge number of simulations and is consequently expensive with respect to computational time. Thus, the variation of parameters is very limited. Generally, it is assumed that the parameters of the capillary bridge, i.e., volume $\tilde{V}$, contact angle θ and gap distance $\tilde{a}$, have a minor effect on the statistical error. In contrast, the influence of roughness is unclear, i.e., it is possible that the statistical error increases with the roughness. Thus, the detailed analysis that is used to finde a sample number n is performed for a single sphere-plate and sphere-sphere configuration and the influence of the other parameters is investigated subsequently for the defined sample number. In particular, the RMS values of the sphere-plate system is set to $\tilde{S}_q = 0.005$ at the sphere and zero at the plate. This is the main configuration of a sphere-plate system that is investigated in section 7.1. For the sphere-sphere system the roughness is varied more intensively as described in section 7.2. Thus, in order to find an upper limit for the statistical error, a very high roughness, i.e., $\tilde{S}_{1\backslash 2} = 0.005\backslash 0.005$, is used for the analysis of the sphere-sphere system.
In figure 6.12 the box plots of the capillary force of a sphere-plate system with $\tilde{V} = 0.1$, $\tilde{S}_q = 0.005$, $\varepsilon = 0.1$, $\theta = 40°$ and $\tilde{a} = 0.1$ are shown. The size of the samples is set to $n = 100$, 500 and 1000. The box plots within one diagram only differ by the random seeds ξ, i.e., the concrete realization of the rough interface with the desired roughness of $\tilde{S}_q = 0.005$. Analogous to the mesh analysis, the results are presented relative to the most accurate solution (eq. (6.5)) which is in this case the mean capillary force $\bar{F}_c$ of a simulation with $n = 10000$ samples. Again, this is only the most accurate solution that could be obtained, rather than the exact solution which corresponds to the mean of the whole population μ. The box plots are generated using the following conventions:

- box ends: 25^{th} and 75^{th} percentile (1^{st} and 3^{rd} quartile)
- whiskers: 1^{st} and 99^{th} percentile
- mid line: 50^{th} percentile (median)
- cross marker: mean

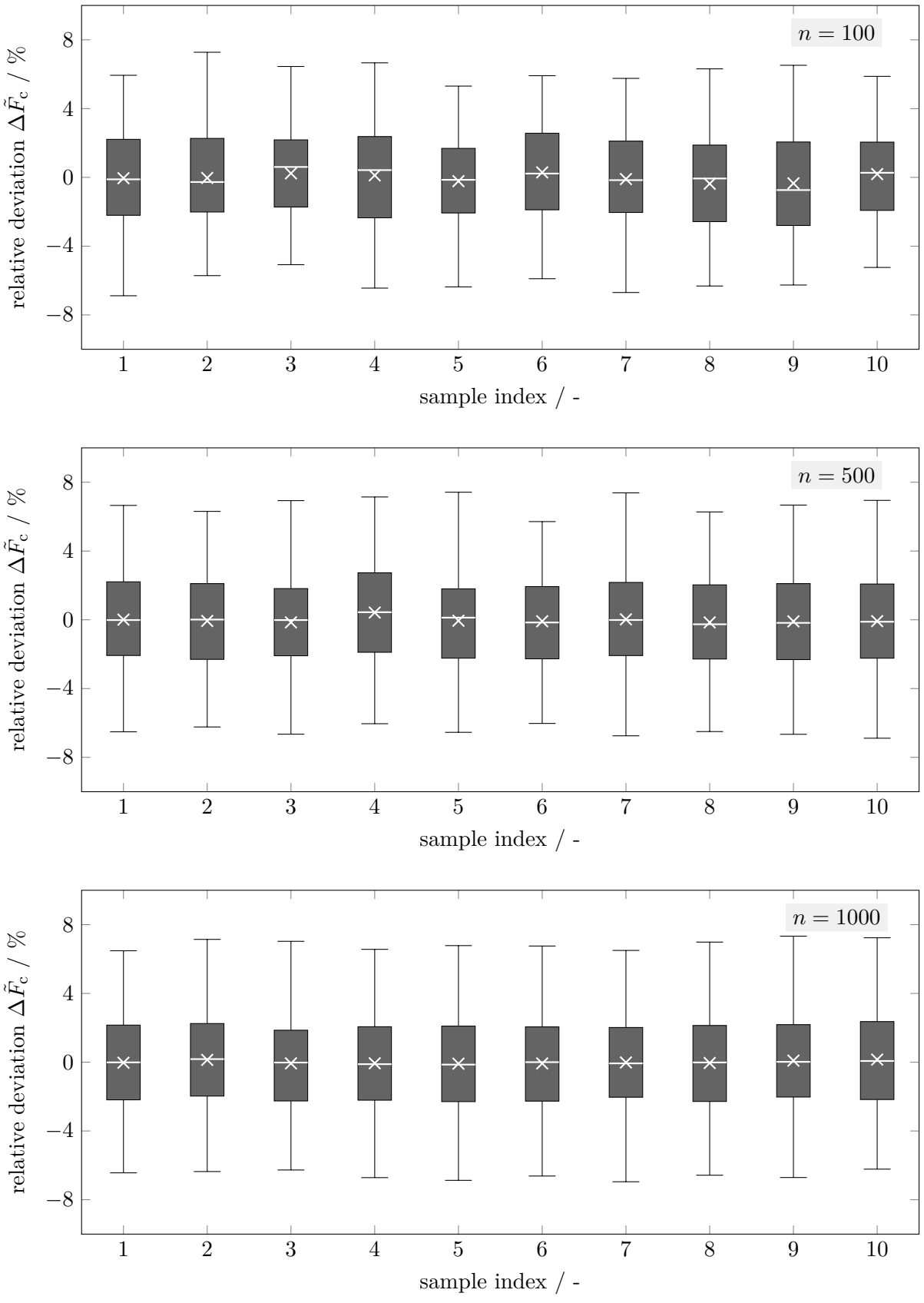

Figure 6.12.: Distributions of the relative capillary force of capillary bridges between a rough sphere and a smooth plate with $\tilde{V} = 0.1$, $\tilde{S}_q = 0.005$, $\varepsilon = 0.1$, $\theta = 40°$ and $\tilde{a} = 0.1$

It is worth mentioning, that, strictly speaking, only the relative deviation of the mean value (cross marker) is a deviation in terms of $\Delta\bar{F}_\mathrm{c} \to 0$ for $n \to \infty$. Of course, the distribution (e.g. the whiskers) will not approach zero for an infinite number of samples. Nevertheless, they are plotted relative to the most accurate solution in this section, since their absolute value is irrelevant for the statistical analysis. Instead, for a sufficiently large sample size they should approach each other. Figure 6.12 shows that with an increasing sample size n the variations between the box plots decrease. For $n = 100$ samples the whiskers show a significant fluctuation. Generally, they are very sensitive and strongly influenced by just a few simulations, since they represent 98 % of the distribution. In fact, for $n = 100$ only the lowest and the largest value are not considered in the box plot. However, also the boxes, i.e., the middle 50 % of the distribution significantly deviate from each other. Moreover, the mean capillary force $\bar{F}_\mathrm{c}$ and the median of $\tilde{F}_\mathrm{c}$ are not equal. Of course, this cannot be assumed a priori, however, the distributions are expected to approach a normal distribution as discussed in section 7.1. Moreover, in figure 6.12 it is shown, that the the mean and median approach each other with an increasing sample number. In particular, the mean differences between the two values are 0.0098 ($n = 100$), 0.0037 ($n = 500$), 0.0026 ($n = 1000$) and 0.0007 ($n = 10000$). Thus, increasing the sample size by a factor of 10 leads to a one order of magnitude smaller difference between $\bar{F}_\mathrm{c}$ and the median of $\tilde{F}_\mathrm{c}$.

For $n = 500$ there is still a significant fluctuation in both, the whiskers and the boxes. For example, the 75^{th} percentile of the 3^{rd} and 4^{th} sample index differ by approximately 1 %. For $n = 1000$ the distributions seem to be relatively stable. There are still fluctuations, especially between the sensitive whiskers, however, the upper and lower quartile seem to be sufficiently accurate. Subsequently, a confidence analysis is presented in order to quantify the statistical uncertainty for the mean capillary force $\tilde{F}_\mathrm{c}$ and the standard deviation s or the sample.

For a normally distibuted parameter u, the mean values $\bar{u}$ are also normally distributed. Thus, the symmetric confidence interval is given by

$$P(\mathrm{CI}_{\bar{\mathrm{u}},u}(\gamma) < \mu_\mathrm{u} < \mathrm{CI}_{\bar{\mathrm{u}},v}(\gamma)) = P\left(\bar{u} - \xi(\gamma)\frac{\sigma_\mathrm{u}}{\sqrt{n}} < \mu_\mathrm{u} < \bar{u} + \xi(\gamma)\frac{\sigma_\mathrm{u}}{\sqrt{n}}\right) = \gamma \qquad (6.6)$$

where ξ is the standrad normal distributed value for the confidence level γ or rather for the significance level α with $\gamma = 1-\alpha$. Note, that the index u refers to the random parameter, whereas the index u indicates the left side of the confidence interval and the index v the right side, respectively. In section 7.1.1 and 7.2.1 it is demonstrated

that the capillary force $\tilde{F}_\mathrm{c}$ can considered to be normally distributed. However, since σ_u in eq. 6.6 is the standard deviations of the whole population, this value is unknown and must be estimated by the standard deviation of the sample (eq. (6.4)). Consequently, the mean capillary force follows Student's t-distribution rather than the normal distribution. However, for $n \to \infty$ Student's t-distribution approaches the normal distribution and usually for $n > 30$ the normal distribution is a reasonable approximation for the distibution of the mean values [Sto17]. Thus, for sufficently large samples, the relative width of the confidence interval of $\bar{F}_\mathrm{c}$ is defined by

$$\mathrm{CI}_{\bar{\mathrm{F}}_\mathrm{c}}(\gamma) = \frac{\mathrm{CI}_{\bar{\mathrm{F}}_\mathrm{c},v}(\gamma) - \mathrm{CI}_{\bar{\mathrm{F}}_\mathrm{c},u}(\gamma)}{\bar{F}_\mathrm{c}} \cdot 100\% = 2\frac{s\xi(\gamma)}{\bar{F}_\mathrm{c}\sqrt{n}} \cdot 100\%. \tag{6.7}$$

Note that $\mathrm{CI}_{\bar{\mathrm{F}}_\mathrm{c}}$ can directly be interpreted as the statistical uncertainty. In particular, the mean of the overall population $\mu_{\mathrm{F}_\mathrm{c}}$ is within the interval of $\pm 0.5\mathrm{CI}_{\bar{\mathrm{F}}_\mathrm{c}}$ with a probability of γ.

The results of eq. (6.7) are illustrated in figure 6.13 (a). It is shown, that the confidence interval decreases with a decreasing confidence level γ. For this work, a confidence level of $\gamma = 98\,\%$ is chosen and discussed subsequently. From figure 6.13 (a) it follows, that with a probability of 98 % the mean capillary force is within an interval significantly below 1 % or $\pm 0.5\,\%$ for all sample sizes. Even for $n = 100$, which is not plotted, $\mathrm{CI}_{\bar{\mathrm{F}}_\mathrm{c}}(98\,\%) = 1.31\,\%$. Since this is already the order of magnitude of

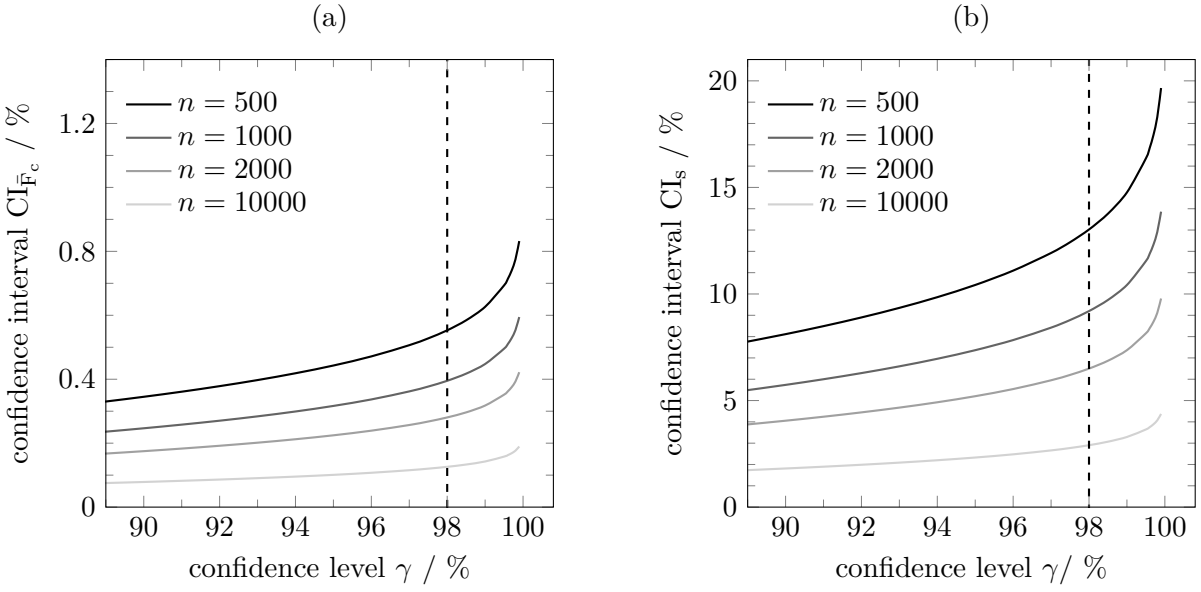

Figure 6.13.: Relative CI of the mean capillary force $\mathrm{CI}_{\bar{\mathrm{F}}_\mathrm{c}}$ (a) of a rough sphere and a smooth plate with $\tilde{V} = 0.1$, $\tilde{S}_\mathrm{q} = 0.005$, $\varepsilon = 0.1$, $\theta = 40°$ and $\tilde{a} = 0.1$ and the general relative CI of the standard deviation CI_s (b)

the numerical error, a sample size between $n = 100$ and $n = 500$ might already be sufficient with respect to the statistical uncertainty of the mean capillary force. With an increasing sample number the confidence interval reduces to $\mathrm{CI}_{\bar{\mathrm{F}}_\mathrm{c}}(98\,\%) = 0.40\,\%$ for $n = 1000$ and $\mathrm{CI}_{\bar{\mathrm{F}}_\mathrm{c}}(98\,\%) = 0.13\,\%$ for $n = 10000$. Both intervals are already very small. However, it must be considered that reducing the statistical uncertainty by a factor of approximately 3, i.e., from 0.40 % to 0.13 %, implies ten times more samples and consequently a tenfold computational time. Overall, a statistically uncertainty of 1 % of the mean capillary force seems to be sufficient and therefore, a sample size between $n = 100$ and $n = 500$ is chosen. However, this sample size must also be large enough for an acceptable uncertainty of the standard deviation which is analyzed subsequently.

The expression $s_\mathrm{u}^2 \left((n-1)\sigma_\mathrm{u}^2\right)^{-1}$ of a random parameter u is chi-squared distributed with $n-1$ degrees of freedom and therefore, the confidence interval for the standard deviation is given by

$$P(\mathrm{CI}_{\mathrm{s_u},u}(\gamma) < \sigma_\mathrm{u}^2 < \mathrm{CI}_{\mathrm{s_u},v}(\gamma)) = P\left((n-1)\frac{s_\mathrm{u}^2}{\chi_u^2(\gamma)} < \sigma_\mathrm{u}^2 < (n-1)\frac{s_\mathrm{u}^2}{\chi_v^2(\gamma)}\right) = \gamma. \quad (6.8)$$

Since the chi-squared distribution is not symmetric the lower and upper lower quantiles, $\chi_u^2(\gamma)$ and $\chi_v^2(\gamma)$, are not equal. Using eq. (6.8) the relative width of the confidence interval for the standard deviation of the capillary force

$$\mathrm{CI_s} = \frac{\mathrm{CI}_{\mathrm{s},v}(\gamma) - \mathrm{CI}_{\mathrm{s},u}(\gamma)}{s} \cdot 100\% = \sqrt{n-1}\left(\sqrt{\frac{1}{\chi_v^2(\gamma)}} - \sqrt{\frac{1}{\chi_u^2(\gamma)}}\right) \cdot 100\% \quad (6.9)$$

is derived. Remarkably, this equation is independent of the standard deviation s, which means that the relative statistical uncertainty of the standard deviation is independent of the physical system. In particular, roughness does not influence statistical uncertainty of the standard deviation although the absolute value of the standard deviation significantly increases with roughness (chapter 7). This is different for the mean capillary force as indicated by eq. (6.7) and discussed later.

In figure 6.13 (b) the relative confidence interval of the standard deviation is presented. Note, that the distribution of the sample standard deviation is asymmetric and therefore, the upper and lower limits of the confidence interval are not simply given by $0.5 \cdot \mathrm{CI_s}$. However, with an increasing sample number or a decreasing confidence level γ the intervals approach each other. From the different scaling of the y-axis it directly becomes clear that the uncertainty of the sample standard deviation s is much higher compared to the mean capillary force $\bar{F}_\mathrm{c}$. The suggested sample sizes in the range of

$n = 100$ to $n = 500$ lead to confidence intervals of $\mathrm{CI_s}(98\,\%) = 29.64\,\%$ (not illustrated in figure 6.13 (b)) and $\mathrm{CI_s}(98\,\%) = 13.03\,\%$, respectively. Thus, even for $n = 500$ the uncertainty is above 10 %, which is considered to be too high. To obtain a confidence interval below 5 % with a confidence level of $\gamma = 98\,\%$ approximately 3000 samples are required. However, this exceeds the available computational resources and, hence, a sample number of $n = 1000$ is the maximum number that can be considered in this work. Thus, the statistical uncertainty of the standard deviation of the sample is $\mathrm{CI_s}(98\,\%) = 9.20\,\%$ with a lower confidence interval of $\mathrm{CI_{s,}}_u(98\,\%) = -4.44\,\%$ and an upper confidence interval of $\mathrm{CI_{s,}}_v(98\,\%) = +4.76\,\%$, respectively.
Overall, a sample number of $n = 1000$ is obtained from the analysis of the mean capillary force and the standard deviation. Using this sample number, the influence of the volume $\tilde{V}$ and the contact angle θ on the statistical uncertainty of the mean capillary force $\bar{F}_\mathrm{c}$ is investigated. In figure 6.14 the relative confidence intervals $\mathrm{CI}_{\bar{\mathrm{F}}_\mathrm{c}}$ for different volumes (a) and contact angles (b) are illustrated. It is shown, that the confidence interval increases with a decreasing volume. For the lowest volume of $\tilde{V} = 0.01$ a confidence interval of $\mathrm{CI}_{\bar{\mathrm{F}}_\mathrm{c}}(98\,\%) = 1.06\,\%$ is obtained. However, this is still around 1 % and significantly below 0.5 % for all other volumes, which is excellent. The differences are traced back to the factor $s \cdot \bar{F}_\mathrm{c}^{-1}$ (eq. (6.7)). In particular, from $\tilde{V} = 0.01$ up to $\tilde{V} = 0.1$ the capillary force increases by a factor of 3 and the standard deviation of the sample by a factor of 1.11. With a further increase of the volume

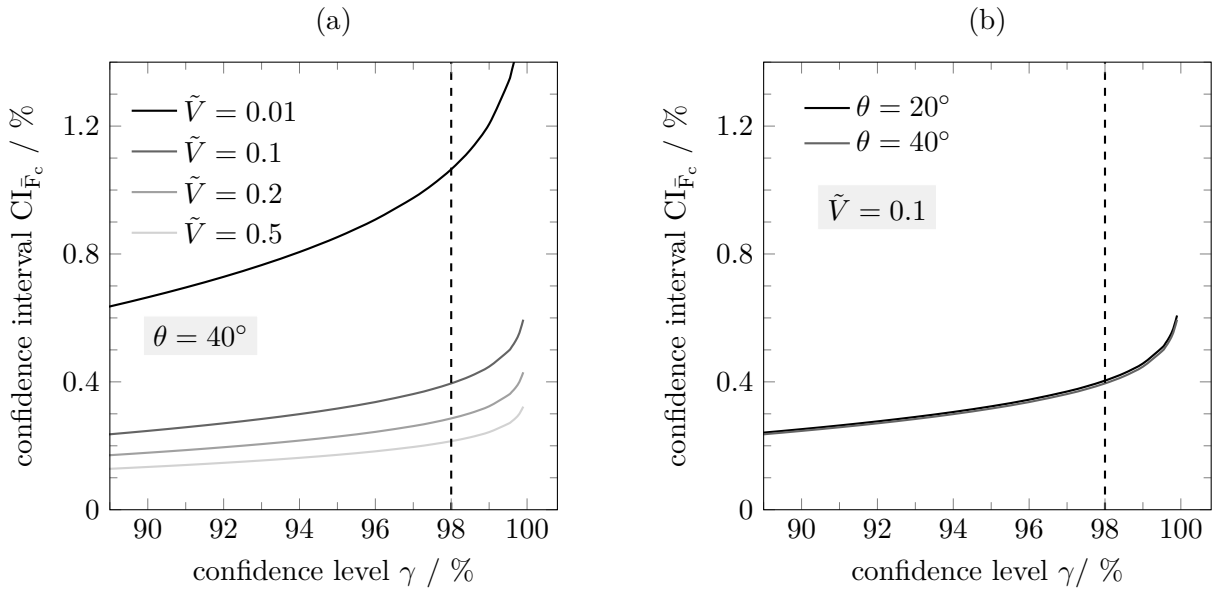

Figure 6.14.: Relative CI of the mean capillary force $\mathrm{CI}_{\bar{\mathrm{F}}_\mathrm{c}}$ of a rough sphere and a smooth plate with $\tilde{S}_\mathrm{q} = 0.005$, $\varepsilon = 0.1$ and $\tilde{a} = 0.1$ for different volumes (a) and contact angles (b) and $n = 1000$ samples

the standard deviation of the sample even decreases whereas the capillary force still increases. Thus, the different uncertainties of the volumes are dominated by the mean capillary force, which increases with the volume.
In figure 6.14 (b) it is illustrated that the contact angle θ does not influence the confidence interval of the mean capillary force. Interestingly, the mean capillary force and the standard deviation of the sample decrease with the same factor with an increasing contact angle. Thus, the factor $s \cdot \bar{F}_c^{-1}$ (eq. (6.7)) is approximately constant which leads to a contact angle independent confidence interval for the mean capillary force. Note, that the behavior of the absolute values of the capillary force and the standard deviation of the sample is discussed more in detail in chapter 7. Subsequently, the influence of the geometry and roughness are investigated by considering different RMS values $\tilde{S}_q$ for a sphere-sphere system.
The analysis of the sphere-plate system already revealed that the relative statistical uncertainty of the standard deviation of the sample, i.e., the confidence intervals CI_s are independent of the physical system. Thus, the results are also valid for the sphere-sphere system and different RMS values and must not be investigated again. Thus, only the confidence intervals of the mean capillary force CI_{F_c} are considers in this section. In particular, equally sized spheres with $\tilde{S}_{q,1\backslash 2} = 0.005\backslash 0.005$, $\tilde{S}_{q,1\backslash 2} = 0.002\backslash 0$ and $\tilde{S}_{q,1\backslash 2} = 0.007\backslash 0$ are analyzed. The volume, the contact angle and the gap distance are kept constant at $\tilde{V} = 0.05$, $\theta = 40°$ and $\tilde{a} = 0.05$. Moreover, the diffusion coefficient ε is set to 0.1.
In figure 6.15 the box plots of the sphere-sphere system with $\tilde{S}_{q,1\backslash 2} = 0.005\backslash 0.005$ are shown. Compared to figure 6.12 the boxes and the whiskers are a lot larger which is traced back to the higher roughness. This, however, does not necessarily imply a higher statistical inaccuracy. Again, the box plots significantly differ for $n = 100$ and even for $n = 500$. For $n = 1000$ the boxes approach each other although slight differences can still be identified. This is consistent with the confidence analysis of the standard deviation of the sample (figure 6.13 (b)) that shows, that $n = 1000$ is a lower limit if CI_s should be below 10 %. Again, it is shown that the mean and the median of the capillary force distribution approach each other, i.e., the mean differences are 0.0090 ($n = 100$), 0.0068 ($n = 500$), 0.0064 ($n = 1000$) and 0.0054 ($n = 10000$). For $n > 100$ the values are higher compared to the sphere-plate system which is, however, traced back to the higher roughness of the sphere-sphere system.
The corresponding confidence analysis is illustrated in figure 6.16 (a). Again it observed, that for $n = 500$ a confidence interval of $CI_{\bar{F}_c}(98\%) = 0.88$ is obtained, which would already be sufficiently accurate. However, the sample size is mainly determined

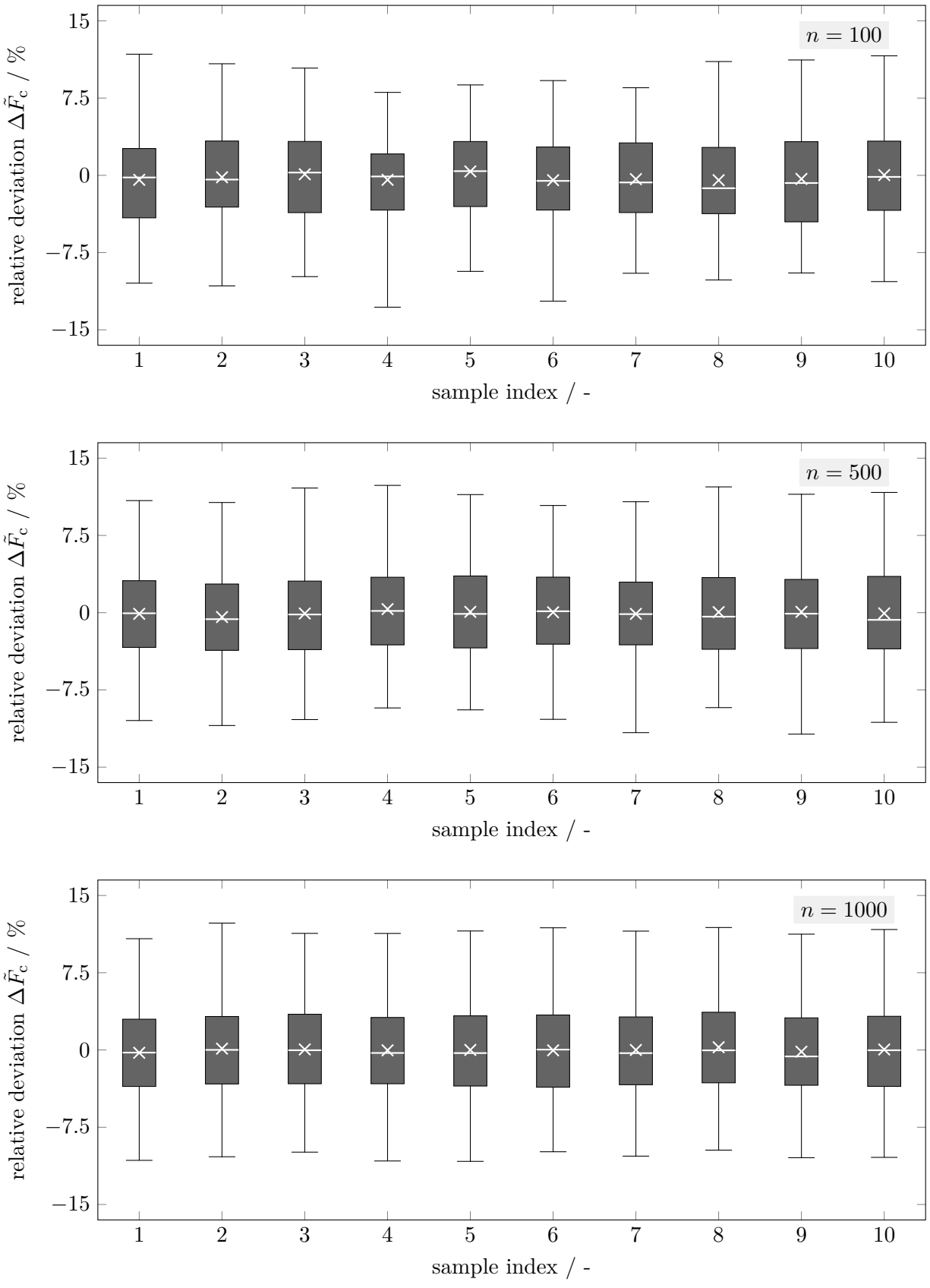

Figure 6.15.: Distributions of the relative capillary force of capillary bridges between two equally rough spheres with $\tilde{V} = 0.05$, $\tilde{S}_{q,1\backslash 2} = 0.005\backslash 0.005$, $\varepsilon = 0.1$, $\theta = 40°$ and $\tilde{a} = 0.05$

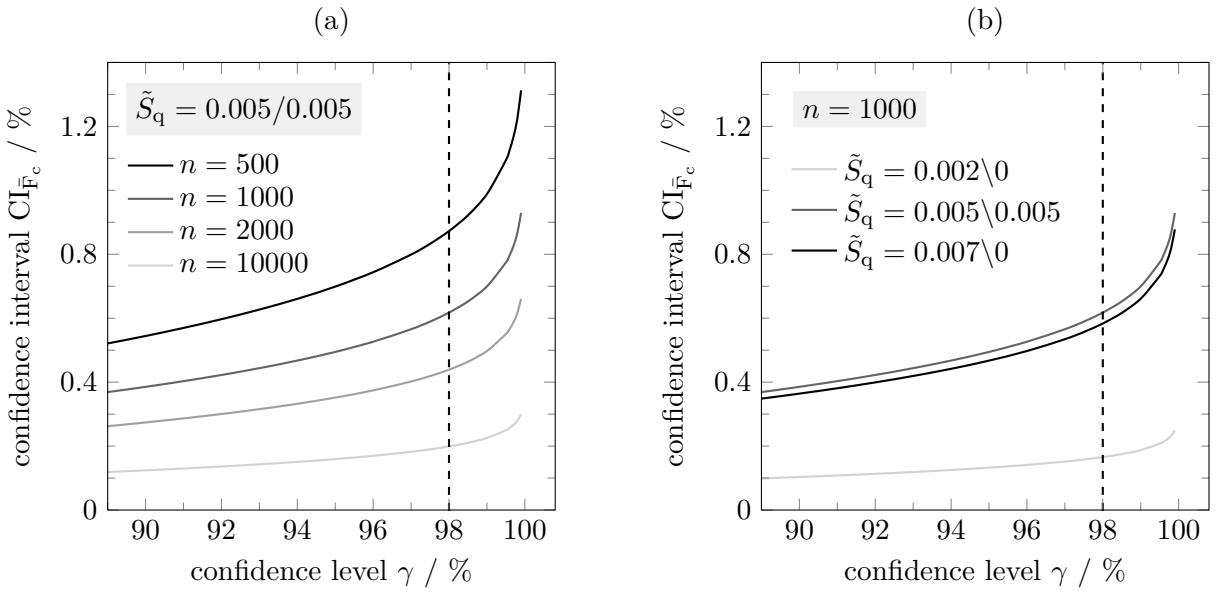

Figure 6.16.: Relative CI of the mean capillary force $\mathrm{CI}_{\bar{F}_c}$ (a) between two equally rough spheres with $\tilde{V} = 0.05$, $\tilde{S}_{q,1\backslash 2} = 0.005\backslash 0.005$, $\varepsilon = 0.1$, $\theta = 40°$ and $\tilde{a} = 0.05$ and differently rough spheres for $n = 1000$ (b)

by the confidence interval of the standard deviation and consequently $n = 1000$ is chosen.

The confidence intervals of the sphere-sphere system are very similar compared to the sphere-plate system (figure 6.13 (a)) which is most probably based on the higher roughness. This is supported by figure 6.16 (b), where the influence of roughness is presented for the sphere-sphere system. It is illustrated, that the difference between $\tilde{S}_{q,1\backslash 2} = 0.005\backslash 0.005$ and $\tilde{S}_{q,1\backslash 2} = 0.007\backslash 0$ is minor, whereas the confidence interval of $\tilde{S}_{q,1\backslash 2} = 0.002\backslash 0$ is significantly lower. This can again be justified by the factor $s \cdot \bar{F}_c^{-1}$ (eq. (6.7)). On the one hand, the mean capillary force is nearly independent of the roughness. In fact, it slightly increases with roughness, which is discussed in section 7.1.3. On the other hand, an increasing roughness leads to a significantly higher standard deviation s. Thus, according to eq. (6.7), the confidence interval of the mean capillary force $\mathrm{CI}_{\bar{F}_c}$ increases with the RMS values $\tilde{S}_q$. However, even for the highest roughness considered in this work, the confidence interval of the mean capillary force is excellent, i.e., $\mathrm{CI}_{\bar{F}_c}(98\,\%) = 0.62\,\%$ for $\tilde{S}_{q,1\backslash 2} = 0.005\backslash 0.005$. Subsequently, the results of this chapter are summarized. In particular, the numerical and the statistical error are related to each other which is essential for identifying optimization potential with respect to the accuracy.

6.4. Overall error

The overall error of the simulation of capillary forces between rough particles consists of the numerical error (section 6.2) and the statistical error (section 6.3). In order to minimize the overall error of a certain parameter, it is important, to choose the simulation parameters with respect to both error types. Reducing the overall error can be done either by a higher mesh resolution (numerical error) or a higher number of samples (statistical error). Nevertheless, both options imply a non-linear increase in the computational time. Thus, it is reasonable, that the two error types have the same order of magnitude. For example, a simulation of a sphere-plate system with $\bar{n}_\mathrm{t} = 3 \cdot 10^4$ mesh cells might reduce the numerical error of the standard deviation of the sample by approximately 1 % compared to $\bar{n}_\mathrm{t} = 1.5 \cdot 10^4$ cells (figure 6.6 (a)). This, however, implies at least a quadruplication of the simulation time if a linear increase is approximately assumed. Thus, with the same computational resources, only $n = 250$ samples can be considered which leads to an increase of the statistical uncertainty from $\mathrm{CI_s}(98\%) = 9.20\,\%$ ($n = 1000$) up to $\mathrm{CI_s}(98\%) = 18.47\,\%$ ($n = 250$) (figure 6.13 (b)). Note, that $n = 250$ is not explicitly plotted in figure 6.13 (b), however, the value is directly obtained by eq. (6.9). This sample calculation illustrates that the numerical error can be reduced by a higher mesh resolution which, however, might be canceled out and even exceeded by the increase of the statistical error if the sample size must be reduced. Thus, for a given simulation time, minimizing the overall error of a certain parameter is considered as an optimization problem between mesh resolution and sample size.

Moreover, it must be considered, that the mean capillary force and the standard deviation of the sample are dominated by different errors. Subsequently, a short summary of the numerical and statistical analysis is given in order to evaluate both errors in relation to each other.

A good convergence of the mean capillary force $\bar{F}_\mathrm{c}$ is demonstrated by the mesh analysis of both, a sphere-plate and sphere-sphere system. For the sphere-plate system the influence of the volume and the contact angle is investigated. The differences between the volumes mainly result from the varying number of mesh triangles. In particular, the largest numerical error is obtained for $\tilde{V} = 0.01$. This very small capillary bridge is not simulated with more triangles, since this requires a significantly lower iteration step. For all systems and parameter configurations the numerical error leads to an overestimation of the mean capillary force which is caused by a significant overestimation of the surface tension force. The relatively inaccurate computation of the surface tension force also leads to an increase of the numerical error with

Table 6.5.: Estimated numerical errors in % for $\theta > 20°$ and the selected meshes marked in section 6.2

parameter	system	$\tilde{V} = 0.01$	$\tilde{V} = 0.05$	$\tilde{V} = 0.1$	$\tilde{V} = 0.2$	$\tilde{V} = 0.5$
$\bar{F}_c$	sphere-plate	2.6		1.2	1.3	0.8
	sphere-sphere		1.0			
s	sphere-plate	3.8		2.1	3.0	2.6
	sphere-sphere		2.5			

a decreasing contact angle. Figure 6.7 shows, that the numerical error of $\theta = 20°$ and $\theta = 40°$ has the same order of magnitude for the selected meshes. Thus, for $\theta > 20°$ the differences between the numerical errors is neglected. However, based on the comparison with the other models (section 6.1), it is expected, that the error significantly increases for $\theta < 20°$. Moreover, it is demonstrated, that roughness does not influence the numerical error of the simulation (figure 6.10). Finally, the estimated numerical errors are summarized in table 6.5 for the different volumes and $\theta > 20°$. In particular, the numerical error of the mean capillary force $\bar{F}_c$ is below 1.5 % for $\tilde{V} > 0.5$ and increases up to 2.6 % for $\tilde{V} = 0.01$.

The mesh convergence of the standard deviation of the sample s is less sharp compared to the mean capillary force. In case of the sphere-plate system the general tendency of convergence is revealed, however, there are still significant fluctuations even between the finest meshes. A better convergence of standard deviation is demonstrated for the sphere-sphere system. The estimated numerical error of the standard deviation of the sample s is below 3 % for $\tilde{V} > 0.05$. Again, a higher error is obtained for $\tilde{V} = 0.01$, i.e., 3.8 %.

The statistical analysis demonstrates excellent confidence intervals for the mean capillary force $\mathrm{CI}_{\bar{F}_c}$. The influence of the volume and the RMS value is again investigated

Table 6.6.: Estimated relative confidence intervals in % for $n = 1000$ and a confidence level of $\gamma = 98\,\%$

parameter	system				
$\bar{F}_c$	sphere-plate	$\tilde{V} = 0.01$	$\tilde{V} = 0.1$	$\tilde{V} = 0.2$	$\tilde{V} = 0.5$
		1.06	0.40	0.29	0.21
	sphere-sphere	$\tilde{S}_{q,1\backslash 2} = 0.002\backslash 0$	$\tilde{S}_{q,1\backslash 2} = 0.007\backslash 0$		$\tilde{S}_{q,1\backslash 2} = 0.005\backslash 0.005$
		0.17	0.58		0.62
s		9.20 for all configurations			

for the sphere-plate and the sphere-sphere system, respectively. The results are summarized in table 6.6. It is shown, that the relative confidence interval increases with a decreasing volume (sphere-plate) and an increasing roughness (sphere-sphere). Nevertheless, a confidence interval significantly below 1 % is obtained for all parameters except for $\tilde{V} = 0.01$, where a slightly higher interval of $\mathrm{CI}_{\mathrm{F_c}}(98\%) = 1.06\,\%$ is computed. In addition to the mean capillary force F_c the standard deviation of the sample s is analyzed. From eq. (6.9) it is directly concluded, that the relative confidence interval of the standard deviation only depends on the sample number n and the significance level γ. For $n = 1000$ a relative confidence interval of $\mathrm{CI}_\mathrm{s}(98\%) = 9.20\,\%$ is derived, which is nearly symmetric. Thus, the simulated values of the standard deviation are within an interval of approximately $-4.44\,\%$ and $+4.76\,\%$ with a confidence level of $\gamma = 98\,\%$.

Finally, the characteristics of the numerical and statistical error are considered. The numerical error is systematic, i.e., it does not lead to a bias when considering general tendencies. Instead, the overall curves are shifted up or down. In contrast, the statistical error is random. Thus, when analyzing very slight tendencies, they must be critically discussed with respect to the statistical error.

From table 6.5 and table 6.6 it becomes clear, that the mean capillary force is simulated with an excellent low overall error. The statistical error, i.e., the relative confidence interval, is approximately half of the numerical error. Since both errors are below 1.3 % for $\tilde{V} > 0.05$, this is a comparable order of magnitude. However, if, for some application, the mean capillary force has to be computed with a higher accuracy, increasing the mesh resolution is more reasonable than increasing the sample size.

The overall error of the standard deviation of the sample is clearly dominated by the statistical error. For $\tilde{V} > 0.05$ the numerical error is below 3 % which is still good. However, the confidence interval is five times as high. Thus, it is very reasonable to increase the sample size. Doubling the sample number n would lead to a confidence interval of $\mathrm{CI}_\mathrm{s}(98\%) = 6.50\,\%$, i.e., a reduction of approximately 30 %. For the given computational resources, a coarser mesh and a higher sample number might be reasonable. However, the mesh convergence of the standard deviation shows fluctuations (figure 6.6 and 6.11) rather than a monotone asymptotic convergence. Thus, with significantly coarser meshes, mesh convergence of the standard deviation cannot be ensured for all parameters. Moreover, the selected mesh should also ensure a minor influence of the contact angle (figure 6.7), i.e., for $\theta > 20°$ the numerical error should be independent of the contact angle. For coarser meshes, a more detailed

mesh analysis with respect to the contact angle is required. Moreover, the estimation of the surface tension force deteriorates with a decreasing mesh resolution. For these reasons, a relatively high and conservative mesh resolution is chosen, that, however, limits the sample size to $n = 1000$. In section 8.3.1 an improved computation of the surface tension force is presented, that allows simulations at a lower mesh resolution with, however, the same numerical error. This provides a significant potential to increase the sample number in order to reduce the statistical uncertainty of the standard deviation.

7. Capillary forces between rough interfaces

In this chapter capillary forces between rough interfaces are analyzed. A sphere-plate system and differently sized sphere-sphere systems are investigated. The numerical parameters of the simulations are discussed in the previous chapter and given in table 6.1. The remesh resolution factor is obtained by the mesh analysis (section 6.2). The sample size is set to $n = 1000$, which results from the analysis of the statistical uncertainty (section 6.3). Again, tolerance interval of 2 % unconverged simulations is accepted.
The distribution of the capillary force is described by the mean capillary force $\bar{F}_\mathrm{c}$ and the standard deviation s. Moreover, an important parameter of interest in this chapter it the relative standard deviation of the capillary force

$$\hat{s} = \frac{s}{\bar{F}_\mathrm{c}} \cdot 100\%, \tag{7.1}$$

i.e., the relative spread width around the mean value. The capillary force is investigated for two different geometries, i.e., between a rough sphere and a smooth plate (section 7.1) and two spheres (section 7.2). Several distributions are exemplarily tested for a normal distribution by qualitative (graphical) methods and a quantitative Kolmogorov-Smirnov test (section 7.1.1 and 7.2.1). For the sphere-plate system, the complex relations between the relative standard deviation and the volume, contact angle and gap distance are investigated (section 7.1.2) and, subsequently, the influence of the root mean square roughness (RMS) is considered (section 7.1.3). This is completed by a deeper analysis of the influence of the RMS in a sphere-sphere system with both spheres being rough. In particular, different RMS values are combined on equally and unequally sized spheres in order to find general relations (section 7.2.2). Finally, also the impact of the diffusion coefficient ε is presented (section 7.2.3).

7.1. Capillary forces between a rough sphere and a smooth plate

In this work, the plane is generally considered to be smooth since a rough plane shows a poor convergence. Exceptionally, in section 7.1.3 some results are presented for a rough plate combined with a smooth sphere.

7.1.1. Analysis of the capillary force distribution

In this section the distribution of the capillary force is analyzed in more detail. Generally, a normal distribution of the capillary force is expected, however, this cannot be presumed without any test. Note, that the accordance with a theoretical distribution does not influence further investigations in this work. However, it has several important implications for the development of a generalized rough capillary force model, which is discussed in section 8.2. Therefore, the system of a smooth plate and a rough sphere with $\tilde{S}_\mathrm{q} = 0.005$ and $\varepsilon = 0.1$ is investigated. The volume, contact angle and the gap distance are set to $\tilde{V} = 0.1$, $\theta = 40°$ and $\tilde{a} = 0.1$, respectively.
In figure 7.1 (a) the cumulative distribution function (CDF) of the capillary force $\tilde{F}_\mathrm{c}$ is presented. The CDF of a random parameter u is defined by

$$\mathrm{CDF}(v) = P(u \leq v), \tag{7.2}$$

where v is the function parameter. Thus, the CDF returns the probability, that u is less or equal than v, which can also be interpreted as the standardized amount of the sample that is below v. For example, from figure 7.1 (a) CDF(4.81)= 17.5 % is obtained, i.e., 17.5 % of the sample forces are below 4.81. The light gray cross marks represent the $n = 1000$ simulated values and the black line corresponds to the theoretical standard distribution. Since the difference between the two curves is

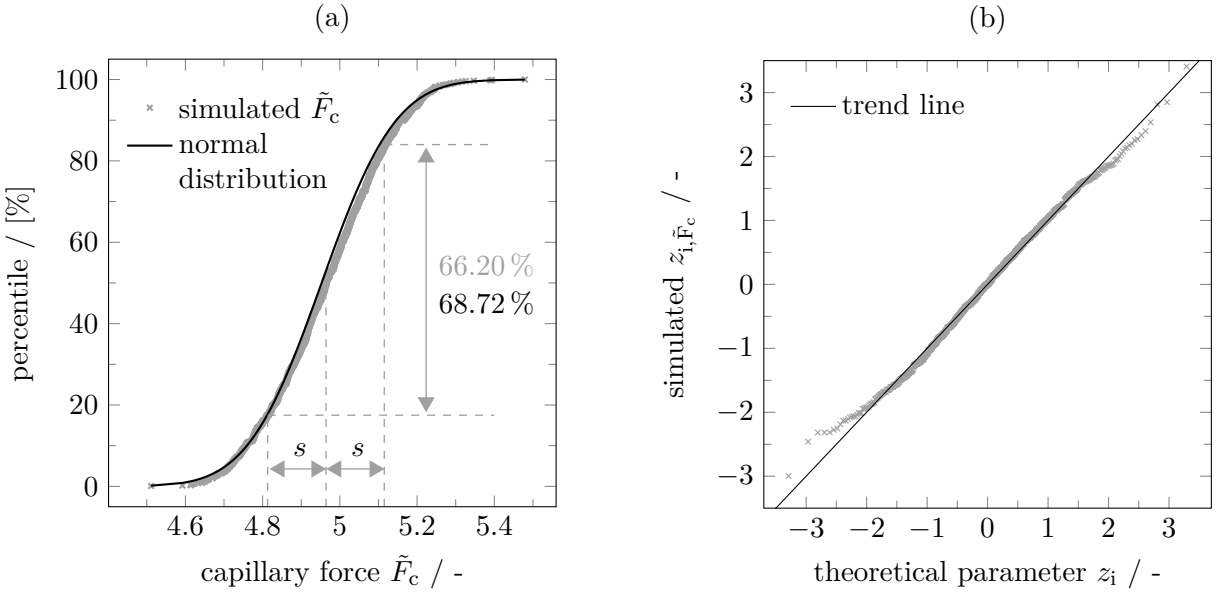

Figure 7.1.: Cumulative distribution function (left) and quantile-quantile plot (right) of the capillary force $\tilde{F}_\mathrm{c}$ between a rough sphere ($\tilde{S}_\mathrm{q} = 0.005$ and $\varepsilon = 0.1$) and a smooth plate with $\tilde{V} = 0.1$, $\theta = 40°$ and $\tilde{a} = 0.1$

marginal, a normal distribution of the simulated values of $\tilde{F}_\mathrm{c}$ is most probable. In normal distributions 68.72 % of the values are within the interval of $[\mu - \sigma, \mu + \sigma]$. For the simulated force distribution $[\bar{F}_\mathrm{c} - s, \bar{F}_\mathrm{c} + s]$ leads to an amount of 66.20 % which is relatively close to the standard distribution.
Another option for a graphical analysis of a distribution is a quantile-quantile-plot (q-q-plot). The idea is, to plot the quantiles of two distributions against each other in order to find the deviations. For a normally distributed random parameter u the standardized parameter

$$z = \frac{u - \mu_\mathrm{u}}{\sigma_\mathrm{u}} \tag{7.3}$$

is introduced, which is standard normal distributed, i.e., its expected value is $\mu_\mathrm{z} = 0$ and its standard deviation is $\sigma_\mathrm{z} = 1$. Thus, the transformation from u to z corresponds to a shifting and a distortion of the CDF. For the simulated $i = 1...n$ values of the capillary force $\tilde{F}_\mathrm{c}$

$$z_{\mathrm{i},\tilde{\mathrm{F}}_\mathrm{c}} = \frac{\tilde{F}_{\mathrm{c,i}} - \bar{F}_\mathrm{c}}{s} \tag{7.4}$$

is obtained. Note, that for a q-q-plot the $i = 1...n$ values must be sorted by size, i.e., $\tilde{F}_{\mathrm{c},0} \leq \tilde{F}_{\mathrm{c},1} \leq ... \leq \tilde{F}_{\mathrm{c,n}}$. The theoretical standard normal distributed parameter is given by

$$z_\mathrm{i} = \Phi^{-1}\left(\frac{i - 0.5}{n}\right). \tag{7.5}$$

Finally, the q-q-plot is obtained by plotting $z_{\mathrm{i},\tilde{\mathrm{F}}_\mathrm{c}}$ against the standard normal distributed z_i. The closer the simulated $z_{\mathrm{i},\tilde{\mathrm{F}}_\mathrm{c}}$ curve approximates the trend line through the origin with a gradient of 1, the more a normal distribution of $\tilde{F}_\mathrm{c}$ can be assumed. In figure 7.1 (b) the q-q-plot of the capillary force is illustrated. Again, a marginal deviation between the capillary force distribution and a normal distribution is shown. In particular, the normal distribution is approximated very well around the mean value, whereas larger deviations are observed at both sides. Nevertheless, the hypotheses of normally distributed forces is supported.
Finally, a quantitative analysis is performed since this enables an efficient check of further samples. Thus, the Kolmogorov–Smirnov test is applied, which is generally used to compare two arbitrary distributions. Consequently, this test can be utilized to test for a known distribution. The null hypothesis is, that the empirical distribution function $F_\mathrm{emp}(u)$ equals the theoretical distribution function $F_\mathrm{theo}(u)$, which is written

as $H_0 : F_{\mathrm{emp}}(u) = F_{\mathrm{theo}}(u)$. The idea of the test is, to find the maximum deviation between the these two distributions, which is given by [Sac02]

$$D = \max \left| F_{\mathrm{emp}}(u) - F_{\mathrm{theo}}(u) \right| . \tag{7.6}$$

The test statistic D is then compared to a critical value $D_{\mathrm{crit}}(\alpha)$, where α is the significance level. Finally, the null hypothesis is rejected for $D > D_{\mathrm{crit}}(\alpha)$. For $n > 35$ the critical values are given by [Sac02]

$$D_{\mathrm{crit}}(\alpha) = \sqrt{\frac{-0.5 \ln(0.5\alpha)}{n}}. \tag{7.7}$$

By applying the Kolmogorov–Smirnov test to the capillary force distribution, the null hypothesis, that the capillary force distribution is a normal distribution, i.e., $H_0 : F(\tilde{F}_{\mathrm{c}}) = \Phi(\tilde{F}_{\mathrm{c}} | \bar{F}_{\mathrm{c}}, s^2)$, is formulated. The critical value for a commonly used significance level of $\alpha = 5\,\%$ is $D_{\mathrm{crit}}(5\,\%) = 0.0429$. Note, that in the context of a hypothesis test the significance level desribes the probability for a first order error, i.e., the null hypothesis is rejected although it is actually true. A test statistic of $D = 0.0230$ is obtained for the capillary force distribution that is illustrated in figure 7.1. Since the test statistic is below the critical value, the null hypothesis is not rejected. Thus, also the quantitative test predicts a normal distribution of the capillary force.

The accordance with a normal distribution is also tested for other capillary force distributions. Thus, one parameter, i.e., the RMS $\tilde{S}_{\mathrm{q}}$, the gap distance $\tilde{a}$, the contact angel θ or the volume $\tilde{V}$, of the described base case is varied. The resulting test statistics of the Kolmogorov–Smirnov test are given in table 7.1. All values are below the critical value which suggests a normal distribution for all parameters set. For the gap distance the test statistic slightly decreases with a decreasing gap distance. The reversed relation is obtained for the RMS, the contact angle and the volume. Nevertheless, these tendencies are very small and only for the volume a clear tendency,

Table 7.1.: Test statistics of the Kolmogorov–Smirnov test for capillary force distributions with different physical parameters.
Critical value: $D_{\mathrm{crit}}(5\,\%) = 0.0429$

base	$\tilde{a}$	D	$\tilde{S}_{\mathrm{q}}$	D	θ	D	$\tilde{V}$	D
0.0230	0.004	0.0165	0.002	0.0265	20°	0.0225	0.01	0.0415
	0.2	0.0237	0.008	0.0203	70°	0.0194	0.5	0.0219

i.e., an increasing test statistic with a decreasing volume, is shown. Thus, the capillary force distribution can still be considered normal for small capillary bridges. A strong volume dependency of the capillary force distribution is generally observed, which is discussed in the next section.

7.1.2. Influence of volume, gap distance and contact angle

In this section the correlation between the distribution of the capillary force and the volume $\tilde{V}$, the gap distance $\tilde{a}$ and the contact angle θ is investigated. First, the influence of the volume is investigated for four different gap distances, i.e., $\tilde{a} = 0.004$, 0.05, 0.1 and 0.2. Capillary bridges with the different volumes are illustrated in figure 7.2 for a gap distance of $\tilde{a} = 0.1$. With an increasing volume all geometrical parameters, i.e., the interface areas and the three-phase contact line, increase whereas the roughness is kept constant. Thus, the proportions between the capillary bridge and the roughness change, which is important for the detailed analysis of the standard deviations.

In figure 7.3 the distributions of the capillary force are plotted as a function of the volume $\tilde{V}$. The distributions are illustrated by box plots using the conventions that are described in section 6.3. Moreover, the capillary force of the basic smooth system $\tilde{F}_{\mathrm{c,sm}}$, i.e., the system before roughness is added, is presented. The contact angle is $\theta = 40°$ and the roughness parameters are $\tilde{S}_{\mathrm{q}} = 0.005$ and $\varepsilon = 0.1$. Samples with a convergence rate below 98 % are indicated by * and are only obtained for $\tilde{a} = 0.2$ and $\tilde{V} = 0.01$ and 0.02, respectively. The capillary force distributions approximate the curves of the smooth system very well. In particular, the mean capillary force $\bar{F}_{\mathrm{c}}$ (cross marker) nearly agrees with the smooth capillary force $\tilde{F}_{\mathrm{c,sm}}$. Even the small maximum at $\tilde{a} = 0.004$ and $\tilde{V} \approx 0.02$ is reproduced. Nevertheless, the mean capillary force

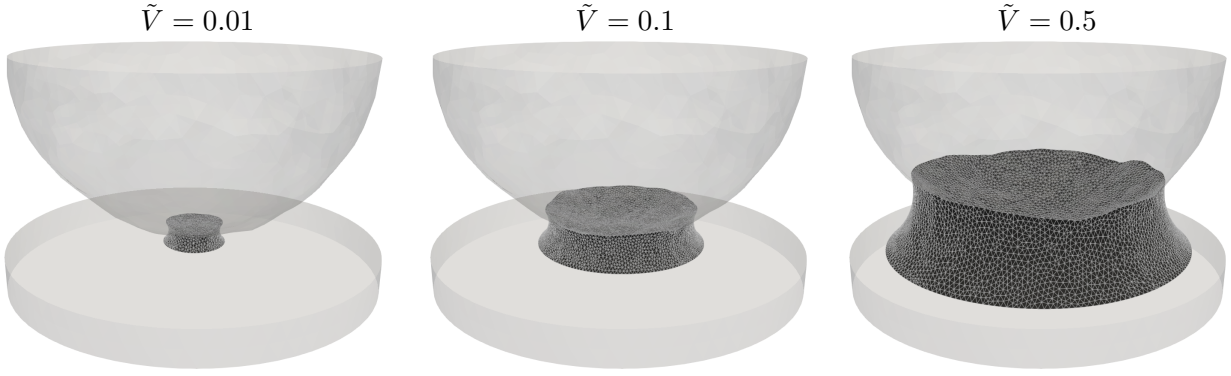

Figure 7.2.: Capillary bridges between a rough sphere and a smooth plate for different volumes ($\theta = 40°$, $\tilde{a} = 0.1$, $\tilde{S}_{\mathrm{q}} = 0.005$, $\varepsilon = 0.1$ and $\xi = 100$)

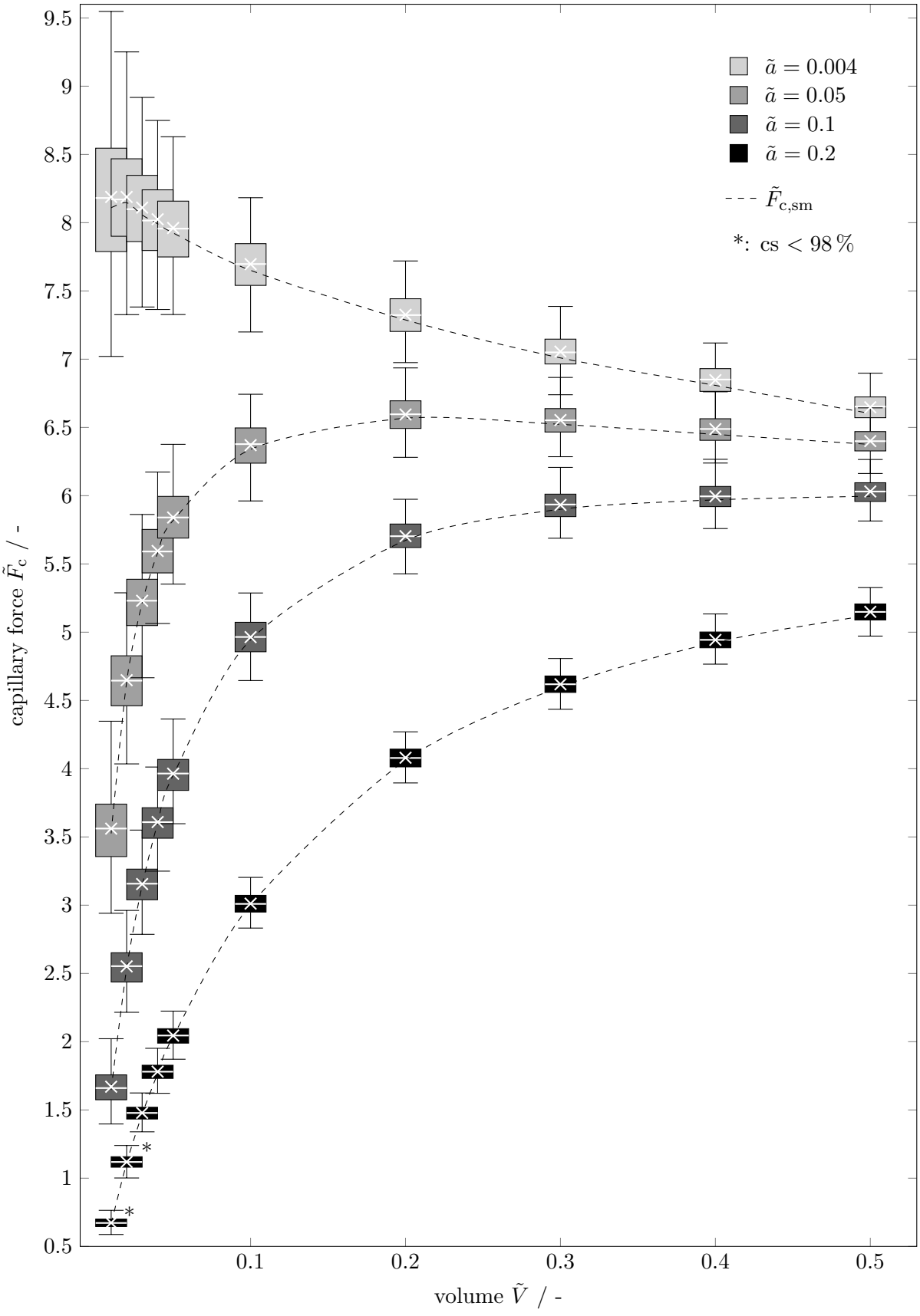

Figure 7.3.: Volume dependent distributions of the capillary force $\tilde{F}_{\mathrm{c}}$ between a rough sphere and a smooth plate and different gap distances ($\theta = 40°$, $\tilde{S}_{\mathrm{q}} = 0.005$ and $\varepsilon = 0.1$)

slightly exceeds the smooth value. This effect increases with a decreasing gap distance. Since the deviation is very small, it might be traced back to a numerical inaccuracy. However, a deeper analysis in section 7.1.3 shows, that the overestimation is caused by the modeling of the rough interfaces. In particular, the applied algorithm reduces the gap distance which leads to an increase of the capillary force. In appendix C the capillary force distributions are also presented for $\tilde{S}_\mathrm{q} = 0.002$ and $\tilde{S}_\mathrm{q} = 0.008$, however, they are not discussed in detail. Note, that for $\tilde{S}_\mathrm{q} = 0.008$ capillary bridges with $\tilde{a} = 0.004$ cannot be obtained due to self intersections of the solids. The smallest gap distance considered in this work, i.e., $\tilde{a} = 0.004$, cannot be combined with an RMS of $\tilde{S}_\mathrm{q} > 0.005$ since the roughness is added to the particle interface without changing the relative position of either the particle or the plate. Thus, for a very narrow gap, this might lead to self-intersection of the solid interfaces. The resulting topological changes of the capillary bridge are extremely complex and cannot be handled by the implemented algorithm. For the very large distance of $\tilde{a} = 0.02$ the simulations with $\tilde{S}_\mathrm{q} > 0.005$ are far to unstable and consequently, only distributions for $\tilde{a} = 0.05$ and $\tilde{a} = 0.1$ are presented in the appendix.

In figure 7.3 it is also demonstrated, that the absolute spread of the distribution decreases with an increasing volume and with a decreasing gap distance. However, with a decreasing gap distance also the mean capillary force $\bar{F}_\mathrm{c}$ increases. Thus, it is reasonable to consider the relative spread of the distribution, i.e., the relative standard deviation $\hat{s}$ defined by eq. (7.1). In figure 7.4 the absolute standard deviation s and the relative standard deviation $\hat{s}$ are plotted. Note, that the values corresponding to the unconverged box plots in figure 7.3 are not illustrated in these diagrams. As already derived from figure 7.3, the standard deviation s decreases with an increasing volume. However, for the large gap distances, i.e., $\tilde{a} = 0.1$ and 0.2, an increasing standard deviation with a maximum is observed for low volumes. In contrast, for the small gap distances a monotonously decreasing standard deviation is observed.

The relative standard deviation $\hat{s}$ decreases with an increasing volume for all gap distances. The gradient of the decrease declines with the volume and for $\tilde{V} > 0.2$ the curves are approximately constant. Thus, for $\tilde{V} < 0.2$ a strong degressive volume dependency of $\hat{s}$ is observed, whereas for $\tilde{V} > 0.2$ a nearly independent behavior is pointed out. All four curves match with each other, i.e., the degressive relation between the relative standard deviation and the volume is independent of the gap distance for $\tilde{V} > 0.1$.

The relative standard deviation $\hat{s}$ is given by the ratio of the standard deviation s and the mean capillary force $\bar{F}_\mathrm{c}$ (figure 7.3, cross marker). For $\tilde{a} = 0.004$ both, the mean

capillary force and the standard deviation, decrease. Since the quotient of these two parameters, i.e., the relative standard deviation, decreases, the decrease of the mean capillary force dominates over the decrease of the standard deviation. For the larger gap distances ($\tilde{a} \geq 0.05$) the capillary force increases with the volume and, at the same time, the standard deviation decreases. This results in an overall decreasing relative standard deviation. It is a very interesting result, that the relative standard deviation seems to be independent of the gap distance, although the curves of the mean capillary force and the standard deviation are qualitatively different. Nevertheless, for low volumes there is a considerable deviation between the gap distances (figure 7.6), which can hardly be estimated from figure 7.4 (b) due to the high slope. Thus, this gap distances dependency is subsequently illustrated more clearly.
In figure 7.5 capillary bridges between three gap distance are presented in order to illustrate the geometrical proportions. With a decreasing gap distance the liquid-solid interface and, consequently, also the three-phase contact line increases. Most probably capillary bridges between the large gap distances cannot emerge from a natural condensation process, which, however, does not imply that such a bridge cannot exist (section 2.4). For example, they might arise by slowly stretching an already existing capillary bridge or by artificially adding fluid to the gap. Thus, the tendencies of the correlations are also pointed out for the large gap distances in this work.

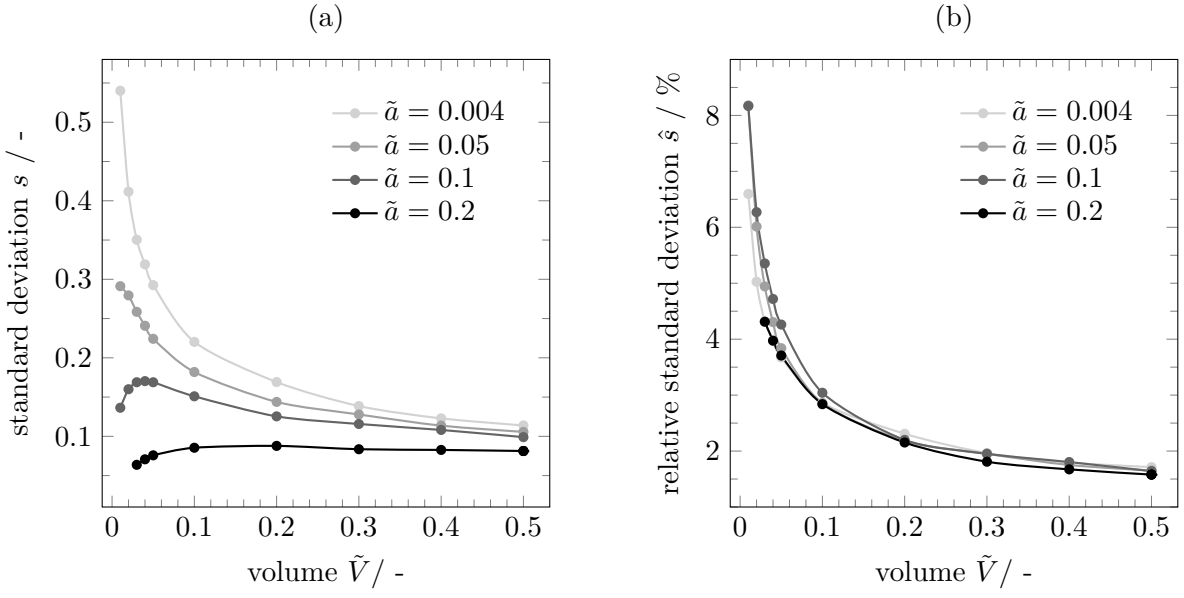

Figure 7.4.: Volume dependent standard deviation s (a) and relative standard deviation $\hat{s}$ (b) of capillary bridges between a rough sphere and a smooth plate for different gap distances ($\theta = 40°$, $\tilde{S}_\mathrm{q} = 0.005$ and $\varepsilon = 0.1$)

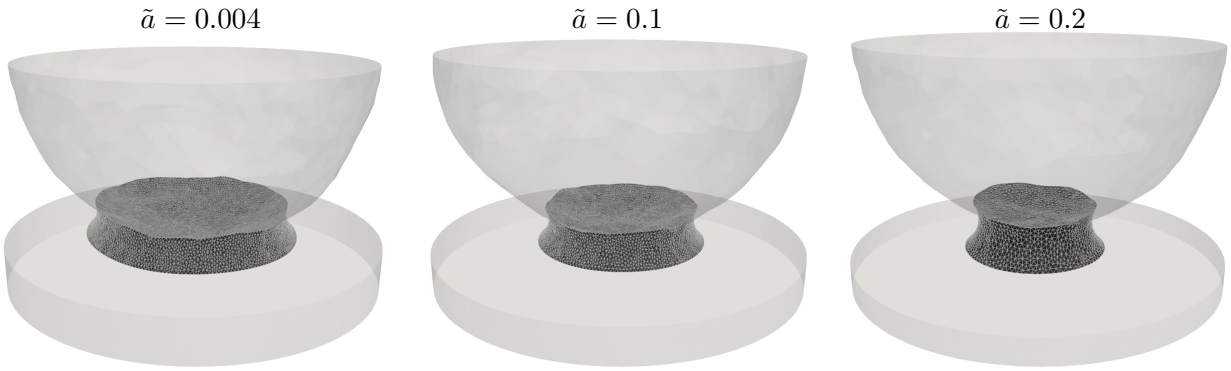

Figure 7.5.: Capillary bridges between a rough sphere and a smooth plate for different gap distances ($\tilde{V} = 0.1$, $\theta = 40°$, $\tilde{S}_\mathrm{q} = 0.005$, $\varepsilon = 0.1$ and $\xi = 100$)

The standard deviation s and the relative standard deviation $\hat{s}$, are explicitly plotted over the gap distance in figure 7.6. Note, that the unconverged simulation points at $\tilde{V} = 0.01$ have a convergence rate of 97 %, i.e., these points might be slightly over- or underestimated, however, a systematic error that is large enough to influence the overall tendency is excluded. The relative standard deviation $\hat{s}$ of $\tilde{V} = 0.1$ (figure 7.6 (b)) is nearly horizontal, i.e., it is independent of the gap distance for this volume. Since figure 7.4 already reveals, that this also holds for $\tilde{V} > 0.1$, larger volumes are not illustrated in figure 7.6.

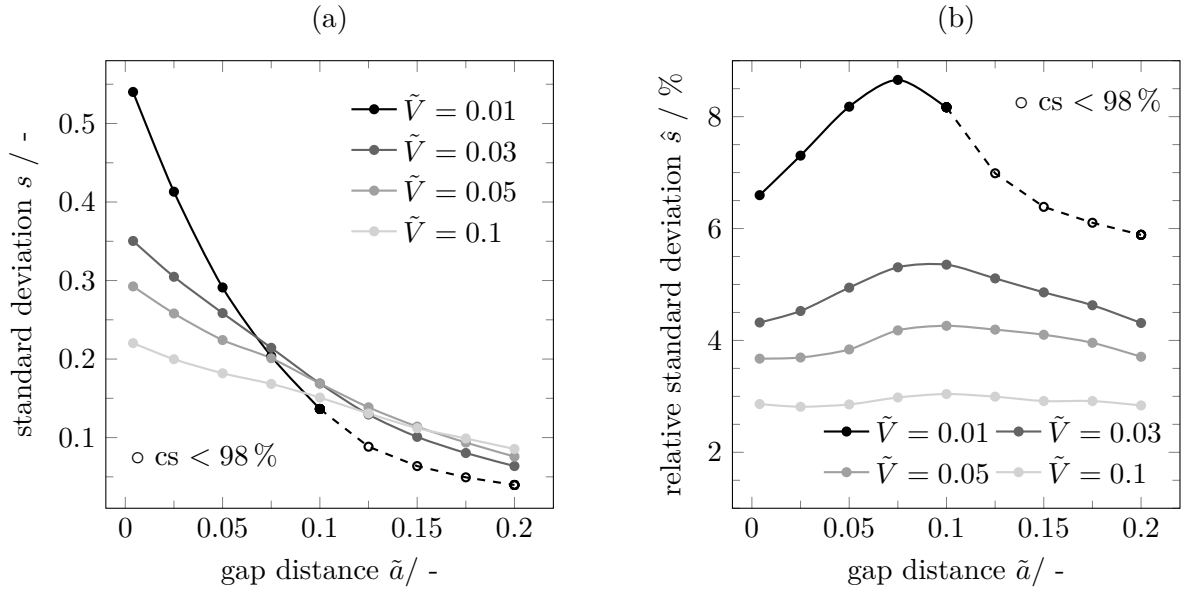

Figure 7.6.: Gap distance dependent standard deviation s (a) and relative standard deviation $\hat{s}$ (b) of capillary bridges between a rough sphere and a smooth plate for different volumes ($\theta = 40°$, $\tilde{S}_\mathrm{q} = 0.005$ and $\varepsilon = 0.1$)

The standard deviation of the capillary force s decreases for an increasing gap distance (figure 7.4 (a)). Interestingly, for $\tilde{V} > 0.01$ the curves exhibit a slight kink at $\tilde{a} = 0.075$. The gradients decrease with both, the gap distance and the volume of the capillary bridge. The mean capillary force is not explicitly plotted as a function of the gap distance, however, from figure 7.3 a generally decreasing capillary force with an increasing gap distance is obtained. Thus, the observed maximum in figure 7.6 (b) is traced back to the decreasing rates of the standard deviation and the capillary force. In particular, for the low gap distances the capillary force rapidly decreases which dominates the relative standard deviation, i.e., the fluctuation increase in relation to the mean capillary force. At larger gap distances the mean capillary force still decreases, however, with a significantly lower gradient. Thus, the relative standard deviation $\hat{s}$ is dominated by the decreasing standard deviation s.
The behavior of the standard deviation s is very complex and the presented tendencies are not straightforward. For example, in figure 7.4 (a) it is not obvious, why the standard deviation would exhibit a maximum for a moderate gap distance ($\tilde{a} = 0.1$) and, at the same time, strongly decrease for a lower gap distances ($\tilde{a} = 0.004$ and 0.05). Similarly, the kink in figure 7.6 (a) cannot be explained without any further information. According to the capillary force equation (eq. (3.7)) the capillary pressure and the three-phase contact line mainly determine the capillary force. In a rough system, both parameters fluctuate and, thus, their standard deviation can be considered for a better understanding of s. However, the relation between the capillary pressure and the three-phase contact line and the volume, gap distance and contact angle, respectively, is highly non-linear and, additionally, the ratio of the capillary pressure force and surface tension force must be taken into account. Due to these complex dependencies and superimposed effects, the behavior of standard deviation of the capillary force cannot directly be traced back to either the standard deviation of the capillary pressure or the three-phase contact line. Nevertheless, the standard deviation of the three-phase contact line on the rough sphere is analyzed in detail in order to exemplarily reveal the complexity of the system.
If an arbitrary system with a random parameter is scaled, the standard deviation of this random parameter is expected to scale with the mean value of this parameter. However, in the case of an increasing or decreasing capillary bridge the size of random parameter, i.e., the asperity size, is not scaled. Instead, only the number of asperities, that influence the capillary bridge, changes with an increasing solid-liquid interface. If now the length of the three-phase contact line increases, the standard deviation is expected to increase for very small three-phase contact lines. This is traced back to

the additional asperities that influence the system. However, if the length of the three-phase contact line is further increased, a maximum is expected at some point, i.e., the standard deviation decreases for large three-phase contact lines. This is traced back to the fact, that the changes more probably cancel each other out, i.e., locally shortening and lengthening might balance each other. This can also be interpreted in terms of the law or large numbers. This theorem of the probability theory states, that for a large sample number the average of the random parameter approximates the expected value. If now each asperity that affects the three-phase contact line is interpreted as random parameter, the sample number increases for an increasing three-phase contact line. Consequently, for a large three-phase contact line the average of these asperities converges towards an expected value and, consequently, also the length of the three-phase contact line converges. Note, that this would theoretically imply a standard deviation of zero in the limiting case which is not the case since there are always outliers that are not balanced out.

In figure 7.7 the relation between the mean length of the three-phase contact line $\bar{l}_{\mathrm{CL}}$ and their standard deviation $s_{\tilde{\mathrm{l}}_{\mathrm{CL}}}$ is presented. In the left diagram the volume is varied at a constant gap distance, whereas in the right diagram the gap distances is varied at a constant volume. Thus, in the right diagram the increasing mean length $\bar{l}_{\mathrm{CL}}$ implies a decreasing gap distance. The above described relation, i.e., a standard deviation $s_{\tilde{\mathrm{l}}_{\mathrm{CL}}}$ that increases first and, with an increasing mean value $\bar{l}_{\mathrm{CL}}$,

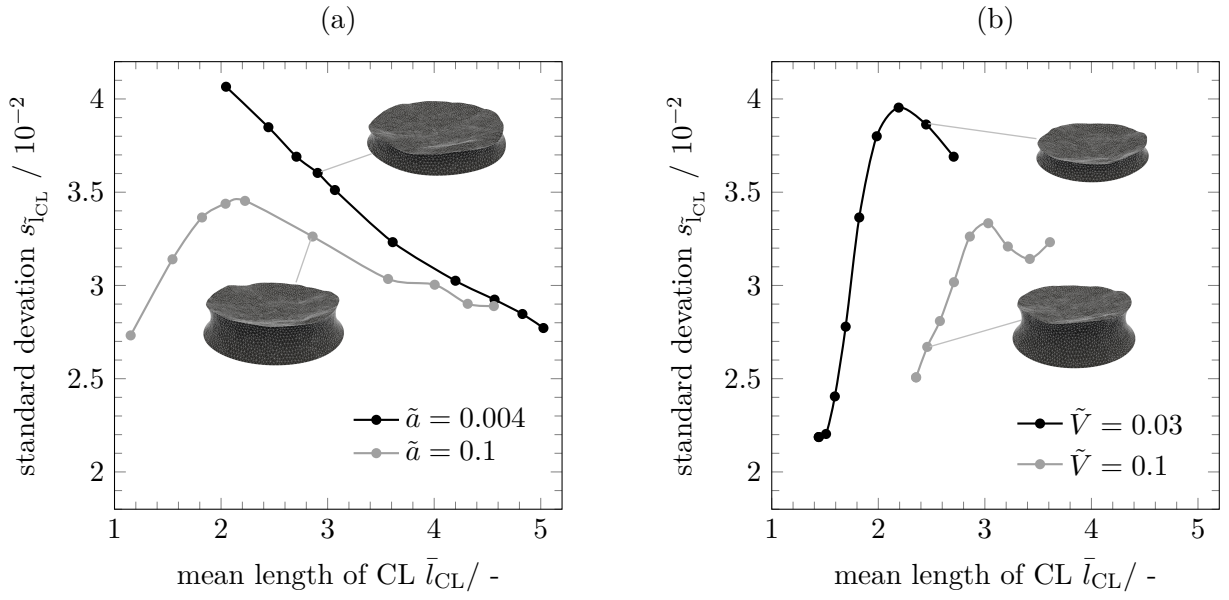

Figure 7.7.: Relation between the mean value and the standard deviation of the length of three-phase contact line $s_{\tilde{\mathrm{l}}_{\mathrm{CL}}}$ of the rough sphere for a varying volume (a) and a varying gap distance (b)

starts to decrease at some point, is principally pointed out in figure 7.7. However, if the standard deviation of the three-phase contact line would be only influenced by the solid geometry, i.e., the asperities, the curves are expected to match with each other. In each diagram two capillary bridges of a sample with the same mean length of the three-phase contact line are exemplarily illustrated. Note, that these bridges do not have exactly the same length of the three-phase contact line, since they are a particular realization of a sample with the same mean value. Although these samples have the same mean length of the three-phase contact line the standard deviation is different. It is qualitatively observed, that the standard deviation decreases with an increasing liquid-gas interface Γ_{lg} or with a decreasing mean curvature. However, the exact mechanism behind the different standard deviations remains unclear at this point. Moreover, the increase for $\tilde{V} = 0.1$ and $\bar{l}_{\mathrm{CL}} = 3.4$ cannot be explained. Nevertheless, the differences between the curves for the variation of the volume and gap distance are traced back to the different evolution of the capillary bridge geometry with either an increasing volume or a decreasing gap distance.

The standard deviation of the capillary pressure is even more complex since it does not depend on the size of the capillary bridge. Thus, a plot analogous to figure 7.7 does not seem to be reasonable. The pressure is determined by the curvature of the liquid-gas interface, which is independent of the area or length of any interface or the three-phase contact line. However, changes at the three-phase contact line, that are caused by different realizations of the roughness, indirectly affect the curvature of the liquid-gas interface, i.e., the mean curvature and the capillary pressure. Note, that in this context differences between three-phase contact lines are not equal to a different length of the three-phase contact lines as plotted in figure 7.7. In fact, two different realizations of the three-phase contact line might have the same length but lead to different capillary pressure since their local path is different.

The presented findings exemplarily demonstrate the highly non-linear relations. Even for a given length of the three-phase contact line , i.e., a given solid-liquid interface, the corresponding standard deviation cannot be estimated due to further dependencies. It is worth mentioning, that the differences cannot be caused by a statistical uncertainty of the sample since the same particle sample is used for all computations. Moreover, the differences are larger than $\pm 4.6\,\%$, which is the relative confidence interval of all standard deviation with $n = 1000$ (section 6.3).

The previous results are all presented for a contact angle of $\theta = 40°$. In figure 7.8 capillary bridges with a contact angle variation are illustrated. At first, the bridges might not seem to differ very much. A closer look at the liquid-gas interface reveals,

however, a very different bending. In section 6.2 it is already explained, that the strong bending at the three-phase contact line causes a relatively inaccurate numerical computation of the co-normal vector $\tilde{\boldsymbol{\mu}}$. Moreover, the different shapes of the capillary bridges lead to different curvatures and capillary pressures, respectively. In particular, the illustrated mean curvatures are $\tilde{H}(20°) = -3.10$, $\tilde{H}(40°) = -2.01$ and $\tilde{H}(70°) = -0.44$.

In figure 7.9 the distributions of the capillary force are plotted as a function of the contact angle θ. Note, that for $\theta = 10\,°$ none of the samples converged. For $\tilde{a} = 0.1$ and 0.2 the distributions consist of 85 % and 89 % of the sample, whereas for $\tilde{a} = 0.004$ and 0.05 less than 50 % converged. Thus, these distributions are not illustrated in figure 7.9. It is demonstrated that the mean capillary force $\bar{F}_\mathrm{c}$ (cross marker) approximates the capillary force of the smooth system $\tilde{F}_\mathrm{c,sm}$ very well. Analogous to figure 7.3, a slight overestimation that increases with a decreasing gap distance is observed. This is discussed more in detail in section 7.1.3. The absolute spread width of the distribution decreases with an increasing contact angle.

Again, the standard deviation of the capillary force s and the relative standard deviation $\hat{s}$ are discussed in detail. In figure 7.10 (a) the standard deviation s of the capillary force is plotted depending on the contact angle. Generally, the contact angle dependency seems to be relatively independent of the gap distance. For all gap distances a decrease is observed, that flattens with an increasing contact angle. The relative standard deviation $\hat{s}$ (figure 7.10 (b)) strongly increases for large contact angles. Generally, the contact angle dependency of the relative standard deviation is divided into two regions, i.e., $\theta \leq 50°$ and $\theta > 50°$. In the first region, a relatively constant behavior is pointed out. For low gap distances ($\tilde{a} = 0.004$ and 0.05) only a slight increase is observed, whereas a moderate decrease is demonstrated for the

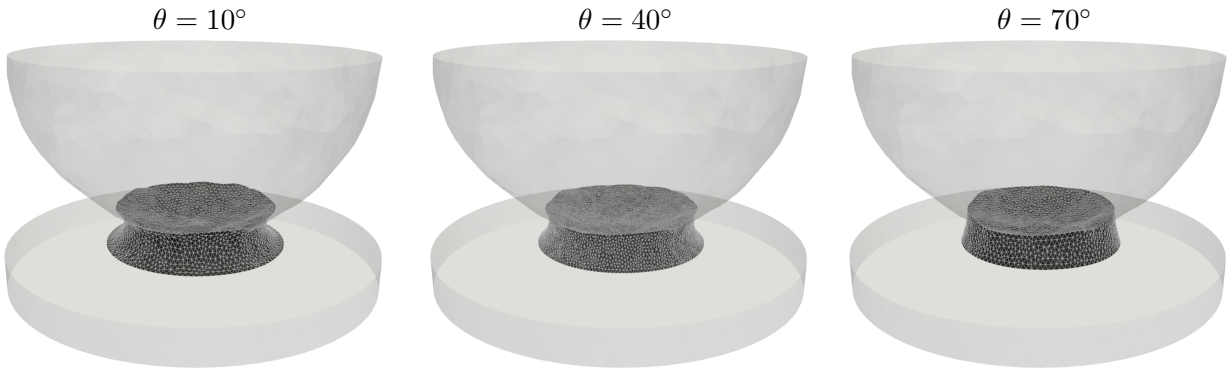

Figure 7.8.: Capillary bridges between a rough sphere and a smooth plate for different contact angles ($\tilde{V} = 0.1$, $\tilde{a} = 0.1$, $\tilde{S}_\mathrm{q} = 0.005$, $\varepsilon = 0.1$ and $\xi = 100$)

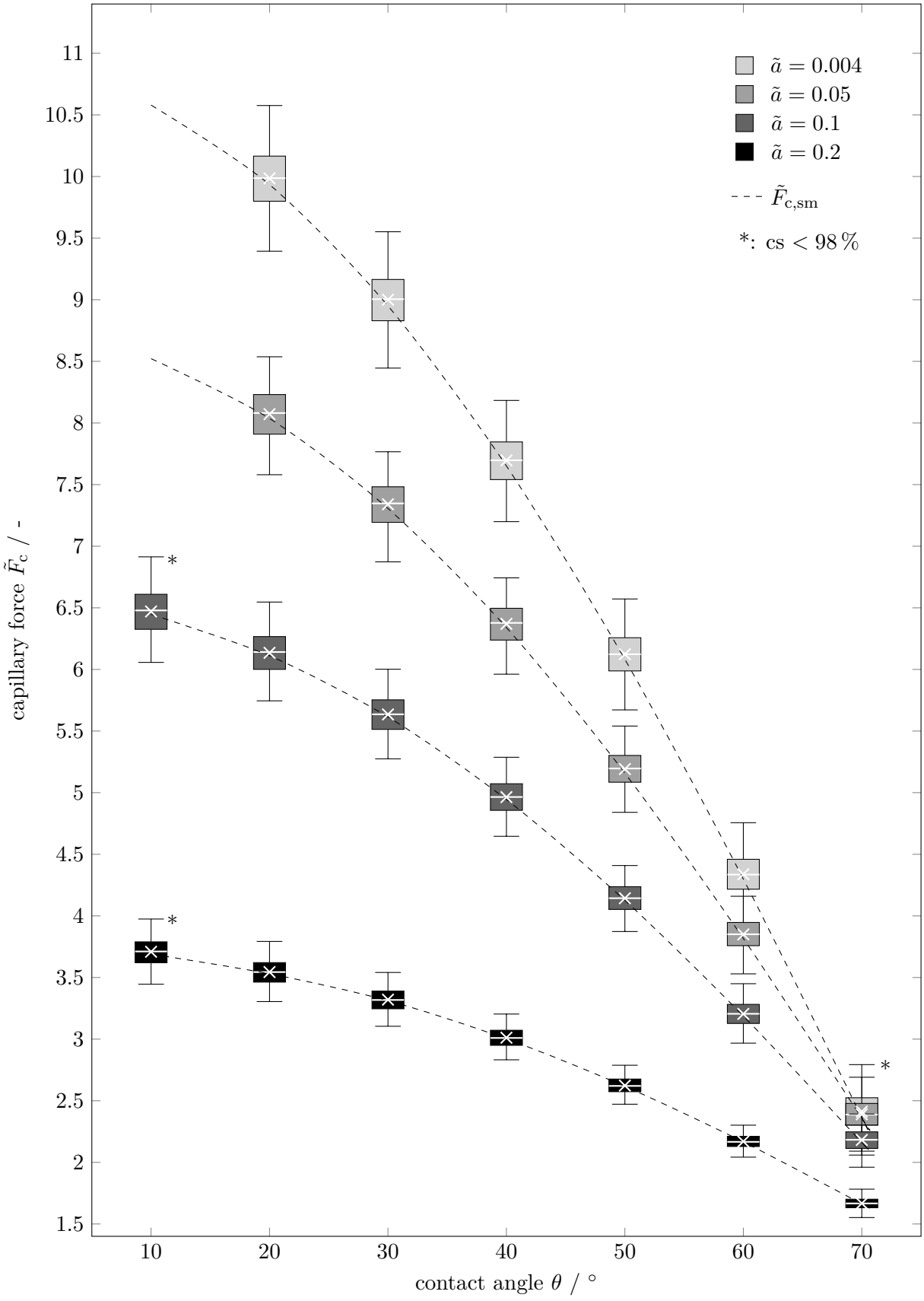

Figure 7.9.: Contact angle dependent distributions of the capillary force $\tilde{F}_{\mathrm{c}}$ between a rough sphere and a smooth plate and different gap distances ($\tilde{V} = 0.1$, $\tilde{S}_{\mathrm{q}} = 0.005$ and $\varepsilon = 0.1$)

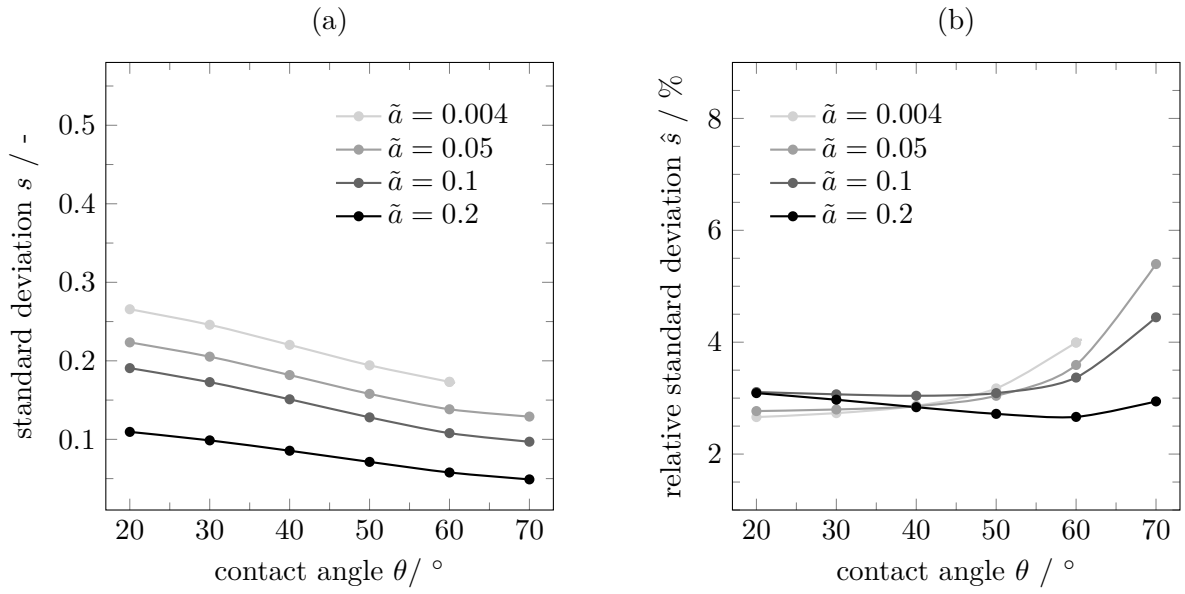

Figure 7.10.: Contact angle dependent standard deviation s (a) and relative standard deviation $\hat{s}$ (b) of capillary bridges between a rough sphere and a smooth plate for different gap distances ($\tilde{V} = 0.1$, $\tilde{S}_\mathrm{q} = 0.005$ and $\varepsilon = 0.1$)

large gap distance ($\tilde{a} = 0.2$). The increase for $\theta > 50°$ is mainly caused by the strong decrease of the mean capillary force (figure 7.9). In particular, the mean capillary force approaches zero and for $\bar{F}_\mathrm{c} = 0$ a non-zero standard deviation is expected which, however, implies an infinite relative standard deviation. Thus, at very low capillary forces, considering the relative standard deviation might not be useful since all physical effects are superimposed by the decreasing denominator in eq. (7.1).
In this section, the influence of the volume, gap distance and contact angle on the distribution of the capillary force and, particularly, the standard deviation s is investigated in detail. It is observed, that for small volumes the standard deviation s strongly depends the volume and the gap distance. However, with an increasing volume the influence of both parameters significantly decreases and might even be neglected for large capillary bridges. Moreover, the impact of the contact angle on the standard deviation is much lower compared to the other two parameters.

7.1.3. Influence of the RMS

In the previous section, the relation between the distribution of the capillary force $\bar{F}_\mathrm{c}$ and the volume $\tilde{V}$, gap distance $\tilde{a}$ and contact angle θ is analyzed. Therefore, the RMS is set to a constant, medium value of $\tilde{S}_\mathrm{q} = 0.005$. Subsequently, the influence of the roughness itself is investigated by varying the RMS at a constant volume, contact angle and the gap distance, i.e., $\tilde{V} = 0.1$, $\theta = 40°$ and $\tilde{a} = 0.1$. Moreover, the diffusion

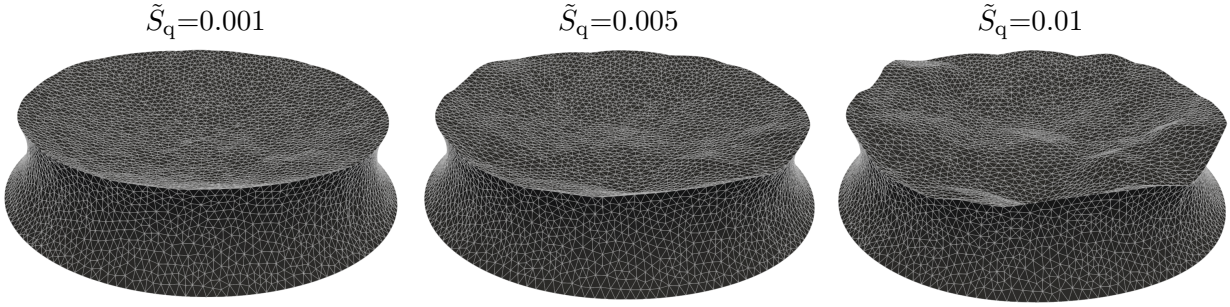

Figure 7.11.: Capillary bridges between a rough sphere and a smooth plate for different RMS ($\tilde{V} = 0.1$, $\theta = 40°$, $\tilde{a} = 0.1$, $\varepsilon = 0.1$ and $\xi = 100$)

coefficient is kept constant at $\varepsilon = 0.1$. Note, that it is generally observed, that a high particle smoothing, i.e., a large ε, is favorable for numerical stability. Thus, a high diffusion coefficient of the rough interface is chosen for the sphere-plate system and its influence on the distribution of the capillary force is analyzed later for the sphere-sphere systems (section 7.2.3) since these generally show a higher numerical stability. In figure 7.11 capillary bridges with a RMS of $\tilde{S}_\mathrm{q} = 0.001$, $\tilde{S}_\mathrm{q} = 0.005$ and $\tilde{S}_\mathrm{q} = 0.01$ are illustrated. The increasing asperities, or more precisely the negative of the solid asperities, is apparent on the solid-liquid interface. Moreover, with an increasing roughness the three-phase contact line deviates stronger from an ideal circle.
The distributions of the capillary force for different RMS are presented in figure 7.12. As expected, the spread of the distribution increases with the RMS. The capillary force of the corresponding smooth sphere-plate system ($\tilde{F}_\mathrm{c}$) is plotted as a reference

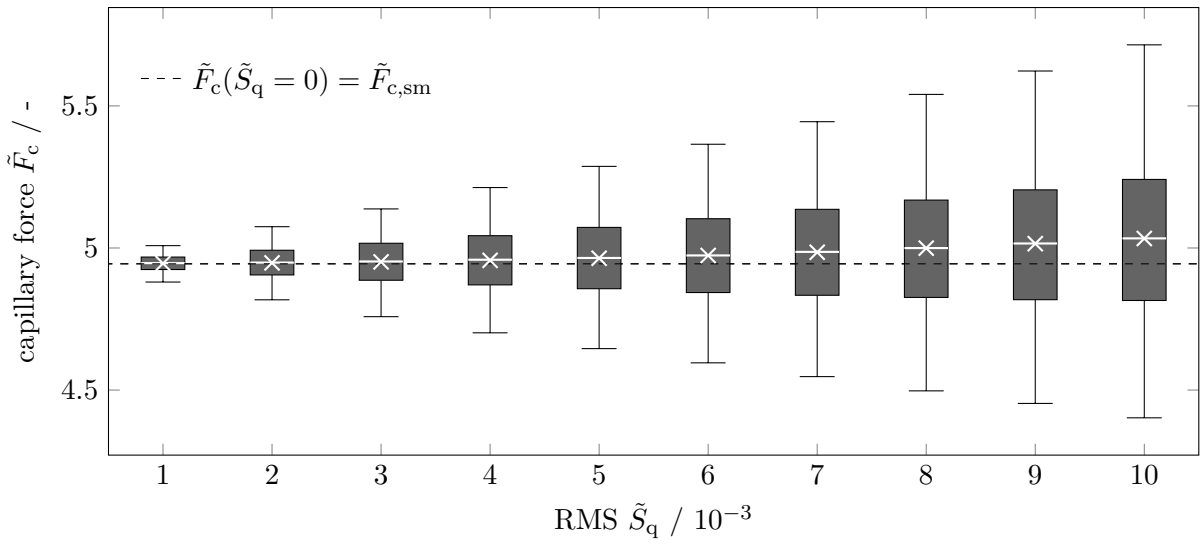

Figure 7.12.: RMS dependent distributions of the capillary force $\tilde{F}_\mathrm{c}$ between a rough sphere and a smooth plate ($\tilde{V} = 0.1$, $\theta = 40°$, $\tilde{a} = 0.1$ and $\varepsilon = 0.1$)

value. For the low RMS, the mean capillary force of the rough system agrees well with the smooth value. Since the rough interface is derived by adding a normal distribution to the smooth interface, it is reasonable to assume, that the mean value corresponds to the capillary force of the smooth system. However, with increasing roughness the mean value increases and exceeds the smooth capillary force. This is traced back to the fact, that the gap distance is changed by the asperities, i.e., the smooth and the rough sphere-plate system do not have the same minimal gap distance.
A more quantitative analysis of the increasing mean capillary force is presented in figure 7.13. The relative deviation of the simulated mean capillary force of the rough sample $\bar{F}_\mathrm{c}$ and the capillary force of the smooth sphere-plate system $\tilde{F}_\mathrm{c,sm}$ is given by

$$\Delta\tilde{F}_\mathrm{c,sm} = \frac{\bar{F}_\mathrm{c} - \tilde{F}_\mathrm{c,sm}}{\tilde{F}_\mathrm{c,sm}} \cdot 100\%. \tag{7.8}$$

In the left diagram, the deviation $\Delta\tilde{F}_\mathrm{c,sm}$ is plotted as a function of the RMS $\tilde{S}_\mathrm{q}$ for different gap distances. For $\tilde{a} = 0.05$ and $\tilde{a} = 0.2$ a convergence rate of 98 % could not be obtained for the highly rough samples. Although the plotted values seem to extrapolate the curves quite well, a slight systematic error cannot be excluded with certainty. Thus, these values are again indicated by the transparent marks and the dashed lines. As already shown by figure 7.12 the difference between the mean values of the rough simulation and the capillary force of the smooth system increases with the RMS and with a decreasing effective gap distance.
Generally, a deviation below 2 % is observed which corresponds to the order of magnitude of the numerical error (table 6.5). However, the numerical error is systematic and mainly depends on the volume and the contact angle rather than on the gap distance and root mean square roughness. The statistical uncertainty is significantly lower (0.40 % for $\tilde{V} = 0.1$, table 6.6) and also not expected to cause a systematic increasing mean capillary force with the RMS. Instead, the deviation between $\bar{F}_\mathrm{c}$ and $\tilde{F}_\mathrm{c,sm}$ is traced back to the decreasing gap distance. In figure 7.13 (b) the ratio of $\tilde{a}_\mathrm{r}$ and $\tilde{a}_\mathrm{sm}$ is plotted, where $\tilde{a}_\mathrm{r}$ is the mean of the minimal gap distance of the rough geometry and $\tilde{a}_\mathrm{sm}$ the distance of the smooth base geometry, i.e., $\tilde{a}_\mathrm{sm} = \tilde{a}$. It is demonstrated, that with an increasing RMS the mean gap distance of the rough system significantly decreases. This is not directly obvious since the rough interface algorithm displaces the points of the smooth base geometry in both directions, i.e., in- and outwards of the sphere (section 5.2.1). Thus, the mean gap distance might be expected to be constant which is, according to figure 7.12 (b), clearly not the case.

This is traced back to the fact, that the gap distance is a minimum rather than an average value and this minimum is influenced by several mesh points of the solid interface. The principle is illustratively explained for a system of two parallel plates. If only one mesh point on a plate would be displaced outwards the plate, the minimal gap distance between the plates reduces. However, if the same point would be displaced inwards the plate, the minimal gap distance remains constant since it is defined by all other points. Consequently, for an average over a huge number of interface realizations, the average minimal gap distance is below the minimal gap distance of the two smooth plates. If now all points on one plate are randomly displaced, the gap distance increases if all points are displaced inwards the plate which is statistically possible, however, not frequently expected. The same principle holds for the sphere-plate system. However, due to the curved interface of the sphere only the mesh points around the closet distance in the smooth system are relevant for the minimal gap distance. With an increasing RMS this area of influence increases since the mesh points are stronger displaced. Consequently, more mesh points must be displaced inwards the sphere in order to obtain a larger gap distance compared to the smooth gap distance. This reduces the probability of larger gap distances and the mean value decreases even stronger. Overall, the decreasing gap distance is traced back to two effects. First, an increasing RMS leads to larger displacements of the solid mesh points and, thus, the gap distance is stronger reduced. Second, the number of solid mesh points that are relevant for the gap distance increases with the RMS and,

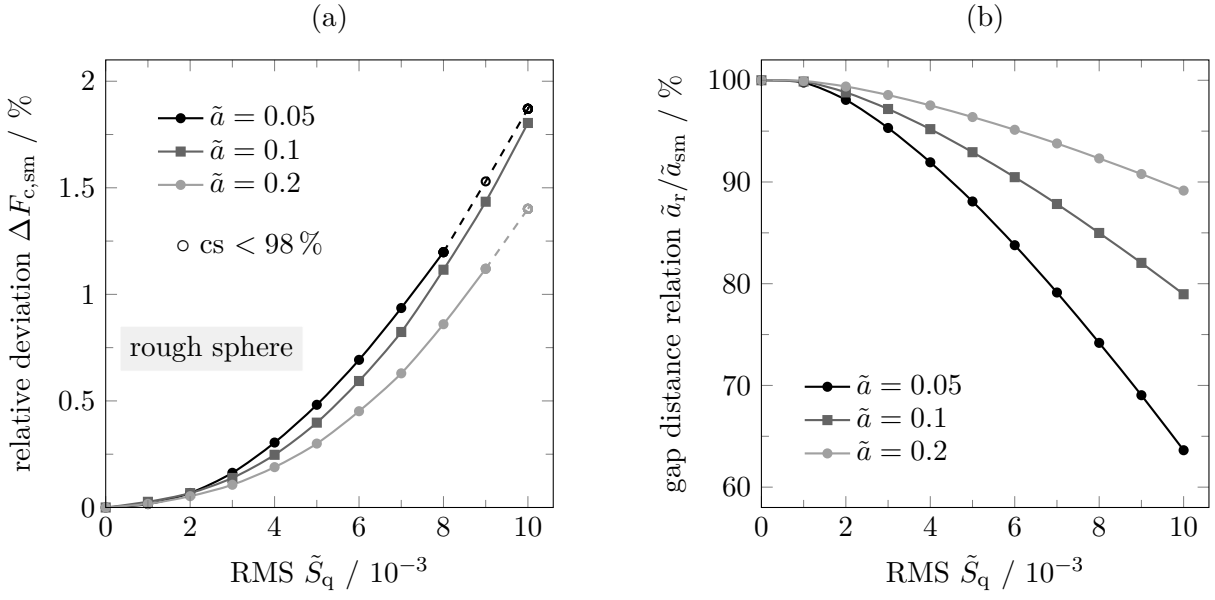

Figure 7.13.: RMS dependency of the relative deviation $\Delta\tilde{F}_{\mathrm{c,sm}}$ for distances (a) and of the relation between the mean rough and the smooth gap distance $\tilde{a}_{\mathrm{r}}/\tilde{a}_{\mathrm{sm}}$ (b)

hence, the probability for larger gap distances decreases. Since both effects lead to a decreasing gap distance, the gradients in figure 7.12 (b) increase with the RMS.
It is worth mentioning, that the mean gap distance reduces stronger if the roughness is applied to the plate rather than to the sphere. This is traced back to the vertex displacement by the rough interface algorithm, i.e., a displacement normal to the solid interface (section 5.2.1). Thus, the displacement direction of the vertices at the plate always corresponds to the direction normal to the gap distance. In contrast, on the sphere the displacement, in relation to the gap distance, is composed by a normal and a tangential component. Since only the normal component effects the gap distance, the reduction is less pronounced compared to the rough plate.
Note, that the absolute decrease of the mean gap distance is similar for all three gap distances. Thus, the relative deviation is largest for the smallest gap distance which leads to the highest relative deviation $\Delta\tilde{F}_{\mathrm{c,sm}}$ for $\tilde{a} = 0.05$. For an RMS of 0.01 the mean gap distance of the rough system is reduced by approximately 40 % and, consequently, a deviation between $\bar{F}_{\mathrm{c}}$ and $\tilde{F}_{\mathrm{c,sm}}$ larger than 2 % might be expected. However, the capillary force generally increases with a decreasing gap distance. Thus, the relative deviation of the capillary force, that is caused by different gap distances, decreases. This is expected to cause a comparable order of magnitude of $\Delta\tilde{F}_{\mathrm{c,sm}}$ for all investigated gap distances (figure 7.12 (a)) although the relative reduction of the mean gap distance is significantly larger for the small gap distances (figure 7.12 (b)). Overall, the accordance of the smooth capillary force and the mean rough capillary force is minor for the investigated systems in this work. Nevertheless, this cannot be assumed in general. For example, when applying the presented method to other geometries or even when considering a different rough interface algorithm, i.e., a vertex displacement other than normal to the solid interface, the order of magnitude of the deviation needs to be estimated again.
In figure 7.12 it is obvious, that the width of the capillary force distribution increases with an increasing roughness. In figure 7.14 the relative standard deviation $\hat{s}$ is plotted for various system configurations. The dark gray square mark lines correspond to a system with $\tilde{V} = 0.1$, $\theta = 40°$, $\tilde{a} = 0.1$ and $\varepsilon = 0.1$. Based on this configuration one parameter is varied in each diagram. It is immediately obvious that the relation between the RMS and the relative standard deviation is linear for all parameter combinations. This is remarkable and offers a great potential for the development of a rough capillary force model that can be applied to a discrete element method (DEM). The general idea of such a model is discussed in section 8.2.

In figure 7.14 (a) the influence of the RMS is plotted for different volumes. As already mentioned, the relative standard deviation proportionally depends on the RMS. The gradient considerably increases with a decreasing volume. Overall, the higher gradient at low volumes is well consistent with the previous observation, that capillary bridges with low volumes are more sensitive towards the variation of another parameter, e.g., the gap distance dependency exhibits a more pronounced maximum at lower volumes (figure 7.6 (b)). The influence of the volume on the gradient of $\tilde{S}_\mathrm{q}$ seems to be an order of magnitude larger compared to the other parameters. This is, however, also traced

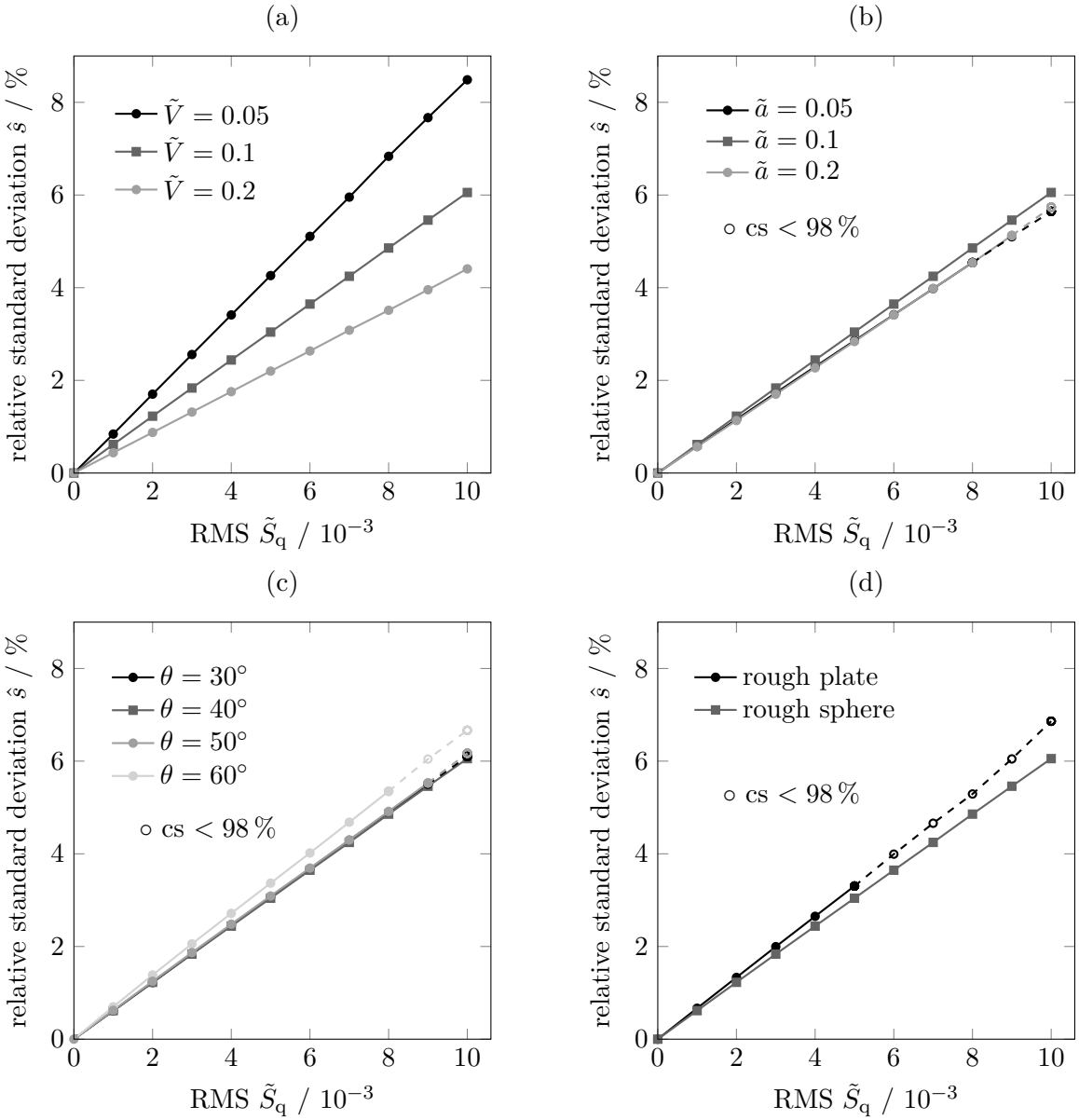

Figure 7.14.: RMS dependency of the relative standard deviation $\hat{s}$. The base system is indicated by the square mark and consists of a rough sphere and smooth plate with $\tilde{V} = 0.1$, $\theta = 40°$, $\tilde{a} = 0.1$ and $\varepsilon = 0.1$

back to the fact, that the volume in figure 7.14 (b), (c) and (d) is set to $\tilde{V} = 0.1$, which is relatively large. From the analysis in section 7.1.2 it is concluded, that the gradients of the other parameters differ more from each other for lower volumes.
In figure 7.14 (b) the roughness dependency is shown for different gap distances $\tilde{a}$. Generally, the influence of the gap distance is minor which is already explained by the relatively large volume. It is worth mentioning, that the relative standard deviation of the median gap distance $\tilde{a} = 0.1$ is slightly above the other two curves, which corresponds to the very weak maximum in figure 7.6 (b) and $\tilde{V} = 0.1$. From the increasing difference between the gap distances in figure 7.14 (a) it is concluded, that the maxima in figure 7.6 (b) are more pronounced for an increased RMS.
A contact angle θ variation is presented in figure 7.14 (c). For $\theta \leq 50°$ the relative standard deviation is independent of the contact angle. This is already demonstrated for $\tilde{S}_\mathrm{q} = 0.005$ in figure 7.10 (b). For $\theta = 60°$the relative standard deviation is slightly above the other curves. The higher relative standard deviation is, however, mainly traced back to the rapid decrease of the capillary force that is caused by the decreasing capillary pressure. At this point it remains unclear, if the observed contact angle dependency also holds for low volumes.
In figure 7.14 (d) the relative standard deviation $\hat{s}$ is presented for the two differently rough systems, i.e., a rough sphere and a rough plate system. First, as a very general result, the convergence of the simulation significantly deteriorates for the rough plate. In the particular case of the system illustrated in figure 7.14 (d), all samples with $\tilde{S}_\mathrm{q} > 0.005$ did not converge with a rate of at least 98 %. The number of converged capillary bridges decreases nearly linear and for $\tilde{S}_\mathrm{q} = 0.01$ only 55 % of the sample converged. Thus, these values cannot be used for any physical interpretation. Nevertheless, for $\tilde{S}_\mathrm{q} \leq 0.005$ the values are computed within the requirements, i.e., a convergence rate of 98 %.
For $\tilde{S}_\mathrm{q} \leq 0.005$ the relative standard deviation of the rough plate system is slightly above the rough sphere system. From the considerations of the minimal gap distance it is concluded, that the mean capillary force is larger for the rough plate system. This is confirmed by the simulations, however, it is not explicitly plotted. Due to the increasing mean capillary force a lower relative standard deviation compared to the rough sphere would be expected. However, since the relative standard deviation of the rough plate system is larger (figure 7.14 (d)) also the absolute standard deviation s must be above the absolute standard deviation of the rough sphere system. This might be traced back to the convex geometry of the sphere. Since roughness is applied normal to the interface, on a convex geometry the displacement of a vertex is com-

posed of a component normal and tangential to the capillary bridge. The tangential components are assumed to have a minor influence on the capillary bridge whereas the normal components are dominant. On a plate, however, a vertex displacement normal to the plate corresponds to a displacement normal to the capillary bridge. Thus, the fluctuations that are cause by a rough plate might be larger compared to the rough sphere. This, however, cannot be certainly concluded without a deeper investigation. However, this is not straightforward due to the unsatisfying convergence behavior of the rough plate.
Nevertheless, the deviation between the two configurations increases with the RMS. However, it cannot be concluded for sure, how large the deviation might be for high roughness. Nevertheless, if the linear increase of $\tilde{S}_\mathrm{q} \leq 0.005$ is extrapolated, the deviation between the two systems seems to be minor for low RMS values. This is particularly interesting with respect to the unsatisfying convergence of the rough plate. If the difference of the capillary force distribution is nearly independent of whether the sphere or the plate interface is considered to be rough, systems with a highly rough plate can be approximately computed by adding the roughness to the spherical interface.
In conclusion, the relative standard deviation $\hat{s}$ linearly depends on the RMS $\tilde{S}_\mathrm{q}$. This is particularly remarkable with respect to the complex dependencies and interdependencies of the volume, contact angle and gap distance. The overall results suggest, that the relations revealed in section 7.1.2 are enhanced by an increasing RMS and reduced by a decreasing RMS, respectively. It is worth mentioning, that the linear increase of the relative standard deviation offers a great potential to develop a relatively simple but sufficiently exact rough capillary force model for DEM simulations as discussed in section 8.2.

7.2. Capillary forces between two rough spheres

In this section an analysis of the capillary force distribution between equally and unequally rough spheres is presented. The volume, contact angle and gap distance are fixed at $\tilde{V} = 0.05$, $\theta = 40°$and $\tilde{a} = 0.05$. First, the distribution is tested and, subsequently, the influence of the RMS $\tilde{S}_{\mathrm{q},1\backslash 2}$ and the diffusion coefficient ε is investigated.

7.2.1. Analysis of the capillary force distribution

In section 7.1.1 the distribution of the capillary force between a rough sphere and a smooth plate is tested to be normal by qualitative and quantitative methods. Gener-

ally, a normal distribution is also expected for the sphere-sphere system, however, this must be verified. Thus, a Kolmogorov–Smirnov test is performed for three different combinations of rough spheres.
For $\tilde{S}_{\mathrm{q},1\backslash 2} = 0.002\backslash 0$, $\tilde{S}_{\mathrm{q},1\backslash 2} = 0.007\backslash 0$ and $\tilde{S}_{\mathrm{q},1\backslash 2} = 0.005\backslash 0.005$ test statistics of $D = 0.0276$, $D = 0.0306$ and $D = 0.0169$ are obtained. Thus, the order of magnitude is consistent with the values obtained for the sphere-plate system (table 7.1). For the critical value $D_{\mathrm{crit}}(5\,\%) = 0.0429$ of the significance level $\alpha = 5\,\%$ the null hypotheses is not rejected and consequently the distribution is estimated to be normal.
Moreover, the tendency of a decreasing test statistic, i.e., a more normal distribution, with an increasing volume is obtained. In particular, for $\tilde{S}_{\mathrm{q},1\backslash 2} = 0.005\backslash 0.005$ also the capillary force distributions for $\tilde{V} = 0.1$ and $\tilde{V} = 0.2$ are tested, which leads to test statistics of $D = 0.0212$ and $D = 0.0155$. Overall, the distribution of the capillary force is tested to be normal for all considered parameter combinations. However, it should be explicitly noted, that the normal distribution of the capillary force is only demonstrated for a normal distribution of the asperities. Hence, it is possible, that another distribution of roughness might lead to different results for the capillary force distribution.

7.2.2. Influence of the RMS

Subsequently, the influence of the RMS on the relative standard deviation between two spheres is investigated. Since the spheres show a good convergence behavior, the combination of different RMS values on the spheres are analyzed. First, a system of two equally sized spheres is analyzed and, subsequently, spheres with $R_1 = 1$ and $R_2 = 0.5$ are considered.
In figure 7.15 (a) the relative standard deviation of the equally sized sphere system is presented for different RMS values. On the x-axis the RMS $\tilde{S}_{\mathrm{q},1}$ is presented, whereas $\tilde{S}_{\mathrm{q},2}$ is set to 0 and to $\tilde{S}_{\mathrm{q},1} = \tilde{S}_{\mathrm{q},2}$. These two plots are emphasized since they are later compared to the system of unequally sized spheres. Additionally, the plots for a constant $\tilde{S}_{\mathrm{q},2}$ of 0.001, 0.004 and 0.007 are illustrated. The mean capillary force is nearly constant. Only a small increase due to the smaller effective gap distance has to be considered. However, for the sphere-sphere system this increase is below 2.6 % even for the highly rough particles with $\tilde{S}_{\mathrm{q},1} = \tilde{S}_{\mathrm{q},2} = 0.007$. Therefore, the plots of the relative and the absolute standard deviation are nearly equal since the mean value is approximately constant. The characteristic diagram is symmetric about the $\tilde{S}_{\mathrm{q},1} = \tilde{S}_{\mathrm{q},2}$-axis since the spheres are completely equal, i.e., $\hat{s}(\tilde{S}_{\mathrm{q},1\backslash 2}) = \hat{s}(\tilde{S}_{\mathrm{q},2\backslash 1})$. The relative standard deviation increases linearly with the RMS $\tilde{S}_{\mathrm{q},1}$ if the other particle

interface is smooth, i.e., $\tilde{S}_{\mathrm{q},2} = 0$. This is also observed for the sphere-plate system where a linear increase is demonstrated for all parameter configurations and a smooth plate interface. Interestingly, the relative standard deviation also increases linear if $\tilde{S}_{\mathrm{q},1} = \tilde{S}_{\mathrm{q},2}$. For $\tilde{S}_{\mathrm{q},2} \neq 0$ and $\tilde{S}_{\mathrm{q},1} \neq \tilde{S}_{\mathrm{q},2}$, a non-linear increase is obtained. However, with an increasing $\tilde{S}_{\mathrm{q},1}$ and, particularly, for $\tilde{S}_{\mathrm{q},1} > \tilde{S}_{\mathrm{q},2}$ for the plots of a constant $\tilde{S}_{\mathrm{q},2}$ are approaching a linear increase.
Moreover, it is demonstrated, that the influence of the RMS values cannot be linearly combined which, in fact, has not be expected. In particular, the standard deviation is largest if a high RMS is observed on a single sphere rather than a moderate value on both spheres. This is traced back to fact, that, if a roughness is applied to both interfaces, the effects of the asperities on both interfaces can cancel each other out. Of course, the influence might also be enhanced in some cases, however, not above the case, where a high roughness is applied to only one interface. Thus, the relative standard deviations $\hat{s}(\tilde{S}_{\mathrm{q},1}, \tilde{S}_{\mathrm{q},2})$ are always below $\hat{s}(\tilde{S}_{\mathrm{q},1} + \tilde{S}_{\mathrm{q},2}, 0)$.
In section 8.2 the development of a rough force model for the implementation in a multi-scale simulation is discussed. With respect to such a model, the interpolation of the target parameters, i.e., the relative standard deviation $\hat{s}$, is very important. The linear increase offers the option of deriving the whole characteristic diagram of the two RMS values (figure 7.15 (a)) by just a few simulations. In particular, the following procedure is suggested:

- Simulate $\hat{s}(\tilde{S}_{\mathrm{q,max}}, \tilde{S}_{\mathrm{q},2})$ with the desired resolution of the RMS, where $\tilde{S}_{\mathrm{q,max}}$ is the maximum RMS that should be considered, i.e., 0.007 in figure 7.15 (a)
- Linearly interpolate $\hat{s}(\tilde{S}_{\mathrm{q},1} = \tilde{S}_{\mathrm{q},2})$ between $(0, 0)$ and $\hat{s}(\tilde{S}_{\mathrm{q,max}}, \tilde{S}_{\mathrm{q,max}})$
- For $\tilde{S}_{\mathrm{q},1} > \tilde{S}_{\mathrm{q},2}$ linearly interpolate $\hat{s}(\tilde{S}_{\mathrm{q},1}, \tilde{S}_{\mathrm{q},2})$ between $\hat{s}(\tilde{S}_{\mathrm{q},2}, \tilde{S}_{\mathrm{q},2})$ and $\hat{s}(\tilde{S}_{\mathrm{q,max}}, \tilde{S}_{\mathrm{q},2})$
- For $\tilde{S}_{\mathrm{q},2} > \tilde{S}_{\mathrm{q},1}$ the RMS values can be switched since $\hat{s}(\tilde{S}_{\mathrm{q},1\backslash 2}) = \hat{s}(\tilde{S}_{\mathrm{q},2\backslash 1})$

This procedure is applied to figure 7.15 (a). For an RMS resolution of $\Delta\tilde{S}_{\mathrm{q}} = 0.001$ 36 simulations of the sample size n must be performed. With the suggested interpolation only 8 simulations are required, i.e., $\hat{s}(0.007, 0)$ to $\hat{s}(0.007, 0.007)$. The relative deviations between the simulated and the interpolated relative standard deviation are presented in figure 7.15 (b). For $\tilde{S}_{\mathrm{q},1} = \tilde{S}_{\mathrm{q},2}$ the deviation is below 0.2 % since a linear relation is pointed out in figure 7.15 (a). Moreover, for $\tilde{S}_{\mathrm{q},1} = 0.007$ the deviations vanish since these parameters are exactly simulated (step 1.). The largest deviations are obtained very close to the $\tilde{S}_{\mathrm{q},1} = \tilde{S}_{\mathrm{q},2}$ axis, which is traced back to the bending

of the constant $\tilde{S}_{q,2}$ curves in figure 7.15 (a). Note, that with the suggested procedure all values between the two straights are interpolated, whereas the values above the $\tilde{S}_{q,1} = \tilde{S}_{q,2}$ are given by the symmetry. Thus, the strongest deviation from a linear curve is obtained for $\tilde{S}_{q,2} = 0.001$ and small $\tilde{S}_{q,1}$. The largest relative deviation (5.89 %) is obtained for $\tilde{S}_{q,1} = 0.002$ and $\tilde{S}_{q,1} = 0.001$, which is mainly traced back to the small absolute value of $\hat{s}$. Nevertheless, the deviations are relatively small when considering the computational costs of the simulation. In this sample case, only one quarter of the original simulation time would be required. Moreover, they must be related to the statistical uncertainty of the standard deviation, i.e., a confidence interval of 9.20 % (section 6.3). A reduced number of simulations points offers the potential to increase the sample size and, hence, the accuracy of the standard deviation. Thus, the overall accuracy of a characteristic diagram is increased. Nevertheless, the deviations of the interpolation might slightly change with a different $\tilde{S}_{q,max}$. However, their order of magnitude is expected to be general since the plots of a constant $\tilde{S}_{q,2}$ approach a linear increase with an increasing $\tilde{S}_{q,1}$. Subsequently, the relative standard deviation is investigated for unequally sized spheres.

In figure 7.16 the relative standard deviation $\hat{s}$ is presented in a three-dimensional diagram. The x and y-axis represent the RMS of the large sphere $\tilde{S}_{q,1}$ and the smaller sphere $\tilde{S}_{q,2}$, respectively, where $R_1 = 1$ and $R_2 = 0.5$. Again, a linear increase is obtained if one the spheres is smooth, i.e., $\tilde{S}_{q,1} = 0$ or $\tilde{S}_{q,2} = 0$, and also for

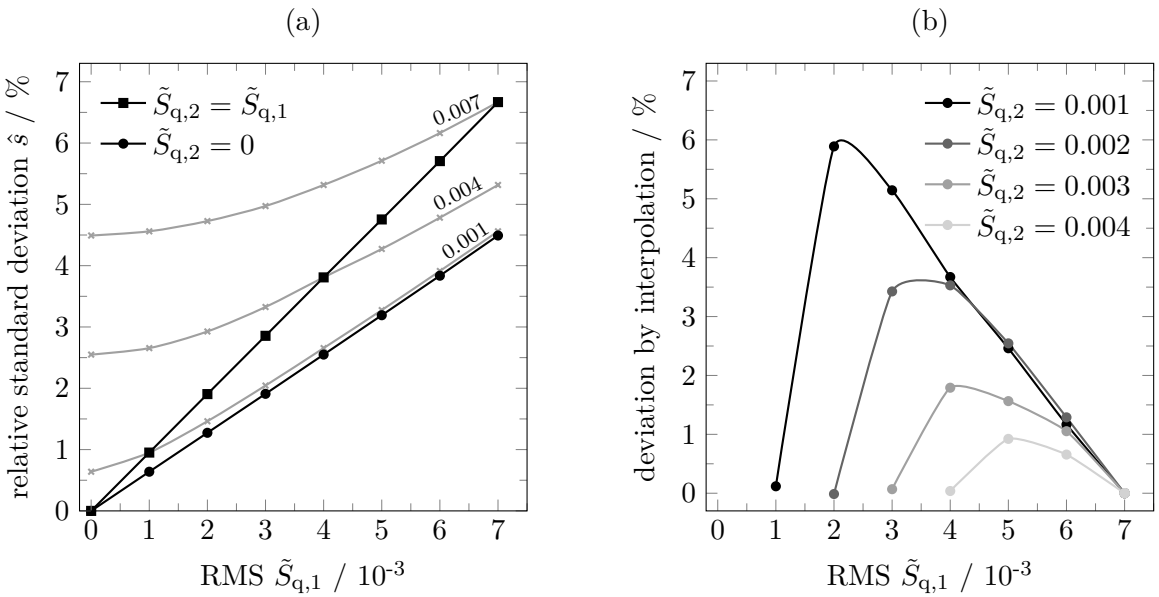

Figure 7.15.: RMS dependency of the relative standard deviation $\hat{s}$ for two equally sized spheres (a) and the deviation from a linear interpolation (b) ($\tilde{V} = 0.05$, $\tilde{a} = 0.05$, $\theta = 40°$ and $\varepsilon = 0.1$)

$\tilde{S}_{q,1} = \tilde{S}_{q,2}$. However, the characteristic diagram is not symmetric anymore. This becomes clearer when considering a two-dimensional plot as presented in figure 7.17. Note, that the marks for the plots of $\tilde{S}_{q,1} = 0$, $\tilde{S}_{q,1} = 0.005$ and $\tilde{S}_{q,1} = \tilde{S}_{q,2}$ correspond in figure 7.16 and figure 7.17.

A comparison of the $\tilde{S}_{q,1} = 0$ plots shows, that the relative standard deviation increases stronger with the RMS of the smaller sphere. This holds for any combination of RMS values, i.e., in figure 7.17 (a) the increase is always stronger between the lines of a constant $\tilde{S}_{q,2}$, whereas in figure 7.17 (b) the increase is much stronger on a line of a constant $\tilde{S}_{q,1}$. The higher fluctuation of the rough small sphere is traced back to the shorter three-phase contact line. For the sphere-plate system it is demonstrated, that the magnitude of the standard deviation cannot directly be estimated from the mean value (figure 7.7). However, the mean length of the three-phase contact line has an order of magnitude of 2 for the small sphere and 2.3 for the large sphere. When considering figure 7.7 a generally decreasing standard deviation with an increasing three-phase contact line seems to be reasonable in this range. Nevertheless, it cannot be concluded with certainty that the smaller three-phase contact line causes the higher fluctuation when roughness is applied to the smaller sphere.

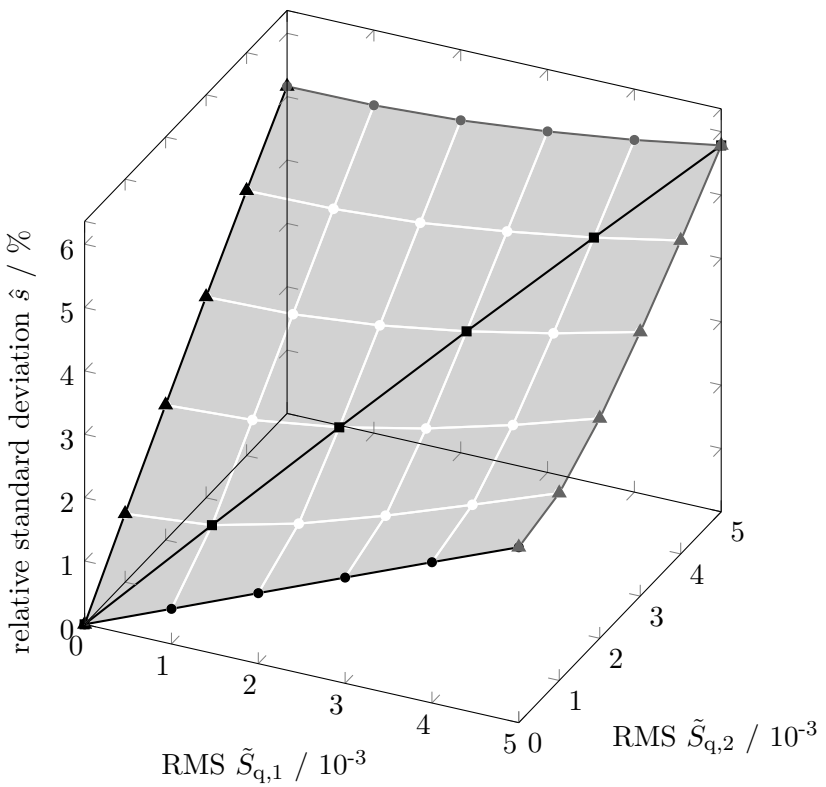

Figure 7.16.: RMS dependency of the relative standard deviation $\hat{s}$ for two unequally sized spheres ($R_2 = 0.5 \cdot R_1$) and $\tilde{V} = 0.05$, $\tilde{a} = 0.05$, $\theta = 40°$ and $\varepsilon = 0.1$

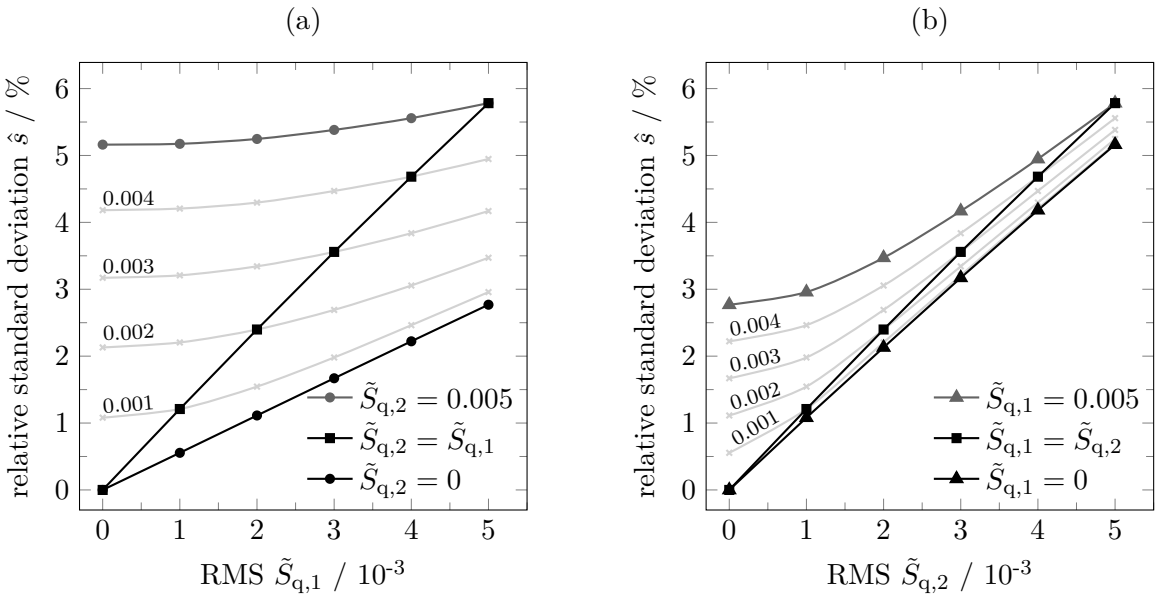

Figure 7.17.: RMS dependency of $\tilde{S}_{q,1}$ (a) and $\tilde{S}_{q,2}$ (b) of the relative standard deviation $\hat{s}$ for two unequally sized spheres ($R_2 = 0.5 \cdot R_1$) and $\tilde{V} = 0.05$, $\tilde{a} = 0.05$, $\theta = 40°$ and $\varepsilon = 0.1$

7.2.3. Influence of the diffusion coefficient

All previously presented results are computed for a constant diffusion coefficient of $\varepsilon = 0.1$. As described in section 5.2.1, an even higher diffusion coefficient does not influence the rough interface since the desired RMS is fixed (eq. (5.18)). However, a lower diffusion coefficient significantly affects the interface topology as illustrated in figure 5.5. In particular, the frequency of the asperities increases with a decreasing diffusion coefficient, which results in sharper edges and higher gradients on the interface. Generally, a high diffusion coefficient is advantageous for numerical stability, which can already be supposed from figure 5.5. In fact, interfaces that combine a high RMS with a low diffusion coefficient cannot be computed with sufficient stability, i.e., particular bridges might still converge, however, the convergence rate of the sample significantly decreases. Thus, the influence of the diffusion coefficient is investigated for a system of a rough and a smooth sphere ($\tilde{S}_{q,2} = 0$) with RMS of $\tilde{S}_{q,1} \leq 0.004$.
In figure 7.18 capillary bridges between the two equally sized spheres with $\tilde{V} = 0.05$, $\theta = 40°$, $\tilde{a} = 0.05$, $\tilde{S}_{q,1} = 0.005$ and $\tilde{S}_{q,2} = 0$ are illustrated. Since the liquid-solid interfaces considerably differ from each other, it is explicitly emphasized that the same RMS is realized on each interface. However, for $\varepsilon = 0.001$ the liquid-solid interface shows significant fluctuations and interface gradients. In contrast, applying a diffusion coefficient of $\varepsilon = 0.01$ leads to a much smoother interface.

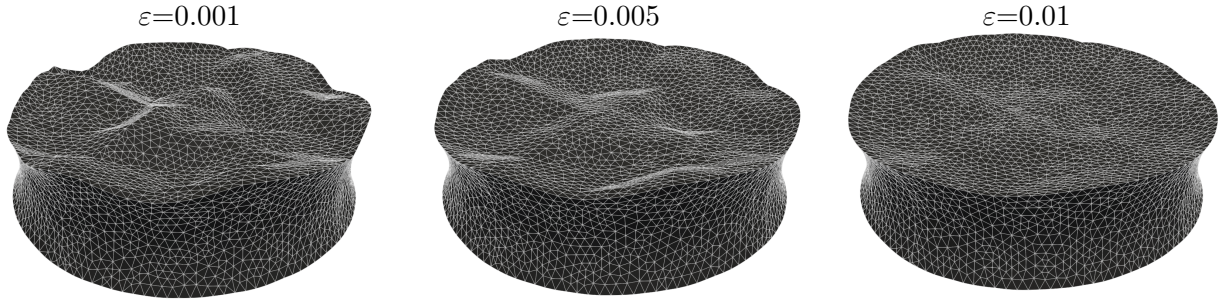

Figure 7.18.: Capillary bridges between two equally sized spheres for different diffusion coefficients ε ($\tilde{V} = 0.05$, $\theta = 40°$, $\tilde{a} = 0.05$, $\tilde{S}_{\mathrm{q},1\backslash 2} = 0.005\backslash 0$ and $\xi = 100$)

The relative standard deviation $\hat{s}$ is plotted in figure 7.19 (a) as a function of the diffusion coefficient ε. The RMS on the rough sphere $\tilde{S}_{\mathrm{q},1}$ varies from 0.001 to 0.004, whereas the other sphere is considered to be smooth, i.e., $\tilde{S}_{\mathrm{q},2} = 0$. For $\tilde{S}_{\mathrm{q},1} = 0.003$ and 0.004 a convergence rate of at least 98 % cannot be obtained for $\varepsilon \leq 0.001$ and, hence, the curves in figure 7.19 (a) end at $\varepsilon = 0.005$. Generally, a slight increase of the standard deviation is observed for a decreasing diffusion coefficient. Nevertheless, the overall influence seems to be almost negligible.
In figure 7.19 (b) the relative deviation $\Delta\hat{s}$ is presented. The deviation is calculated according to eq. (6.5) with $\hat{s}_{\mathrm{rv}} = \hat{s}_{\varepsilon=0.1}$. Thus, the curves in figure 7.19 (b) show the percentage increase that is obtained in figure 7.19 (a). Due to this normalization, the influence of the diffusion coefficient can be better estimated. In particular, it is demonstrated, that the relative standard deviation increases up to 15 % for a de-

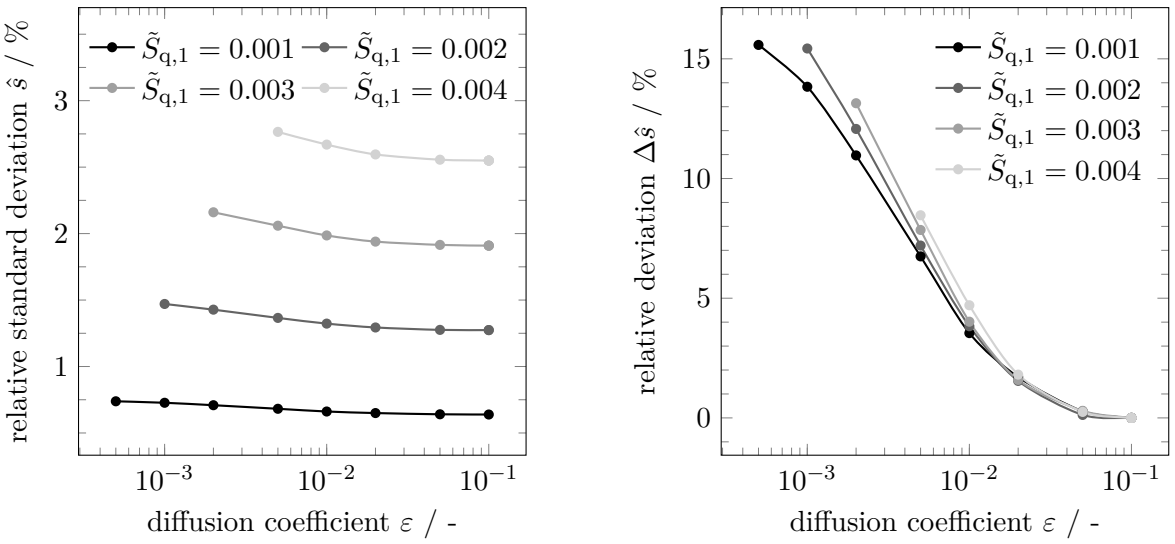

Figure 7.19.: Diffusion coefficient dependent relative standard deviation of the capillary force ($\tilde{V} = 0.05$, $\tilde{a} = 0.05$, $\theta = 40°$ and $\tilde{S}_{\mathrm{q},2} = 0$)

creasing diffusion coefficient from $\varepsilon = 0.1$ to $\varepsilon = 0.001$. Moreover, the gradient is slightly RMS dependent. For $\varepsilon = 0.005$ the difference between the four RMS curves is approximately 0.5 %. This difference increases with a lower diffusion coefficient and for $\varepsilon = 0.001$ the difference between $\tilde{S}_{\mathrm{q},1} = 0.001$ and 0.002 is already 1.6 %. Thus, from the presented curves it is concluded, that the increase of the standard deviation is stronger for higher RMS values, which, however, cannot be simulated with the current numerical setup due to the numerical instability.
Overall, the description of a rough interface only by the RMS seems to be insufficient as already discussed in section 3.7.1. The RMS considers the standard deviation from the centerline of the interface, i.e., the asperity height variation. However, it does not consider the asperity fluctuation and gradients, respectively. Nevertheless, particles with very sharp and edgy interfaces (for example figure 5.5, $\tilde{S}_{\mathrm{q}} = 0.01$ and $\varepsilon = 0.001$ or 0.01) do not seem to be highly relevant for practical applications. Generally, three different regimes for the smoothin coefficient can be obtained:

- $\varepsilon > 0.1$
  the interface of the rough particle is approximately constant due to the rough interface algorithm (section 5.2.1) and, consequently, diffusion coefficients larger than 0.1 do not have to be considered

- $0.1 > \varepsilon > 0.01$
  the influence of the diffusion coefficient on the relative standard deviation capillary force is below 5 % and might therefore be neglected

- $\varepsilon < 0.01$
  the influence of the diffusion coefficient rapidly increases and should consequently be considered in the computation of the capillary force distribution

In this chapter the novel method is applied to analyze the capillary forces between rough interfaces. The distribution of the capillary force is tested to be normal for all investigated systems and parameter combinations. For the sphere-plate system an intensive analysis of the influence of the volume, the gap distance and the contact angle on the capillary force distribution is presented and highly non-linear relations are pointed out. It is shown, that the standard deviation is nearly constant and independent of the gap distance for large bridge volumes. For low volumes, however, the influence of the gap distance and the contact angle might become significant. In addition to these parameters also the influence of the RMS is analyzed. It is shown, that the relative standard deviation increases linearly with the RMS in the system

with a smooth plane. Moreover, combinations of different RMS values on the interfaces are investigated for equally and unequally sized spheres. Again a linear relation between the relative standard deviation and the RMS is observed if either one interface is smooth or if both interfaces exhibit the same roughness. For the equally sized spheres it is demonstrated, that the characteristic diagram of the RMS can be approximated with an interpolation scheme that significantly reduces the computational effort. The characteristic diagram of the unequally sized spheres is apparently not symmetric. In fact, the relative standard deviation increases stronger if the roughness is applied to the smaller sphere. The diffusion coefficient is interpreted as the frequency of the asperities, i.e., a high diffusion coefficient implies a low frequency and less sharp gradients on the interface. It is demonstrated, that the influence of the diffusion coefficient is negligible for relatively high values and increases for very small coefficients. In this context it must be considered, that very low diffusion coefficients cannot be simulated when combined with a high RMS. However, with respect to real physical particles, the low diffusion coefficients seem to be of minor interest. In the next chapter, the results are discussed with respect to their application to further research and, moreover, evolution potential of the numerical implementation is deduced.

8. Discussion and outlook

In this chapter the results and the implementation of the method are discussed with respect to three different aspects. First, the questions of existence, uniqueness and stability on highly rough interfaces are discussed (section 8.1). Second, the application of the presented model for future investigations is discussed (section 8.2). In particular, the development of the rough force and torque model, that is suitable for the simulation of a particle cluster via a discrete element method (DEM) is analyzed. Third, hands-on experiences with the algorithm as well as the detailed analysis of the data reveal significant potential to improve the numerical implementation which is finally presented (section 8.3).

8.1. Existence, uniqueness and stability of static solutions

The presented method allows the computation of capillary bridges between complex rough interfaces. This, however, rises the questions of existence, stability and uniqueness of these solutions. In the literature it is frequently not distinguished between existence and stability. For example, the maximum separation distance for which a capillary bridge can exist is discussed as a stability problem, however, strictly speaking this is a question of existence (section 3.6). In this work, existence is associated with the question, if a solution of the Young-Laplace equation is found. Thereupon, this solution can be either stable or unstable (section 3.4.3), i.e., from a mathematical perspective, the energy state can be a minimum or a saddle point. Moreover, with respect to volatile liquids, also a thermodynamic stability of these solutions can be considered, which, however, is discussed in section 2.4 and is not covered in this discussion.

The existence of capillary bridges is usually investigated with respect to a certain particle distance. However, on highly rough interfaces also other aspects must be considered. In figure 8.1 a capillary bridge is illustrated for a given contact angle θ. Case (a) represents a possible capillary bridge. For a slightly shifted liquid-gas interface, i.e., case (b), a self-intersection between the liquid-gas interface Γ_{lg} and the solid interface Γ_{s} results. In the current implementation of the code the level-set between the solid interface Γ_{s} and the liquid-solid interface Γ_{ls} is minimized, which inherently

requires slight numerical intersections between these two interfaces directly at the three-phase contact line. Thus, an unwanted and unphysical intersection between the liquid-gas interface Γ_{lg} and a large asperity as presented in case (b) cannot be detected straight forward by the code. In particular, a criterion for the typ of intersection would have to be developed. For the results presented in chapter 7 such an intersection does most probably not occur since the particles are less rough than illustrated in figure 8.1. Nevertheless, for highly rough interfaces this local phenomenon might significantly influence the capillary bridge. Wang et al. [Wan09] investigate capillary bridges arising from condensation. The rough interfaces are modeled by two superimposed sinus curves which is a two dimensional fractal. They argue, that with an increasing humidity the meniscus is pinned at the edge of an asperity until the energy level is high enough to directly jump to the next asperity. Thus, according to their model, the same capillary bridge exists at different energy levels and the development of the meniscus is discrete. However, at this point it remains unclear how the physical capillary bridge looks like in case (b).
Another aspect is demonstrated in case (c). If the three-phase contact line starts at the right side of an asperity, the contact angle boundary condition might lead to a locally convex curvature. However, also other physical aspects, such as an additional condensation between two asperities are conceivable. Thus, the physical solution is unclear and, in particular, it remains open, whether molecular effects beyond the described model must be considered for these cases.
With respect to the stability, it is generally not impossible that the capillary bridge might locally change between convex and concave as long as the mean curvature remains constant. The Plateau sequence already includes unduloids with one inflection point, i.e., a changing sign of the principal radius r_1 from negative to positive (section 3.2). However, Orr et al.[Orr75] argue, that a capillary bridge with more

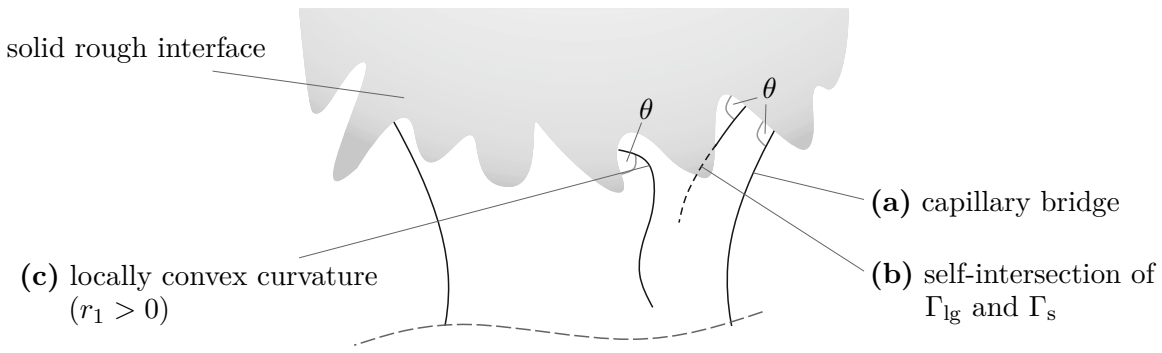

Figure 8.1.: Existence of capillary bridges at highly rough interfaces

than one inflection point is most probably unstable and Fel and Rubinstein [Fel15] proofed this in the case of capillary bridges between parallel plates. Nevertheless, they also demonstrate stable capillary bridges with two inflection points between two spheres [Rub14]. Thus, even in these simple, axissymmetric cases a closed form solution of stability cannot be obtained.

In the rough and complex three-dimensional case, an analysis of the stability is generally possible. Therefore, the eigenvalues of the Hessian (eq. (5.22)) must be determined, which is very expensive with respect to computational time. Nevertheless, the implemented Newton scheme is of second order and, thus, it is robust towards unstable solutions. In particular, it does involve information of the second order derivative which must be non-zero. Thus, the solution does not converge towards an unstable saddle point of the energy. This is demonstrated in [Sch22] for capillary bridges that are obtained by Rubinstein and Fel [Rub14]. In particular, the algorithm does not converge towards an unstable unduloid meniscus even if this meniscus is chosen as initial guess. Instead, the Newton scheme convergences towards the solution that is predicted to be stable.

Another stability analysis is presented by Farmer and Bird [Far15]. They experimentally observed non-axisymmetric capillary bridges for very large volumes and convex menisci. However, a simulation with *Surface Evolver* usually leads to the well known symmetric solution. Only by an artificial perturbation of this solution, the non-axisymmetric solution, that is consistent with the experimental observation, is obtained. In contrast, the presented method directly leads to the axially shifted capillary bridge which is traced back to the second order Newton scheme.

However, although a stable solution is obtained by the algorithm, it cannot be ensured that this is the only existing and stable capillary bridge for the given system configuration. The three-dimensional situation at the rough interface is much more complex than illustrated in figure 8.1. Thus, slightly different stable capillary bridges with the same predefined parameters might exist. In this context, also random parameters of the emerging process of the capillary bridge might determine which capillary bridge is realized. However, the emerging process if far beyond the presented model. Nevertheless, even if the question of uniquness cannot be answered in this work, it seems to be reasonable that the differences between possible solutions are minor with respect to the mean capillary force and the standard deviation of an overall rough interface sample. Thus, these parameters might be robust towards the existence of further capillary bridges.

8.2. Development of a rough force model for DEM simulations

The general idea of a multi-scale simulation is presented in figure 8.2. The behavior of a particle cluster is frequently investigated by a DEM that is first presented by Cundall and Strack [Cun79]. The principle of this method is to solve Newton's law of motion for each particle, i.e., $m\mathbf{a} = \mathbf{F}$, where m is the mass of a particle, $\mathbf{a}$ its acceleration vector and $\mathbf{F}$ the net force vector acting on the mass. Moreover, the particle rotation is included via $\mathrm{I}\boldsymbol{\alpha} = \boldsymbol{\tau}$, with I being the moment of inertia of the particle, $\boldsymbol{\alpha}$ the angular acceleration vector and $\boldsymbol{\tau}$ the torque vector. Due to the particle interaction, a system of coupled differential equations results. The force is composed by various components such as gravitation, contact forces, viscous forces and interparticle forces, which are further subdivided into van der Waals, electrostatic and capillary forces (section 3.1). Thus, deriving the net force acting on each particle is very complex and can apparently not be done simultaneously within a DEM simulation. Instead, simple analytical force models, such as eq. 3.12, or databases are required, which can then be implemented in a larger scale simulation in order to consider the lower scale effects. Similarly, the results of a DEM simulation, such as the viscosity of a powder material, can subsequently be implemented in a continuum model corresponding to a computational fluid dynamic (CFD) simulation since on this scale the direct consideration of each particle is impossible.

At present, the DEM models for capillary forces are based on a single value, i.e., the capillary force, that depends on several parameters such as volume V, particle distance a and particle radius R. Examples are presented in [Cha18; Lia98; Liu11; Mik98; Mug00; Tsu16]. Using the results presented in here, this single value can be replaced by a force distribution that accounts for the particle roughness. However,

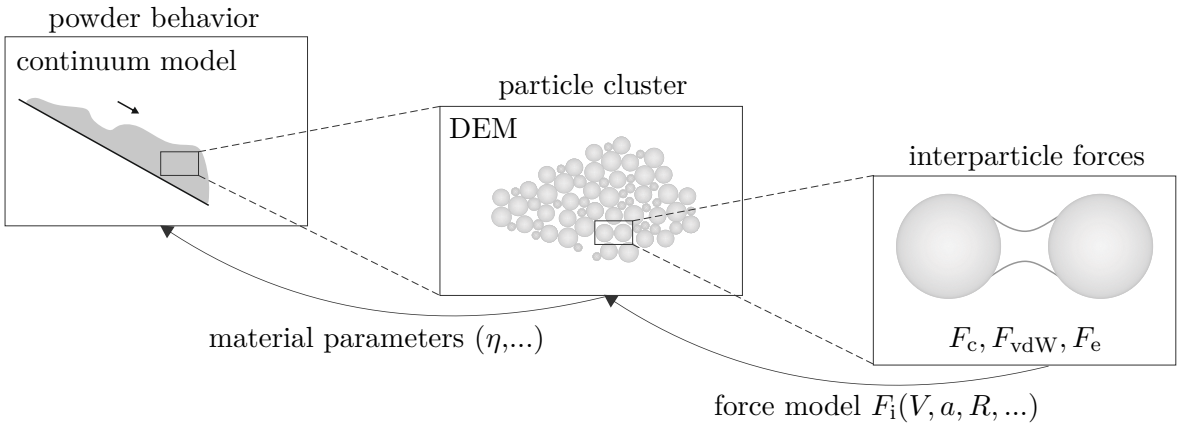

Figure 8.2.: Multiscale simulation of wet granular materials and powders

the expected influence on the behavior of the particle cluster should be discussed before descrbing a possible implementation.
A very important result of this work is, that the capillary force is normally distributed, which could not be asssumed a priori. In addition it is shown, that the mean capillary force $\bar{F}_\mathrm{c}$ can be approximated very good by the capillary force of the smooth reference system. As explained in section 7.1.3 the slightly larger values of the rough systems are traced back to the reduced effective mean gap distance. Thus, the effect of a normally distributed capillary force on the behavior of a homogenous and spherical particle cluster might be minor since higher and lower force most probably cancel each other statistically out. However, the presented method can be applied to an arbitrary particle shape. Thus, for particles other than rough spheres, considering the actual particle shape might influence the powder behavior. Moreover, for non-symmetric bridges between rough particles also capillary torque is expected and at this point the mean value and the distribution of the capillary torque are unknown. Thus, eq. 3.10 can be implemented into the presented method in order to analyse the torque distribution and to estimate its possible impact on a non-symmetric or even rough DEM model. Note, that a complete capillary force model also includes the rupture distance to estimate the radius of action. Generally, it is possible to compute these distances with the presented model, however, this is not part of this work and, hence, not discussed further on.
Although the impact of a normally distributed capillary force as presented in this work is assumed to be minor from the current point of view, the application to an extended DEM model is theoretically discussed since other types of particle shapes might be considered in the future. The general idea for the implementation of capillary force and torque distributions is, to develop a database that returns the mean values and their standard deviations.

Capillary force distribution

In section 7.1.1 and 7.2.1 the distribution of the capillary force is tested to be normally distributed which is an important result of this work. The accordance with a theoretical distribution is an important aspect with respect to the setup of a database since the probability of a certain value can be derived from two parameters, i.e., the standard deviation σ and the expected value μ. For the distribution of the capillary force these two values are estimated by s and $\bar{F}_\mathrm{c}$.

Interpolation of the mean capillary force and the standard deviation

The two parameters of interest, i.e., s and $\bar{F}_\mathrm{c}$, depend on the input parameters volume $\tilde{V}$, gap distance of the smooth base system $\tilde{a}$, contact angle θ_i, RMS $\tilde{S}_\mathrm{i}$ and ε which must be evaluated for a defined geometry. In section 7.1.2 it is demonstrated, that the volume, gap distance and contact angle significantly depend on each other. For low volumes the influence of the gap distance and contact angle on the relative standard deviation $\hat{s}$ might be significant whereas for large volumes a gap distance independent relative standard deviation is observed. The mean capillary force agrees well with the capillary force of the smooth system. Thus, for an independent relative standard deviation $\hat{s}$ the absolute standard deviation of many parameter configurations might be obtained by the smooth capillary force $\tilde{F}_\mathrm{c,sm}$ and the relative standard deviation. This might reduce the number of required rough simulations. However, the characteristic diagrams of the volume, gap distance and contact angle must be investigated in detail for each interface geometry. Consequently, it does not seem to be possible to develop simple analytical expressions for these dependencies and, thus, the application of a database seems to be reasonable.
The relative standard deviation turned out to increase linear with $\tilde{S}_1$ if $\tilde{S}_2 = 0$ and also for $\tilde{S}_1 = \tilde{S}_2 = 0$. For $\tilde{S}_2 \neq 0$ the deviation from a linear dependency increases with $\tilde{S}_2$. However, for low $\tilde{S}_2$ an approximately linear increase can be assumed which offers the possibility to reduce the required simulations for database. Only for very high values additional simulations might be reasonable. The influence of ε is negligible for rough interfaces that are not too edgy. Only for very high gradients, i.e., $\varepsilon < 0.01$ the diffusion coefficient must be taken into account. However, these particles might not be of highly practical interest.
Overall, the dependencies of the RMS and the diffusion coefficient are very suitable for developing a DEM database. This is in particular important with respect to the complicated interdependencies of the volume, gap distance and contact angle that most frequently cannot be interpolated from just a few simulations. Thus, a characteristic diagram of these parameters must be obtained with a relatively high resolution. However, for each point in this diagram differently rough particles can be obtained by interpolation. This is exemplarily demonstrated in section 7.2.2 for two equally sized spheres. In particular, the whole characteristic diagram can be obtained by only 8 simulations within an accuracy of 6 % or, with an accuracy below than 3 % by considering 13 simulations, respectively. It is worth mentioning, that this approximation neglects the increasing mean capillary force that is caused by the slightly decreased gap distance (section 7.1.3). However, in figure 7.13 it is demonstrated, that this

influence is below 2.6 % for the highly rough spheres and might, consequently, be neglected. Moreover, these interpolation inaccuracies must be related to the statistical uncertainty of 9.20 %. In particular, it seems to be reasonable to reduce the number of simulation points and accept a deviation of 3 %, which allows a larger sample size. This would significantly reduce the dominating the statistical uncertainty and, consequently, improve the overall accuracy. Nevertheless, these considerations are only reasonable with respect to predefined computational resources.
Overall, the development of a database seems to be possible with a moderate simulation time. Of course, the computational resources define the accuracy of such a database. In particular, the accuracy depends on the numerical and statistical error (section 6.2 and 6.3) as well as on the resolution of the characteristic diagrams.

Volume vs. pressure method

The probably most important aspect for the development of a database is its application to a real physical problem. In particular, the difference between a constant volume and a constant pressure method must be considered. In this context it is important to know, that computation of the standard deviation already depends on using either the volume or pressure approach, i.e., $s_{\text{volume method}} \neq s_{\text{pressure method}}$. This is very different from the calculation of the capillary force between smooth interfaces, since there, the output is independent of the used method.
The effect is explained by considering a theoretical case that is illustrated figure 8.3. The capillary bridge is obtained between the solid interface of a given random seed ξ_{i}. Now, it is assumed, that an additional asperity occurs in the inner interface Γ_{sl} due to a different realization of the same roughness, i.e., a different random seed $\xi_{\text{i+1}}$. In a constant pressure method this would not change the three-phase contact line or the liquid-gas interface Γ_{lg}. Only the area of the liquid-solid interface $\tilde{A}_{\text{ls}}$ and the volume $\tilde{V}$ change. However, both parameters are not directly used for the computation of the capillary force (eq. (3.7)) and, consequently, a constant capillary force results for ξ_{i} and $\xi_{\text{i+1}}$. If, however, a constant volume method is applied, the liquid volume is displaced outwards by the additional asperity since it must be kept constant. Thus, the liquid-gas interface Γ_{lg} and, consequently, its area $\tilde{A}_{\text{lg}}$ and mean curvature $\tilde{H}$, change. In addition, also the liquid-solid interface Γ_{sl} and the three-phase contact line vary from the other realization of the interface roughness. Thus, in this theoretical case a standard deviations of $s_{\text{pressure method}} = 0$ and $s_{\text{volume method}} > 0$ would be obtained. Note, that this effect is the same for a vanishing asperity that causes a inwards displacment of the volume.

Of course, a different random seed does, in the very most cases, not purely change asperities inside the liquid-solid interface. Thus, when applying a pressure method, different asperities on the three-phase contact line lead to a different liquid-solid interface Γ_{sl} and also to a different liquid-gas interface area $\tilde{A}_{\mathrm{lg}}$. However, the mean curvature $\tilde{H}$ and the capillary pressure $\Delta\tilde{p}$, respectively, are a priori kept constant (eq. (2.15)), which significantly influences the expected standard deviation. From the capillary force equation (eq. (3.7)) it is concluded, that the surface tension force depends on the length and orientation of the three-phase contact line, which fluctuates in either the pressure or volume approach. However, if the pressure is assumed to be constant, the fluctuation of the pressure force depends only on the normal area of the solid-liquid interface. In contrast, in a constant volume approach, the capillary pressure itself fluctuates additionally to all other parameters in eq. (3.7).
From these considerations, a smaller standard deviation is expected in a constant pressure method since changes of the inner asperities do not influence the liquid-gas interface. The difference between the two approaches most probably increases with a dominant pressure force. However, the order of magnitude can hardly be estimated since neither the geometrical changes of the capillary bridge, i.e., the solid-liquid and the liquid-gas interface, nor the effect of these influences can be predicted. In contrast to the standard deviation, the mean capillary force is assumed to be relatively independent of the choice of either a volume or pressure method. The expected higher spread width of the capillary force in a volume approach is estimated to occur in both directions, i.e., lower and higher capillary forces are expected. Since there is no reason to assume a shift in one of the directions a constant mean value of the capillary force is probable. This would also be consistent with the smooth system, where the capillary force is independent of either the volume or pressure approach.
The difference between the volume and the pressure method must be considered in the development of a rough capillary force model for a DEM simulation. In a particle cluster the constant parameter is either the humidity or the volume. In

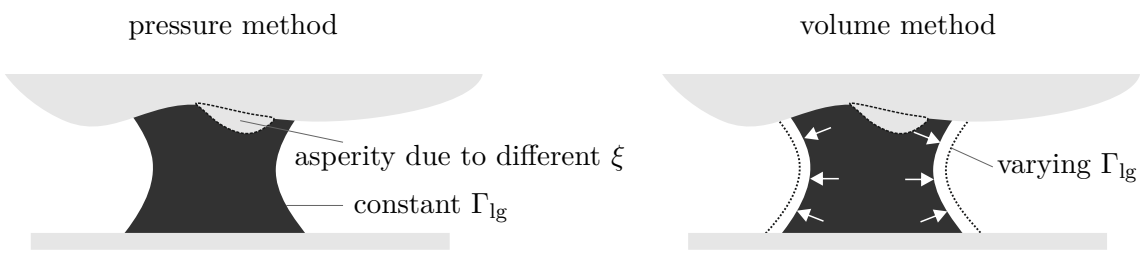

Figure 8.3.: Influence of inner asperities in a constant pressure and a constant volume method

the case of non-volatile liquids the application of the volume method seems to be reasonable since stable and independen capillary bridges with a different capillary pressure exist. In contrast, for volatile liquids such as water, the humidity would be constant in a practical approach. Thus, in a thermodynamic equilibrium the system consists of capillary bridges with the same capillary pressure. However, the convergence towards a thermodynamic equilibrium is a time-dependent process. In particular, the condensation or evaporation of liquid takes time which must be related to the characteristic time scale of the system. A pressure constraint seems to be reasonable for infinitely slow systems, whereas a volume constraint is associated with infinitely fast particle movements. Since a real system is neither infinitely slow nor infinitely fast, the dominant effects must be estimated for the model and even a combined pressure and volume approach is conceivable. In any case, the development of an explicitly pressure constraint method for rough capillary bridges is desirable for the modeling of volatile liquids in a particle cluster.

One option would be to iterate the volume for each simulation i of the sample n for the given pressure Δp. However, the relative standard deviation of the capillary pressure in the constant volume method turns out to be roughly below 6 % for a pressure that is not close to zero. Thus, in order to cancel out this fluctuation, an iteration of the volume for a given capillary pressure must be significantly below 1 %, which requires a huge number of iterations. In fact, the simulation time linearly increases with these iterations. Moreover, when considering the mesh resolution and the number of samples, an accurate iteration for a constant capillary pressure does not seem to be possible without extraordinary computational resources. Thus, an algorithm that directly solves eq. (5.16) for the capillary pressure $\Delta\tilde{p}$ is desirable. From a mathematical point of view this seems to be straight forward since only the unknown in the system of equations change.

Overall, the result presented in this work seem to be applicable to a multi-scale DEM. However, the use of either a pressure or volume approach must be considered carefully with respect to the physics of the simulated particle cluster. Moreover, a suitable database that is, on the one hand sufficiently accurate and, on the other hand, efficient enough with respect to the computational time of a DEM, needs to be developed.

8.3. Evolution of the numerical implementation

The numerical implementation of the optimization problem is very sophisticated and requires several adaptions of the classical Newton scheme. By the intensive use of

the simulation code and the data analysis, several tendencies are observed such as the significant overestimation of the surface tension force (section 6.2) or the rather slow and dissatisfying convergence of the contact angles. A deep and rather complex analysis of the source of these tendencies reveals optimization potentials. Reducing the simulation time is particularly interesting with respect to the relatively large numerical uncertainty of the standard deviation (section 6.3) since a confidence interval below 5 % requires approximately $n = 5000$ samples, i.e., 5 times as much simulation time. Subsequently, several optimization options are proposed.

8.3.1. Computation of the surface tension force

The convergence of the capillary pressure force and the surface tension force is very different as demonstrated and discussed in section 6.2 (figure 6.8). The overall convergence of the capillary bridge geometry is very good. However, the subsequent computation of the surface tension force requires a huge number of mesh triangles to sufficiently resolve the bending of the liquid-gas interface at the three-phase contact line. Otherwise, the liquid-gas co-normal vector $\tilde{\boldsymbol{\mu}}_{\mathrm{lg}}$ cannot be computed with sufficient accuracy which results in an severe overestimation of the surface tension force. As illustrated in figure 6.9 the bending increases with a decreasing contact angle θ and a less convex solid geometry, i.e., the bending of the capillary bridge is stronger at the plate.

The computation of the surface tension force is improved by changing the computation of the liquid-gas co-normal vector $\tilde{\boldsymbol{\mu}}_{\mathrm{lg}}$. The good convergence of the capillary bridge geometry is concluded from the convergence of the pressure force and the agreement of the three-phase contact line with the Dörmann model (table 6.3). Thus, optimization procedure does not need to be changed and only the computation of the co-normal vector, subsequent to the optimization, is adapted. One option would be, to estimate the co-normal by a higher order scheme, i.e., considering more triangles rather than only the triangle at the three-phase contact line (first order scheme). However, this is complex and not straightforward on an unstructured triangular mesh. Note, that figure 6.9 is only a schematic, two-dimensional illustration and in the three-dimensional situation the midpoints of the triangles are not in one line.

Another option is, to calculate a new co-normal vector $\tilde{\boldsymbol{\mu}}^{*}_{\mathrm{lg}}$ from the liquid-solid interface. It is reasonable to assume, that the three-phase contact line triangles of the liquid-solid interface are more accurate compared to the three-phase contact line triangles of the liquid-gas interface, since the bending of the liquid-solid interface is a lot smaller. Thus, from the co-normal $\tilde{\boldsymbol{\mu}}_{\mathrm{ls,i,j}}$ a new co-normal $\tilde{\boldsymbol{\mu}}^{*}_{\mathrm{lg,i,j}}$ is obtained for all

j triangles of the three-phase contact line i with $\langle \tilde{\boldsymbol{\mu}}_{\mathrm{ls,i,j}}, \tilde{\boldsymbol{\mu}}^*_{\mathrm{lg,i,j}} \rangle = \cos(\theta_{\mathrm{i}})$. This implies the exact realization of contact angle θ. Subsequently, the surface tension force is computed according to eq. (3.7) using the new co-normal $\tilde{\boldsymbol{\mu}}^*_{\mathrm{lg,i,j}}$.
This procedure is implemented and the results are compared to the Dörmann [Dör18] method. In table 8.1 deviations, that are defined by eq. (6.1), of the capillary force and the surface tension force are pointed out. Note, that the values of the old method correspond to table 6.3, however, they are again presented here for a direct comparison. The pressure force and the length of the three-phase contact line are omitted since they are not affected by the new computation method.
In table 8.1 it is demonstrated that the capillary force $F_{\mathrm{c,new}}$ is now underestimated compared to the Dörmann method. The order of magnitude of the deviation does not significantly change. For $\theta = 40°$ the absolute deviations are even slightly higher when using the new method. This is traced back to the new estimation of the surface tension force. Using the old method, the surface tension force is strongly overestimated since the effective contact angles are overestimated. In particular, deviations up to 36.68 % are obtained. When now using the new method, the surface tension force is underestimated. For $\theta = 10°$ an overestimation of more than 30 % at the plate reduces to an underestimation below 2 % and, at the sphere, a decrease from approximately 10 % down to 2 % is obtained. For $\theta = 40°$ the surface tension force is also underestimated with round about 1.5 %. Generally, an underestimation seems to be reasonable due to the polygon representation of the three-phase contact line since the length of a polygon is shorter compared to the smooth curve. This is consistent with table 6.3, where it is demonstrated that the three-phase contact line of this model is always underestimated compared to the Dörmann model.

Table 8.1.: Deviation in % between the old and the new computation of the surface tension force and the Dörmann [Dör18] for $\tilde{V} = 0.1$ and
1: $\theta_1 = \theta_2 = 10°$; 2: $\theta_1 = \theta_2 = 40°$;
a: $\tilde{a} = 0.004$; b: $\tilde{a} = 0.1$

	total		sphere (i=1)				plate (i=2)			
	F_{c}	$F_{\mathrm{c,new}}$	$F_{\mathrm{c,1}}$	$F_{\mathrm{c,1,new}}$	$F_{\mathrm{s,1}}$	$F_{\mathrm{s,1,new}}$	$F_{\mathrm{c,2}}$	$F_{\mathrm{c,2,new}}$	$F_{\mathrm{s,2}}$	$F_{\mathrm{s,2,new}}$
1a	1.74	-1.61	1.13	-1.54	8.29	-1.26	2.34	-1.68	36.68	-1.83
1b	2.31	-1.69	1.72	-1.75	9.10	-1.62	2.89	-1.62	32.76	-1.87
2a	0.64	-0.84	-0.06	-0.87	1.16	-0.60	1.34	-0.81	5.84	-1.09
2b	0.96	-0.97	0.42	-1.08	2.01	-0.75	1.49	-0.86	5.30	-1.41

The overestimation of the capillary force F_c with the old computation method is caused by the significant overestimation of the surface tension force. However, since the pressure force is underestimated (table 6.3), the two inaccuracies partially canceled each other out. With the new method both, the capillary pressure and the surface tension force, are underestimated and, thus, the inaccuracies add up. Overall, the absolute order of magnitude of the capillary force deviation does not change significantly. However, this is only the case for the presented capillary bridges, that are dominated by the capillary pressure force. With the improved method the capillary force with a high surface tension force ratio is accurately computed. Moreover, a great potential is offered by a significantly improved convergence as discussed subsequently.

The mesh study for $\theta = 20°$ and $\theta = 40°$, that is discussed in section 6.2, is performed using the new computation of the surface tension force. The results are illustrated in figure 8.4. The results of the old method correspond to the results that are presented in figure 6.7 and 6.8. In figure 8.4 (a) and (b) the convergence of the surface tension force $\bar{F}_s$ is demonstrated. Note, that with the new method the surface tension force is underestimated compared to the exact solution. Thus, the relative deviation $\Delta\bar{F}_s$ actually approach zero from below. However, in order to compare the convergence of the two methods, the absolut value $\left|\Delta\bar{F}_s\right|$ is presented in figure 8.4 (a) and (b).

For both contact angles a significantly improved convergence is demonstrated. Even for the coarsest mesh the maximum deviation from the most accurate solution is below 5 %. Moreover, the differences between the sphere and the plate are already below 1 % for approximately $0.7 \cdot 10^4$ ($\theta = 20°$) and $0.2 \cdot 10^4$ ($\theta = 40°$) mesh triangles. For both contact angles a maximal numerical error below 1 % is obtained for $1 \cdot 10^4$ triangles although this mesh resolution is significantly below the resolutions that are used in this work.

In figure 8.4 (c) and (d) the convergence of the mean capillary force $\bar{F}_c$ is presented. Analogous to the mean surface tension force, the mean capillary force of the new method is underestimated compared to the exact solution, i.e., $\left|\Delta\bar{F}_c\right|$ is plotted for a better comparison. The convergence towards a larger exact solution results from the fact, that both, the capillary pressure force and the surface tension force are underestimated and, consequently, this also holds for the capillary force. The curves of the new method are better converged since they are approximately horizontal for high mesh resolutions. Thus, the most accurate solution is considered to be very close to the exact solution. The gradients are below 0.07 % per 10^4 triangles. The numerical error of the old method is obtained by the relative deviation $\Delta\bar{F}_c$ and the

estimated deviation between the most accurate and the exact solution. Thus, an estimated error of 2.1 % is obtained for $\tilde{V} = 0.1$ (table 6.5). Using the new method, this error is obtained with a significantly lower mesh resolution, which is indicated by the dashed lines. In fact, with half as much triangles the numerical error is reduced by approximately 50 % and an overall numerical error significantly below 1 % is obtained. Note, that the curves of the old and new method both converge towards zero since the deviation from their most accurate solution is plotted. However, the absolute values differ from each other. In particular, the capillary force of the new method is 2.14 % ($\theta = 20°$) and 1.34 % ($\theta = 40°$) below the capillary force of the old method. In section 6.2 the deviation between the most accurate and the exact solution, i.e., the extrapolation of the convergence curve, is approximated by 0.6 %. Thus, this deviation might be higher than estimated, i.e., the numerical errors of the mean capillary force might be roughly 0.7 % ($\theta = 40°$) to 1.5 % ($\theta = 20°$) higher.
The improved computation of the surface tension force also influences the convergence of the standard deviation s that is pointed out in figure 8.4 (e) and (f). Just as the forces, the standard deviation of the new method convergences from an underestimated value, i.e., $-\Delta s$ is plotted in figure 8.4 for a better comparison with the previous results. Apparently, the standard deviation obtained by the new method shows less fluctuations. This might be traced back to the fact, the both force components converge from smaller to larger values. In contrast, when using the old method, the capillary pressure force and the surface tension force show opposed convergence direction (figure 6.8). For $\theta = 40°$ the standard deviation of the new method is better converged compared to the lower contact angle. However, in contrast to the capillary force, no full convergence is achieved and, consequently, the deviation between the most accurate solution and the exact solution must be considered. The averages of the last three gradients are 0.36 % ($\theta = 20°$) and 0.17 % ($\theta = 40°$) per 10^4 triangles. If, again, a nearly doubled number of triangles is used to approximate the exact solution, i.e., $3 \cdot 10^4$ triangles, roughly 1.1 % and 0.6 % are obtained. The overall error of the old method is estimated to be 2.1 % (table 6.5). Thus, if this error should be achieved by the new method, the relative deviation Δs is 1 % for $\theta = 20°$ and 1.5 % for $\theta = 40°$, which is indicated by the dashed lines. Note, that for $\theta = 40°$ the standard deviation is just about in the convergence region and, therefore, a higher mesh resolution is recommended.
Again, the reference values, i.e., the most accurate solutions, differ from each other. The most accurate standard deviation of the new method is 1.89 % ($\theta = 20°$) and 1.79 % ($\theta = 40°$), respectively, below the standard deviation of the old method.

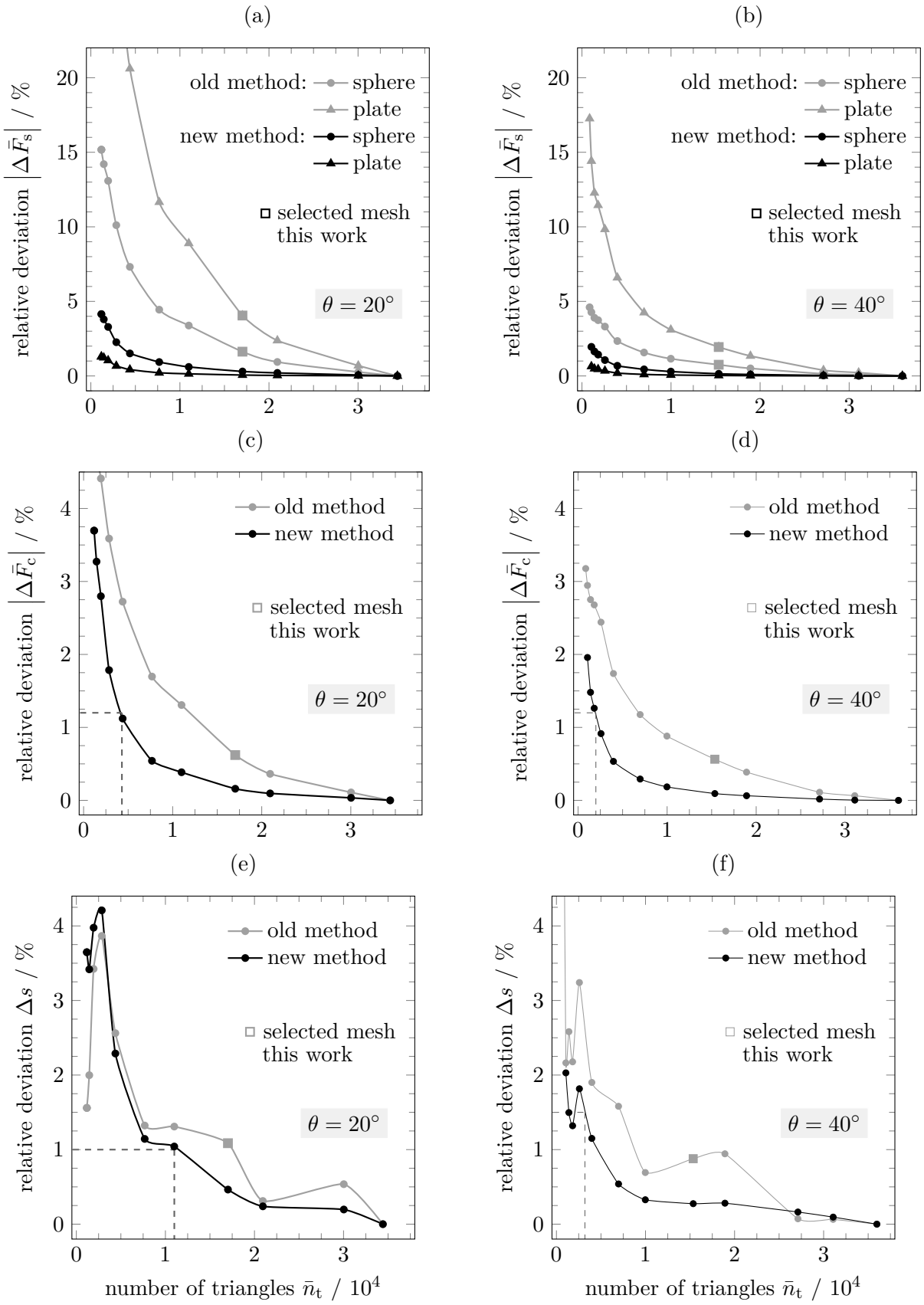

Figure 8.4.: Comparison of the mesh study for the old and the new computation of the surface tension force for a sphere-plate system with $\tilde{V} = 0.1$, $\tilde{a} = 0.1$, $\tilde{S}_\mathrm{q} = 0.005$ and $\varepsilon = 0.1$

In section 6.2 the deviation between the most accurate solution and the exact solution is estimated to be roughly 1.2 %. However, since the standard deviation of the new method is not fully converged the exact solution can hardly be estimated. Moreover, the standard deviation of the old method decreases whereas an increase is observed when using the new method. Consequently, both solutions approach each other and the deviation between the methods is reduced. Thus, when considering the old method, the estimated difference between the most accurate and the exact solution of 1.2 % seems to have a reasonable order of magnitude.
The improved convergence of the surface tension force implies a huge potential to increase the overall accuracy of the simulations. In section 6.4 the relation between the numerical and the statistical error is discussed. The accuracy of the mean capillary force is mainly determined by the numerical error, however, on a very good level. In contrast, the confidence interval of the standard deviation is 9.20 % which is relatively inaccurate and an order of magnitude larger than the numerical error. Thus, performing simulations with the selected meshes in this work and, hence, decreasing the numerical error, is not optimal. Instead, when considering both, the mean capillary force and the standard deviation, a mesh resolution of $0.75 \cdot 10^4$ triangles is sufficiently accurate. This will even reduce the numerical error of the mean capillary force by approximately 0.7 % ($\theta = 20°$) and 1 % ($\theta = 40°$), i.e., a numerical error significantly below 1 % is obtained. The numerical improvement of the standard deviation is, however, contact angle dependent and less pronounced for the low contact angle. In fact, for $\theta = 20°$ the numerical error of the standard deviation slightly increases by 0.1 % for the suggested mesh resolution, whereas a decrease by approximately 1 % is obtained for $\theta = 40°$. Simulations with the reduced mesh resolutions require an averaged simulation time of only one third of the previously selected mesh resolutions. Thus, with the same computational resources, the sample number can be increased to $n = 3000$ which leads to a confidence interval of $\mathrm{CI_s}(98\,\%) = 5.31\,\%$ (eq. (6.9)), i.e., an improvement by 3.89 %. This is remarkable and demonstrates the necessity to balance the numerical and the statistical error.
In conclusion, both, the mean capillary force and the standard deviation are simulated with a higher accuracy. On the one hand, the numerical error of the mean capillary force is reduced by $0.7-1\,\%$ whereas the reduction of the confidence interval is roughly estimated to be 0.2 % (figure 6.13 (a)). On the other hand, the numerical error of the standard deviation is nearly constant ($\theta = 20°$) and improved by 1 % ($\theta = 40°$), however, the reduction of the confidence interval by 3.89 % is remarkable. Thus, the

improved computation of the surface tension force has a great potential for the future applications of the presented work and is implement as default method.

8.3.2. Restricted displacement in the Newton scheme

A general observation from the hands-on experiences is an increasing simulation time and a more unstable convergence for $\theta < 40°$ at all volumes and gap distances. The large computation times are caused by the number of iteration steps. In particular, the number of iteration steps increases by approximately 50 % if the contact angle is reduced from $\theta = 40°$ to $\theta = 10°$. For $\theta > 40°$ also an increase of iterations is observed, however, on a very moderate level, which is not as significant for the simulation time and convergence.
The contact angle dependency of the iteration steps is traced back to the vertex displacement in the Newton scheme (eq. (5.24)). As described in section 5.2.2 optimality requires a displacement of the three-phase contact line vertices that is tangential to the liquid-solid interface, i.e., in the direction of $\tilde{\boldsymbol{\mu}}_{\mathrm{sl}}$ (eq. (5.15)). However, this is derived for a problem formulation without a touch constraint. In fact, a displacement in the direction of $\tilde{\boldsymbol{\mu}}_{\mathrm{sl}}$ invalidates the touch constraint on a curved solid interface (figure 5.7). Thus, an additional displacement to account for the touch constraint is required. In the original implementation of the algorithm, the co-normal direction $\tilde{\boldsymbol{\mu}}_{\mathrm{lg}}$ is chosen to span the $\mathbb{R}^2$, since this is advantageous in the code set up. However, any other vector could have been selected as long as it is linear independent of $\tilde{\boldsymbol{\mu}}_{\mathrm{sl}}$.
With a decreasing contact angle θ also the linear independence of $\tilde{\boldsymbol{\mu}}_{\mathrm{sl}}$ and $\tilde{\boldsymbol{\mu}}_{\mathrm{lg}}$ decreases and finally, for $\theta = 0°$ they even become linearly dependent. This is the main reason, why $\theta = 0°$ cannot be simulated with sufficient accuracy. Note, that it is possible to simulate contact angles below 10° on a very coarse mesh, since the numerical deviation between $\tilde{\boldsymbol{\mu}}_{\mathrm{sl}}$ and $\tilde{\boldsymbol{\mu}}_{\mathrm{lg}}$ is large enough on these meshes. However, the results are not accurate at all. For $\theta = 20° - 30°$ the simulations mainly converge, however, the computational time is considerably large and might be 5 times as high compared to larger contact angles. This disadvantageous dependency between the number of iterations and the contact angle is solved by using a vector other than $\tilde{\boldsymbol{\mu}}_{\mathrm{lg}}$ to account for the contact condition. In fact, the best choice is the vector normal to the solid

interface, since this is the shortest direction to contact. Thus, instead of $\tilde{\boldsymbol{\mu}}_{\mathrm{lg}}$ the vector $\tilde{\mathbf{n}}_{\mathrm{sl,i}}$ is used and eq. (5.24) is changed to

$$\mathbf{V}(\tilde{\mathbf{s}}_{\mathrm{j}}) = \begin{cases} \alpha_1(\tilde{\mathbf{s}}_{\mathrm{j}})\tilde{\mathbf{n}}_{\mathrm{sl,i}}(\tilde{\mathbf{s}}_{\mathrm{j}}) + \alpha_2(\tilde{\mathbf{s}}_{\mathrm{j}})\tilde{\boldsymbol{\mu}}_{\mathrm{sl,i}}(\tilde{\mathbf{s}}_{\mathrm{j}}), & \tilde{\mathbf{s}}_{\mathrm{j}} \in \Gamma_{\mathrm{lg}} \cap \Gamma_{\mathrm{sl}} \\ \alpha_1(\tilde{\mathbf{s}}_{\mathrm{j}})\tilde{\mathbf{n}}_{\mathrm{lg}}(\tilde{\mathbf{s}}_{\mathrm{j}}), & \tilde{\mathbf{s}}_{\mathrm{j}} \in \Gamma_{\mathrm{lg}} \wedge \tilde{\mathbf{s}}_{\mathrm{j}} \notin \Gamma_{\mathrm{ls}} \\ \alpha_1(\tilde{\mathbf{s}}_{\mathrm{j}})\tilde{\mathbf{n}}_{\mathrm{ls}}(\tilde{\mathbf{s}}_{\mathrm{j}}) + \zeta(\tilde{\mathbf{s}}_{\mathrm{j}})\mathbf{V}_{\tan}(\tilde{\mathbf{s}}_{\mathrm{CL}}), & \tilde{\mathbf{s}}_{\mathrm{j}} \in \Gamma_{\mathrm{ls}} \wedge \tilde{\mathbf{s}}_{\mathrm{j}} \notin \Gamma_{\mathrm{lg}}. \end{cases} \tag{8.1}$$

Note, that only the first case, i.e., the displacement of the three-phase contact line vertices is changed. By implementing eq. (8.1) a significant improvement of the convergence behavior at low contact angles is expected, which, however, has not been tested yet.

8.3.3. Iteration step

The necessity to reduce the computational time in order to increase the sample size and, consequently, the accuracy, is discussed previously. A further potential is the iteration step size. In this work, the step of both, the gradient decent and the Newton scheme, is fixed and based on hands-on experiences. Thus, the step size is a worst case estimation, i.e., it must be small enough to account for a stable simulation of the smallest triangles. However, larger triangles could be combined with a larger step size, which significantly reduces the number of iterations and, consequently, the simulation time.

The size of the triangles decreases with either a decreasing volume of the capillary bridge at a constant number of triangles, or a higher mesh resolution at a constant volume. In this work, the constant step size is a compromise between simulation time and accuracy at low volumes. In section 6.2 it is demonstrated, that the selected step is still too large for a finer mesh resolution at $\tilde{V} = 0.01$. However, with respect to a manageable computational time, it is too small for $\tilde{V} = 0.5$, i.e., these simulations require significantly more computational time (table 6.4), however, without any benefit with respect to the accuracy.

A solution to this issue is an adaptive step size in the Newton scheme that converges each capillary bridge with an optimal step size in each step. Note, that the step could also be adapted in the gradient decent scheme. However, since this scheme is only used to compute a good initial guess for the Newton scheme, this does not seem to be necessary.

The self adapting step size is very useful for an optimal convergence speed. However, in section 8.3.1 it is demonstrated, that the improved computation of the surface ten-

sion force allows a high accuracy at significantly lower mesh resolutions than presented in this work. Thus, the potential for a further decrease of the computational time is lower. Nevertheless, when considering capillary bridges at very different volumes (figure 7.2) it seems to be reasonable to use different step sizes in order to ensure a stable convergence for all parameters.

In this chapter the existence, uniqueness and stability of the results is discussed. For highly rough particles two different situations are identified, i.e., a self-intersection of the liquid-gas and the solid interface and a locally convex curvature. In both cases, the physics of the capillary bridge system remains unclear. With respect to the algorithm it is pointed out, that solutions that are stable since they are obtained by the second order Newton scheme, however, the existence of further stable solutions cannot be excluded. Moreover, the development of a rough force model for a DEM simulation is discussed. The complex characteristic diagrams of the volume, gap distance and contact angle seem to require the development of a database rather than analytical expressions. Moreover, the application of either the volume or pressure method must be considered carefully since the standard deviation depends on the choice of method. Finally, comprehensive potential do improve the numerical implementation of the algorithm is pointed out. In particular, the different computation of the co-normal vector accelerates the convergence of the surface tension force which significantly reduces the required mesh resolution. Thus, for future work, the overall error can be reduced by considering larger sample sizes at moderate computational times.

9. Summary

In this work a novel method to compute capillary forces between arbitrary and, more specifically, rough interfaces is presented. The considered capillary bridge model is based on an energy minimization approach. In particular, the total free energy is minimized constrained by a predefined volume and given solid interfaces. The Lagrangian is derived and formulated without an explicit expression for the mean curvature. In fact, this is one of the major advantages of the novel method, since the approximation of the curvature usually causes significant numerical issues. A combined gradient decent and Newton scheme, that is tailor made for the capillary bridge problem, are applied to solve the Lagrangian. In the Newton scheme the displacement direction of the vertices is defined individually for each interface (Γ_{lg} and $\Gamma_{\mathrm{sl,i}}$) and also for the three-phase contact lines ($\Gamma_{\mathrm{lg}} \cup \Gamma_{\mathrm{sl,i}}$). Moreover, numerical stability is increased by a remeshing procedure with an additional correction of critical triangles at the three-phase contact line. Since the method is applied to investigate the influence of roughness, a rough interface model is implemented as well. Here, a normal asperity height distribution is added to a smooth base geometry. However, since this leads to very sharp edges and large gradients, which are numerically fragile and frequently nonphysical, a diffusion step according to the Laplace equation is added. By the means of this, the rough interface is smoothed at a constant root mean square roughness (RMS).

The novel method is verified by comparing it with results of the literature for smooth interfaces. A verification with a rough interface model is not possible, since, to the best of the authors knowledge, capillary bridges between directly resolved rough interfaces have not yet been simulated. A comparison with the elliptic integral approach of Orr et al. [Orr75] and the shooting method of Dörmann [Dör18] shows a very good agreement of the capillary forces and the geometrical parameters such as the mean curvature of the three-phase contact line. The maximum deviation of the capillary force is significantly below 3 %. However, it is also revealed that the surface tension force is considerably overestimated by the novel method, in particular, for low contact angles. Due to this finding, the surface tension component is considered in detail in the mesh study. In this analysis, a poor convergence of this force component is

demonstrated which is traced back to an inaccurate computation of the co-normal vector μ. Therefore, a relatively high mesh resolution is required in order to obtain accurate results.

The investigation of rough interfaces requires a statistical approach. In particular, the same RMS can be realized by an infinite number of asperity realizations. For a given RMS and diffusion coefficient ϵ, a distribution of the capillary force is derived. Hence, the mean value and the standard deviation are the parameters of interest and the numerical error as well as the statistical uncertainty are conservatively estimated for both of them. The numerical error for medium and larger volumes ($\tilde{V} > 0.5$) is evaluated to be below 1.5 %, while the numerical error of the standard deviation is approximated to be below 3 %. For very low volumes both errors increase up to 2.6 % and 3.8 % for $\tilde{V} > 0.01$. Overall, the numerical accuracy is good and the meshes are selected as a compromise between accuracy and computational time. The statistical uncertainty is described by confidence intervals. For a sample size of $n = 1000$ and a significance level of 98 % the confidence interval of the capillary force is 1.06 % for $\tilde{V} > 0.01$ and considerably below 1 % for all other volumes. In contrast, for the standard deviation a confidence interval of 9.20 % is obtained, which is independent of the simulation parameters. For a confidence interval below 5 % a sample size of approximately $n = 5000$ is required which, unfortunately exceeded the available computational resources in this work. In conclusion, the numerical error of the mean capillary force is slightly higher compared to the statistical error and the order of magnitude of the overall error is satisfying. In contrast, the overall error of the standard deviation is clearly dominated by the statistical uncertainty. In fact, a confidence interval of 9.20 % is dissatisfying and, consequently, a larger sample size is favorable for future research.

Subsequent to the evaluation of the method an application to rough interfaces is presented. First, the distribution of the capillary force is determined to be normal for all investigated systems and parameter configurations which is an important result of this work. For the system of a rough sphere and a smooth plane the influence of the classical capillary parameters, i.e., the volume, gap distance and contact angle, is analyzed and highly non-linear dependencies are observed. The investigation of the RMS shows, that the mean value of the capillary force is slightly above the capillary force of the smooth system. This finding is traced back to the gap distance being reduced by the addition of the asperities. A very interesting relation is obtained for the RMS and the standard deviation. It turned out that, if one of the interfaces is considered to be smooth, the standard deviation linearly increases with the RMS.

This is also demonstrated for systems of equally and unequally sized spheres. Furthermore, a linear dependency is observed, if the same RMS is applied to both interfaces. Combinations of differently rough interfaces reveal a non-linear dependency, which, however, can still be approximated sufficiently accurate by linear interpolation in order to reduce the computational effort. For unequally sized spheres the fluctuation of the capillary force is dominated by the RMS of the smaller sphere which is traced back to increasing asperity size in relation to the three-phase contact line. Finally, the influence of the diffusion coefficient is investigated. It is pointed out that the impact on the standard deviation becomes significant if the coefficient approaches zero. Although very edgy particles appear to be of minor physical interest it shows, that the classical characterization of rough interfaces only by the RMS might not be sufficient enough.

Finally, the existence, uniqueness and stability of the results is critically discussed. All solutions of the presented method can potentially exist in real physical systems, however, it cannot be excluded that more solutions exist. Due to the usage of the second order Newton scheme, real minima, rather than saddle points or maxima, are obtained and, consequently, the presented solutions are all stable.

Moreover, the results are analyzed with respect to their application in a discrete element method. The normal distribution and the linear dependencies with the RMS offer a great potential to develop a suitable database. However, the complex dependencies with the volume, gap distance and contact angle require a lot of computational resources to provide a sufficient number of data points. Additionally, the difference between the volume and the pressure approach must be considered. In particular, the distribution of the capillary force depends on the selected method. Thus, with respect to a DEM implementation, it must be considered which method is more suitable to describe the real physical process.

The hands-on experience with the method and the large amount of data also revealed evolution potential of the numerical implementation. A different computation of the co-normal vector μ is already realized and a fundamental improvement of the mesh convergence and the accuracy is demonstrated. In particular, the numerical error can be reduced while simultaneously reducing the simulation time. The main benefit of this implementation is, however, the large potential to increase the sample size due to the faster convergence and to reduce the dominant statistical uncertainty of the standard deviation for future work.

Generally, the presented method offers a huge potential to investigate capillary briges with an abritray shape. Besides roughness, this could also be any non-spherical par-

ticle. Thus, in the future, it will be very useful for the understanding of experimental results such the large fluctuations that are observed in AFM methods since the the actual particle or tip shape can be considered.

References

[Ack96] H. D. Ackler, R. H. French, and Y.-M. Chiang. "Comparisons of Hamaker Constants for Ceramic Systems with Intervening Vacuum or Water: From Force Laws and Physical Properties". In: *Journal of Colloid and Interface Science* 179.2 (1996), pp. 460–469.

[Ada02] M. J. Adams, S. A. Johnson, J. P. K. Seville, and C. D. Willett. "Mapping the Influence of Gravity on Pendular Liquid Bridges between Rigid Spheres". In: *Langmuir: the ACS journal of surfaces and colloids* 18.16 (2002), pp. 6180–6184.

[Ada97] A. W. Adamson and A. P. Gast. *Physical chemistry of surfaces*. 6th ed. A Wiley-Interscience publication. New York: Wiley, 1997.

[Ami04] A. Amirfazli and A. W. Neumann. "Status of the three-phase line tension: A review". In: *Advances in Colloid and Interface Science* 110.3 (2004), pp. 121–141.

[And00] Y. Ando. "The effect of relative humidity on friction and pull-off forces measured on submicron-size asperity arrays ". In: *Wear* 238.1 (2000), pp. 12–19.

[Arc57] J. F. Archard. "Elastic deformation and the laws of friction". In: *Proceedings of the Royal Society of London. Series A. Mathematical and Physical Sciences* 243.1233 (1957), pp. 190–205.

[Ard13] R. Ardito, A. Corigliano, and A. Frangi. "Modelling of spontaneous adhesion phenomena in micro-electro-mechanical systems". In: *European Journal of Mechanics - A/Solids* 39.3 (2013), pp. 144–152.

[Ard14] R. Ardito, A. Corigliano, A. Frangi, and F. Rizzini. "Advanced models for the calculation of capillary attraction in axisymmetric configurations". In: *European Journal of Mechanics - A/Solids* 47 (2014), pp. 298–308.

[Asa10] D. B. Asay, M. P. de Boer, and S. H. Kim. "Equilibrium Vapor Adsorption and Capillary Force: Exact Laplace–Young Equation Solution and Circular Approximation Approaches". In: *Journal of Adhesion Science and Technology* 24.15-16 (2010), pp. 2363–2382.

[Ata02] A. Ata, Y. I. Rabinovich, and R. K. Singh. “Role of surface roughness in capillary adhesion”. In: *Journal of Adhesion Science and Technology* 16.4 (2002), pp. 337–346.

[Ata17] M. Ataei, H. Chen, T. Tang, and A. Amirfazli. “Stability of a liquid bridge between nonparallel hydrophilic surfaces”. In: *Journal of Colloid and Interface Science* 492 (2017), pp. 207–217.

[Avo08] P. Avouris, B. Bhushan, D. Bimberg, K. von Klitzing, H. Sakaki, R. Wiesendanger, and M. Nosonovsky. *Multiscale Dissipative Mechanisms and Hierarchical Surfaces*. Berlin, Heidelberg: Springer Berlin Heidelberg, 2008.

[Bai99] V. G. Baidakov and G. S. Boltachev. “Curvature dependence of the surface tension of liquid and vapor nuclei”. In: *Physical Review E* 59.1 (1999), pp. 469–475.

[Bar07] L. Barbieri, E. Wagner, and P. Hoffmann. “Water wetting transition parameters of perfluorinated substrates with periodically distributed flat-top microscale obstacles”. In: *Langmuir : the ACS journal of surfaces and colloids* 23.4 (2007), pp. 1723–1734.

[Bay87] E. Bayramli and T.G.M van de Ven. “An experimental study of liquid bridges between spheres in a gravitational field”. In: *Journal of Colloid and Interface Science* 116.2 (1987), pp. 503–510.

[Bed09] A. Bedarkar and X.-F. Wu. “Capillary torque in a liquid bridge between two angled filaments”. In: *Journal of Applied Physics* 106.11 (2009).

[Ben14] E. Bendito, M. J. Bowick, and A. Medina. “A Natural Parameterization of the Roulettes of the Conics Generating the Delaunay Surfaces”. In: *Journal of Geometry and Symmetry in Physics* (2014).

[Ber97] L. Bergström. “Hamaker constants of inorganic materials”. In: *Advances in Colloid and Interface Science* 70 (1997), pp. 125–169.

[Bhu11] B. Bhushan and Y. C. Jung. “Natural and biomimetic artificial surfaces for superhydrophobicity, self-cleaning, low adhesion, and drag reduction”. In: *Progress in Materials Science* 56.1 (2011), pp. 1–108.

[Bhu13] B. Bhushan. *Introduction to tribology*. 2nd ed. Tribology in Practice Series. John Wiley & Sons, Ltd, 2013.

[Big12] M. Bigerelle, T. Mathia, and S. Bouvier. “The multi-scale roughness analyses and modeling of abrasion with the grit size effect on ground surfaces”. In: *Wear* 286-287 (2012), pp. 124–135.

[Bin86] G. Binnig, C. F. Quate, and C. Gerber. “Atomic Force Microscope”. In: *Physical Review Letters* 56.9 (1986), pp. 930–933.

[Bis82] F. de Bisschop and W. Rigole. “A Physical Model for Liquid Capillary Bridges between Adsorptive Solid Spheres: The Nodoid of Plateau”. In: *Journal of Colloid and Interface Science* 88.1 (1982), pp. 117–128.

[Blo10] B. J. Block, S. K. Das, M. Oettel, P. Virnau, and K. Binder. “Curvature dependence of surface free energy of liquid drops and bubbles: A simulation study”. In: *The Journal of Chemical Physics* 133.15 (2010), p. 154702.

[Boc98] L. Bocquet, E. Charlaix, S. Ciliberto, and J. Crassous. “Moisture-induced ageing in granular media and the kinetics of capillary condensation”. In: *Nature* 396.6713 (1998), pp. 735–737.

[Boe07] M. P. de Boer and P. C. T. de Boer. “Thermodynamics of capillary adhesion between rough surfaces”. In: *Journal of Colloid and Interface Science* 311.1 (2007), pp. 171–185.

[Bor05] C. K. Bora, E. E. Flater, M. D. Street, J. M. Redmond, M. J. Starr, R. W. Carpick, and M. E. Plesha. “Multiscale roughness and modeling of MEMS interfaces”. In: *Tribology Letters* 19.1 (2005), pp. 37–48.

[Bos15] J. B. Bostwick and P. H. Steen. “Stability of Constrained Capillary Surfaces”. In: *Annual Review of Fluid Mechanics* 47.1 (2015), pp. 539–568.

[Bou82] E. A. Boucher, M. J. B. Evans, and S. McGarry. “Capillary phenomena”. In: *Journal of Colloid and Interface Science* 89.1 (1982), pp. 154–165.

[Bra92a] J. U. Brackbill, Douglas B. Kothe, and C. Zemach. “A Continuum Method for Modeling Surface Tension”. In: *Journal of Computational Physics* 100 (1992), pp. 335–354.

[Bra92b] K. A. Brakke. “The surface evolver”. In: *Experimental Mathematics* 1.2 (1992), pp. 141–165.

[Bra97] K. A. Brakke. “The Surface Evolver and the stability of liquid surfaces”. In: *Philosophical Transactions of the Royal Society of London. Series A: Mathematical, Physical and Engineering Sciences* 354.1715 (1997), pp. 2143–2157.

[Bro12] D. J. Broesch and J. Frechette. “From concave to convex: Capillary bridges in slit pore geometry”. In: *Langmuir: the ACS journal of surfaces and colloids* 28.44 (2012), pp. 15548–15554.

[Bro13] D. J. Broesch, F. Dutka, and J. Frechette. “Curvature of capillary bridges as a competition between wetting and confinement”. In: *Langmuir: the ACS journal of surfaces and colloids* 29.50 (2013), pp. 15558–15564.

[Bru18] C. Bruel, S. Queffeulou, T. Darlow, N. Virgilio, J. R. Tavares, and G. S. Patience. “Experimental methods in chemical engineering: Contact angles”. In: *The Canadian Journal of Chemical Engineering* 97.4 (2018), pp. 832–842.

[Buf57] F. P. Buff and H. Saltsburg. “Curved Fluid Interfaces. II. The Generalized Neumann Formula”. In: *The Journal of Chemical Physics* 26.1 (1957), pp. 23–31.

[Bun07] M. J. Bunker, M. C. Davies, M. B. James, and C. J. Roberts. “Direct observation of single particle electrostatic charging by atomic force microscopy”. In: *Pharmaceutical research* 24.6 (2007), pp. 1165–1169.

[But05] H.-J. Butt, B. Cappella, and M. Kappl. “Force measurements with the atomic force microscope: Technique, interpretation and applications”. In: *Surface Science Reports* 59.1-6 (2005), pp. 1–152.

[But08] H.-J. Butt. “Capillary forces: Influence of roughness and heterogeneity”. In: *Langmuir: the ACS journal of surfaces and colloids* 24.9 (2008), pp. 4715–4721.

[But09] H.-J. Butt and M. Kappl. “Normal capillary forces”. In: *Advances in Colloid and Interface Science* 146.1-2 (2009), pp. 48–60.

[But10a] H.-J. Butt, W. J. P. Barnes, A. del Campo, M. Kappl, and F. Schönfeld. “Capillary forces between soft, elastic spheres”. In: *Soft Matter* 6.23 (2010), p. 5930.

[But10b] H.-J. Butt and M. Kappl. *Surface and interfacial forces*. Physics textbook. Weinheim: Wiley-VCH Verlag GmbH & Co, 2010.

[Cas44] A. B. D. Cassie and S. Baxter. “Wettability of porous surfaces”. In: *Transactions of the Faraday Society* 40 (1944), p. 546.

[Cha07] A. Chau, S. Régnier, A. Delchambre, and P. Lambert. “Three-dimensional model for capillary nanobridges and capillary forces”. In: *Modelling and Simulation in Materials Science and Engineering* 15.3 (2007), pp. 305–317.

[Cha10] A. Chau, S. Régnier, A. Delchambre, and P. Lambert. “Theoretical and Experimental Study of the Influence of AFM Tip Geometry and Orientation on Capillary Force”. In: *Journal of Adhesion Science and Technology* 24.15-16 (2010), pp. 2499–2510.

[Cha18] E. L. Chan and K. Washino. “Coarse grain model for DEM simulation of dense and dynamic particle flow with liquid bridge forces”. In: *Chemical Engineering Research and Design* 132 (2018), pp. 1060–1069.

[Che08] W. Chen, Y. Cai, and J. Zheng. “Constructing Triangular Meshes of Minimal Area”. In: *Computer-Aided Design and Applications* 5.1-4 (2008), pp. 508–518.

[Che11] Y. Chen, Y. Zhao, H. Gao, and J. Zheng. “Liquid bridge force between two unequal-sized spheres or a sphere and a plane”. In: *Particuology* 9.4 (2011), pp. 374–380.

[Chu05] K.-H. Chung, Y.-H. Lee, and D.-E. Kim. “Characteristics of fracture during the approach process and wear mechanism of a silicon AFM tip”. In: *Ultramicroscopy* 102.2 (2005), pp. 161–171.

[Cra97] V. S. J. Craig. “An historical review of surface force measurement techniques”. In: *Colloids and Surfaces A: Physicochemical and Engineering Aspects* 129-130 (1997), pp. 75–93.

[Cun79] P. A. Cundall and O. D. L. Strack. “A discrete numerical model for granular assemblies”. In: *Géotechnique* 29.1 (1979), pp. 47–65.

[Dai98] Z. Dai and S. Lu. “ Liquid bridge rupture distance criterion between spheres”. In: *International Journal of Mineral Processing* 53.3 (1998), pp. 171–181.

[Dar10] P. Darabi, T. Li, K. Pougatch, M. Salcudean, and D. Grecov. “Modeling the evolution and rupture of stretching pendular liquid bridges”. In: *Chemical Engineering Science* 65.15 (2010), pp. 4472–4483.

[Del07] F. W. DelRio, M. L. Dunn, L. M. Phinney, C. J. Bourdon, and M. P. de Boer. “Rough surface adhesion in the presence of capillary condensation”. In: *Applied Physics Letters* 90.16 (2007), p. 163104.

[Del41] C. Delaunay. “Sur la surface de révolution dont la courbure moyenne est constante”. In: *Journal de Mathématiques Pures et Appliquées* 6 (1841), pp. 309–320.

[Dem14] Y. Demirel. *Nonequilibrium thermodynamics: Transport and rate processes in physical chemical and biological systems*. 3rd ed. Amsterdam, Boston, and Heidelberg: Elsevier, 2014.

[Der34] B. Derjaguin. "Untersuchungen über die Reibung und Adhäsion, IV". In: *Kolloid-Zeitschrift* 69.2 (1934), pp. 155–164.

[Dim11] V. P. Dimiri, R. P. Srivastava, and N. Vedanti. "Fractals and Chaos". In: *Encyclopedia of Solid Earth Geophysics*. Ed. by H. K. Gupta. Dordrecht: Springer Netherlands, 2011, pp. 297–302.

[Dör14] M. Dörmann and H.-J. Schmid. "Simulation of Capillary Bridges between Nanoscale Particles". In: *Langmuir: the ACS journal of surfaces and colloids* 30.4 (2014), pp. 1055–1062.

[Dör15] M. Dörmann and H.-J. Schmid. "Simulation of Capillary Bridges between Particles". In: *Procedia Engineering* 102 (2015), pp. 14–23.

[Dör18] M. Dörmann. "Zur Modellierung von Kapillarbrücken zwischen nanoskaligen Partikeln". Dissertation. Paderborn: Universität Paderborn, 2018.

[Dre02] J. Drelich, C. Fang, and C. White. "Measurement of interfacial tension in Fluid-Fluid Systems". In: *Encyclopedia of Surface and Colloid Science*. Ed. by Inc. M. Dekker. 2002, pp. 3152–3166.

[Dzi06] G. Dziuk and J. E. Hutchinson. "Finite element approximations to surfaces of prescribed variable mean curvature". In: *Numerische Mathematik* 102.4 (2006), pp. 611–648.

[Eel87] J. Eells. "The surfaces of Delaunay". In: *The Mathematical Intelligencer* 9.1 (1987), pp. 53–57.

[Erl71] M. A. Erle, D. C. Dyson, and N. R. Morrow. "Liquid bridges between cylinders, in a torus, and between spheres". In: *AIChE Journal* 17.1 (1971), pp. 115–121.

[Fac14] M. H. Factorovich, V. Molinero, and D. A. Scherlis. "Vapor pressure of water nanodroplets". In: *Journal of the American Chemical Society* 136.12 (2014), pp. 4508–4514.

[Far06] M. Farshchi-Tabrizi, M. Kappl, Y. Cheng, J. Gutmann, and H.-J. Butt. "On the adhesion between fine particles and nanocontacts: An atomic force microscope study". In: *Langmuir: the ACS journal of surfaces and colloids* 22.5 (2006), pp. 2171–2184.

[Far15] T. P. Farmer and J. C. Bird. “Asymmetric capillary bridges between contacting spheres”. In: *Journal of Colloid and Interface Science* 454 (2015), pp. 192–199.

[Fel15] L. G. Fel and B. Y. Rubinstein. “Stability of axisymmetric liquid bridges”. In: *Zeitschrift für angewandte Mathematik und Physik* 66.6 (2015), pp. 3447–3471.

[Fis26] R. A. Fisher. “On the capillary forces in an ideal soil; correction of formulae given by W. B. Haines”. In: *The Journal of Agricultural Science* 16.3 (1926), pp. 492–505.

[Fis81] L. R. Fisher and J. N. Israelachvili. “Direct measurement of the effect of meniscus forces on adhesion: A study of the applicability of macroscopic thermodynamics to microscopic liquid interfaces”. In: *Colloids and Surfaces* 3.4 (1981), pp. 303–319.

[For82] M. A. Fortes. “Axisymmetric liquid bridges between parallel plates”. In: *Journal of Colloid and Interface Science* 88.2 (1982), pp. 338–352.

[Fuj99] M. Fuji, K. Machida, T. Takei, T. Watanabe, and M. Chikazawa. “Effect of Wettability on Adhesion Force between Silica Particles Evaluated by Atomic Force Microscopy Measurement as a Function of Relative Humidity”. In: *Langmuir : the ACS journal of surfaces and colloids* 15.13 (1999), pp. 4584–4589.

[Gag16] G. Gagneux, O. Millet, B. Mielniczuk, and M. S. El Youssoufi. “Theoretical and experimental study of pendular regime in unsaturated granular media”. In: *European Journal of Environmental and Civil Engineering* 21.7-8 (2016), pp. 840–853.

[Gao07] L. Gao and T. J. McCarthy. “How Wenzel and cassie were wrong”. In: *Langmuir : the ACS journal of surfaces and colloids* 23.7 (2007), pp. 3762–3765.

[Gau30] C. F. Gauss. “Principia generalia theoriae figurae fluidorum”. In: *Commentarii Societ. Regiae Scientiarum Gottingensis* 7 (1830).

[Gen10] P.-G. de Gennes, F. Brochard-Wyart, and D. Quéré. *Capillarity and wetting phenomena: Drops, bubbles, pearls, waves*. New York: Springer, 2010.

[Geu09] C. Geuzaine and J.-F. Remacle. “Gmsh: a three-dimensional finite element mesh generator with built-in pre- and post-processing facilities”. In: *International Journal for Numerical Methods in Engineering* 79.11 (2009), pp. 11309–1331.

[Gib93] J. W. Gibbs. *Thermodynamics*. Vol. 1. The scientific papers of J. Willard Gibbs. Woodbridge, Conn.: Ox Bow Press, 1993.

[Gio16] N. Giovambattista, A. B. Almeida, A. M. Alencar, and S. V. Buldyrev. “Validation of Capillarity Theory at the Nanometer Scale by Atomistic Computer Simulations of Water Droplets and Bridges in Contact with Hydrophobic and Hydrophilic Surfaces”. In: *The Journal of Physical Chemistry C* 120.3 (2016), pp. 1597–1608.

[Gre01] J. A. Greenwood and J. J. Wu. “Surface Roughness and Contact: An Apology”. In: *Meccanica* 36.6 (2001), pp. 617–630.

[Gre66] J. A. Greenwood and J. B. P. Williamson. “Contact of nominally flat surfaces”. In: *Proceedings of the Royal Society of London. Series A. Mathematical and Physical Sciences* 295.1442 (1966), pp. 300–319.

[Grö03] T. Gröger, U. Tüzün, and D. M. Heyes. “Modelling and measuring of cohesion in wet granular materials”. In: *Powder Technology* 133.1-3 (2003), pp. 203–215.

[Hai25] W. B. Haines. “Studies in the physical properties of soils: II. A note on the cohesion developed by capillary forces in an ideal soil”. In: *The Journal of Agricultural Science* 15.4 (1925), pp. 529–535.

[Hal98] T. C. Halsey and A. J. Levine. “How Sandcastles Fall”. In: *Physical Review Letters* 80.14 (1998), pp. 3141–3144.

[Har06] D.J.E. Harvie, M. R. Davidson, and M. Rudman. “An analysis of parasitic current generation in Volume of Fluid simulations”. In: *Applied Mathematical Modelling* 30.10 (2006), pp. 1056–1066.

[Har15] O. Harireche, A. Faramarzi, and A. M. Alani. “Prediction of inter-particle capillary forces for non-perfectly wettable granular assemblies”. In: *Granular Matter* 17.5 (2015), pp. 537–543.

[Her19] S. Herminghaus, C. Semprebon, and M. Brinkmann. “Capillary Interaction in Wet Granular Assemblies: Part 1”. In: *Particles in Contact*. Ed. by Sergiy Antonyuk. Springer International Publishing, 2019, pp. 239–275.

[Hil52] T. L. Hill. “Statistical Thermodynamics of the Transition Region between Two Phases. I. Thermodynamics and Quasi-thermodynamics”. In: *The Journal of Physical and Colloid Chemistry* 56.4 (1952), pp. 526–531.

[Hir07] C. Hirsch. *Numerical computation of internal and external flows: Introduction to the fundamentals of CFD*. New ed. Oxford: Butterworth-Heinemann, 2007.

[Hir81] C. W. Hirt and B. D. Nichols. “Volume of Fluid (VOF) Method for the Dynamics of Free Boundaries”. In: *Journal of Computational Physics* 39 (1981), pp. 201–225.

[His75] T. Hisakado. “Surface roughness and deformation of contact asperities between a rough and a flat surface”. In: *Wear* 35.1 (1975), pp. 53–61.

[Hor12] M. Horsch, H. Hasse, A. K. Shchekin, A. Agarwal, S. Eckelsbach, J. Vrabec, E. A. Müller, and G. Jackson. “Excess equimolar radius of liquid drops”. In: *Physical review. E, Statistical, nonlinear, and soft matter physics* 85.3 (2012), p. 031605.

[Hor90] U. Hornung and H. D. Mittelmann. “A finite element method for capillary surfaces with volume constraints”. In: *Journal of Computational Physics* 87.1 (1990), pp. 126–136.

[Hot74] K. Hotta, K. Takeda, and K. Iinoya. “The capillary binding force of a liquid bridge”. In: *Powder Technology* 10.4-5 (1974), pp. 231–242.

[Ili06] S. D. Iliev and N. Pesheva. “Nonaxisymmetric drop shape analysis and its application for determination of the local contact angles”. In: *Journal of Colloid and Interface Science* 301.2 (2006), pp. 677–684.

[Ili16] S. D. Iliev and N. Pesheva. “Contact-angle hysteresis on periodic microtextured surfaces: Strongly corrugated liquid interfaces”. In: *Physical review. E* 93.6 (2016), p. 062801.

[Ili18] S. D. Iliev, N. Pesheva, P. Iliev, V. M. Vassilev, S. G. Nikolov, M. D. Datcheva, and Y. P. Ivanova. “Wetting of doubly periodic rough surfaces in Wenzel’s regime”. In: *MATEC Web of Conferences* 145 (2018), p. 03006.

[Ili95] S. D. Iliev. “Iterative method for the shape of static drops”. In: *Computer Methods in Applied Mechanics and Engineering* 126.3-4 (1995), pp. 251–265.

[ISO12] BS EN ISO 25178-2. *Geometrical product specifications (GPS). Surface texture. Areal. Terms, definitions and surface texture parameters*. 2012.

[Isr11] J. N. Israelachvili. *Intermolecular and surface forces*. 3. ed. Burlington, MA: Academic Press, 2011.

[Isr72] J. Israelachvili and D. Tabor. "The measurement of van der Waals dispersion forces in the range 1.5 to 130 nm". In: *Proceedings of the Royal Society of London. Series A. Mathematical and Physical Sciences* 331.1584 (1972), pp. 19–38.

[Jon02] R. Jones, H. M. Pollock, J. A. S. Cleaver, and C. S. Hodges. "Adhesion Forces between Glass and Silicon Surfaces in Air Studied by AFM: Effects of Relative Humidity, Particle Size, Roughness, and Surface Treatment". In: *Langmuir: the ACS journal of surfaces and colloids* 18.21 (2002), pp. 8045–8055.

[Ken80] K. Kenmotsu. "Surfaces of revolution with prescribed mean curvature". In: *Tohoku Mathematical Journal* 32.1 (1980), pp. 147–153.

[Kir49] J. G. Kirkwood and F. P. Buff. "The Statistical Mechanical Theory of Surface Tension". In: *The Journal of Chemical Physics* 17.3 (1949), pp. 338–343.

[Kli04] A. Klingner, J. Buehrle, and F. Mugele. "Capillary bridges in electric fields". In: *Langmuir : the ACS journal of surfaces and colloids* 20.16 (2004), pp. 6770–6777.

[Kno12] C. R. Knospe and H. Haj-Hariri. "Capillary force actuators: Modeling, dynamics, and equilibria". In: *Mechatronics* 22.3 (2012), pp. 251–256.

[Ko10] J.-A. Ko, H.-J. Choi, M.-Y. Ha, S.-D. Hong, and H.-S. Yoon. "A study on the behavior of water droplet confined between an atomic force microscope tip and rough surfaces". In: *Langmuir: the ACS journal of surfaces and colloids* 26.12 (2010), pp. 9728–9735.

[Koc04] H. V. Koch. "Sur une courbe continue sans tangente, obtenue par une construction géométrique élémentaire". In: *Arkiv for Matematik, Astronomi och Fysik* 1 (1904), pp. 681–704.

[Kog98] K. Koga, X. C. Zeng, and A. K. Shchekin. "Validity of Tolman's equation: How large should a droplet be?" In: *The Journal of Chemical Physics* 109.10 (1998), pp. 4063–4070.

[Koh00] M. M. Kohonen and H. K. Christenson. "Capillary Condensation of Water between Rinsed Mica Surfaces". In: *Langmuir: the ACS journal of surfaces and colloids* 16.18 (2000), pp. 7285–7288.

[Koh04] M. M. Kohonen, D. Geromichalos, M. Scheel, C. Schier, and S. Herminghaus. “On capillary bridges in wet granular materials”. In: *Physica A: Statistical Mechanics and its Applications* 339.1-2 (2004), pp. 7–15.

[Koh99] M. M. Kohonen, N. Maeda, and H. K. Christenson. “Kinetics of Capillary Condensation in a Nanoscale Pore”. In: *Physical Review Letters* 82.23 (1999), pp. 4667–4670.

[Kus10] H. Kusumaatmaja and R. Lipowsky. “Equilibrium morphologies and effective spring constants of capillary bridges”. In: *Langmuir : the ACS journal of surfaces and colloids* 26.24 (2010), pp. 18734–18741.

[Lam05] P. Lambert and A. Delchambre. “Parameters ruling capillary forces at the submillimetric scale”. In: *Langmuir: the ACS journal of surfaces and colloids* 21.21 (2005), pp. 9537–9543.

[Lam08] P. Lambert, A. Chau, A. Delchambre, and S. Régnier. “Comparison between two capillary forces models”. In: *Langmuir: the ACS journal of surfaces and colloids* 24.7 (2008), pp. 3157–3163.

[Lan02] D. Langbein. *Capillary Surfaces*. Springer Tracts in Modern Physics. Berlin: Springer, 2002.

[Lap05] P. S. Laplace. *Supplément au livre X du Traitée de Méchanique Céleste*. Paris: Couveier, 1805.

[Lau17] J. T. Laube. “On the mechanical interactions between TiO2 nanoparticles”. Dissertation. Bremen: Universität Bremen, 2017.

[Law14] K.-Y. Law. “Definitions for Hydrophilicity, Hydrophobicity, and Superhydrophobicity: Getting the Basics Right”. In: *The journal of physical chemistry letters* 5.4 (2014), pp. 686–688.

[Laz99] A. de Lazzer, M. Dreyer, and H. R. Rath. “Particle−Surface Capillary Forces”. In: *Langmuir: the ACS journal of surfaces and colloids* 15.13 (1999), pp. 4551–4559.

[Lem18] E. W. Lemmon, I. H. Bell, Huber M. L., and M. O. McLinden. *NIST Standard Reference Database 23: Reference Fluid Thermodynamic and Transport Properties-REFPROP, Version 10.0, National Institute of Standards and Technology*. 2018.

[LeV02] R.-J. LeVeque. *Finite volume methods for hyperbolic problems*. Cambridge texts in applied mathematics. Cambridge and New York: Cambridge University Press, 2002.

[Li20] X. Li, M. Dong, H. Zhang, S. Li, and Y. Shang. “Effect of surface roughness on capillary force during particle-wall impaction under different humidity conditions”. In: *Powder Technology* 371 (2020), pp. 244–255.

[Li92] Y. Li and F. E. Talke. “A Model for the Effect of Humidity on Stiction of the Head/Disk Interface”. In: *Tribology Transactions* 35.3 (1992), pp. 429–434.

[Lia16] G. Lian and J. P. K. Seville. “The capillary bridge between two spheres: New closed-form equations in a two century old problem”. In: *Advances in Colloid and Interface Science* 227 (2016), pp. 53–62.

[Lia93] G. Lian, C. Thornton, and M. J. Adams. “A Theoretical Study of the Liquid Bridge Forces between Two Rigid Spherical Bodies”. In: *Journal of Colloid and Interface Science* 161.1 (1993), pp. 138–147.

[Lia98] G. Lian, C. Thornton, and M. J. Adams. “Discrete particle simulation of agglomerate impact coalescence”. In: *Chemical Engineering Science* 53.19 (1998), pp. 3381–3391.

[Lie17] D. Lievano, S. Velankar, and J. J. McCarthy. “The rupture force of liquid bridges in two and three particle systems”. In: *Powder Technology* 313 (2017), pp. 18–26.

[Lin15] N. W. Linder. “Numerical Simulation of Complex Wetting”. Dissertation. Darmstadt: TU Darmstadt, 2015.

[Liu11] P. Y. Liu, R. Y. Yang, and A. B. Yu. “Dynamics of wet particles in rotating drums: Effect of liquid surface tension”. In: *Physics of Fluids* 23.1 (2011), p. 013304.

[Log12] A. Logg, K.-A. Mardal, and G. N. Wells, eds. *Automated Solution of Differential Equations by the Finite Element Method*. Vol. 84. Lecture Notes in Computational Science and Engineering. Springer Berlin Heidelberg, 2012.

[Lu07] N. Lu, B.n Wu, and C. P. Tan. “Tensile Strength Characteristics of Unsaturated Sands”. In: *Journal of Geotechnical and Geoenvironmental Engineering* 133.2 (2007), pp. 144–154.

[Luo13] T. Luo, X. Liu, Y. Chen, W. Huang, and Z. Liu. “Design and laser fabrication of controllable non-Gaussian roughness surfaces at microscale”. In: *Applied Surface Science* 276 (2013), pp. 95–100.

[Mae06] N. Maeda. “Phase transitions of capillary-held liquids in a slit-like pore”. In: *The journal of physical chemistry. B* 110.51 (2006), pp. 25982–25993.

[Maj90] A. Majumdar and B. Bhushan. “Role of Fractal Geometry in Roughness Characterization and Contact Mechanics of Surfaces”. In: *Journal of Tribology* 112.2 (1990), pp. 205–216.

[Mal12] A. Malijevský and G. Jackson. “A perspective on the interfacial properties of nanoscopic liquid drops”. In: *Journal of physics. Condensed matter : an Institute of Physics journal* 24.46 (2012), p. 464121.

[Man10] K. K. Manesh, B. Ramamoorthy, and M. Singaperumal. “Numerical generation of anisotropic 3D non-Gaussian engineering surfaces with specified 3D surface roughness parameters”. In: *Wear* 268.11-12 (2010), pp. 1371–1379.

[Man77] B. B. Mandelbrot. *Fractals: Form, chance, and dimension*. San Francisco: Freeman, 1977.

[Mar06] A. Marmur. “Soft contact: Measurement and interpretation of contact angles”. In: *Soft Matter* 2.1 (2006), pp. 12–17.

[Mar09] A. Marmur. “Solid-Surface Characterization by Wetting”. In: *Annual Review of Materials Research* 39.1 (2009), pp. 473–489.

[Mar11] E. Marchandise, C. Carton de Wiart, W. G. Vos, C. Geuzaine, and J.-F. Remacle. “High-quality surface remeshing using harmonic maps-Part II: Surfaces with high genus and of large aspect ratio”. In: *International Journal for Numerical Methods in Engineering* 86.11 (2011), pp. 1303–1321.

[Mar71] C. Marangoni. “Über die Ausbreitung der Tropfen einer Flüssigkeit auf der Oberfläche einer anderen”. In: *Annalen der Physik und Chemie* 219.7 (1871), pp. 337–354.

[Mar93] A. Marmur. “Tip-surface capillary interactions”. In: *Langmuir: the ACS journal of surfaces and colloids* 9.7 (1993), pp. 1922–1926.

[Mas10] M. Mastrangeli, J.-B. Valsamis, C. van Hoof, J.-P. Celis, and P. Lambert. “Lateral capillary forces of cylindrical fluid menisci: A comprehensive quasi-static study”. In: *Journal of Micromechanics and Microengineering* 20.7 (2010), p. 075041.

[Mas65] S. G. Mason and W. C. Clark. “Liquid bridges between spheres”. In: *Chemical Engineering Science* 20.10 (1965), pp. 859–866.

[Maz86] D. N. Mazzone, G. I. Tardos, and R. Pfeffer. “The effect of gravity on the shape and strength of a liquid bridge between two spheres”. In: *Journal of Colloid and Interface Science* 113.2 (1986), pp. 544–556.

[Maz87] D. N. Mazzone, G. I. Tardos, and R. Pfeffer. “The behavior of liquid bridges between two relatively moving particles”. In: *Powder Technology* 51.1 (1987), pp. 71–83.

[Meg11] D. Megias-Alguacil and L. J. Gauckler. “Accuracy of the toroidal approximation for the calculus of concave and convex liquid bridges between particles”. In: *Granular Matter* 13.4 (2011), pp. 487–492.

[Meh80] V. P. Mehrotra and K.V.S. Sastry. “Pendular bond strength between unequal-sized spherical particles”. In: *Powder Technology* 25.2 (1980), pp. 203–214.

[Mel66] J. C. Melrose. “Model calculations for capillary condensation”. In: *AIChE Journal* 12.5 (1966), pp. 986–994.

[Mik98] T. Mikami, H. Kamiya, and M. Horio. “Numerical simulation of cohesive powder behavior in a fluidized bed”. In: *Chemical Engineering Science* 53.10 (1998), pp. 1927–1940.

[Mit93] H. D. Mittelmann. “Symmetric capillary surfaces in a cube”. In: *Mathematics and Computers in Simulation* 35.2 (1993), pp. 139–152.

[Mol93] D. J. Mollot, J. Tsamopoulos, T.-Y. Chen, and N. Ashgriz. “Nonlinear dynamics of capillary bridges: Experiments”. In: *Journal of Fluid Mechanics* 255 (1993), pp. 411–435.

[Mug00] Y. Muguruma, T. Tanaka, and Y. Tsuji. “Numerical simulation of particulate flow with liquid bridge between particles (simulation of centrifugal tumbling granulator)”. In: *Powder Technology* 109.1-3 (2000), pp. 49–57.

[Nay71] P. R. Nayak. “Random Process Model of Rough Surfaces”. In: *Journal of Lubrication Technology* 93.3 (1971), pp. 398–407.

[Naz12] A. H. Nazemi and A. Majnooni-Heris. “A mathematical model for the interactions between non-identical rough spheres, liquid bridge and liquid vapor”. In: *Journal of Colloid and Interface Science* 369.1 (2012), pp. 402–410.

[Neu74] A. W. Neumann. “Contact angles and their temperature dependence: Thermodynamic status, measurement, interpretation and application”. In: *Advances in Colloid and Interface Science* 4.2-3 (1974), pp. 105–191.

[Ngu19] H. N. G. Nguyen, O. Millet, and G. Gagneux. “Liquid bridges between a sphere and a plane - Classification of meniscus profiles for unknown capillary pressure”. In: *Mathematics and Mechanics of Solids* 24.10 (2019), pp. 3042–3060.

[Niv06] R. K. Niven. “Force stability of pore-scale fluid bridges and ganglia in axisymmetric and non-axisymmetric configurations”. In: *Journal of Petroleum Science and Engineering* 52.1-4 (2006), pp. 1–18.

[Nos07] M. Nosonovsky. “On the range of applicability of the Wenzel and Cassie equations”. In: *Langmuir : the ACS journal of surfaces and colloids* 23.19 (2007), pp. 9919–9920.

[Orr75] F. M. Orr, L. E. Scriven, and A. P. Rivas. “Pendular rings between solids: Meniscus properties and capillary force”. In: *Journal of Fluid Mechanics* 67.4 (1975), pp. 723–742.

[Osh88] S. Osher and J. A. Sethian. “Fronts propagating with curvature-dependent speed: Algorithms based on Hamilton-Jacobi formulations”. In: *Journal of Computational Physics* 79.1 (1988), pp. 12–49.

[Ouy01] Q. Ouyang, K. Ishida, and K. Okada. “Investigation of micro-adhesion by atomic force microscopy”. In: *Applied Surface Science* 169-170.14 (2001), pp. 644–648.

[Pad69] J. F. Padday. “Surface Tension: Part I. The Theory of Surface Tension”. In: *Surface and Colloid Science*. Ed. by E. Matijević. Vol. 1. New York: Wiley-Interscience, 1969, pp. 39–260.

[Pak05] O. H. Pakarinen, A. S. Foster, M. Paajanen, T. Kalinainen, J. Katainen, I. Makkonen, J. Lahtinen, and R. M. Nieminen. “Towards an accurate description of the capillary force in nanoparticle - surface interactions”. In: *Modelling and Simulation in Materials Science and Engineering* 13.7 (2005), pp. 1175–1186.

[Pan12] H. Pan, Y.-K. Choi, Y. Liu, W. Hu, Q. Du, K. Polthier, C. Zhang, and W. Wang. “Robust modeling of constant mean curvature surfaces”. In: *ACM Transactions on Graphics* 31.4 (2012), pp. 1–11.

[Pay11] A. F. Payam and M. Fathipour. “A capillary force model for interactions between two spheres”. In: *Particuology* 9.4 (2011), pp. 381–386.

[Pel01] N. A. Pelekasis, K. Economou, and J. A. Tsamopoulos. “Linear oscillations and stability of a liquid bridge in an axial electric field”. In: *Physics of Fluids* 13.12 (2001), pp. 3564–3581.

[Pep00] X. Pepin, D. Rossetti, S. M. Iveson, and S. J. R. Simons. “Modeling the Evolution and Rupture of Pendular Liquid Bridges in the Presence of Large Wetting Hysteresis”. In: *Journal of Colloid and Interface Science* 232.2 (2000), pp. 289–297.

[Pie68] W. B. Pietsch. “ Tensile Strength of Granular Materials ”. In: *Nature* 217.5130 (1968), pp. 736–737.

[Pla64] J. Plateau. “The figures of equilibrium of a liquid mass”. In: *The Annual Report of the Smithsonian Institution* (1864), pp. 338–369.

[Pol02] K. Polthier and W. Rossman. “Discrete constant mean curvature surfaces and their index”. In: *Journal für die reine und angewandte Mathematik (Crelles Journal)* 2002.549 (2002), p. 13.

[Qia17] L. Qiang-Nian, Z. Jia-Qi, and Z. Feng-Xi. “Exact Solution for Capillary Bridges Properties by Shooting Method”. In: *Zeitschrift für Naturforschung A* 72.4 (2017), pp. 315–320.

[Rab00a] Y. I. Rabinovich, J. J. Adler, A. Ata, R. K. Singh, and B. M. Moudgil. “Adhesion between Nanoscale Rough Surfaces: I. Role ofAsperity Geometry”. In: *Journal of Colloid and Interface Science* 232.1 (2000), pp. 10–16.

[Rab00b] Y. I. Rabinovich, J. J. Adler, A. Ata, R. K. Singh, and B. M. Moudgil. “Adhesion between Nanoscale Rough Surfaces: II. Measurement and Comparison with Theory”. In: *Journal of Colloid and Interface Science* 232.1 (2000), pp. 17–24.

[Rab02] Y. I. Rabinovich, J. J. Adler, M. S. Esayanur, A. Ata, R. K. Singh, and B. M. Moudgil. “Capillary forces between surfaces with nanoscale roughness”. In: *Advances in Colloid and Interface Science* 96.1-3 (2002), pp. 213–230.

[Rab05] Y. I. Rabinovich, M. S. Esayanur, and B. M. Moudgil. “Capillary forces between two spheres with a fixed volume liquid bridge: Theory and experiment”. In: *Langmuir: the ACS journal of surfaces and colloids* 21.24 (2005), pp. 10992–10997.

[Rem10] J.-F. Remacle, C. Geuzaine, G. Compère, and E. Marchandise. “High-quality surface remeshing using harmonic maps”. In: *International Journal for Numerical Methods in Engineering* 83.4 (2010), pp. 403–425.

[Ren14] R. J. Renka. “ A trust region method for constructing triangle-mesh approximations of parametric minimal surfaces”. In: *Applied Numerical Mathematics* 76 (2014), pp. 93–100.

[Ren15] R. J. Renka. “A Simple and Efficient Method for Modeling Constant Mean Curvature Surfaces”. In: *SIAM Journal on Scientific Computing* 37.4 (2015), A2076–A2099.

[Ren95] R. J. Renka and J. W. Neuberger. “Minimal Surfaces and Sobolev Gradients”. In: *SIAM Journal on Scientific Computing* 16.6 (1995), pp. 1412–1427.

[Res02] F. Restagno, L. Bocquet, J. Crassous, and E. Charlaix. “Slow kinetics of capillary condensation in confined geometry: Experiment and theory”. In: *Colloids and Surfaces A: Physicochemical and Engineering Aspects* 206.1-3 (2002), pp. 69–77.

[Rob01] F. Robbe-Valloire. “Statistical analysis of asperities on a rough surface”. In: *Wear* 249.5-6 (2001), pp. 401–408.

[Rub14] B. Y. Rubinstein and L. G. Fel. “Theory of axisymmetric pendular rings”. In: *Journal of Colloid and Interface Science* 417 (2014), pp. 37–50.

[Rum74] H. Rumpf. “Die Wissenschaft des Agglomerierens”. In: *Chemie Ingenieur Technik - CIT* 46.1 (1974), pp. 1–11.

[Rus96] A. I. Rusanov and V. A. Prokhorov. *Interfacial tensiometry.* Vol. 3. Studies in interface science. Amsterdam: Elsevier, 1996.

[Ryn03] P. R. Rynhart, R. McLachlan, J. R. Jones, and R. McKibbin. “Solution of the Young-Laplace equation for three particles”. In: *Research Letters in the Information and Mathematical Sciences* 5 (2003), pp. 119–127.

[Sac02] L. Sachs. *Angewandte Statistik: Anwendung statistischer Methoden.* 10th ed. Berlin: Springer, 2002.

[Sáe90] A. E. Sáez and R. G. Carbonell. “The equilibrium and stability of menisci between touching spheres under the effect of gravity”. In: *Journal of Colloid and Interface Science* 140.2 (1990), pp. 408–418.

[Sam11] B. Samuel, H. Zhao, and K.-Y. Law. “Study of Wetting and Adhesion Interactions between Water and Various Polymer and Superhydrophobic Surfaces”. In: *The Journal of Physical Chemistry C* 115.30 (2011), pp. 14852–14861.

[Sch13] R. Schwarze, A. Gladkyy, F. Uhlig, and S. Luding. “Rheology of weakly wetted granular materials: A comparison of experimental and numerical data”. In: *Granular Matter* 15.4 (2013), pp. 455–465.

[Sch22] S. Schmidt, M. Gräßer, and H.-J. Schmid. “A Shape Newton Scheme for Deforming Shells with Application to Capillary Bridges”. In: *SIAM Journal on Scientific Computing* 44.4 (2022).

[Sch82] H. Schubert. *Kapillarität in porösen Feststoffsystemen*. Berlin, Heidelberg etc.: Springer, 1982.

[Sed00] D. L. Sedin and K. L. Rowlen. “Adhesion forces measured by atomic force microscopy in humid air”. In: *Analytical chemistry* 72.10 (2000), pp. 2183–2189.

[Seg51] J. A. Segner. “De figuris superficierum fluidarum”. In: *Commentarii Societ. Regiae Scientiarum Gottingensis* 1 (1751), pp. 301–372.

[Sem16] C. Semprebon, M. Scheel, S. Herminghaus, R. Seemann, and M. Brinkmann. “Liquid morphologies and capillary forces between three spherical beads”. In: *Physical review. E* 94.1-1 (2016), p. 012907.

[Shi07] H. Shinto, D. Komiyama, and K. Higashitani. “Lattice Boltzmann study of capillary forces between cylindrical particles”. In: *Advanced Powder Technology* 18.6 (2007), pp. 643–662.

[Sir06] L. Sirghi, R. Szoszkiewicz, and E. Riedo. “Volume of a nanoscale water bridge”. In: *Langmuir : the ACS journal of surfaces and colloids* 22.3 (2006), pp. 1093–1098.

[Sou06] F. Soulié, F. Cherblanc, M. S. El Youssoufi, and C. Saix. “Influence of liquid bridges on the mechanical behaviour of polydisperse granular materials”. In: *International Journal for Numerical and Analytical Methods in Geomechanics* 30.3 (2006), pp. 213–228.

[Sto00] K. Stout, L. Blunt, W. Dong, E. Mainsah, N. Luo, T. Mathia, P. Sullivan, and H. Zahouani. *Development of methods for the characterisation of roughness in three dimensions*. Rev. reprint. London: Penton, 2000.

[Sto17] T.C. Stocker and I. Steinke. *Statistik - Grundlagen und Methoden*. Berlin, Boston: De Gruyter Oldenbourg, 2017.

[Sun16] X. Sun and M. Sakai. "Direct numerical simulation of gas-solid-liquid flows with capillary effects: An application to liquid bridge forces between spherical particles". In: *Physical review. E* 94.6-1 (2016), p. 063301.

[Sun18a] X. Sun, H. J. Lee, S. Michielsen, and E. Wilusz. "Profile of capillary bridges between two vertically stacked cylindrical fibers under gravitational effect". In: *Applied Surface Science* 441 (2018), pp. 791–797.

[Sun18b] X. Sun and M. Sakai. "A liquid bridge model for spherical particles applicable to asymmetric configurations". In: *Chemical Engineering Science* 182 (2018), pp. 28–43.

[Sus94] M. Sussman, P. Smereka, and S. Osher. "A Level Set Approach for Computing Solutions to Incompressible Two-Phase Flow". In: *Journal of Computational Physics* 114.1 (1994), pp. 146–159.

[Tab69] D. Tabor and R. H. S. Winterton. "The direct measurement of normal and retarded van der Waals forces". In: *Proceedings of the Royal Society of London. Series A. Mathematical and Physical Sciences* 312.1511 (1969), pp. 435–450.

[Tak10] A. Takei, K. Matsumoto, and I. Shimoyama. "Capillary torque caused by a liquid droplet sandwiched between two plates". In: *Langmuir: the ACS journal of surfaces and colloids* 26.4 (2010), pp. 2497–2504.

[Tan18] Y. Tang and S. Cheng. "Capillary forces on a small particle at a liquid- vapor interface: Theory and simulation". In: *Physical Review E* 98.3 (2018), p. 517.

[Thu93] T. Thundat, X.-Y. Zheng, G. Y. Chen, and R. J. Warmack. "Role of relative humidity in atomic force microscopy imaging". In: *Surface Science Letters* 294.1-2 (1993), pp. L939–L943.

[Tol48] S. Tolansky. *Multiple-beam Interferometry of Surfaces and Films*. London: Oxford Clarendon Press, 1948.

[Tol49a] R. C. Tolman. "The Effect of Droplet Size on Surface Tension". In: *The Journal of Chemical Physics* 17.3 (1949), pp. 333–337.

[Tol49b] R. C. Tolman. "The Superficial Density of Matter at a Liquid–Vapor Boundary". In: *The Journal of Chemical Physics* 17.2 (1949), pp. 118–127.

[Tom28] G. A. Tomlinson. “ Molecular Cohesion ”. In: *The London, Edinburgh, and Dublin Philosophical Magazine and Journal of Science* 37.6 (1928), pp. 695–712.

[Tse03] Y. G. Tselishchev and V. A. Val’tsifer. “Influence of the Type of Contact between Particles Joined by a Liquid Bridge on the Capillary Cohesive Forces”. In: *Colloid Journal* 65.3 (2003), pp. 385–389.

[Tsu16] Y. Tsunazawa, D. Fujihashi, S. Fukui, M. Sakai, and C. Tokoro. “Contact force model including the liquid-bridge force for wet-particle simulation using the discrete element method”. In: *Advanced Powder Technology* 27.2 (2016), pp. 652–660.

[Tuk12] Z. Tukovic and H. Jasak. “A moving mesh finite volume interface tracking method for surface tension dominated interfacial fluid flow”. In: *Computers & Fluids* 55 (Feb. 2012), pp. 70–84.

[Ubb97] O. Ubbink. “Numerical prediction of two fluid systems with sharp interfaces”. Dissertation. London: Imperial College of Science, Technology & Medicine, 1997.

[Unv92] S. O. Unverdi and G. Tryggvason. “A front-tracking method for viscous, incompressible, multi-fluid flows”. In: *Journal of Computational Physics* 100.1 (1992), pp. 25–37.

[Urs99] M. E. D. Urso, C. J. Lawrence, and M. J. Adams. “Pendular, Funicular, and Capillary Bridges: Results for Two Dimensions”. In: *Journal of Colloid and Interface Science* 220.1 (1999), pp. 42–56.

[Val13] J.-B. Valsamis, M. de Volder, and P. Lambert. “Physical Background”. In: *Surface Tension in Microsystems*. Ed. by P. Lambert. Microtechnology and MEMS. Berlin, Heidelberg etc.: Springer Berlin Heidelberg, 2013.

[van08] P. J. van Zwol, G. Palasantzas, and J. Th M. de Hosson. “Influence of roughness on capillary forces between hydrophilic surfaces”. In: *Physical review. E, Statistical, nonlinear, and soft matter physics* 78.3 (2008), p. 031606.

[van09] A. E. van Giessen and E. M. Blokhuis. “Direct determination of the Tolman length from the bulk pressures of liquid drops via molecular dynamics simulations”. In: *The Journal of Chemical Physics* 131.16 (2009), p. 164705.

[van10] J. W. van Honschoten, N. Brunets, and N. R. Tas. “Capillarity at the nanoscale”. In: *Chemical Society reviews* 39.3 (2010), pp. 1096–1114.

[Vir09] A. Virozub, N. Haimovich, and S. Brandon. “ Three-dimensional simulations of liquid bridges between two cylinders: Forces, energies, and torques”. In: *Langmuir: the ACS journal of surfaces and colloids* 25.22 (2009), pp. 12837–12842.

[Vog06] T. I. Vogel. “Convex, rotationally symmetric liquid bridges between spheres”. In: *Pacific Journal of Mathematics* 2 (2006), pp. 367–377.

[Vog80] W. Vogelsberger, M. Ziese, and G. Rudakoff. “Die Krümmungsabhängigkeit der Oberflächenspannung zylindrischer Flüssigkeitsmenisken im Tolman’schen Bild”. In: *Zeitschrift für Physikalische Chemie* 261.1 (1980).

[Wal83] P. Walstra. “Formation of emulsions: Basic Theory”. In: *Encyclopedia of emulsion Technology*. Ed. by P. Becher. Vol. 1. New York: Marcel Decker, 1983, pp. 57–128.

[Wan09] J. Wang, J. Qian, and H. Gao. “Effects of capillary condensation in adhesion between rough surfaces”. In: *Langmuir: the ACS journal of surfaces and colloids* 25.19 (2009), pp. 11727–11731.

[Wan16] L. Wang, F. Su, H. Xu, W. Rong, and H. Xie. “Capillary bridges and capillary forces between two axisymmetric power–law particles”. In: *Particuology* 27 (2016), pp. 122–127.

[Wan17] J.-P. Wang, E. Gallo, B. François, F. Gabrieli, and P. Lambert. “Capillary force and rupture of funicular liquid bridges between three spherical bodies”. In: *Powder Technology* 305 (2017), pp. 89–98.

[Wan20] H. Wang, P. Jia, L. Wang, F. Yun, G. Wang, X. Wang, and M. Liu. “Research on the loading–unloading fractal contact model between two three-dimensional spherical rough surfaces with regard to friction”. In: *Acta Mechanica* 231.10 (2020), pp. 4397–4413.

[Was17] K. Washino, E. L. Chan, T. Matsumoto, S. Hashino, T. Tsuji, and T. Tanaka. “Normal viscous force of pendular liquid bridge between two relatively moving particles”. In: *Journal of Colloid and Interface Science* 494 (2017), pp. 255–265.

[Wei89] A. L. Weisenhorn, P. K. Hansma, T. R. Albrecht, and C. F. Quate. “Forces in atomic force microscopy in air and water”. In: *Applied Physics Letters* 54.26 (1989), pp. 2651–2653.

[Wen36] R. N. Wenzel. “Resistance of solid surfaces to wetting by water”. In: *Industrial & Engineering Chemistry* 28.8 (1936), pp. 988–994.

[Wik12] H. S. Wiklund and T. Uesaka. “ Simulations of shearing of capillary bridges”. In: *The Journal of Chemical Physics* 136.9 (2012), p. 094703.

[Wil00] C. D. Willett, M. J. Adams, S. A. Johnson, and J. P. K. Seville. “Capillary Bridges between Two Spherical Bodies”. In: *Langmuir: the ACS journal of surfaces and colloids* 16.24 (2000), pp. 9396–9405.

[Wu19] D. Wu, P. Zhou, B. Zhao, T. Howes, and G. Wang. “Liquid redistribution upon the liquid-bridge rupture between two unequal particles with a minimal energy method”. In: *Powder Technology* 354 (2019), pp. 165–173.

[Xia00] X. Xiao and L. Qian. “Investigation of Humidity-Dependent Capillary Force”. In: *Langmuir: the ACS journal of surfaces and colloids* 16.21 (2000), pp. 8153–8158.

[Xu98] L. Xu, A. Lio, J. Hu, D. F. Ogletree, and M. Salmeron. “Wetting and Capillary Phenomena of Water on Mica”. In: *The journal of physical chemistry. B* 102.3 (1998), pp. 540–548.

[Yan10] L. Yang, Y. Tu, and H. Fang. “Modeling the rupture of a capillary liquid bridge between a sphere and plane”. In: *Soft Matter* 6.24 (2010), p. 6178.

[Yan98] W. Yan and K. Komvopoulos. “Contact analysis of elastic-plastic fractal surfaces”. In: *Journal of Applied Physics* 84.7 (1998), pp. 3617–3624.

[You05] T. Young. “III. An essay on the cohesion of fluids”. In: *Philosophical Transactions of the Royal Society of London* 95 (1805), pp. 65–87.

[You13] S. You and M. P. Wan. “Mathematical models for the van der Waals force and capillary force between a rough particle and surface”. In: *Langmuir: the ACS journal of surfaces and colloids* 29.29 (2013), pp. 9104–9117.

[You14] S. You and M. P. Wan. “Modeling and experiments of the adhesion force distribution between particles and a surface”. In: *Langmuir: the ACS journal of surfaces and colloids* 30.23 (2014), pp. 6808–6818.

[Yua13] Y. Yuan and T. R. Lee. “Contact Angle and Wetting Properties”. In: *Surface science techniques*. Ed. by G. Bracco and B. Holst. Vol. 51. Springer series in surface sciences. Berlin: Springer, 2013.

[Zha17] C. Zhang, Z. Liu, and Y. Dong. “Effects of adsorptive water on the rupture of nanoscale liquid bridges”. In: *Applied Clay Science* 146 (2017), pp. 487–494.

[Zha96] X. Zhang, R. S. Padgett, and O. A. Basaran. “Nonlinear deformation and breakup of stretching liquid bridges”. In: *Journal of Fluid Mechanics* 329 (1996), pp. 207–245.

A. Toroidal approximation for different geometries

The toroidal approximations are presented in the literature by various authors. Here, the equations are taken from Tselishchev and Val'tsifer [Tse03].

sphere-plate:

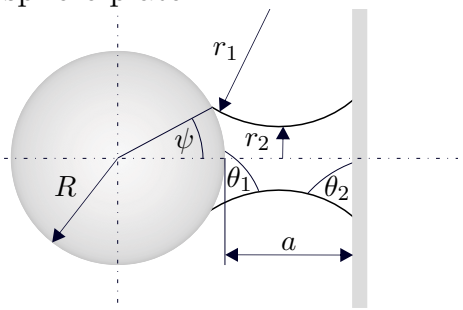

$$r_1 = -\frac{R(1-\cos\psi)+a}{\cos(\psi+\theta_1)+\cos\theta_2}$$

$$r_2 = R\sin\psi + r_1\left[1-\sin(\psi+\theta_1)\right]$$

$$F_\mathrm{c} = \pi\sigma R\sin\psi\left[2\sin(\psi+\theta_1) - R2H\sin\psi\right]$$

sphere-sphere:

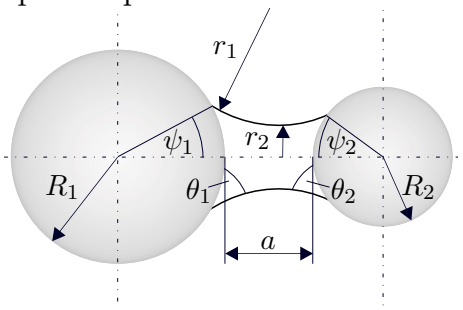

$$r_1 = -\frac{R_1(1-\cos\psi_1)+R_2(1-\cos\psi_2)+a}{\cos(\psi_1+\theta_1)+\cos(\psi_2+\theta_2)}$$

$$r_2 = R_1\sin\psi_1 + r_1\left[1-\sin(\psi_1+\theta_1)\right]$$

$$F_\mathrm{c} = \pi\sigma R_1\sin\psi_1\left[2\sin(\psi_1+\theta_1) - R_1 2H\sin\psi_1\right]$$

cone-plate:

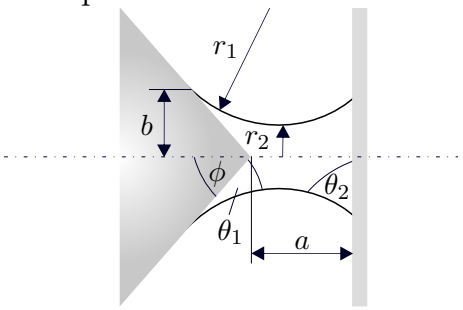

$$r_1 = -\frac{b(\tan\phi)^{-1}+a}{\sin(\phi-\theta_1)+\cos\theta_2}$$

$$r_2 = b + r_1\left[1-\cos(\phi-\theta_1)\right]$$

$$F_\mathrm{c} = \pi\sigma b\left[2\cos(\phi-\theta_1) - b2H\right]$$

cone-cone:

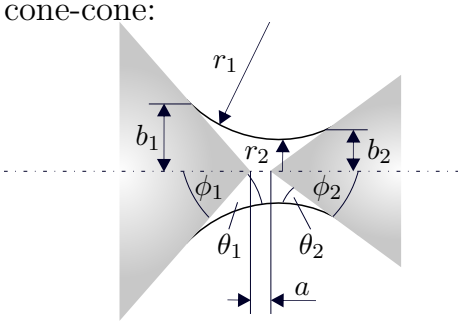

$$r_1 = -\frac{b_1(\tan\phi_1)^{-1} + b_2(\tan\phi_2)^{-1} + a}{\sin(\phi_1 - \theta_1) + \sin(\phi_2 - \theta_2)}$$

$$r_2 = b_1 + r_1\left[1 - \cos(\phi_1 - \theta_1)\right]$$

$$F_\mathrm{c} = \pi\sigma b_1\left[2\cos(\phi_1 - \theta_1) - b_1 2H\right]$$

plate-plate:

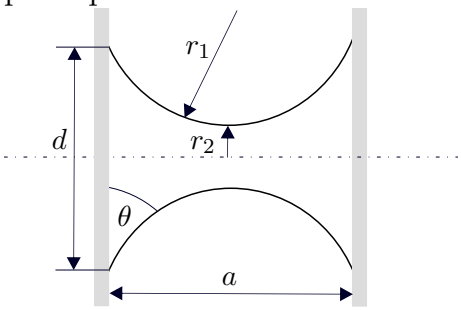

$$r_1 = -\frac{a}{2\cos\theta}$$

$$r_2 = \frac{d}{2} + r_1\left[1 - \sin\theta\right]$$

$$F_\mathrm{c} = \pi\sigma d\left[\sin\theta - \frac{dH}{2}\right]$$

B. Young-Laplace equation with gravity

In figure B.1 a capillary bridge is illustrated in an arbitrary coordinate system, however, the gravitational accelerating g acts in the z-direction. According to the Young-Laplace equation the pressure jump at the interface, i.e., the capillary pressure, is given by

$$\Delta p = p_\mathrm{i} - p_\mathrm{o} = \sigma 2H \qquad \text{and} \qquad \Delta p_0 = p_{\mathrm{i},0} - p_{\mathrm{o},0} = \sigma 2H_0 \tag{B.1}$$

for an arbitrary level at the interface and a reference level 0. Further more, the pressure differences in- and outside the interface are given by

$$p_{\mathrm{i},0} - p_\mathrm{i} = \rho_\mathrm{l} g z_0 - \rho_\mathrm{l} g z \qquad \text{and} \qquad p_{\mathrm{o},0} - p_\mathrm{o} = \rho_\mathrm{g} g z_0 - \rho_\mathrm{g} g z \tag{B.2}$$

where ρ_l and ρ_g are the densities of liquid and air, i.e., the densities in- and outside the interface. The difference between the mean curvatures is given by

$$\sigma 2(H_0 - H) = (p_{\mathrm{i},0} - p_{\mathrm{o},0}) - (p_\mathrm{i} - p_\mathrm{o}) | \text{ insert } B.2 \tag{B.3}$$

$$\Leftrightarrow \sigma 2(H_0) - H = (\rho_\mathrm{l} - \rho_\mathrm{g})(z_0 - z) \tag{B.4}$$

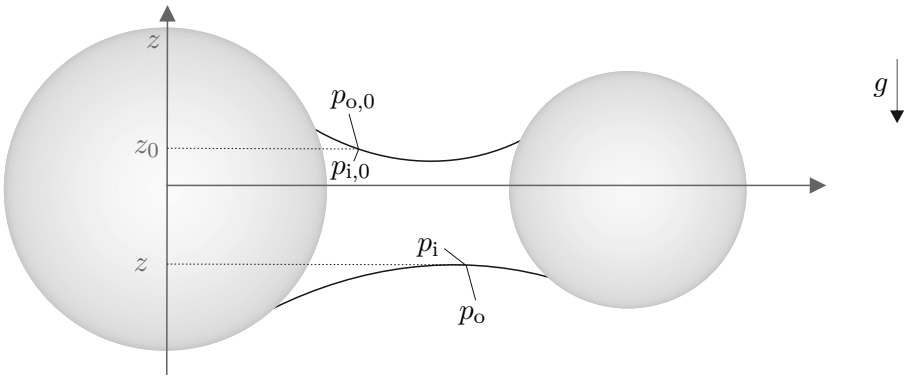

Figure B.1.: Illustration of a capillary bridge in a gravitational field

From this equation it directly follows that the curvature between the two levels must increase or decrease, respectively, according to the gravitational term. By inserting the pressure difference $\Delta p_0 = p_{\mathrm{i},0} - p_{\mathrm{o},0}$ at the reference level one obtains

$$\Delta p_0 + g(z - z_0)\,(\rho_\mathrm{l} - \rho_\mathrm{g}) = \sigma 2H \tag{B.5}$$

and only, if $z_0 \coloneqq 0$ this leads to often formulated equation

$$\Delta p_0 + (\rho_\mathrm{l} - \rho_\mathrm{a}) g z = \sigma 2H. \tag{B.6}$$

From this derivation is becomes clear, that z is distance in gravitational direction from a reference level, that must be on the interface, rather than a coordinate in an absolute reference frame, which is often not clearly pointed out. Thus, if the gravitational field is given by the three-dimensional vector $\mathbf{g}$, eq. B.5 is formulated in a more general way by

$$\Delta p_0 + \langle \mathbf{g}, \mathbf{s} - \mathbf{s}_0 \rangle\,(\rho_\mathrm{l} - \rho_\mathrm{g}) = \sigma 2H \tag{B.7}$$

where $\mathbf{s}$ and $\mathbf{s}_0$ are the position vectors of the interface level and $\langle ., . \rangle$ the scalar product, i.e., the proportion of $\mathbf{s} - \mathbf{s}_0$ in the direction of $\mathbf{g}$.

C. Boxplots sphere-plate

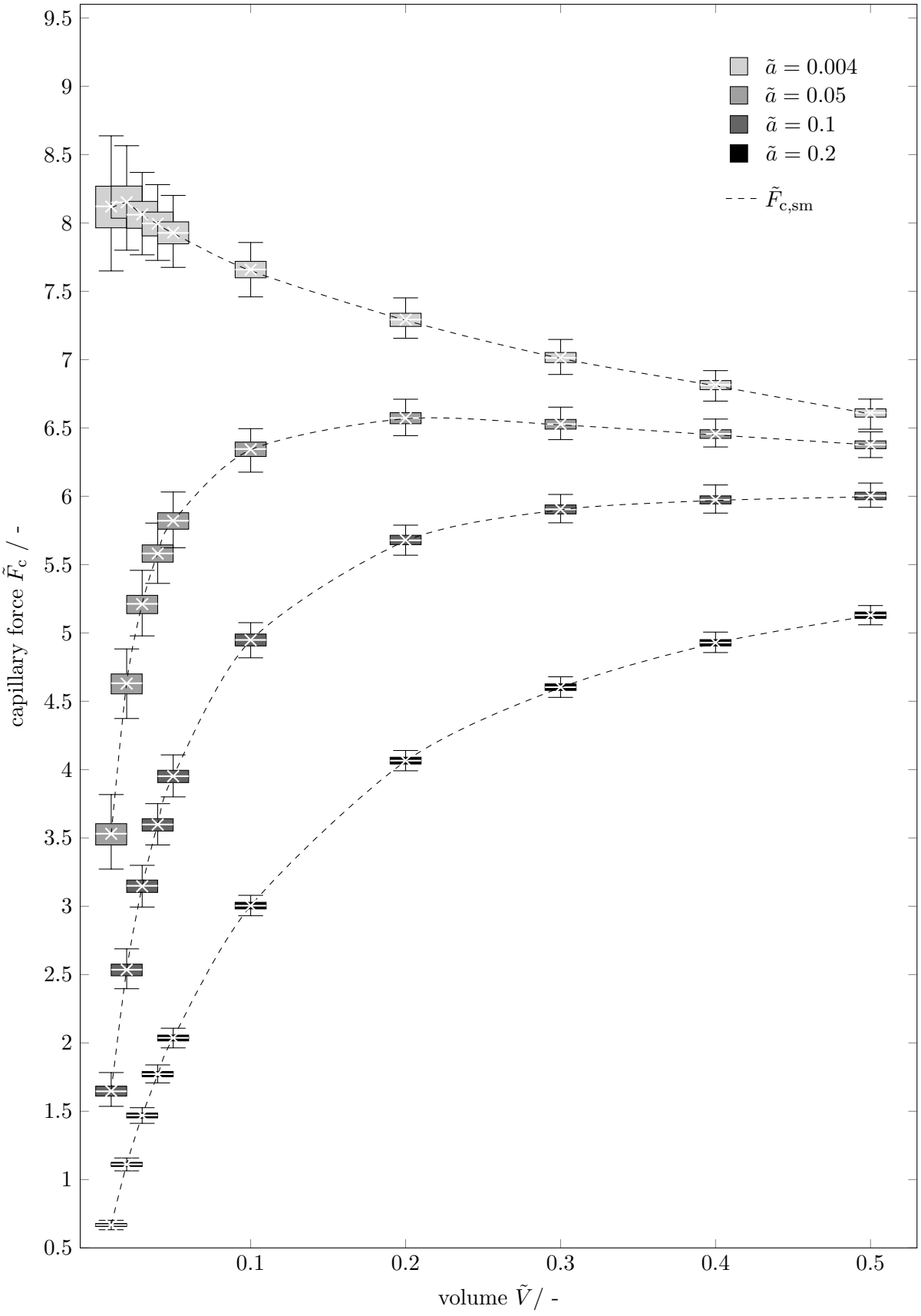

Figure C.1.: Volume dependent distributions of the capillary force $\tilde{F}_{\mathrm{c}}$ between a rough sphere and a smooth plate and different gap distances ($\theta = 40°$, $\tilde{\mathbf{S}}_{\mathrm{q}} = \mathbf{0.002}$ and $\varepsilon = 0.1$)

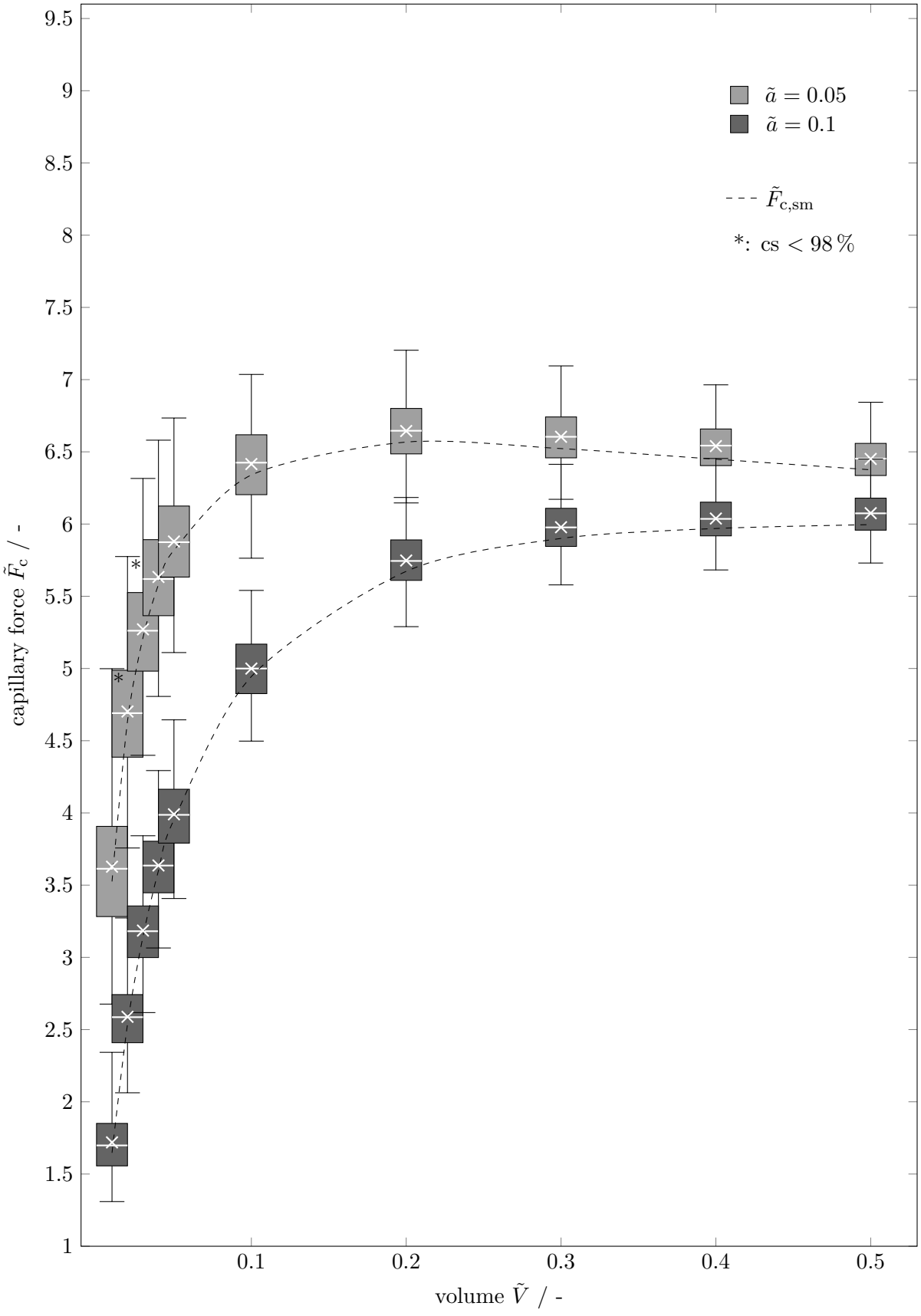

Figure C.2.: Volume dependent distributions of the capillary force $\tilde{F}_c$ between a rough sphere and a smooth plate and different gap distances ($\theta = 40°$, $\tilde{\mathbf{S}}_q = \mathbf{0.008}$ and $\varepsilon = 0.1$)

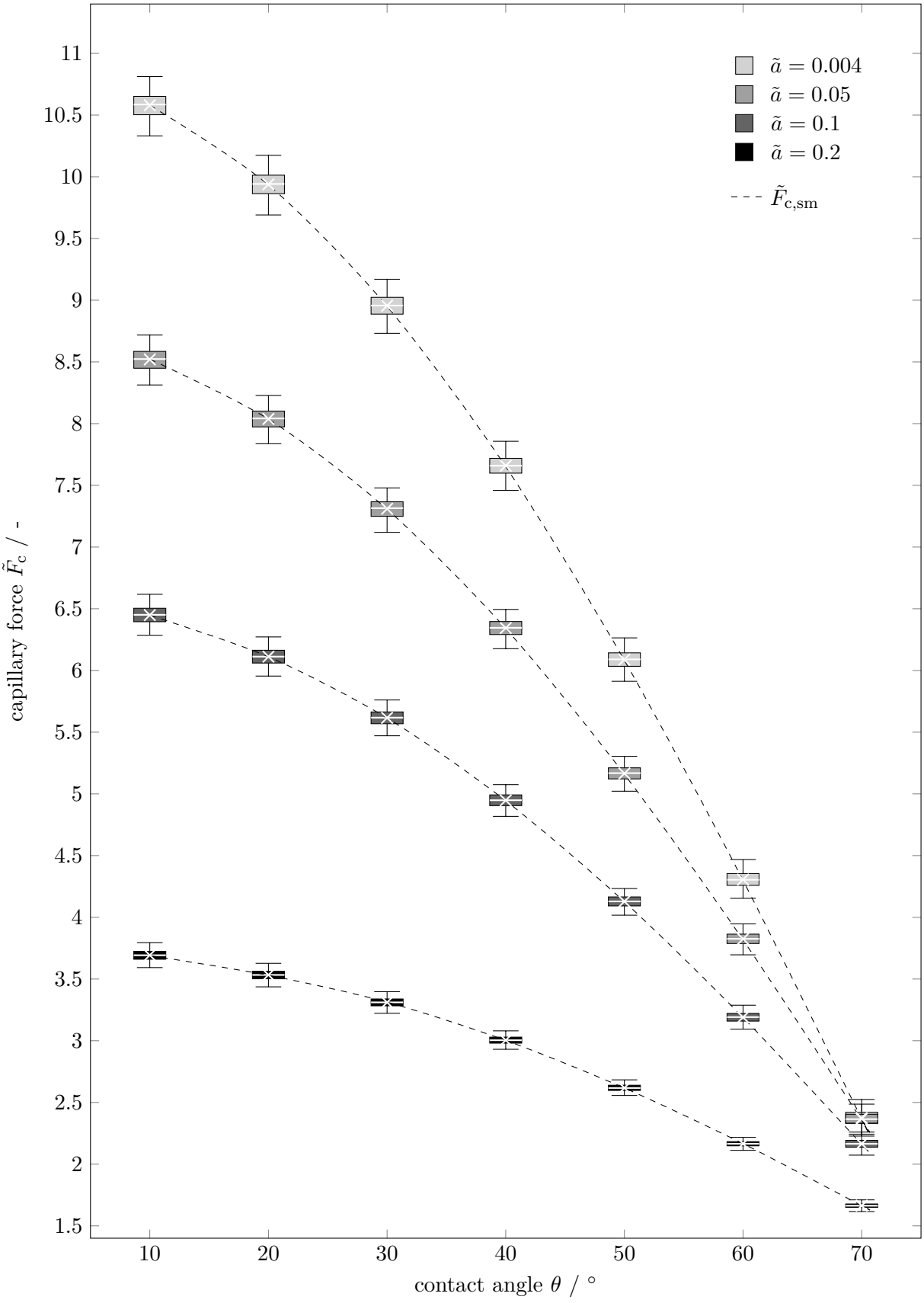

Figure C.3.: Contact angle dependent distributions of the capillary force $\tilde{F}_{\mathrm{c}}$ between a rough sphere and a smooth plate and different gap distances ($\tilde{V} = 0.1$, $\tilde{\mathbf{S}}_{\mathrm{q}} = \mathbf{0.002}$ and $\varepsilon = 0.1$)

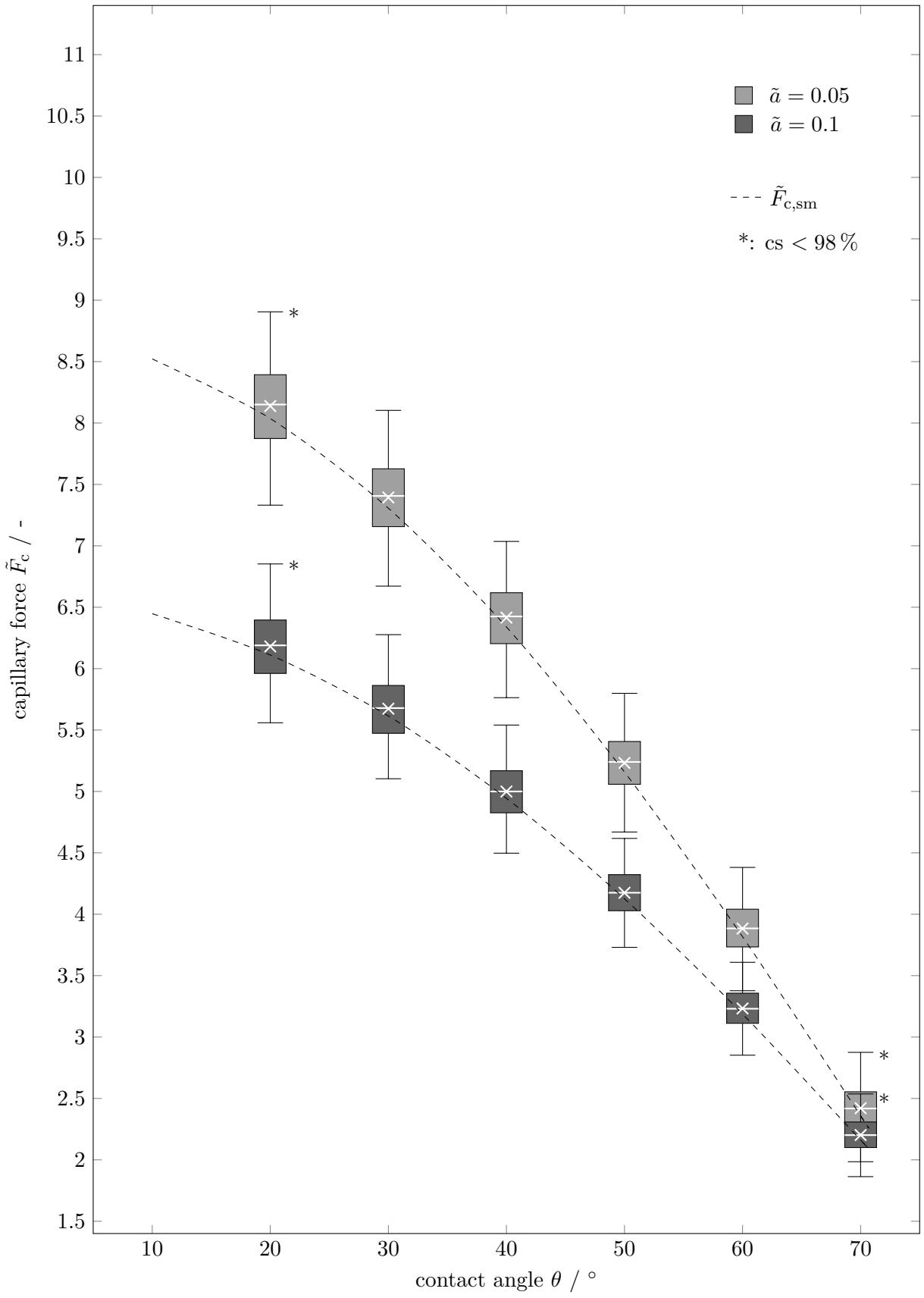

Figure C.4.: Contact angle dependent distributions of the capillary force $\tilde{F}_{\mathrm{c}}$ between a rough sphere and a smooth plate and different gap distances ($\tilde{V} = 0.1$, $\tilde{\mathbf{S}}_{\mathrm{q}} = \mathbf{0.008}$ and $\varepsilon = 0.1$)

Erklärung zur Zitation von Inhalten aus studentischen Arbeiten

In Ergänzung zu meinem Antrag auf Zulassung zur Promotion in der Fakultät für Maschinenbau der Universität Paderborn erkläre ich gemäß §11 der Promotionsordnung und unter Beachtung der Regelung zur Zitation studentischer Arbeiten:

Die von mir vorgelegte Dissertation habe ich selbstständig verfasst, und ich habe keine anderen als die dort angegebenen Quellen und Hilfsmittel benutzt. Es sind keine Inhalte studentischen Ursprungs (studentische Arbeiten) in dieser Dissertation enthalten.

Paderborn, 29. März 2023